UNIVERSITÀ DEGLI STUDI DI TRENTO

Doctoral School in Civil, Environmental and Mechanical Engineering

Topic 1. Civil and Environmental Engineering

Elena Tomasi

Improving air quality assessment over complex terrain by optimizing meteorological and pollutant transport modeling

2017 - Doctoral thesis

The Alpine region is a sensitive area to air pollution, as it presents specific characteristics, which expose it to a greater environmental burden with respect to flat areas. During the last decades, the scientific community has developed many different modeling tools to tackle the problem of air pollution. This issue demands at least three distinct procedures: the modeling of the meteorological fields, the modeling of the transport and dispersion of the pollutants and the modeling of the emitting sources. Each of these procedures performs differently across different space and time scales and carries its own strengths and weaknesses, which affect results in terms of pollutant dispersion patterns. The present work focuses on testing and improving different modeling tools at a local scale, over very complex topography, where most of them are brought to work at the limit of their applicability, but they are still the best available tools to face the problem. Different case studies are used in this research in order to evaluate strengths and deficiencies of the models and, where possible, to improve their performance. The experimental datasets used for this purpose come from both previously performed field campaigns and specifically designed campaigns, including meteorological and air quality observations. The performance of Land Surface Models within the Weather Research and Forecasting Model is evaluated and improved, focusing on their ability in reproducing near-ground variables, with specific attention to the frequent ground thermal inversion occurring in the mountainous areas. The performance of dispersion models recommended for applications over complex terrain is also tested and their results are compared with unique measurements (PM10 vertical profiles and tracer gas ground concentration), under challenging wintertime conditions. Atmospheric turbulence parameterizations are also analyzed, in order to understand their role and effects in a modeling chain for dispersion assessment purposes.

Elena Tomasi received her Master's egree in Environmental Engineering with honours in 2013, at the University of Trento, Italy. She attended the Doctoral School in Civil, Environmental and Mechanical Engineering of the University of Trento in the field of atmospheric sciences (FIS06) from 2014 to 2017. Her main research focus is the numerical modeling of pollutants' dispersion in the atmosphere, over complex terrain. In this context, her major research interests include boundary layer processes, turbulence in compressible fluids and energy exchanges at the ground-atmosphere interface. During her Ph.D., she spent six months at the National Center for Atmospheric Research, Boulder, Colorado, as a visiting student of the Advanced Study Program. During this period, she worked on the interaction between meteorological and dispersion models, with specific focus on the turbulence parameterizations involved in the Planetary Boundary Layer and dispersion schemes.

UNIVERSITY OF TRENTO - Italy
Department of Civil, Environmental and Mechanical Engineering

Doctoral School in Civil, Environmental and Mechanical Engineering
Topic 1. Civil and Environmental Engineering - XXIX cycle 2014/2016

Doctoral Thesis - December 2017

Elena Tomasi

Improving air quality assessment over complex terrain by optimizing meteorological and pollutant transort modeling

Supervisors
Prof. Dino Zardi, University of Trento
Co-supervisor
Lorenzo Giovannini, University of Trento

Credits of the cover image Elena Tomasi 2016

University of Trento
Doctoral School in Civil, Environmental and Mechanical Engineering
http://web.unitn.it/en/dricam
Via Mesiano 77, I-38123 Trento
Tel. +39 0461 282670 / 2611 - *dicamphd@unitn.it*

To all those who believed
this one was my way
and kept me on track.
And to Ray,
who all along this way
always kept me safe.

Acknowledgments

First of all I would like to thank my supervisors Prof. Dino Zardi and Eng. Lorenzo Giovannini for their great help and constant support in my research.

Thanks to Eng. Gianluca Antonacci, who helped me and followed me in my approach to the pollutants' dispersion modeling and always gave me the best IT support.

Thanks to Prof. Enrico Ferrero, and Dr. Stefano Alessandrini for their invaluable help and assistance for the usage of the SPRAYWEB model and for the fruitful discussions on my research.

Thanks also to Dr. Branko Kosovic for hosting me at NCAR for my Advanced Study Program six-month visit and for his great help in running my WRF simulations.

The Agrometeorological Unit of the Edmund Mach Foundation, The Meteorological Office of the Autonomous Province of Trento, The Meteorological Office of the Autonomous Province of Bolzano and the Environmental Agency of the Provinces of Trento and Bolzano (APPA TN and APPA BZ) are kindly acknowledged for data from their weather stations.

Contents

List of Figures

List of Tables

Chapter 1

Introduction

The main focus of this thesis work is the air quality assessment over complex terrain, which is a relevant issue for both social and scientific motivations.

Mountainous regions are particularly sensitive to air quality issues because of their specific and peculiar environment and conformation. On one side, mountainous areas, such as the Alps (specific focus of this research), host unique and rich ecosystems, which are sensitive to external stresses, such as atmospheric pollution. On the other side, the topography of mountainous regions led to a specific distribution of the population, and a consistent distribution of human activities, which cause an increased exposure of receptors to air pollution, with respect to flat regions. Indeed, most of the population living in mountainous regions is concentrated along the main valley floors, along with most of the human activities: transport infrastructures (motorway and railways), small industries, recreational and disposal plants. Moreover, the volume of air available for the dispersion of pollutants is highly reduced by the complex topography of these areas, which often develops deep and narrow valleys. As a result, a large part of the population of mountainous regions live very close to important pollution sources and is exposed to at-

mospheric pollution episodes enhanced by the complex terrain, with relevant repercussions on its health and general well being (Heimann et al., 2007). For these reasons the impact of atmospheric pollution is heavier in mountainous regions than over flat terrain.

In this context, air quality studies performed with coupled meteorological and dispersion models are increasingly needed, when careful environmental analyses, such as ambient air quality monitoring, environmental impact assessments of new plants, and evaluations of the effectiveness of new corrective actions have to be carried out. Nevertheless, such applications over complex terrain still pose many challenges, due to the inherent difficulties in accurately modeling both atmospheric and dispersion processes. Usually for dispersion simulations, especially over complex terrain, the modeling approach consists of three main components: (i) the production of 3D meteorological fields, (ii) the transfer of these meteorological fields to the dispersion model, and (iii) the calculation of the pollutants' dispersion. Complexities in each of these steps result aggravated over complex terrain.

First, when mesoscale numerical weather prediction (NWP) models are used to produce the meteorological fields a very high resolution is needed to properly capture the characteristics of the complex topography. In addition, complex terrain develops many local terrain-induced and thermally-driven phenomena which are hard to capture and to properly describe for the numerical models (Steyn et al., 2013), even at a high resolution, but are at the same time critical for the realization and identification of air pollution episodes. Examples of these typical mountainous meteorological phenomena are the ground-based thermal inversions and the up- and down-valley winds. The former are usually associated with wind calms and trap the released pollutants near the ground, impeding their fast dilution above the valleys' crests; the latter can lead to pollutants'

re-circulation episodes, carrying back and forward the contaminants channeled in the valleys (Whiteman, 2000). The proper identification of these phenomena depend on many different schemes implemented in the numerical meteorological models, from the land surface scheme (which calculates the mass and energy surface fluxes), to the planetary boundary layer scheme (which treats the atmospheric turbulence).

As to the dispersion modeling, the presence of these specific meteorological conditions imposes that the dispersion models applied over complex terrain are able to deal with atmospheric heterogeneity and non-steady-state conditions. Traditional Gaussian models are inadequate for these kind of applications, while more complex puff-Gaussian models are recommended in this context for operational purposes (EPA, 2005). Nevertheless, different research studies suggest that even more sophisticated dispersion models, such as Lagrangian models, are needed over complex terrain to properly capture the effects of complexities of the atmospheric fields on the dispersion patterns (Szintai et al., 2010; Alessandrini et al., 2005). In addition, the performance of a dispersion model also relies on the characterization of the atmospheric turbulence, which is usually performed by a meteorological pre-processor, producing the turbulence-related variables.

Meteorological preprocessors for dispersion models can derive turbulence parameters from observations, from the mean meteorological fields received as input or directly from the external NWP model. The accurateness on this information heavily influences the overall performance of the dispersion models and strictly depends on the reliability of the parameterizations used to obtain turbulence characteristics. In most cases, meteorological preprocessors apply a form of similarity approach (Hanna, 1982; Scire et al., 2000b), where the standard turbulence characteristics are derived from surface layer scales. Nevertheless, most of this relations were derived from data

sets and experiments for flat terrain, where the turbulence structure is much different from the one over complex terrain. Alternative, experimental approaches for the calculation of turbulence parameters directly use information (e.g. the turbulence kinetic energy) from the NWP model planetary boundary layers schemes. These approaches directly rely on the accuracy of the PBL schemes and their ability to properly describe the atmospheric turbulence over complex terrain.

In this thesis work, different aspects of the modeling chain to simulate atmospheric pollutant dispersion are addressed, with the aim of identifying, developing and improving the practices to approach this problem over complex terrain in real cases. Chapter 2 presents the most relevant theoretical aspects. Chapter 3 provides an overview of the different data sets used to evaluate or to optimize the results of the analyses conducted. Chapter 4 is devoted to the optimization of the modeling of wintertime meteorological phenomena, which are relevant for atmospheric dispersion, over complex terrain, with specific focus on the treatment of snow cover in land surface schemes. Chapter 5 compares different modeling approaches for the study of a local source emission over complex terrain, highlighting the deficiencies of standard recommended approaches. In the last Chapter (Chapter 6), the attention is focused on the comparison of different approaches used to obtain the turbulence structure, in different dispersion models.

Chapter 2

Modeling pollutant dispersion over complex terrain

2.1 Air quality and mountain boundary layer meteorology

The fate of a pollutant emitted by human activities or natural sources depends on the meteorological conditions of the atmosphere in which it is released. Specifically, the dispersion of the pollutant is a result of the transport generated by the mean wind flow, of the diffusion generated by the atmospheric turbulence within the boundary layer and of chemical reactions that can occur. As both the main sources of air pollution and the receptors happen to reside in the atmospheric boundary layer, its characteristics are the main focus and concern for air dispersion modeling. In this very peculiar region of the atmosphere, the flow and the turbulence fluxes are strictly influenced by the interaction of the atmosphere with its underlying surface. Indeed, the surface acts as a source and sink of energy and momentum to the

atmosphere (Businger, 1982), directly affecting its turbulent structure in terms of temperature, wind speed and scalar content (e.g. the moisture content).

Over flat terrain the boundary layer is horizontally uniform in space and develops with a well defined daily cycle, which allows a rather easy prediction of its structure characteristics. During the day, the uniform irradiation of the surface leads to the formation of a 1-2 km-thick well mixed boundary layer, where turbulence is fully developed and the convection is enhanced; otherwise, during nighttime, the surface cooling leads to the development of a stable layer, where vertical mixing is limited and turbulence decays (Steyn et al., 2013).

On the contrary, over complex terrain, the structure of the boundary layer varies in space and time and the development of locally driven phenomena (e.g. up- and down-slope flows, ground-based thermal inversions) can highly influence its structure, by enhancing or suppressing the turbulent mixing. The flows, and therefore the boundary layer structure, over mountainous areas are highly influenced by the complex orography, which develops both terrain-forced flows and thermally driven circulations, arising from differential heating of neighboring regions (Whiteman, 2000). Examples of these flows are the Foehn winds for the terrain-forced flows, and the slope winds, the along- and cross-valley wind systems and the mountain-plain wind systems for the thermally driven circulations. The coexistence and interaction of these phenomena over many time and space scales complicates and alters the atmospheric dispersion of pollutants and it is often difficult to asses whether their presence positively contribute to the dispersion or not. Indeed, while the terrain-induced flows are usually strong enough to enhance the dispersion of pollutants and clean the atmosphere, the role of thermally driven flows is much more uncertain. For example, the diurnally forced

winds over mountainous areas are usually persistent, and guarantee a rather constant ventilation of the region. Nevertheless, on the other hand, their cyclic nature can lead to a re-circulation of locally emitted pollutants, their long-range scale can enhance the advection of pollutants emitted elsewhere and their structure can lead to repeated cases of fumigation of the valley walls.

One of the most critical phenomenon for air quality issues, typical in mountainous areas, is the formation and persistence of ground-based thermal inversions. This phenomenon usually develops in wintertime, when nights are particularly long, sky is clear and wind speeds are very low. Under these conditions the valley floor is subject to strong surface cooling and the katabatic flows along the sidewalls drain cool air to the valley bottom, creating a cold-air pool. As temperature increases with height, the atmosphere is strongly stratified, the turbulent mixing is suppressed and the pollutants remain trapped and undiluted in a limited volume of air. These structures often persist in mountain valleys and basins for many days because, during wintertime, the diurnal irradiance is too weak to produce convection and to breakup the inversion and only synoptic forcing (i.e. cold fronts or Foehn winds) is therefore able to remove it. The effects of ground-based thermal inversions are even worsened by the fact that the conditions leading to their formation are the same that tend to enhance the emissions of pollutants at the ground: wintertime cold nights usually invite the population to increase the use of domestic heating, which, in mountainous area such as the Alpine valleys, is often represented by biomass burning. In addition, ground-based thermal inversions are often poorly simulated by meteorological models, together with the calm wind conditions that enhance them. Indeed, in order to properly simulate it, meteorological models must run at very high resolutions and must be able to properly resolve local processes, accurately describe the interaction between the surface and

the atmosphere, and apply turbulence parameterizations suitable for stable conditions.

The complexities introduced by the mountainous terrain in the meteorological fields are therefore many and diverse, and they are still challenging to capture for the most advanced and state-of-the-art meteorological models (Steyn et al., 2013). In addition to this, issues arise from the dispersion modeling also, as most of the traditional dispersion models (Gaussian models especially) and their turbulence parameterizations have been developed for applications over flat terrain, under horizontal homogeneous conditions. On the contrary, over complex terrain, a dispersion model must be able to deal with the inhomogeneity of the meteorological fields, in order to capture the complexity of the dispersion patterns.

2.2 Modeling approach for local scale air pollution episodes

The present work focuses on meteorological and air quality modeling over complex terrain, at a local scale. The main aim of the analysis is to test, select and possibly improve available modeling instruments for the simulation and evaluation of air pollution episodes in mountainous areas, from locally-emitted pollutants. For this reason, it is useful to clarify which approaches are more common and more effective for these kind of studies, and which variables are of primary importance. Interestingly, as will be shown in the present work, often happens that community-approved models for applications over complex terrain show flaws and deficiencies when brought to specific applications in this peculiar context (Szintai et al., 2010; Alessandrini et al., 2005). For this reason, a continuous testing and evaluation of these instruments is of essential importance, as it can improve the understanding of the application limits of the models and, sometimes,

it can lead to an optimization of the models themselves.

The factors that determine the concentration of a locally-emitted non reacting pollutant, at ground level, are essentially three: (i) the characteristics of the sources of that specific pollutant, (ii) the mean wind field and (iii) the atmospheric turbulence, described by means of the statistical properties of the meteorological field. These three factors are responsible, respectively, (i) for the total amount of pollutant present in the atmosphere (and its initial spatial distribution), (ii) for the transport of the pollutant along preferential trajectories and with specific speeds, and (iii) for the turbulent diffusion of the substance around the main flow direction. From a modeling point of view, the way through which these three factors are calculated and combined together determines the quality of the final results in terms of ground concentrations.

The modeling of the emission sources strictly depends on the type of case study, on its time-scale and on the availability of data and information in the specific region. When air quality dispersion studies are carried out for a single specific source (e.g. environmental assessment studies for new plants), emission rates and characteristics are usually known and the uncertainty on the final results related to the emission factor is basically removed (an example of this case is presented in Chapters 3 and 6). On the contrary, when the attention is focused on more than one source (e.g. analyses of critical air pollution episodes), it is unlikely that the emission rate of each single source is given. In these cases, the uncertainty on the emissions rapidly grows as many approximations must be applied: for the sake of computational timing, only the most relevant sources are selected for the simulation, some of them are grouped, each source is given a geometric fictitious shape, and each one is assigned an emission rate. The standard approach to calculate this emission rate is to use annual-average emission rates coming from available national inven-

tories and to modulate them over time (and potentially over space) on the basis of the specific case study requirements. An example of this procedure in presented in Chapter 4, Section 4.2, where the uncertainties relative to the emission sources are minimized following European standard procedures.

The meteorological field for an air quality dispersion simulation can come from very different models, with very different degrees of confidence. It is not uncommon to drive air dispersion simulations with diagnostic meteorological fields, obtained by means of diagnostic meteorological models. This technique allows the calculation of a 3D meteorological field from observed data in different locations by weather stations and other meteorological instruments. The model essentially interpolates and extrapolates the measurements over the domain, taking into account physical constrains such the mass conservation or the divergence minimization. The reliability of the results is strictly related to the quality and quantity of the observations given as input. While this method is very fast and easily applicable over different areas, it usually produces poor results over complex terrain, where the coexistence of many different local phenomena is hardly properly represented by a limited number of observations (an example of the application of this technique and its results over complex terrain is presented in Chapter 5). A second option to obtain the meteorological field is the application of full-physics prognostic numerical models (e.g. the Weather Research and Forecasting (WRF) model). These models allow the calculations of 3D meteorological fields from the basic conservation equations for atmospheric flows, a set of specified parameterizations and given boundary and initial conditions. These models require much more computational time to be run, especially if they are applied over complex terrain, where high resolution is required to properly identify the local processes. Nevertheless, they present at least three relevant advantages: they

have prognostic capability, they provide physically consistent mean meteorological fields, and they can provide additional information from which the standard deviations of the mean flow can be calculated (e.g. scaling velocities and temperatures, turbulent kinetic energy, dispersion coefficients). These variables are derived by different schemes implemented in the meteorological model and can be very useful for the dispersion model in order to calculate atmospheric dispersion rates, as explained in the following.

Given a detailed description of the emission sources and a trustworthy meteorological mean field, the role of a dispersion model is that to combine these information, to calculate the atmospheric dispersion rates and to produce results in terms of pollutant concentration. Many different types of dispersion models have been developed in the past decades, following different approaches to the problem of pollution dispersion. Among the others it can be cited the Gaussian models, the Gaussian-puff models and the Lagrangian particle models (Zannetti, 2005), which are of direct interest for the present work.

It is interesting to notice that, no matter the theories on which these models were developed, they all depend on the same boundary layer turbulence parameters (Hanna, 1982) for the calculation of the atmospheric dispersion. Specifically, the parameters that are useful for the dispersion modeling are (i) the mean wind velocities U, V and W, (ii) the standard deviations of the wind field σ_U, σ_V and σ_W and (iii) the associated time scales T_U, T_V and T_W. While the mean flow velocity must for sure be provided by the meteorological model, the turbulence characteristics of the field are calculated or obtained in different ways by different dispersion models. Information on the turbulence structure can be directly extracted from measured data, internally calculated from scaling variables (which can be again either internally calculated from the mean flow with a micrometeoro-

logical parameterization or extracted from an external meteorological model) or extracted from the meteorological model. The procedure to calculate the turbulence parameters usually implies a process of parameterization, for any kind of dispersion model. Nevertheless, the degree of uncertainty in the calculation of these quantities can be reduced, for example, by using the most physically-based available information, i.e. the one provided by the prognostic meteorological model (if available). Chapter 6 of this work presents a sensitivity analysis of different dispersion models to the calculation of turbulence parameters. In the following sections of this chapter, instead, more detailed information are given on the procedure followed by the models utilized in this work for the calculations of the turbulent parameters.

Even if all the dispersion models basically rely on the above mentioned boundary layer turbulence parameters, the mathematical structure of each model plays a fundamental role in its performance, as each model uses specific turbulence parameters and in different ways. In this sense the distinction between Gaussian and Lagrangian models is of essential importance, especially over complex terrain, as their capabilities are tested in very difficult conditions.

2.3 Modeling of the atmospheric boundary layer

As atmospheric diffusion is a direct result of atmospheric turbulence (Hanna, 1982), the boundary layer is the main focus when dealing with air pollution dispersion. The modeling of this specific portion of the atmosphere is usually dealt by meteorological models, but sometimes it is the dispersion model itself that takes care of applying specific parameterizations to the mean flow in order to provide the turbulence parameters. While the latter case is discussed in the following Section 2.4, this Section presents the most common pro-

cedures used to calculate the boundary layer characteristics within a prognostic numerical model, together with their advantages and deficiencies. The meteorological model used in the present thesis is the Weather Research and Forecasting (WRF, Skamarock et al. (2008)): for this reason, in this Section the parameterizations used within this specific model to treat the boundary layer region and to calculate its turbulent parameters are presented.

The WRF model is a state-of-the-art numerical weather prediction (NWP) model developed for both research and operational activities at the National Center for Atmospheric Research (NCAR, Boulder CO). Many other research centers and laboratories contribute to the development of WRF: the National Centers for Environmental Prediction (NCEP), the Earth System Research Laboratory (ESRL) of the National Oceanic and Atmospheric Administration (NOAA), the Air Force Weather Agency (AFWA), the Naval Research Laboratory (NRL) of the Department of Defence (DOD), the Center for Analysis and Prediction of Storms (CAPS) of the University of Oklahoma and the Federal Aviation Administration (FAA). The scientific community developing and applying WRF is very wide and guarantees that this instrument is always up-to-date with the new advances in the understanding of the physics of the atmosphere (Dudhia, 2011a).

The WRF model numerically solves the Euler equations for a compressible fluid, in non-hydrostatic conditions, written in a terrain following reference system:

$$\eta = \frac{p_{dh} - p_{dht}}{\mu_d} \qquad \text{with} \qquad \mu_d = p_{dhs} - p_{dht} \tag{2.1}$$

where μ_d is the dry mass per unit area (kg m^{-2}) within the column in the model domain, p_{dh} is the hydrostatic component of pressure of the dry atmosphere and p_{dhs} and p_{dht} are the values at the surface and at the top boundary respectively. The Euler equations are recalled in

Equations from 2.2 to 2.10:

- Conservation equation for dry-air mass:

$$\partial_t \mu_d + (\nabla \cdot \mathbf{V}) = 0 \tag{2.2}$$

- Conservation equations for momentum:

$$\partial_t U + (\nabla \cdot \mathbf{V}u) + \mu_d \alpha \partial_x p + \frac{\alpha}{\alpha_d} \partial_\eta p \partial_x \phi = F_U \tag{2.3}$$

$$\partial_t V + (\nabla \cdot \mathbf{V}v) + \mu_d \alpha \partial_y p + \frac{\alpha}{\alpha_d} \partial_\eta p \partial_y \phi = F_V \tag{2.4}$$

$$\partial_t W + (\nabla \cdot \mathbf{V}w) - g\left(\frac{\alpha}{\alpha_d} \partial_\eta p - \mu_d\right) = F_W \tag{2.5}$$

- Conservation equation for energy:

$$\partial_t \Theta + (\nabla \cdot \mathbf{V}\theta) = F_\Theta \tag{2.6}$$

- Material derivative of the geopotential:

$$\partial_t \phi + \frac{1}{\mu_d}\left[(\mathbf{V} \cdot \nabla \phi) - gW\right] = 0 \tag{2.7}$$

- Diagnostic relation for the inverse density:

$$\partial_\eta \phi = -\alpha_d \mu_d \tag{2.8}$$

- Equation of state for moist air:

$$p = p_0 \left(\frac{R_d \theta_m}{p_0 \alpha_d}\right)^\gamma \tag{2.9}$$

- Conservation equation for moisture:

$$\partial_t Q_m + (\nabla \cdot \mathbf{V}q_m) = F_{Q_m} \tag{2.10}$$

where: $\mathbf{V} = \mu\mathbf{v} = (U, V, W)$, being $\mathbf{v}$ the 3D covariant velocity vector; θ is the potential temperature and $\Theta = \mu_d\theta$; $\phi = gz$ is the geopotential, being g and z the gravitational acceleration and the vertical coordinate; p is the atmospheric pressure; $\alpha_d = 1/\rho_d$ is the specific volume; p_0 is a reference pressure, R_d is the gas constant in the state equation for dry air; $\gamma = c_p/c_v = 1.4$ is the ratio of the specific heats for dry air; α is the specific density taking into account the full parcel density $\alpha = \alpha_d(1 + q_v + q_c + q_r + q_i + ...)^{-1}$, being q_* the mixing ratios (mass per unit of dry air) for water vapor, cloud, rain, ice, etc; $\theta_m = \theta(1 + (R_v/R_d)q_v) \approx (1 + 1.61q_v)$; $Q_m = \mu_d q_m$ with $m = v, c, i, ...$; and F_i are the external forcing (the Coriolis, curvature, mixing terms and physical forcing; Wang et al., 2013).

The model solves these equations on an Arakawa-C grid staggered in space, obtaining scalars in the grid-cell centers and the vectors on the grid-cell sides. The model uses time-split integration to

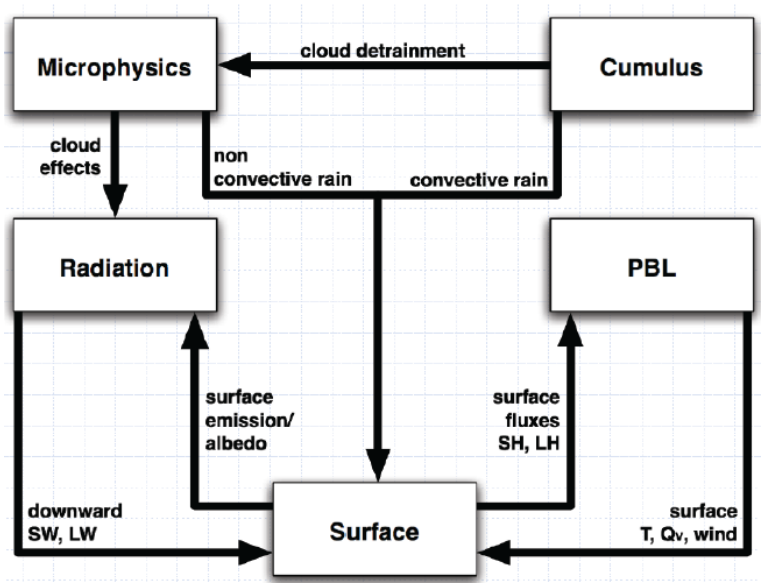

Figure 2.1: Interactions among the physics categories in the WRF model (Dudhia, 2011b).

solve the governing equations: the third-order Runge-Kutta time integration scheme is applied for slow or low-frequency modes while an integration over smaller time steps is performed for high-frequency acoustic modes.

	Variable	**RAD**	**MP**	**CP**	**PBL**	**SFC**
Atmospheric State or Tendencies	Momentum			I	I/O	
	Pot. Temp.	I/O	I/O	I/O	I/O	
	Water Vapor	I	I/O	I/O	I/O	
	Cloud	I	I/O	O	I/O	
	Precip	I	I/O	O		
Surface Fluxes	LW Up	I				O
	LW Down	O				I
	SW Up	I				O
	SW Down	O				I
	Sfc Cnvct Rain			O		I
	Sfc Res. Rain		O			I
	Heat Flux				I	O
	Moisture Flux				I	O
	Surface Stress				I	O

Table 2.1: Adapted from Wang et al. (2013). Physics Interactions. Columns correspond to model physical processes: radiation (RAD), microphysics (MP), cumulus parameterization (CP), planetary boundary layer/vertical diffusion (PBL), and surface physics (SFC). Rows corresponds to model variables where I and O indicate whether a variable is input or output (updated) by a physical process.

The solution of the Euler equations allows the calculation of the mean wind field U, V and W, which constitutes the essential information for pollutant dispersion analyses. The mean wind field is indeed what drives the transport of pollutants in any kind of dispersion model. Nevertheless, a meteorological prognostic model is able

to provide many more information about the conditions of the atmosphere. Ineed, in order to solve the governing equations, the NWP model has to rely on a relevant number of parameterizations. These parameterizations are necessary in order to describe all those physical processes which cannot be explicitly resolved by the model, as they realize at too small or too fast spatial and temporal scales, or they are too complex to be mathematically described. Results from these parameterizations strongly influence the calculation of the meteorological variables in the WRF model, as they intervene on the forcing terms of the governing equations, and, in addition, they produce information on many other secondary variables. Within WRF, 6 different categories of physics parameterizations are implemented: (1) the microphysics, (2) the cumulus parameterization, (3) the planetary boundary layer (PBL), (4) the land-surface model, (5) the radiation and (6) the diffusion. All these parameterizations directly influence the main equations and interact one with each other. Figure 2.1 and Table 2.1 try to summarize these interactions in the WRF model, in order to clarify the role of each parameterization.

In the present work, the attention is focused on the role of the surface and PBL parameterizations. Specifically, three schemes are described in the following: the land surface scheme, responsible for the calculation of the land-surface fluxes directly used as input from the PBL scheme, the surface layer scheme, responsible for the calculation of the friction stresses at the atmosphere-land interface, and the PBL scheme, responsible for the calculation of turbulent fluxes and vertical diffusion. The flow chart presented in Figure 2.2 summarizes the interactions among these three physics schemes, which will be further explained in the following sections.

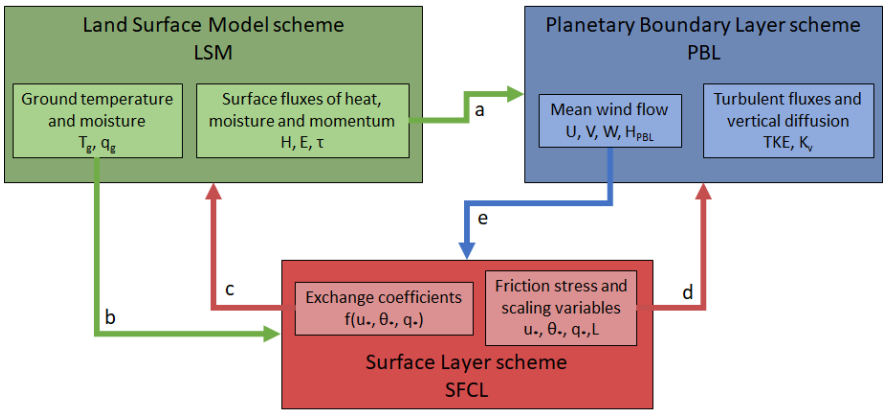

Figure 2.2: Interactions among the three analyzed physics categories in the WRF model.

2.3.1 Role of the Land Surface Scheme

The role of the land surface model (LSM) within WRF is to calculate the energy and mass fluxes at the interface between the ground and the atmosphere. This model is of fundamental importance as:

- it regulates the interaction of the atmosphere with its only physical boundary;
- it allows the calculation of energy and mass fluxes at a smaller spatial scale with respect to the numerical grid;
- it directly drives the PBL scheme, which reads the surface fluxes as boundary conditions and is very sensitive to this information;
- it allows the simulation local phenomena which are driven and fed by the variability of ground variables, such as the surface albedo, the ground temperature, the soil moisture and the snow cover.

The land surface model represents a very complex tile of the meteorological model, especially when applied at very high resolutions, as

happens for simulations over complex terrain. In these conditions, the information relative to the surface characteristics is essential to guarantee reliable results but, at the same time, it is unlikely to find at the desired resolution. This problem is discussed in Chapter 4, where examples of the effect of an erroneous initialization of snow cover are analyzed.

The LSMs use information about both the atmosphere and the soil as input variables. Input concerning the atmospheric conditions comes from other WRF parameterizations: the condition of the flow from the surface layer scheme and the PBL scheme, the radiative forcing from the radiation scheme, the precipitation rates from the microphysics and cumulus parameterizations (see Figure 2.1 and Table 2.1). Information regarding the surface characteristics comes from the boundary conditions set by the user during the initialization process of the model and include: the land use cover, the vegetation type cover, the topography, the snow cover, the soil moisture, etc.. Many other characteristics are needed to run the LSMs, such as the albedo of the surface, the maximum albedo, the vegetated fraction of each cell, but they are listed as function of the main input data within the WRF model.

The LSMs combine all this information in order to calculate the mass and energy surface fluxes, by iteratively solving the energy and mass balances at the surface with the temperature and moisture as unknowns. In particular, the main results of these schemes are:

- the sensible heat flux

$$H = \rho c_p u_* \theta_* \tag{2.11}$$

- the latent heat flux;

$$E = \rho u_* q_* \tag{2.12}$$

- the momentum flux

$$\tau = \rho u_*^2 \tag{2.13}$$

- the outgoing short- and longwave radiation;

where ρ is the air density, c_p is the air heat capacity at constant pressure, u_* is the friction velocity, θ_* is the surface-layer temperature scale and q_* is the surface-layer humidity scale. All these variables are very relevant for the atmospheric dispersion, as they directly influence the results of the PBL parameterization (Figure 2.2, a). Other variables are also generated from the LSM, such as the ground temperature and moisture. These variables are very important as well, as they are essential parameters in the application of the similarity theory performed by the surface layer scheme (Figure 2.2, b). In addition, it must be noted that the surface fluxes depend on the scaling variables u_*, θ_* and q_* calculated by the surface layer scheme (Figure 2.2, c): these two parameterizations therefore act as source and sink of information one to the other.

Many different LSMs are available in the WRF model for the user to choose, on the basis of the specific case study. They differ in many aspects of the treatment of the surface, for example by taking into account one or more layers of soil and of snow, considering or not the presence of vegetation, treating the cell as whole unit or subtiling it, etc.. In the present thesis, two land surface models are applied for different case studies: the *Noah Land Surface Model* (Noah LSM - Chen and Dudhia (2001)) and the *Noah Land Surface Model with MultiParametrization options* (Noah_MP LSM - Niu et al. (2011)). These models have been consecutively developed, and the Noah_MP model is an augmentation of the previous, simpler model. The characteristics of these two models, which is mostly of interest for this work, are presented in detail in Chapter 4.

2.3.2 Role of the Surface Layer Scheme

The surface layer scheme deals with the transfer of information from the ground surface to the atmosphere. Its role is to calculate friction velocities and exchange coefficients to be given to the LSM to calculate the surface energy and moisture fluxes (Figure 2.2, b) and the surface stress for the PBL scheme (Figure 2.2, d). In order to obtain these variables, the surface layer scheme relies on different similarity theories, which are based on the assumption that in the surface atmospheric boundary layer the mechanical generation of turbulence is greater than the buoyant generation or consumption and therefore turbulent fluxes and stresses are nearly constant with height. Under this hypothesis, the vertical profiles of variables are logarithmic, and velocity scales can be calculated as follows:

- friction velocity

$$u_* = \frac{kV_r}{ln\left(\frac{z_r}{z_0}\right) - \Phi_m} \tag{2.14}$$

- surface-layer temperature scale

$$\theta_* = \frac{k\Delta\theta}{ln\left(\frac{z_r}{z_{0h}}\right) - \Phi_h} \tag{2.15}$$

- surface-layer humidity scale

$$q_* = \frac{k\Delta q}{ln\left(\frac{z_r}{z_{0q}}\right) - \Phi_h} \tag{2.16}$$

where subscript r refers to a reference level, usually the lowest model level, k is the Von Karman constant, z_r is the reference level height, z_{0i} are the surface roughnesses for momentum and for h heat (usually defined for a given land-use type), $\Delta\theta = \theta_r - \theta_{sfc}$ is the temperature anomaly between the reference level and the surface and $\Delta q = q_r - q_{sfc}$

is the difference in moisture between the reference level and the surface. It is important to notice that Equations 2.14-2.16 contain variables coming from both the PBL scheme (V_r, θ_r, q_r) and the LSM (θ_{sfc} and q_{sfc}) (Figure 2.2, e and b, respectively). The Φ_i terms represent stability functions introduced in the equations to correct the logarithmic profiles on the basis of the atmospheric stability. There are no theoretical reasons, beyond similarity, supporting the stability functions, which are therefore derived from experiments.

After calculating these Surface Layer scales (SL scales hereafter), the surface layer scheme estimates the exchange coefficients for momentum, heat and moisture to be fed in the land surface scheme for the calculation of the surface fluxes (Figure 2.2, c). The definition of the exchange coefficient for heat is:

$$C_{hs} = \frac{ku_*}{ln\left(\frac{z}{z_0}\right) - \Phi_h} \tag{2.17}$$

Within the WRF model, different surface layer schemes are implemented. They basically differ one from each other in the calculation of the stability functions Φ_i and of the roughness lengths z_{0i} and in the definition of the logarithmic profile. The two surface layer schemes most commonly used for WRF simulations are the one based on the Paulson (1970), Dyer and Hicks (1970) and Webb (1970) stability functions (MM5) and the Eta surface layer scheme (Janjic, 1996; Z. I. Janjic, 2002) which is based on the similarity theory from Monin and Obukhov (1954). Currently, each surface layer scheme is linked to specific PBL schemes.

2.3.3 Role of the Planetary Boundary Layer Scheme

Planetary boundary layers schemes provide boundary layer turbulent fluxes of heat, moisture and momentum and vertical diffusion in the whole column of air (but two different kinds of parameterizations

are used for within the PBL and above), acting as the connection to transfer energy, momentum and scalars from the surface towards the free atmosphere and vice versa. Turbulent fluxes have to be parameterized as they account for turbulent eddies operating at spatial and temporal scales which are too small to be explicitly resolved at the numerical grid scale. All PBL schemes within the WRF model are one-dimensional, which means that they calculate fluxes only over the vertical direction, under the hypothesis that vertical and horizontal gradients have different spatial scales. Horizontal eddy diffusion is taken care of by another parameterization in WRF, the diffusion scheme, which is not covered in this thesis work.

A complete theoretical development of PBL formulations can be found in many sources (Stull, 1988; Wyngaard, 2010) and is not reported here. In the present work, only the basics are recalled, in order to highlight the differences between different PBL schemes, which are useful in view of pollutant dispersion modeling.

The main feature characterizing each turbulence scheme is the order of the turbulence closure. The closure problem arises after decomposing the variables of the motion equations into average and fluctuating components. The fluctuating components represent the turbulent perturbation of the mean flow and they constitute the unknowns in the Reynolds Averaged Navier-Stokes (RANS) set of equations. It is possible to derive prognostic equations for each turbulent flux (n-order statistical moment), but this leads to the introduction of additional unknowns, which are n+1-order statistical moments of the meteorological field. This means that, in order to find a closure for turbulent fluxes, an empirical relation for specific x-order statistical moments must be introduced. The order of the closure technique corresponds to the highest order of the statistical moment for which a prognostic equation is provided in the scheme. Higher order moments are parameterized introducing in the scheme specific

length scales and closure constants, derived either from physical experiments and measurements (e.g. Mellor and Yamada, 1982) or from Large Eddy Simulations (LES, e.g. Nakanishi and Niino, 2004, used in this research).

For air dispersion purposes, a substantial information is the standard deviation of the wind flow, i.e. the root average value of the squared velocity fluctuations:

$$\sigma_{U_i} = \sqrt{\overline{u_i'^2}} \tag{2.18}$$

This variable is the second order statistical moment of the wind velocity and therefore only second-order (or 1.5 order) PBL schemes calculate this variable trough a prognostic equation. Usually, PBL schemes of 1.5 order or above provide information about this variable in the form of turbulent kinetic energy:

$$TKE = e = \frac{1}{2}\left(\overline{u_x'^2} + \overline{u_y'^2} + \overline{u_z'^2}\right) \tag{2.19}$$

which must therefore be decomposed on the three directions to obtain the standard deviation of the wind field in each direction (see Section 2.4.2).

On the contrary, first-order closure schemes do not solve equations for the second order moments of the velocity fields. What they usually do is to introduce Boussinesq-type closure (J. Boussinesq, 1877) which is a parameterization that calculates turbulent fluxes as functions of vertical gradients and of a diffusion coefficient K:

$$\overline{X'w'} = -K_x \frac{\partial \overline{X}}{\partial z} \tag{2.20}$$

where X is a generic variable and K_x is the dispersion coefficient relative to the X variable: K_m for momentum, K_H for heat and K_{moist} for moisture. This kind of simple and rather basic closure is still

widely used for meteorological modeling over a variety of spatial scales. The value of the dispersion coefficient K_x is derived in different ways from the different schemes, as a function of known variables, closure constants and stability conditions of the atmosphere.

The second relevant characteristic for a PBL scheme is the treatment of the mixing, which can be local or non-local. From a theoretical point of view (Canuto, 1992; Ferrero and Colonna, 2006), the non-local mixing is intrinsically taken into account by 3^{rd} order closures, which explicitly resolve third order moments. Lower order closures, instead, usually adopt different strategies in order to somehow reproduce the non-local mixing, by means of semi-empiric relations (Stull, 1984; Hong et al., 2006).

The Mellor-Yamada Nakanishi Niino PBL scheme

The 1.5-order Mellor-Yamada Nakanishi Niino (MYNN, Nakanishi and Niino, 2004) PBL scheme is used in Chapter 6 to perform the meteorological simulations and to derive the dispersion coefficients, with different levels of approximation. For this reason it appears useful to recall here the main characteristics of this PBL scheme, as implemented in the WRF model.

The MYNN PBL scheme is a 1.5-order closure scheme which solves the prognostic equation for the turbulent kinetic energy.

$$\frac{\partial q^2}{\partial t} = -\frac{\partial}{\partial z}\left\langle w'(u'^2 + v'^2 + w'^2 + 2p/\rho)\right\rangle - 2\left(\langle u'w'\rangle \frac{\partial U}{\partial z} + \langle v'w'\rangle \frac{\partial V}{\partial z}\right) + 2\frac{g}{\Theta_0}\left\langle w'\theta'_V\right\rangle - 2\epsilon \tag{2.21}$$

where $q^2 = 2TKE$ is twice the turbulent kinetic energy, p is the pressure, g is the gravitational acceleration, Θ_V is the virtual potential temperature and ϵ is the dissipation rate of the momentum. The scheme also includes other prognostic equations for other turbulent

variables (i.e. $\langle\theta_l^2\rangle$, $\langle\theta_l q_w\rangle$, $\langle q_w^2\rangle$ not reported here). In order to solve the closure problem, the scheme provides parameterizations for both the dissipation rate term ϵ and for the turbulent fluxes (again we report here only equations relative to the momentum equation):

$$\epsilon = \frac{q^3}{B_1 L} \tag{2.22}$$

$$-\langle u'w'\rangle = Lq S_M \frac{\partial U}{\partial z} \tag{2.23}$$

$$-\langle v'w'\rangle = Lq S_M \frac{\partial V}{\partial z} \tag{2.24}$$

where B_1 is a closure constant, L is the master length scale calculated by means of a diagnostic equation ($L = f(z, L_{M-O}, \Theta, q)$) and S_M is a stability function which is written as a function of other closure constants, L and vertical gradients of the mean velocities. Note that the product LqS_M represents here the vertical diffusion coefficient K_M which is therefore a function of the estimated turbulent kinetic energy.

The MYNN scheme therefore relies on the imposition of a set of 9 closure constants, which have been calculated and calibrated against LES data in Nakanishi (2001) over flat terrain. The result of this calibration led to the following values for the constants:

$$(A_1, A_2, B_1, B_2, C_1) = (1.18, 0.665, 24.0, 15.0, 0.137) \tag{2.25}$$

$$(C_2, C_3, C_4, C_5) = (0.7, 0.323, 0.0, 0.2) \tag{2.26}$$

which differ from the original values proposed by Mellor and Yamada (1982), after a calibration against field measurements:

$$MY82(A_1, A_2, B_1, B_2, C_1) = (0.92, 0.74, 16.6, 10.1, 0.08) \tag{2.27}$$

As it will be shown in Chapter 6, the PBL scheme is very sensitive

to the values of the closure constants. Indeed, for the analyzed case study, where the scheme is applied over very complex terrain, a test with modified closure constants is performed and relevant differences are found in the results. New values for the closure constants are adopted following Trini Castelli et al. (2001) and Trini Castelli et al. (1999), who derived them on the basis of turbulence data from a wind-tunnel experiment (Khurshudyan et al., 1990) over an idealized valley. The updated constant values are the following:

$$TCF05(A_1, A_2, B_1, B_2, C_1) = (2.135, 0.64, 35.94, 61, 0.167) \qquad (2.28)$$

2.4 Interfacing meteorological and dispersion models

2.4.1 The CALMET/CALPUFF model

CALPUFF is a multi-layer, multi-species non-steady-state gaussian-puff dispersion model which can simulate the effects of time- and space-varying meteorological conditions on pollutant transport, transformation, and removal Scire et al. (2000b). It is a preferred/recommended dispersion model by the US Environmental Protection Agency (EPA) for applications over complex terrain (EPA, 2005). CALPUFF can use the 3D meteorological fields produced by its preprocessor CALMET to drive the transport and dispersion of pollutants in the atmosphere. The model is able to model different types of sources (point, line, volume and area sources) with constant and variable emissions, and is able to treat non-steady-state meteorological conditions which can be produced by CALMET in different ways as shown in the following Section 2.4.1. Given these two main types of input, the dispersion of the pollutants is driven by vertically- and horizontally-varying dispersion coefficients, calculated on the basis of meteorological information, as explained in Section 2.4.1. Many

other features characterize the CALMET/CALPUFF model, such as the treatment of the puffs on the basis of the vertical wind shear, the plume rise options, the building downwash effects, etc., but the way the model interfaces with the meteorological input is the main focus of this work. For this reason, these features only are reported here.

Meteorological input

The CALPUFF model delegates the production of the meteorological input to its pre-processor model: CALMET. CALMET basically has two options to produce a meteorological input for CALPUFF: (i) creating a meteorological input on the basis of meteorological measurements (diagnostic approach), and (ii) creating a meteorological input on the basis of results from a NWP model (e.g. the WRF model) (the fields can be prognostic or diagnostic depending on the NWP model simulation).

Regardless of the source of the meteorological data, the process used by CALMET to produce the 3D wind field proceeds in three main steps (see Figure 2.3): the production of a "First guess initial field", the adjustment of this first field for terrain kinematic effects, slope flows, and terrain blocking effects, and the introduction of observations in the 3D field by means of interpolation, smoothing and divergence minimization procedures. The 3D wind field thus obtained is then directly passed as input onto CALPUFF model.

The creation of a diagnostic meteorological field on the basis of measurements only is a very delicate procedure, especially when performed over complex terrain. Indeed, the 3D field has to be produced over a specified spatial resolution on the basis of local information, which are usually sparse and differently representative of the flow field. Over complex terrain, as already highlighted, the structure of the wind field is characterized by local phenomena which are hardly caught by sparse measurement locations. Nevertheless, if

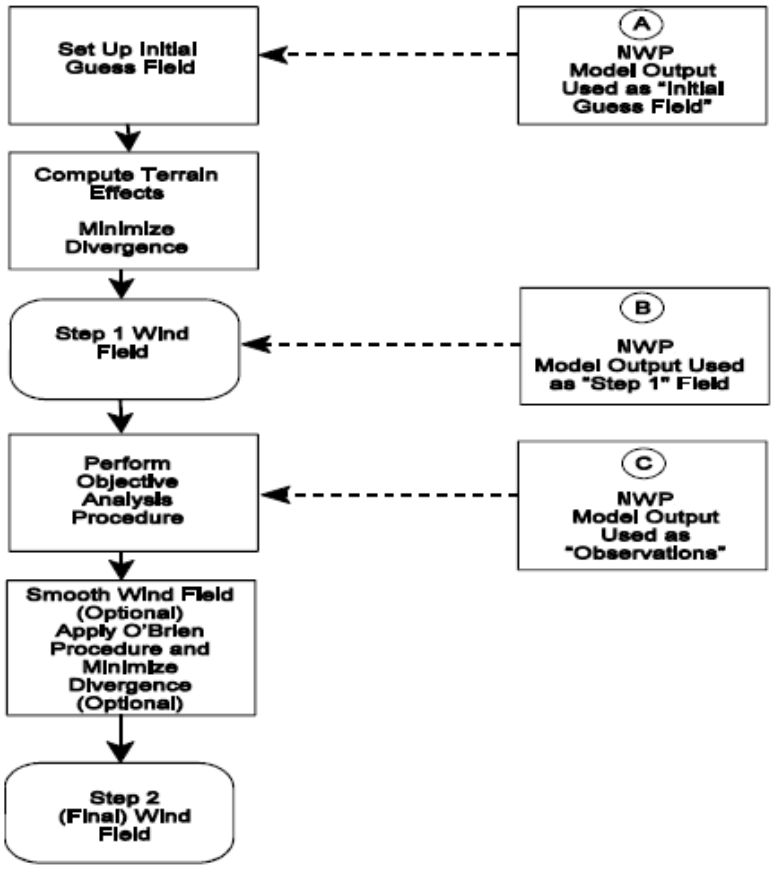

Figure 2.3: Flow diagram of the wind model in CALMET. Winds derived from a NWP model can be introduced as the initial guess field A, or the I Step field B. NWP model wind data can also be treated as ”observations” C. Reproduced from Scire et al. (2000a)

this option is selected it is essential to apply the available corrections in the CALMET model, which work at reconstructing the effects of the terrain on the flow. These corrections include: the calculation of the kinematic and blocking effects of the terrain (Liu and Yocke, 1980; Allwine and Whiteman, 1985), the introduction of slope flows (Mahrt, 1982), the adjustments of vertical velocities from O’Brien (1970) and

the smoothing and minimization of the divergence of the flow. An example of results that can be obtained with this kind of approach over complex terrain is presented in Chapter 5.

When CALMET is used to produce the wind field from a prognostic model output, its role drastically changes, especially if the NWP model is run at a resolution which is similar to the one chosen for the dispersion simulation. Indeed, under this hypothesis, the NWP model should be already able to identify the main features of the atmospheric flow and the role of CALMET reduces to an interpolation and re-projection instrument. Nevertheless, the user can choose to feed the 3D numerical wind field into CALMET at three different stages: as the initial guess field, as the step 1 flow field or as observations (Figure 2.3). This choice allows the user to regulate the intensity of the intervention that CALMET performs on the input flow field. An example of this approach is presented in Chapter 6, where the resolution of the WRF model simulation is already very fine and the CALMET model is therefore used as an operational interface between the meteorological and dispersion models, with little changes in the WRF output.

Parameterizations for dispersion coefficients

The dispersion in the CALPUFF model is driven by the horizontal and vertical Gaussian dispersion coefficients, σ_y and σ_z. These quantities are calculated in the model, at the beginning and end of each time step, as the sum of a turbulent term σ_{*t} and a buoyancy term σ_{*b}. The latter term refers to the phase of plume rise only, at the time of the release, while the former term includes both atmospheric and buoyancy-induced dispersion (BID). For this reason, the present work focuses on the calculation of the turbulent terms σ_{*t} only.

Different options are available in the CALPUFF model to obtain the turbulent dispersion coefficients. The three main options are: (i)

computing them from turbulence observations (when available), (ii) internally calculating the dispersion coefficients from parametrized values of wind standard deviations σ_V and σ_W, (iii) internally calculating the dispersion coefficients from Pasquill-Gifford-Turner (PGT) stability classes (Pasquill and Smith, 1983). The second procedure, which is the recommended default option (Scire et al., 2000b) and the one tested in this thesis work, is briefly summarized in the following.

- Parameterization based on Surface Layer scales

  The turbulent dispersion coefficients are calculated as function of the wind speed standard deviations and time:

$$\sigma_{yt} = f(\sigma_V, t) \tag{2.29}$$

$$\sigma_{zt} = f(\sigma_W, t) \tag{2.30}$$

  Standard deviations of the flow field are calculated on the basis of the SL scales using equations from 2.31 to 2.41, which provide the proper values and vertical variations for σ_i in the convective, neutral, and stable layers and for intermediate conditions without physically unrealistic discontinuities. This formulation is the result of the combination of different empirical relations and theoretical considerations from Panofsky et al. (1977); Hicks (1985); Arya (1984); Blackadar and Tennekes (1968); Nieuwstadt (1984); Hanna et al. (1986).

  – Convective boundary layer ($L < 0$):

$$\sigma_V = \left[4\,u_*^2 a_n^2 + 0.35\,w_*^2\right]^{\frac{1}{2}} \tag{2.31}$$

    * Surface Layer ($z \leq 0.1\,H_{mix}$)

$$\sigma_W = \left[1.6\,u_*^2 a_n^2 + 2.9\,u_*^2 \left(-\frac{z}{L}\right)^{\frac{2}{3}}\right]^{\frac{1}{2}} \tag{2.32}$$

$$a_n = \exp\left[-0.9\left(\frac{z}{H_{mix}}\right)\right] \tag{2.33}$$

* Mixed Layer ($0.1H_{mix} < z \leq 0.8H_{mix}$)

$$\sigma_W = \left[1.15\,u_*^2 a_n^2 + 0.35\,w_*^2\right]^{\frac{1}{2}} \tag{2.34}$$

* Entrainment Layer ($0.8H_{mix} < z \leq H_{mix}$)

$$\sigma_W = \left[1.15\,u_*^2 a_n^2 + a_{cl}\,0.35 w_*^2\right]^{\frac{1}{2}} \tag{2.35}$$

$$a_{cl} = \left[\frac{1}{2} + \frac{H_{mix} - z}{0.4H_{mix}}\right] \tag{2.36}$$

* Entrainment Layer ($H_{mix} < z \leq 1.2H_{mix}$)

$$\sigma_W = \left[1.15\,u_*^2 a_n^2 + a_{c2}\,0.35\,w_*^2\right]^{\frac{1}{2}} \tag{2.37}$$

$$a_{c2} = \left[\frac{1}{3} + \frac{1.2H_{mix} - z}{1.2H_{mix}}\right] \tag{2.38}$$

– Neutral-stable boundary layer ($L \to \infty$), ($L > 0$):

$$\sigma_V = u_*\left[\frac{1.6C_s\frac{z}{L} + 1.8a_n}{1 + \frac{z}{L}}\right] \tag{2.39}$$

$$\sigma_W = 1.3u_*\left[\frac{C_s\frac{z}{L} + a_n}{1 + \frac{z}{L}}\right] \tag{2.40}$$

$$C_s = \left(1 - \frac{z}{H_{mix}}\right)^{\frac{3}{4}} \tag{2.41}$$

As shown above, when no turbulence measurements are available, the remaining dispersion options rely on the meteorological information provided by CALMET for the calculation of the dispersion coefficients (and on some input data such as the land-use cover). It is therefore useful to understand which variables are produced and how they are produced by CALMET. The CALMET model only extracts from WRF values of wind speed and direction, temperature,

pressure, water vapor content, cloud cover and precipitation. The CALMET model does not extract values from WRF produced by the land surface model and by the surface layer model. Nevertheless, this information is essential to calculate the dispersion coefficients. In order to provide these quantities, the CALMET model is equipped with an internal micrometeorological model which performs the calculation of the surface fluxes and the SL scales, such as the friction velocity u_*, the temperature scale θ_*, the convective velocity scale w_*, the Monin-Obukhov length L and the mixing height H_{mix}. We refer to Scire et al. (2000a) for the complete formulation implemented in CALMET to calculate these quantities. What must be stressed is that the parameterizations used in the CALMET model are much more simplified with respect to the one implemented in a NWP model such as the WRF model. Indeed, the WRF LSMs and SFC layer scheme are more complex, rely on more detailed input data and run online with the PBL scheme, exchanging information at each time step. The internal micrometeorological model in CALMET therefore increases the uncertainties on the calculated values of both the SL scales and the dispersion coefficients, by introducing additional parameterizations which are no more consistent with the PBL results.

2.4.2 The SPRAYWEB model

The SPRAYWEB model is a 3D purely lagrangian stochastic particle model (Tinarelli et al., 2000; Alessandrini and Ferrero, 2009) which is designed to take into account the spatial and temporal variability of both the meteorological mean flow and turbulence. The model can simulate time-varying emissions from point, area and line sources. SPRAYWEB is particularly suitable for applications over complex terrain, where the meteorological fields are characterized by local phenomena which introduce great spatial (and temporal) inhomogeneity. Indeed, the model simulates the emitted plumes with a great number

of virtual particles characterized by a (small) pollutant mass, which passively follow the turbulent motion of the input meteorological field. The main trajectory of each particle is driven by the local mean wind field (given as input to the model), while its dispersion is determined by turbulent velocities obtained by solving the Lagrangian Langevin stochastic differential equations (Thomson, 1987), using the statistical characteristics of the atmospheric turbulence. With this approach, the trajectory of each particle is independent from the others, different parts of the same plume can experience different atmospheric conditions, and the effect of in-homogeneous meteorological fields on the dispersion is accounted for. The SPRAYWEB model interpolates the input wind flow in the position of each particle to calculate its mean velocity and direction: only concentration results are returned on a user-specified grid, as they are calculated by averaging over time the mass of all the particles in a given volume (the volume of the fixed cell).

	Read from WRF	**Estimated**
2D variable fields	terrain height	
	H_{mix}	
	u_*	
	L	
	Veg class	
	Precip	
	R_n	
		z_0, w_*

	Read from WRF	**Calculated**
3D variable fields	levels' height	
	U, V, W	
	θ	
	RH	
	T	
		σ_U, σ_V, σ_W
		T_{L_U}, T_{L_V}, T_{L_W}
		Skew

Table 2.2: Meteorological variables read from WRF, estimated or calculated in the WRF-SPRAYWEB Interface.

The SPRAYWEB model must be fed with a meteorological mean

flow from external sources, while it internally calculates the turbulent velocities. In the following, the main features of the meteorological interface developed to feed SPRAYWEB with output from the WRF model are presented. The design and development of this WRF-SPPRAYWEB Interface (WSI hereafter) have been conducted within this thesis work, on the basis of a first implementation from Bisignano et al. (2016). The WSI has two main objectives: (i) interpolate the mean fields provided by WRF on a numerical grid which is congruent with the one expected as input by SPRAYWEB, and (ii) calculate the standard deviations of the wind flow (σ_i) and the Lagrangian time scales (T_{L_i}, $i = U, V, W$) which are needed to solve the Langevin equation for the dispersion in SPRAYWEB. In Section 2.4.2 the first procedure is assessed, while Section 2.4.2 deals with the calculation of σ_i and T_{L_i} ($i = U, V, W$). Table 2.2 summarizes the meteorological variables which are read from WRF, estimated and calculated by the WSI ().

Vertical interpolation of meterological variables

The WSI performs an interpolation of WRF output on the vertical direction only, as the two models operate on two different vertical grids. While WRF works with time-varying, terrain following pressure levels, the SPRAYWEB model needs the meteorological input on a time-fixed, terrain following height grid. The SPRAYWEB vertical coordinate s is defined as follows:

$$s = \frac{z - z_g(x, y)}{z_{top} - z_g(x, y)} \tag{2.42}$$

where z is the height above mean sea level, $z_g(x, y)$ is the terrain height (m.s.l.), and z_{top} is the domain maximum height (m.s.l.). The s-coordinate is defined so that the ground floor corresponds to $s = 0$ and the top of the domain corresponds to $s = 1$.

To perform the interpolation between the two reference systems the user has just to choose an array of fixed heights z in a specific point of the domain, which will be used to calculate the constant s levels over which the interpolation will be done. The interface then proceeds to interpolate the WRF variables over this new time-fixed vertical grid by means of a linear interpolation. The 3D variables which are extracted from WRF, interpolated and passed to the SPRAYWEB model are: the wind components U, V and W, the potential temperature θ, the relative humidity RH and the ground elevation of the s levels z_s. In addition to these variables, the wind standard deviations and the Lagrangian time scales are also subject to the interpolation over the user-specified vertical levels, after they have been calculated (see next section).

Parameterizations for dispersion coefficients

The second role of the WSI is to calculate the characteristics of the atmospheric turbulence to be passed to the dispersion model. The variables that have to be calculated are: the wind standard deviations σ_i and the Lagrangian time scales T_{L_i} ($i = U, V, W$). Both these quantities directly affect the results of the Langevin equations, i.e. the velocity fluctuations that the virtual particles will experience.

In the WSI, several parameterizations have been implemented for the calculation of these quantities, with different levels of approximation. In the following the available options, among which the user can choose, are briefly described.

- Hanna (1982) parameterization (SL scales)

  The Hanna (1982) parameterization calculates the values of wind standard deviations and Lagrangian time scales as functions of the SL scales. The following relations were formulated on the basis of analyses from field experiments (Hanna, 1968;

Kaimal et al., 1976; Caughey et al., 1979; Hanna, 1981), theoretical considerations (Panofsky et al., 1977; Irwin, 1979) and a second-order closure model (Wyngaard and Coté, 1974).

– Convective boundary layer ($L < 0$):

$$\sigma_{U,V} = u_* \left(12 + 0.5 \frac{H_{mix}}{|L|}\right)^{\frac{1}{3}} \tag{2.43}$$

$$T_{L_{U,V}} = 0.15 \frac{H_{mix}}{\sigma_U} \tag{2.44}$$

* Surface Layer ($z \leq 0.03 H_{mix}$)

$$\sigma_W = 0.96 w_* \left(3 \frac{z}{H_{mix}} - \frac{L}{H_{mix}}\right)^{\frac{1}{3}} \tag{2.45}$$

* Mixed Layer ($0.03 H_{mix} < z < 0.4 H_{mix}$)

$$\sigma_W = min \begin{bmatrix} 0.96 w_* \left(3 \frac{z}{H_{mix}} - \frac{L}{H_{mix}}\right)^{\frac{1}{3}} \\ \\ 0.763 w_* \left(\frac{z}{H_{mix}}\right)^{0.175} \end{bmatrix} \tag{2.46}$$

* Entrainment Layer ($0.4 H_{mix} < z < 0.96 H_{mix}$)

$$\sigma_W = 0.722 w_* \left(1 - \frac{z}{H_{mix}}\right)^{0.207} \tag{2.47}$$

* Entrainment Layer ($0.96 H_{mix} < z < H_{mix}$)

$$\sigma_W = 0.37 w_* \tag{2.48}$$

For the Lagrangian time scales on the vertical direction:

* ($z < 0.1 H_{mix}$) and ($z < -L$)

$$T_{L_W} = 0.1 \frac{z}{\sigma_W} \frac{1}{0.55 + 0.38 \frac{z}{L}} \tag{2.49}$$

* $(z < 0.1 H_{mix})$ and $(z > -L)$

$$T_{L_W} = 0.59 \frac{z}{\sigma_W} \tag{2.50}$$

* $(z > 0.1 H_{mix})$

$$T_{L_W} = 0.15 \frac{H_{mix}}{\sigma_W} \left(1 - \exp\left[\frac{-5z}{H_{mix}}\right]\right) \tag{2.51}$$

– Stable boundary layer $(L > 0)$:

$$\sigma_U = 2 u_* \left(1 - \frac{z}{H_{mix}}\right) \tag{2.52}$$

$$\sigma_W = 1.3 u_* \left(1 - \frac{z}{H_{mix}}\right) \tag{2.53}$$

$$T_{L_U} = 0.15 \frac{H_{mix}}{\sigma_U} \left(\frac{z}{H_{mix}}\right)^{0.5} \tag{2.54}$$

$$T_{L_V} = 0.07 \frac{H_{mix}}{\sigma_V} \left(\frac{z}{H_{mix}}\right)^{0.5} \tag{2.55}$$

$$T_{L_W} = 0.10 \frac{H_{mix}}{\sigma_W} \left(\frac{z}{H_{mix}}\right)^{0.8} \tag{2.56}$$

– Neutral boundary layer $(L \to \infty)$:

$$\sigma_U = 2 u_* exp\left[-\frac{3 f_z}{u_*}\right] \tag{2.57}$$

$$\sigma_W = 1.3 u_* exp\left[-\frac{2 f_z}{u_*}\right] \tag{2.58}$$

$$T_L = \frac{0.5 \frac{z}{\sigma_W}}{1 + 15 \frac{f_z}{u_*}} \tag{2.59}$$

- CALPUFF parameterization (SL scales)

  In order to conduct some tests, and to compare CALPUFF results with SPRAYWEB results, the parameterization imple-

mented in CALPUFF to calculate wind standard deviations from the SL scales has been implemented in the WSI also. Equations are therefore those reported in equations from 2.31 to 2.41 for the standard deviations, while the calculation of lagrangian time scales follows Hanna (1982) parameterization.

- Turbulent Kinetic Energy (TKE) parameterization

  This parameterization (Ferrero et al., 2003) allows the calculation of wind standard deviations and Lagrangian time scales from the TKE and the vertical dispersion coefficient returned by PBL parameterizations based on the Mellor and Yamada (1982) closure scheme. The idea is to decompose the information about the variances of the wind velocity held in the TKE on the three spatial directions by means of the γ parameter, defined in Mellor and Yamada (1982). Indeed, following Mellor and Yamada (1982), for a Cartesian reference system:

$$\gamma = \frac{1}{3} - 2\frac{A_1}{B_1} \tag{2.60}$$

$$q^2 = 2TKE \tag{2.61}$$

$$\sigma_U = \sigma_V = \sqrt{(1-\gamma)q^2} \tag{2.62}$$

$$\sigma_W = \sqrt{\gamma q^2} \tag{2.63}$$

  where A_1 and B_1 are the turbulence closure constants discussed in Section 2.3.3. Given the wind velocity standard deviations, the Lagrangian time scales can be calculated (Ferrero et al., 2003) from the vertical diffusion coefficient K_M returned by the PBL scheme:

$$T_{L_i} = \frac{K_M}{\sigma_i^2} \qquad i = U, V, W \tag{2.64}$$

The Hanna (1982) and CALPUFF parameterizations are pretty

similar in their structures and the main differences lie in the empirical curves used to calculate the wind velocity standard deviations. The WSI allows the extraction of the SL scales needed for these parameterizations directly from WRF results, i.e. from the LSM and SFC layer scheme of WRF. This represents a great advantage with respect to the CALPUFF procedure, which instead introduces additional parameterizations with the internally performed similarity theory.

The TKE parameterization formally has two great advantages if compared with the previous ones. First, it is consistent with the parameterization used in the WRF PBL scheme and does not introduce any additional empirical approximations in the procedure to calculate the turbulence characteristics (the constants A_1 and B_1 are the same of the PBL scheme applied). Second, it is based on a physical quantity, the TKE, which is calculated by means of a prognostic equation in the PBL scheme. For these reasons, the uncertainties associated with this procedure to obtain turbulence characteristics should be much reduced with respect to the previous ones. Chapter 6 presents a comparison of results from these different parameterizations and their performance against observed ground concentrations collected during the BTEX (Chapter 3) field campaign.

Chapter 3

Case study databases

In this chapter the main databases used in this thesis work are presented. The work aims at evaluating, and possibly improving, the performance of different numerical models. To this purpose, trustful and reliable set of data are needed for comparison. Here observations originate from different data sets, collected during different intensive field campaigns performed in different periods. However, the complex terrain and the wintertime conditions pool together all the data sets. In addition, all the data sets include not only standard observations, but each of them presents specific characteristics which make it unique and one of a kind. Two out of the three data sets (the Aldeno data set, Section 3.1, and the Merano data set, Section 3.2) are archive data set, collected in 2006 and 2010. The third one comes from the Bolzano Tracer Experiment, which was designed, set up and performed as an integral part of this doctoral thesis. Each section of this chapter is dedicated to a specific case study and to its data set, including both meteorological and air quality information. Data coming from all these case studies will be used as validation data sets, or as input data, to the numerical simulations performed and discussed in the following chapters of this thesis work.

3.1 The Aldeno case study - ALPNAP project

The Aldeno intensive field campaign was carried out in wintertime 2006, within the project ALPNAP - Monitoring and Minimization of Traffic-Induced Noise and Air Pollution Along Major Alpine Transport Routes (Heimann et al., 2007). The project was funded by the European Union by means of the European Regional Development Fund (ERDF), as part of the INTERREG IIB Alpine Space Program. The project had the main aim of collecting and describing state-of-the-art scientific methodologies to measure and forecast noise and air pollution for applications over the Alpine region. During the project, different intensive field campaigns were carried out, in different target areas: the instrumental set up deployed was one of a kind, in terms of number and variety of the instruments and of spatial extension of the measurements along the transversal section of the valley. In the present thesis work, data from the Aldeno Field Campaign are utilized. This field campaign took place in the lower part of the Adige Valley, in the eastern Italian Alps (Figure 3.1(a)), close to the town of Aldeno. The aim of the campaigns was to collect both meteorological and air quality data in the close surrounding of the town. In order to enlarge the validation dataset for the simulations, additional data coming from permanent weather stations distributed along the valley floor are used in the present work.

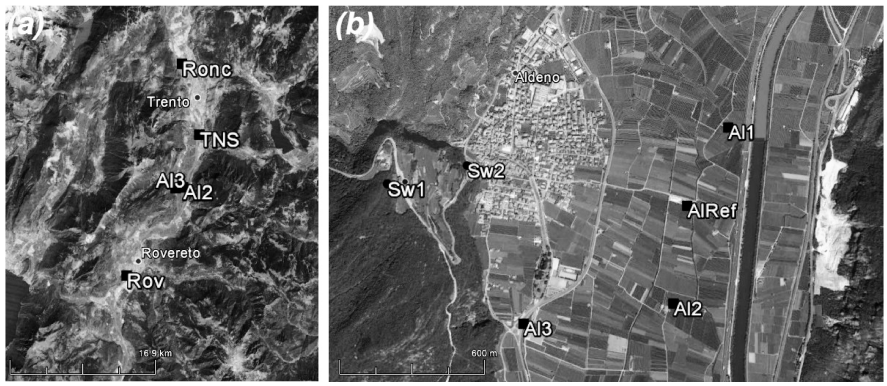

Figure 3.1: Topography of the lower part of the Adige Valley: (a) study domain with the cities of Trento and Rovereto, the town of Aldeno and the permanent weather stations used in this paper; (b) zoom on the town of Aldeno with the measurement stations of the ALPNAP project (squares for valley floor stations and dots for sidewall stations; background map from **Google Earth**).

3.1.1 Study area

The Aldeno field campaign focused on the surrounding area of the town of Aldeno, located in the lower Adige Valley. The portion of the valley of interest here is about 45 km long, 2 km wide and mainly north-south oriented and centered in the town of Aldeno. The valley floor height ranges between 150 m above mean sea level (MSL) in the southern part, up to 200 m MSL in the northern part, and the surrounding mountain peaks range between 1500 m and 2000 m MSL. The terrain is very complex, as the sidewalls are mostly very steep, especially in the northwestern side of the valley. The cities of Trento and Rovereto are included in the study area together with other minor urbanized centers, including the town of Aldeno (Figure 3.1(b)). Except for these urban areas, the land use of the valley floor is mainly agricultural (apple orchards), while most of the sidewalls are covered with deciduous broadleaf and evergreen needleleaf forests.

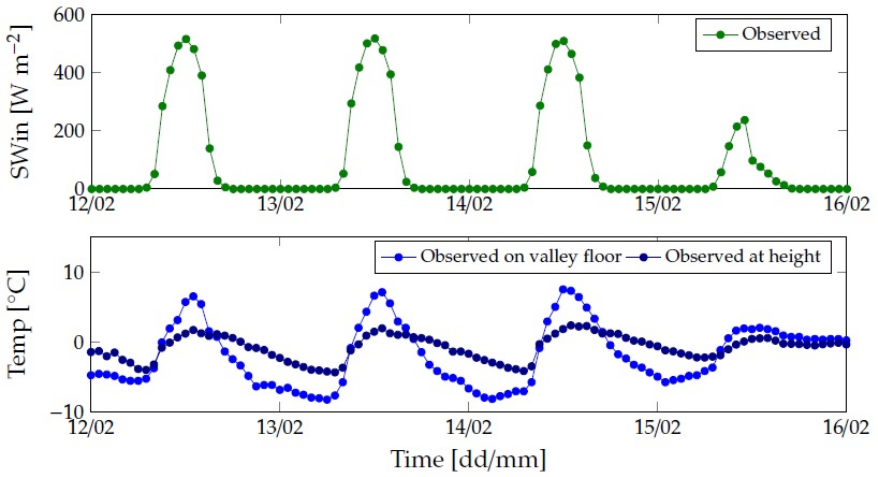

Figure 3.2: Observed values of incoming SW radiation at the reference station in the center of the Adige Valley (top panel) and 2-m temperature measurements recorded in the valley floor and at height (bottom panel).

3.1.2 Study period

The ALPNAP measurement campaign in Aldeno lasted approximately one month, in February 2006. For the present case study, four representative days were selected, i.e. the period 12-15 February 2006. During these days specific and interesting meteorological conditions occurred. First, a transition from clear sky to cloudy conditions occurred between the third and the last day (top panel of Figure 3.2). Second, a ground-based thermal inversion built up during nighttime and broke up in the central hours of the day during the study period (bottom panel of Figure 3.2). Third, a 15-day-old snow, fallen at the end of January 2006, was covering the ground, as shown in Figure 3.3.

Figure 3.3: Snow-covered ground during the ALPNAP Field Campaign.

3.1.3 Meteorological data set

Two different sources of meteorological data are used for the present analysis. The first dataset comes from the ALPNAP Aldeno Field Campaign (a complete description of the ALPNAP field instrumentation can be found in de Franceschi and Zardi (2009)). In particular, observations registered by a meteorological station located on the valley floor including 4-channel net radiometer (AlRef); a conventional station on the valley floor (Al1); two portable thermohygrometers located on the western sidewall at different elevations (Sw1 and Sw2, namely at 390 and 240 m MSL). Figure 3.1(b) shows the locations of the stations and Figure 3.4 the instrumentation types. All the stations provide measurements of 2-m temperature. The AlRef station also recorded observations of incoming and outgoing short- and longwave radiation: as measurements of surface fluxes are of funda-

mental importance for the evaluation of LSM results, AlRef station is used as the reference weather station to evaluate model simulations. This dataset gives a complete view of the evolution of the principal meteorological variables on the valley floor close to Aldeno and the thermohygrometers on the western valley sidewall allow evaluating the vertical thermal structure inside the valley (e.g. the development of ground-based thermal inversions).

Figure 3.4: One of the Hobo thermohygrometers (Onset Mod. HoBo H8 Pro) and the 4-channel net radiometer (Kipp e Zonen Mod. CNR-1) deployed during the ALPNAP Aldeno Field Campaign.

In order to increase the number of validation points for the model simulations and to integrate the Aldeno dataset, the second set of measurements is used. It is composed of observations from five permanent weather stations (Al2, Al3, Ronc, TNS and Rov) operated by the local Meteorological Office, Meteotrentino, and by the Edmund Mach Foundation. All these stations provide 2-m temperature measurements on the valley floor of the Adige Valley (Figure3.1(b)).

3.1.4 Air quality data set

The ALPNAP Aldeno Field Campaign also collected observations of pollutant concentrations in the air. The Environmental Protection Agencies of the Provinces of Trento and Bolzano and of the Veneto

Region deployed four mobile air quality stations in the area, partly on the valley floor and partly on the sidewalls. As no simulations of air pollution dispersion have been carried out for the Aldeno case study, the present work does not go into details of measured pollutant concentrations.

Station	Type	Observations	Lat	Lon	Height MSL [m]
AlRef	Valley floor	2-m T, SW, LW	45.974	11.104	181
Sw1	Sidewall	2-m T	45.975	11.083	390
Sw2	Sidewall	2-m T	45.976	11.086	240
Al1	Valley floor	2-m T	45.978	11.107	182
Al2	Valley floor	2-m T	45.969	11.103	186
Al3	Valley floor	2-m T	45.968	11.092	198
Ronc	Valley floor	2-m T	46.096	11.101	195
TNS	Valley floor	2-m T	46.023	11.127	191
Rov	Valley floor	2-m T	45.878	11.020	168

Table 3.1: Summary of the main characteristics of the stations producing data for the Aldeno Case Study ('2-m T' refers to the 2-m temperature, 'SW' and 'LW' to the short- and longwave radiation).

3.2 The Merano case study

During 2010 winter season, vertical profiles of both meteorological quantities and pollutant concentrations were collected over three different Italian sites (Terni Valley, Po Plain and Adige Valley) for a project (Ferrero et al., 2014) led by the University of Milano Bicocca, in collaboration with the Institute for Applied Remote Sensing (EURAC, Bolzano), the University of Perugia, the University of Trento and the Aerosol d.o.o. private company. The main aim of this field campaign was the measurement of black carbon (BC) vertical profiles

by means of balloon soundings: in addition to BC concentrations, observations of aerosol size distribution, chemical composition of air samplings and meteorological variables were recorded. The measurement campaign lasted 45 days and resulted in the collection of 120 vertical profiles. In the present work, we use temperature and particulate matter vertical profiles data performed in the Merano basin, in the eastern Italian Alps. These measurements represent a unique set of data, which allows the analysis and understanding of the interaction between the vertical thermal structure of the boundary layer and the relative dispersion of pollutants. In addition to these data, the present work also uses data from a permanent weather station and an air quality station located near the sampling point, in order to have additional ground measurements of both wind speed and direction and particulate matter. These stations are run by the local Meteorological Service (Ufficio Idrografico di Bolzano) and the local Environmental Protection Agency (APPA Bolzano), respectively.

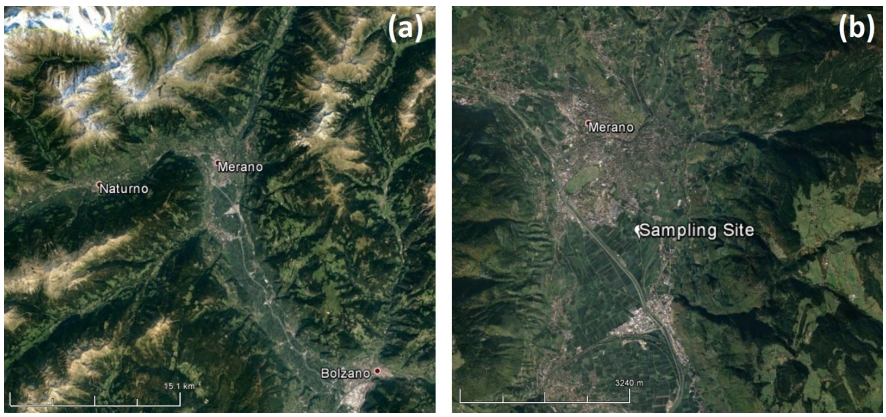

Figure 3.5: Topography of the Merano area: (a) study domain with the town of Merano at the conjunction of the Venosta, the Passiria and the Adige Valleys; (b) zoom on the town of Merano with the sampling site of the wintertime campaign of 2010 (background map from **Google Earth**).

3.2.1 Study area

Merano is a small town located at the intersection of three main Alpine valleys: the Venosta Valley, mainly E-W oriented, the Passiria Valley and the Adige Valley, mainly NS oriented. Another secondary small valley, the Ultimo Valley, merges the Adige Valley few kilometers to the South of the town of Merano (Figure 3.5(a)). The Adige and Venosta Valleys are quite wide, with valley floor width ranging between 1.5 and 2.5 km. On the contrary, the Passiria and Ultimo Valleys are V shaped and very narrow.

The analyzed area is roughly 45 km squared, and is characterized by a very complex topography: the main valley floor ranges between 250 and 300 m MSL while the surrounding mountain peaks reach 2-3000 m MSL, with the steepest sidewalls in the Venosta Valley. The terrain is little urbanized, except for the town of Merano and few others minor centers, lying mainly in the Adige Valley. The valley floors are mainly dedicated to agriculture, while the mountainous area is covered with evergreen needleleaf forests or bare ground. The sampling site for the balloon launches was located in a rural area south of Merano (Figure 3.5(b)), close to the location of a permanent air quality station operated by the local Environmental Protection Agency (Merano 2 station, APPABZ).

3.2.2 Study period

The 2010 field campaign in Merano lasted from 3 to 13 March, and over 40 vertical aerosol and meteorological profiles were collected. In the present work, the attention is focused on the first day of measurements, during which four vertical profiles were recorded. Figure 3.6 shows the observations collected in terms of vertical profiles of temperature and PM10, together with wind speed and direction recorded by a close weather station. The vertical thermal profile observed in

the early morning clearly shows a ground-based thermal inversion which broke up later during the day. The wind regime was calm, with the development of an up-valley wind along the Adige Valley, blowing from midday to the late afternoon. Snow was not present on the valley floor, covering the ground only above 1500 m.

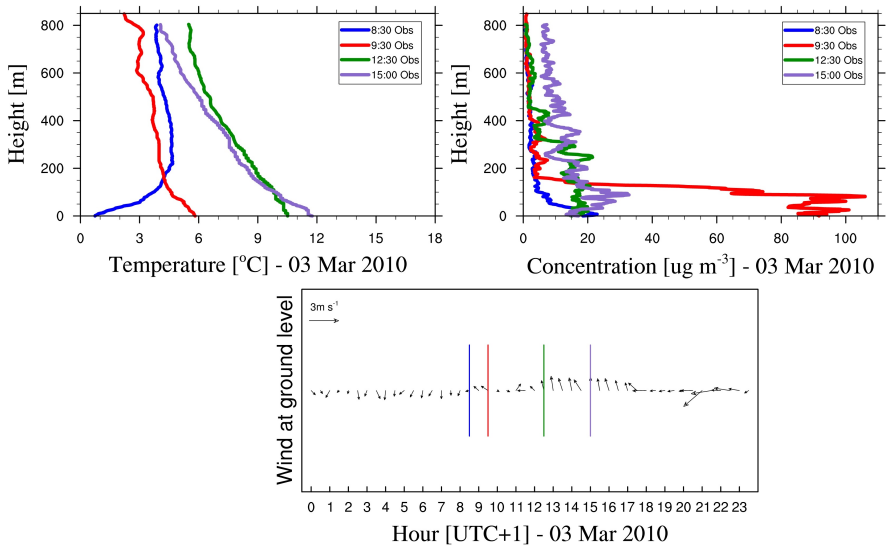

Figure 3.6: Vertical profiles of measured temperature (left top panel) and PM10 concentration (right top panel) and ground wind speed and direction measured troughout the day (bottom panel; the colored lines identify the timing of the vertical soundings performed).

3.2.3 Meteorological data set

Vertical soundings in Merano were performed by means of a helium-filled tethered balloon (diameter 4.5 m, volume 47.8 m^3, payload 40 kg), equipped with a meteorological station, a micro-Aethalometer, an optical particle counter and a portable cascade impactor (Figure 3.7). The balloon had an ascent/descent rate of 30 m min^{-1}. With a measurement time resolution of 6 s, the resulting vertical resolution was of 3 m. The balloon reached heights of 600-800 m, depending on

the sounding. The meteorological variables recorded are pressure, temperature and relative humidity.

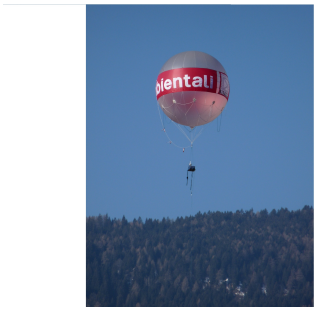

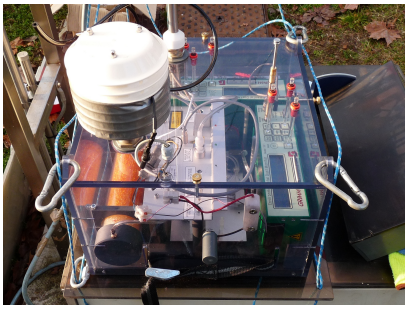

Figure 3.7: Helium-filled tethered balloon performing one of the soundings and its instrumental equipment deployed during the Merano Field Campaign.

3.2.4 Air quality data set

The instrumentation carried by the tethered balloon allowed the measurement of different air quality indicators. The micro-Aethalometer measured the BC concentrations and absorption coefficient; the optical particle counter allowed the determination of particle numbersize distribution and the portable cascade impactor collected PM samples. The temporal and spatial resolution of the air quality measurements are the same of the meteorological observations. In the present work, the attention is focused on the vertical profiles of PM10. As shown in Figure 3.6, measurements highlight the development of high PM10 concentrations very close to the ground, in the early morning (8:30 LST vertical profile). This high concentration builds up during the whole morning (9:30 LST profile), until the particulate matter is gradually dispersed upwards (12:30 LST profile), later distributing homogeneously along the vertical direction (15:00 LST profile). This temporal evolution of the PM10 concentration perfectly fits the evolution of the meteorological conditions of the lower atmosphere and the si-

multaneous cycle of the local pollutant sources. In the early morning, most of the population turns on its wood stoves to heat up homes: this intense emission, combined with the ground-based thermal inversion, explains the high concentrations of PM10 recorded near the ground, where the pollutants are trapped. While the day proceeds and the temperature increases, the local sources are turned off, and the increased atmospheric mixing allows a more efficient dispersion of PM10 towards upper layers of the atmosphere.

3.2.5 Emission data set

In order to run dispersion simulations, an emission dataset was created, taking into account all the main local sources of particulate matter. The study area presents point, areal and linear sources. The point sources are 12, mainly distributed along the valley floors. They include three district heating plants, some local manufacturing and agri-food industrial plants, and two recreational thermal plants. The areal emission sources are mainly the domestic heating, which is extensively utilized during wintertime, and the secondary traffic. The emission rates of both the point and areal sources were retrieved from the regional Italian emission inventory INEMAR (APB, 2010), developed according to the best practices reported in the European Environment Agency (EEA) guidelines (EAA, 2009). The linear sources consist of the major national and regional roads in the area. The emission rate for each axis was calculated by means of the EU standard model COPERT IV (Gkatzoflias et al., 2012), as explained in detail in Section 4.2.1. This procedure requires as input data the number of transiting vehicles, the fleet composition and the mean vehicle speed. For each road within the study area, these data were obtained from data sets provided by the local institute for statistics, ASTAT (number of transiting vehicles and mean velocities), and by the Italian federation of motorists, ACI (fleet composition).

3.3 The Bolzano Tracer Experiment case study - BTEX

The Bolzano Tracer Experiment (BTEX) is an experiment conducted during the 2016 and 2017 winter seasons. The experiment consisted in the release of a passive tracer gas from the stack of an incinerator plant and in the measurements of ground concentrations in the surroundings. The experiment took place in the Bolzano Basin, in the Eastern Italian Alps. The set up and performance of this experiment have been integral part of the present thesis work. Numerous partners participated in the BTEX: EcoCenter S.p.A., the incinerator company, as the leading partner and primary stakeholder and sponsor; the University of Trento, as the coordinating partner, scientific supervisor and modeling team together with CISMA Srl, a local engineering company specialized in environmental modeling; EcoResearch Srl, as the main research laboratory responsible for the chemical analysis of the collected samplings and for the insertion of the tracer gas in the incinerator stack; the local environmental protection agency (APPA BZ) as supervisor and stakeholder of the project; and the Mario Negri Institute, as secondary research laboratory. BTEX was conducted in the framework of a wider project, with the final aim of locating a permanent network of air-quality stations for monitoring purposes. The main aim of the experiment itself was that of collecting a unique validation data set of tracer ground concentrations, which can be used to validate modeling results of a meteorological and dispersion modeling chain. Few experiments such BTEX have been performed in the past (e.g. the Kincaid and Bull Run experiments, Hanna and Paine (1989)), and even fewer present such a complex orography (e.g. the TRANSALP-90 experiment Ambrosetti et al. (1994)). During the winter-season field campaign of 2016 two releases of tracer gas were performed, but no valid measurements of tracer concentrations were

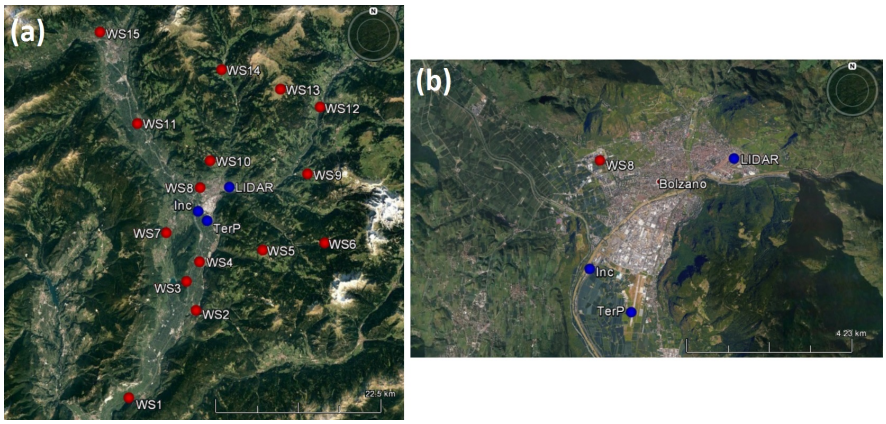

Figure 3.8: Bolzano basin with its tributary valleys. Locations of the available weather stations are also highlighted: "Inc" incinerator plant and SODAR; "TerP" thermal profiler; "LIDAR" LIDAR instrumentation; "WS" ground weather stations (background map from Google Earth).

collected at the ground. For this reason, this first phase of the experiment has been used as a preliminary test period, during which meteorological measurements were recorded and the behavior of different numerical models was analyzed. Instead, during the winter season 2017 other two releases of the tracer gas were performed, and successful measurements of ground concentrations were collected. In the following sections the data set collected during both the phases of BTEX are presented.

3.3.1 Study area

The city of Bolzano (262 m a.s.l.) lies in the middle of a wide basin at the junction of the Adige Valley, mainly north-south oriented, with the Isarco Valley, joining from the East, and the Sarentino Valley, from the North. Figure 3.8(a) shows the study area in the Bolzano basin, its tributary valleys and all available meteorological measurement stations. In the considered study area, the Adige Valley is approximately 2-3 km wide while the Sarentino and Isarco Valleys are V shaped and very narrow. The sidewalls of the Adige Valley are very

steep, especially on the Eastern side of the valley. Mountain peaks reach between 1500-2000 m MSL heights. The climate of Bolzano is continental, characterized by warm summers and cold winters. Wind regimes are dominated by terrain effects (Dosio et al., 2001), developing thermally-driven winds (de Franceschi and Zardi, 2009), which however are mostly absent or very weak during wintertime (de Franceschi et al., 2009). This aspect, in connection with the frequent occurrence of ground-based inversions at the valley floor, determines frequent critical conditions for air quality. The incinerator is located 2 km Southwest of the town of Bolzano, very close to the western sidewall of the Adige Valley (see Figure 3.8(b)). The waste incinerator plant became operative in July 2013, with a maximum waste treatment capacity of 130000 t y^{-1} and a flow rate of 110000 Nm^3 h^{-1} released at 60 m above ground level at 413 K. This new plant required policy makers to improve the forecast of dispersion processes in the area (Ragazzi et al., 2013), with the aid of both atmospheric and dispersion modeling. Figure 3.9 shows the incinerator plant and its stack.

Figure 3.9: The incinerator plant of Bolzano (left, from Google Earth) and its stack (right, looking South).

3.3.2 Study period

The measurement field campaign of BTEX mainly focused on the winter seasons of 2016 and 2017. During 2016 winter season (phase 1), only meteorological measurements were collected, while during 2017 winter season (phase II), both meteorological and tracer gas concentration at the ground were collected. In the present work the attention is focused on two key days: January 27^{th} , 2016, during phase I, and February 14^{th}, 2017, during phase II. January 27^{th} 2016 was chosen as the reference test case as it presented most of the typical wintertime meteorological conditions, relevant for the stagnation of locally emitted atmospheric pollutants: a strong ground-based thermal inversion, developing up to 700 m above the bottom of the valley, and relatively weak wind speeds. February 14^{th} 2017 is the case study of phase II as it is the day during which two releases of the tracer gas were performed. The first tracer release took place in the early morning, with a weakly stable atmosphere and weak north-westerly winds at the incinerator plant. The second release took place in the early afternoon, in weakly convective conditions and weak southerly winds. During both the test cases, the sky was clear and no strong synoptic forcing occurred.

3.3.3 Meteorological data set

The meteorological data set collected during BTEX and used in the present analysis is a collection of data coming from a set of permanent weather stations, from a permanent thermal profiler and from specific instrumentation deployed for the experiment. The permanent station network and the thermal profiler are both managed by the local meteorological service. Their location is shown in Figure 3.8(a), where the weather stations are numbered with increasing latitude.

Figure 3.10: The SODAR instrumentation installed on the roof of the incinerator plant.

These stations collect both 2-m temperature and 10-m wind speed and direction observations which are used in the present analysis. The thermal profiler (RPO Attex Mod. MTP 5-HE) measures temperature up to ~1000 m with a spatial resolution of 50 m. It is located close to the airport, in the center of the Adige Valley, 3 km southwest of the city of Bolzano. The instrumentation specifically deployed for BTEX consists in a SODAR and a LIDAR wind profilers. The SODAR instrumentation (Scintec Mod. MFAS-64) was located on the roof of the incinerator plant (40 m a.g.l.), in order to have information of the wind vertical profile close to the stack. The instrument was able to measure up to ~300 m above the roof-top (i.e. ~340 m above ground level) with a spatial resolution of 10 m and a temporal resolution of 10 min. The SODAR was deployed in the field for the whole period of the BTEX project. Figure 3.10 shows the SODAR installation on the roof of the incinerator plant.

The LIDAR instrumentation (Leosphere Sas Mod. WINDCUBE 3D 100S) was installed at the exit of the Isarco Valley, in the northwestern part of the town of Bolzano (see Figure 3.8). This location is of particular interest as the analysis carried out during phase I of BTEX demonstrated the existence of a nocturnal valley jet blowing along the

Isarco Valley during cold winter nights. When activated, this strong valley jet crosses the Bolzano basin, flowing from the North-East towards the South, passing over the incinerator plant. In order to have a precise depiction of the Isarco Valley jet, during the second phase of BTEX (i.e. winter season 2016-2017), the LIDAR instrumentation was deployed. It measured vertical profiles of wind speed and direction up to ~1100 m, every 10 min, with a spatial resolution of 10 m. Figure 3.11 shows the LIDAR instrumentation installed on the roof of a tall building in the north-eastern part of Bolzano.

Figure 3.11: The LIDAR instrumentation installed on the roof of a tall building in the north-eastern part of Bolzano (left) and the perspective on the Isarco Valley, looking East, from the instrumentation site (right).

Table 3.2 reports all the information relative to the stations utilized in BTEX. In the following subsection the main meteorological conditions on the two days analyzed for this work are presented.

Station	Type	Observations	Lat	Lon	Height MSL [m]
SODAR	Vertical profiler	10-m sp. WSD, up to 360m	46.469	11.309	288
LIDAR	Vertical profiler	10-m sp. WSD, up to 1100m	46.498	11.352	290
TerP	Vertical profiler	50-m sp. T, up to 1000m	46.457	11.325	250
WS1	standard		46.240	11.186	212
WS2	standard		46.347	11.305	250
WS3	standard		46.382	11.289	224
WS4	standard		46.406	11.311	230
WS5	standard		46.420	11.427	1470
WS6	standard		46.429	11.537	1128
WS7	standard	2-m T,	46.442	11.252	495
WS8	standard	10-m WSD	46.498	11.313	255
WS9	standard		46.513	11.506	840
WS10	standard		46.530	11.332	970
WS11	standard		46.577	11.201	290
WS12	standard		46.595	11.529	490
WS13	standard		46.616	11.460	2260
WS14	standard		46.641	11.355	970
WS15	standard		46.688	11.137	330

Table 3.2: Summary of the main characteristics of the stations producing data for the analysis of BTEX ('2-m T' refers to 2-m temperature measurements, 'WSD' stands for Wind Speed and Direction measurements and 'sp.' stands for *spaced*).

27th January 2016

The main meteorological features of this test day are analyzed on the basis of the data measured by the thermal vertical profiler, by the SODAR and by ground weather stations. Figure 3.12 presents the vertical temperature structure of the atmosphere as recorded by the thermal profiler.

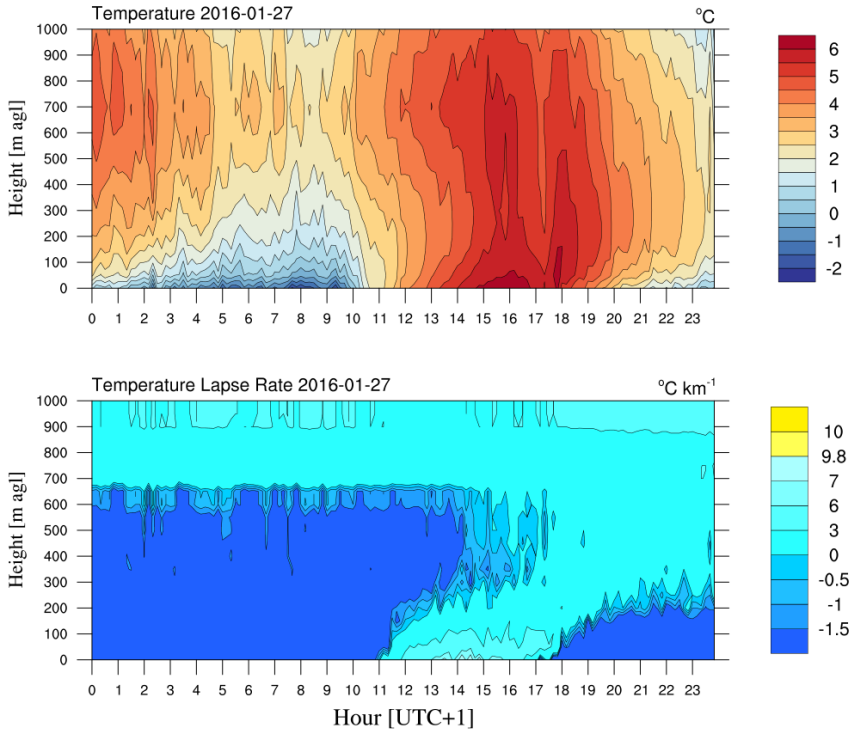

Figure 3.12: Time-height diagrams of temperature and temperature lapse rate observed by the thermal profiler on January, 27^{th}, 2016. In the temperature lapse rate plot (bottom panel) blue, cyan and yellow colors identify thermal inversion, stable conditions and unstable conditions, respectively.

The top panel shows the temperature field while the bottom panel shows the respective temperature gradient: the color scale of the temperature lapse rate diagram is such that blue, cyan and yellow colors

represent thermal inversion, stable conditions and unstable conditions, respectively. The observations clearly show the persistence of a deep and strong ground-based thermal inversion throughout most part of the day. From 11 to 16 Local Standard Time (LST, i.e. UTC+1), the thermal inversion breaks, but the atmosphere remains stable.

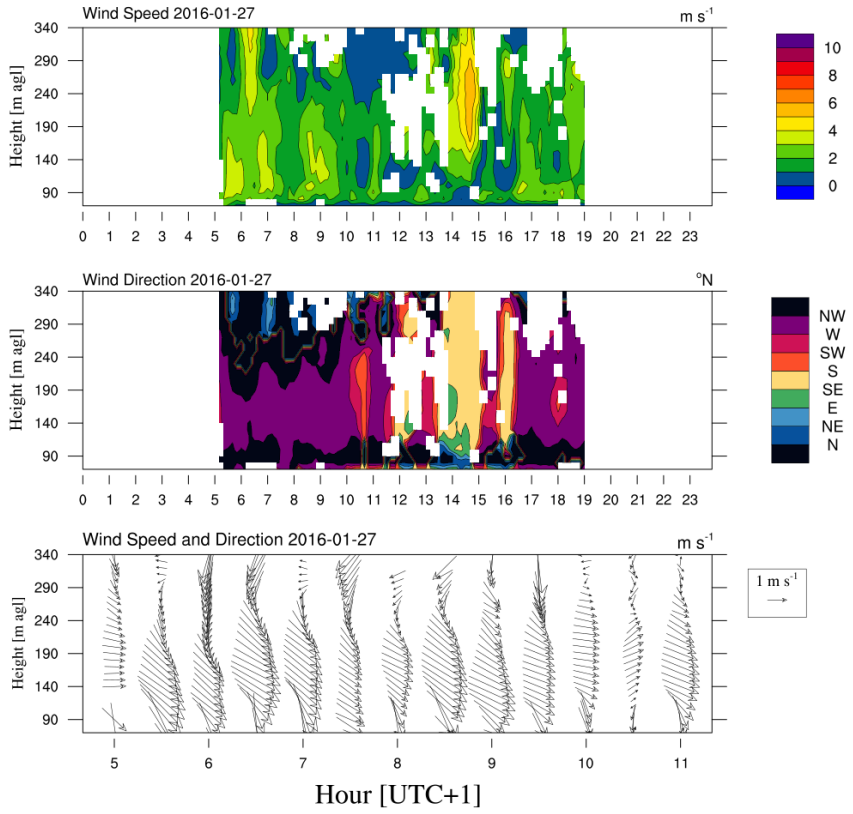

Figure 3.13: Time-height diagrams of wind speed (top panel) and direction (middle panel) measured by the SODAR on the roof of the incinerator plant. Bottom panel shows the evolution of the wind vertical profile during the morning hours from 5 to 11 LST.

Figure 3.13 shows the wind speed (top panel) and direction (middle panel) as measured from the SODAR instrumentation, on the roof of the incinerator plant. The measurements were taken from 5 to 19 LST only, because of issues linked to effects the noise produced by

the instrument on the surrounding neighborhoods. The observations show from 5 to 10 LST a drainage flow from the Adige Valley, up to ~200 m agl. In the upper layers, instead, a strong northerly wind flows over the incinerator. These measurements clearly state that, over the plant, two different wind regimes exist at different heights, with completely different speed and direction. This evidence highlights that modeling the dispersion of the emitted pollutants is extremely complex, as small differences in the calculation of the effective release height can lead to completely different impact scenarios (see Figure 3.13 bottom panel and Section 5.1.1 for details).

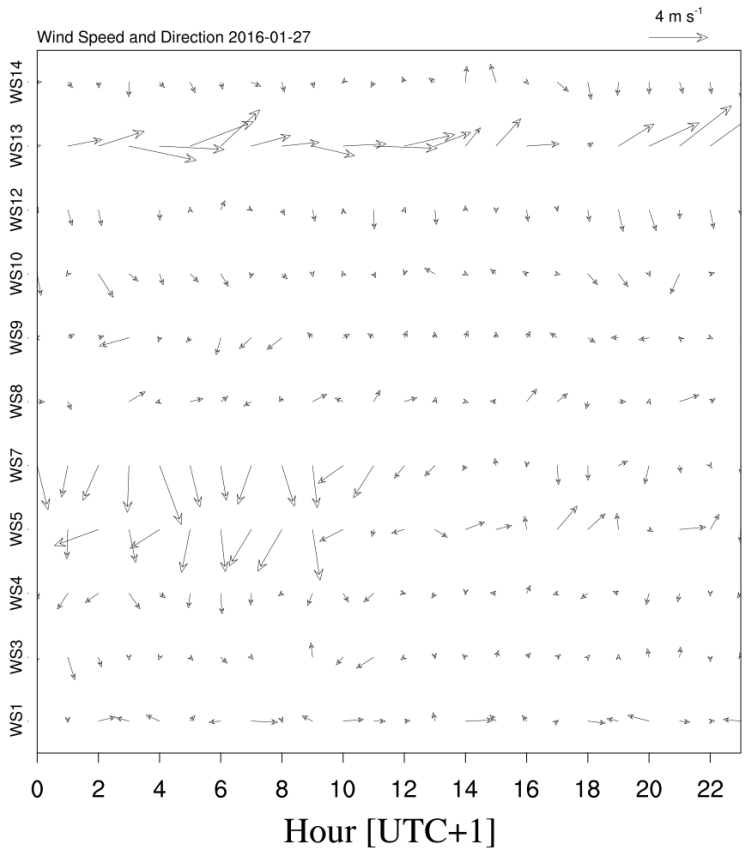

Figure 3.14: 10-m wind speed and direction measured by different weather stations. WS5, WS7 and WS13 are stations well above the valley floor.

Figure 3.14 shows the measurements of 10-m wind speed and direction collected by the weather stations. All the stations on the valley floors measured calm and weak winds, while stronger flows were recorded by the stations well above the valley floor only (namely WS5, WS7 and WS13). The meteorological conditions characterizing January, 27^{th}, are therefore typical wintertime conditions, relevant for the stagnation of locally emitted pollutants.

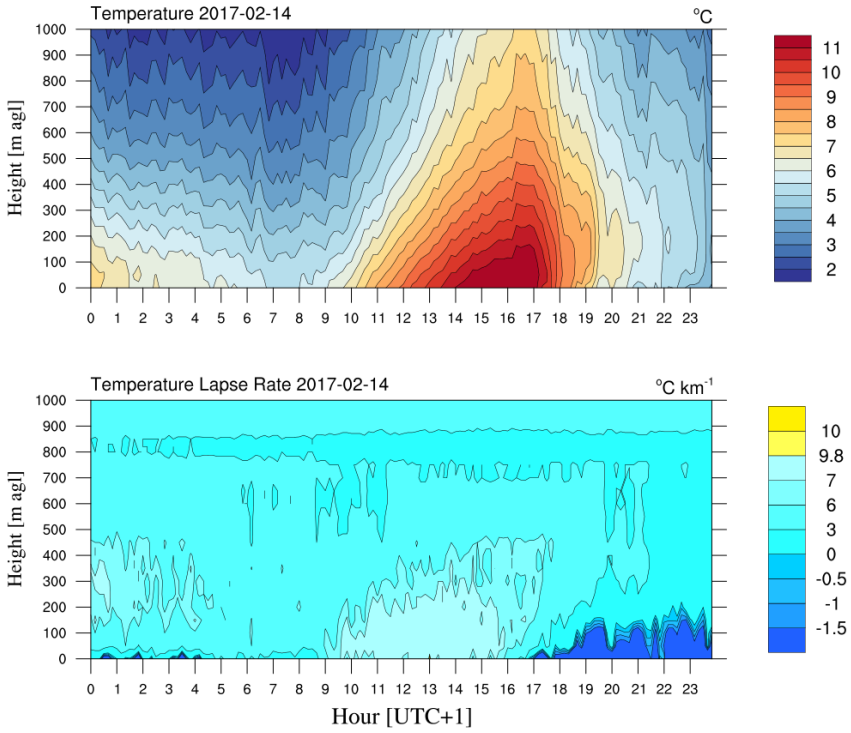

Figure 3.15: Time-height diagram of temperature and temperature lapse rate observed by the thermal profiler on February, 14^{th}, 2017. In the temperature lapse rate plot (bottom panel) blue, cyan and yellow colors identify thermal inversion, stable conditions and unstable conditions, respectively.

14th February 2017

February, 14^{th}, 2017, is the day when the two releases of tracer gas were performed. The meteorological conditions are analyzed on the basis of the observations from the thermal profiler, the SODAR, the LIDAR and the ground weather stations. Figure 3.15 shows the time-height diagram of temperature and temperature lapse rate. Observations show that the atmosphere was weakly stable throughout the whole day and almost neutral from 10 to 16 LST.

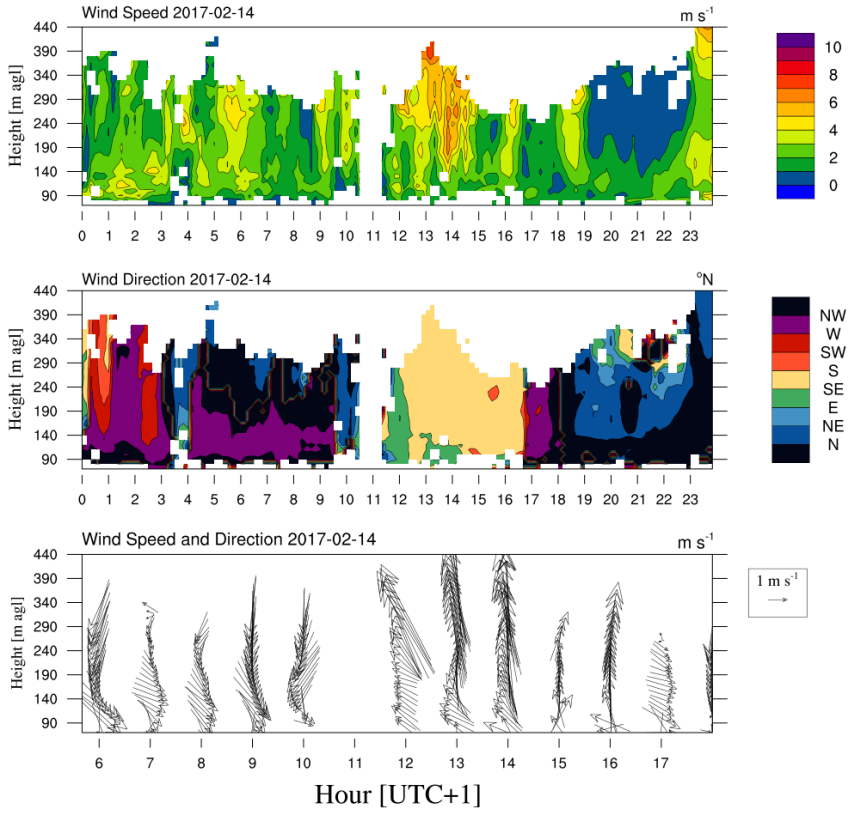

Figure 3.16: Time-height diagrams of wind speed (top panel) and direction (middle panel) measured by the SODAR on the roof of the incinerator plant. Bottom panel shows the evolution of the wind vertical profile during the central hours of the day, from 6 to 17 LST.

Figure 3.16 presents the measurements taken by the SODAR. In this case the instrument was operated for the whole day, and observations are available continuously except for an interruption between 10:30 and 11:30 LST due to a problem with the instrument. Recorded wind speeds are higher than in the first test day, but similar directions are recorded, especially in the early morning till 10 LST. In this time window it is possible to notice again two different flows in the lower and upper layers of the atmosphere: a north-westerly flow up to 150 m and a north/north-easterly wind above. From 11 till 16 LST, an up-valley wind flows in the Adige Valley, with southerly direction. In this period the SODAR measures very high wind speed, especially in the upper layers. However, these observations are not reliable, as with a southerly wind the plume is flying over the SODAR and its very high temperature (140 ^{o}C) interferes with the instrument, compromising its observations. Nevertheless, the direction of the measurements is not affected by the air temperature. In the late afternoon the wind looses strength and the direction turns again to north/northeast.

A different picture is given from the measurements taken by the LIDAR instrumentation, located only few kilometers away from the incinerator (Figure 3.17). The LIDAR instrumentation recorded observations above 300 m MSL. The instrument detected a strong drainage flow descending the Isarco Valley (which is north-easterly oriented) during the night until 10 LST. The wind speed is very high, with intensities greater than 10 m s^{-1}, and the jet reaches heights of 800 m MSL. In the late morning the jet flow ceases, while an up-valley, south-westerly wind takes place. Its intensity is lower, but it extends through a deeper layer, reaching heights above 1 km. After 16 LST the up-valley wind starts to decrease gradually from the lowest to the highest layers and the north-easterly jet wind grows again. It is likely that the strong drainage wind along the Isarco Valley flows into the Bolzano Basin and is forced to change direction by the orographic co-

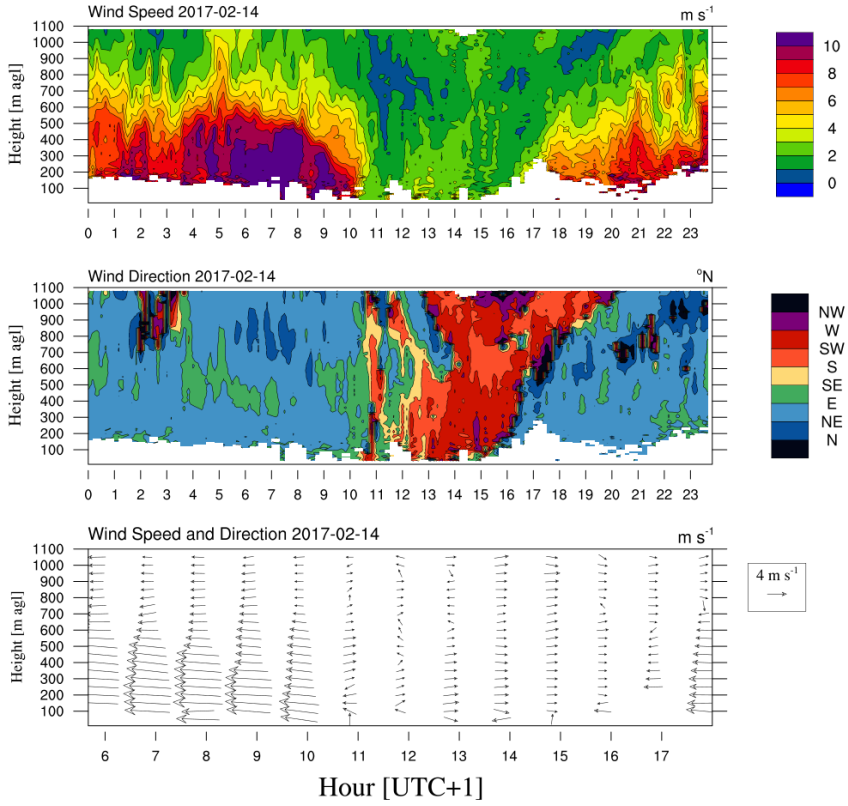

Figure 3.17: Time-height diagram of wind speed (top panel) and direction (middle panel) measured by the LIDAR located at the exit of the Isarco Valley. Bottom panel shows the evolution of the wind vertical profile during the central hours of the day, from 6 to 17 LST.

nstrains, which channel it in the Adige Valley. The strong, northerly-oriented flow recorded by the SODAR in the morning, and in the late afternoon, is therefore the jet from the Isarco Valley. It is interesting to notice that in the previous test day, the SODAR captured this flow at higher altitudes and with weaker strength. This is probably due to the fact that the air temperature in the basin is much lower on the 27^{th} of January and this cold pool prevents the jet flow to descend in the lowest layers of the atmosphere. On the contrary, on the 14^{th} of February, the cold pool in the Bolzano Basin is absent and the jet is

able to get closer to the ground. Information on this phenomena can be read from the 10-m wind measurements also.

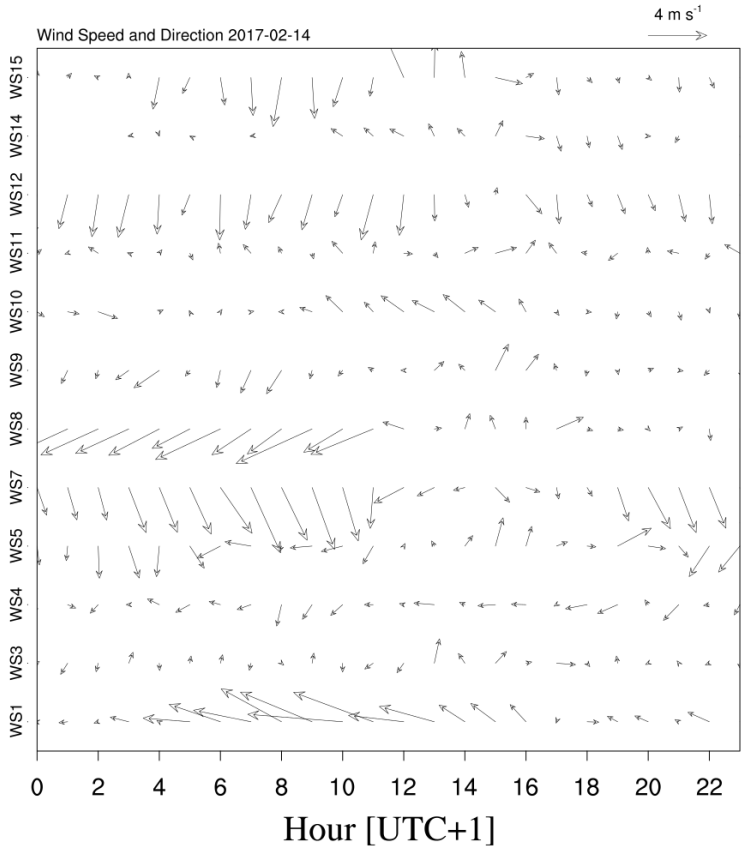

Figure 3.18: 10-m wind speed and direction measured by different weather stations.

Figure 3.18 presents the observations recorded by all the available permanent weather stations. It is interesting to notice the intensities and directions recorded in the stations WS12, WS8 and WS7: all the three stations measure a strong wind during the night till 10-11 LST; the direction of this flow is from the North in the station in the Isarco Valley, form the North-East in the Bolzano Basin, and from the North/North-West on the Caldaro plain. This evidence

suggests that the three stations lie along the Isarco Valley jet axis and are consistent with the measurements taken by the LIDAR and the SODAR equipments. The other valley floor stations measured low winds throughout the day, slightly stronger when blowing from South in the central hours of the day.

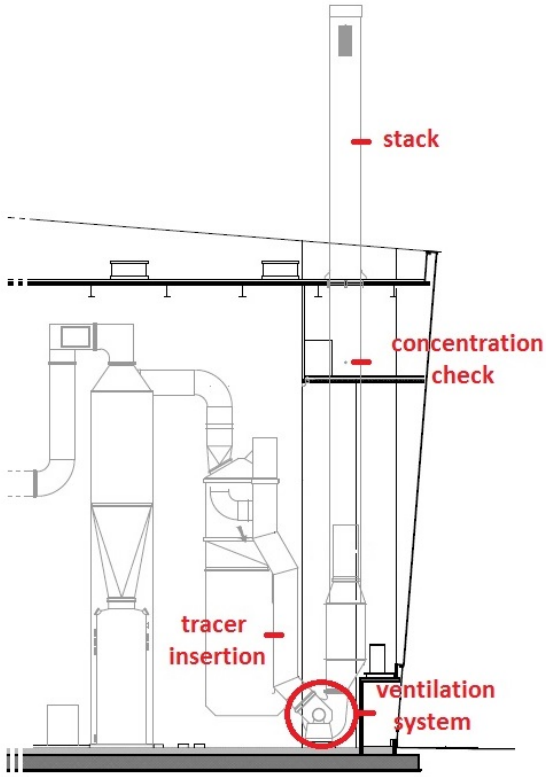

Figure 3.19: A vertical section of the incinerator plant with the locations of the insertion of the tracer, of the ventilation system and of the measurements of tracer concentrations.

3.3.4 Air quality data set

An air quality data set, relative to tracer gas concentrations at ground level, is available for the 14^{th} of February 2017 only. During this day, two releases of tracer gas were performed, one in the early morn-

ing, at 7 LST, and one in the early afternoon, at 12:45 LST. The first release lasted 1 h, the second 1.5 h. The tracer gas used is sulfur hexafluoride (SF_6). This gas is particularly suitable for this kind of experiments as it is strongly inactive, non-toxic, odorless, colorless, non-flammable and extremely stable at both ambient air and emitted smoke (140 ^oC) temperatures. In addition, it is not naturally present in the atmosphere with concentrations higher than 10 pptv. Thanks to these properties, SF_6 was used as passive tracer in the past for many different dispersion studies and experiments, especially in urbanized contexts (Allwine and Flaherty, 2006; Britter et al., 2002; Vandop et al., 1998; Britter and Hanna, 2003; Martin et al., 2011). The releases were performed by inserting 99% pure SF_6 at the basis of the incinerator stack, before the ventilation system which guaranteed a uniform mixing of the tracer in the smoke emitted by the plant. The inflow of SF_6 was regulated, so that the concentration of gas at the emission was constant. In order to have the precise value of the tracer concentration emitted at the chimney, continuous and real-time measurements were taken right before the exit of the smoke from the stack, with two mass spectrometers. Figure 3.19 presents a vertical section of the incinerator plant where the locations of the insertion of tracer, of the ventilation system and of the tracer concentration measurements are highlighted. Table 3.3 reports the main characteristics of each release, such as information about the duration of the release and about the released mass of tracer.

	Hour [LST]	**Duration [h]**	**Released tracer [kg]**	**Sampling points**
1^{st} release	7:00	1	150	14
2^{nd} release	12:45	1.5	450	14

Table 3.3: Summary of the main characteristics of the two tracer gas releases performed during BTEX on 14 February 2017.

The sampling procedure consisted in the deployment of 14 sampling teams distributed in the Bolzano Basin and its tributary valleys. 7 sampling teams maintained the same location during both the releases, forming a fixed sampling grid. The location of these sampling teams was chosen on the basis of the expected area of impact of the plume and of the distribution of the population.

Figure 3.20: Locations of the fixed sampling grid (yellow pins) and of the moving sampling grid (blue pins) during the 1^{st} (morning) release (left panel), and the 2^{nd} (afternoon) release (right panel).

As shown in Figure 3.20, 4 of the fixed sampling points are located in Bolzano, one in the industrial zone of Vurza, one close to the town of Laives and one very close to the incinerator plant, on the sidewall of the Adige Valley. The remaining seven sampling teams were located in different locations during the two releases, forming the moving sampling grid. These sampling teams were located on the basis of the results of a real-time modeling chain run during the experiment day. The modeling chain consisted of WRF simulations with observational nudging, coupled with two different dispersion models, CALPUFF and SPRAYWEB. The location of the moving sam-

pling points is presented in Figure 3.20 for both the releases.

Figure 3.21: Vacuum bottles used for the sampling of ambient air during BTEX. In the left panel the incinerator plant is visible in the back ground.

Each of the sampling team collected sampling of ambient air with a set of 1-l vacuum-filled glass bottles with automatic filling valves (see Figure 3.21). Sampling of 1 h or 20 min were collected with this equipment. Three of the sampling teams also collected an additional set of measurements, during the experiment, by means of teflon bags filled by air pumps.

The timing and the choice of sampling type were again decided on the basis of real-time dispersion forecast. The collected samples were analyzed by the laboratories of EcoResearch and Mario Negri Institute by means of mass spectroscopy analysis with a detection limit of 30 pptv.

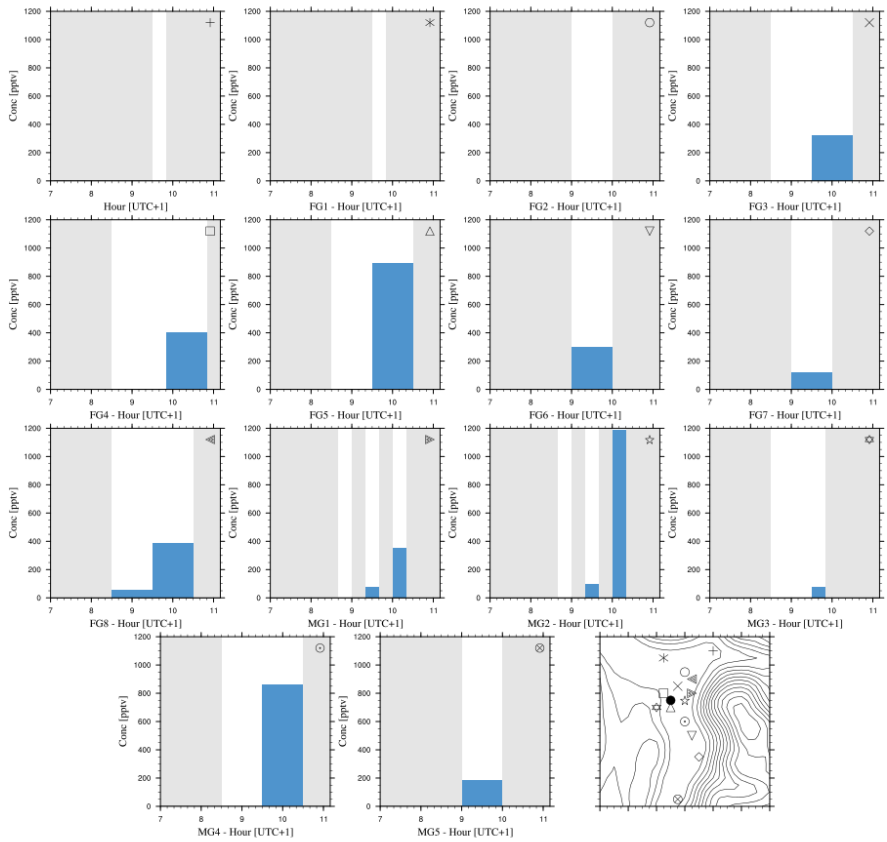

Figure 3.22: The blue histograms show the concentration of tracer gas measured at ground level by the different sampling teams with the vacuum bottles. Grey background means no measurements taken. During the morning release no representative measurements were taken with the teflon bags. The last panel shows the location of each sampling team with different marker styles.

Figure 3.22 shows the sampling data collected during the 1^{st} release experiment. Sampling begun at 8:30 LST but detectable concentrations were recorded by only one sampling point, located Northeast to the plant. As the release started at 7 LST, we can state that the tracer took at least 2 hours to reach the ground in most of the sampling points. This slow dispersion of the tracer is consistent with

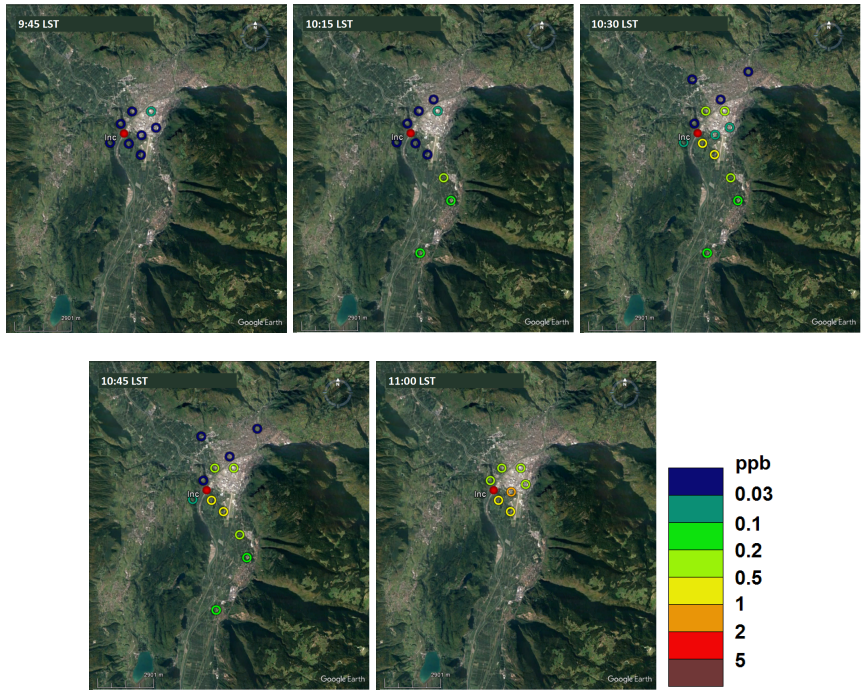

Figure 3.23: Time evolution of the tracer concentrations measured during the 1^{st} release experiment. Panels from the top left corner to the bottom right corner correspond to 9:45, 10:15, 10:30, 10:45, 11:00 LST (background maps from Google Earth).

the stability of the atmosphere, discussed in the above sections. Concentrations started to increase after 9 LST in the sampling points located in the eastern part of the Adige Valley, especially the ones towards the South. Only later tracer was detected in the westerly sampling points. The measurements therefore suggest that the plume moved firstly toward South-east and later diffused in the whole Adige Valley. The tracer never reached the furthest sampling points located to the North of the incinerator plant, consistently with the wind speed and direction measured in the area. Figure 3.23 shows the measured concentrations on the map, at five different times, in order to give an idea of the dispersion pattern.

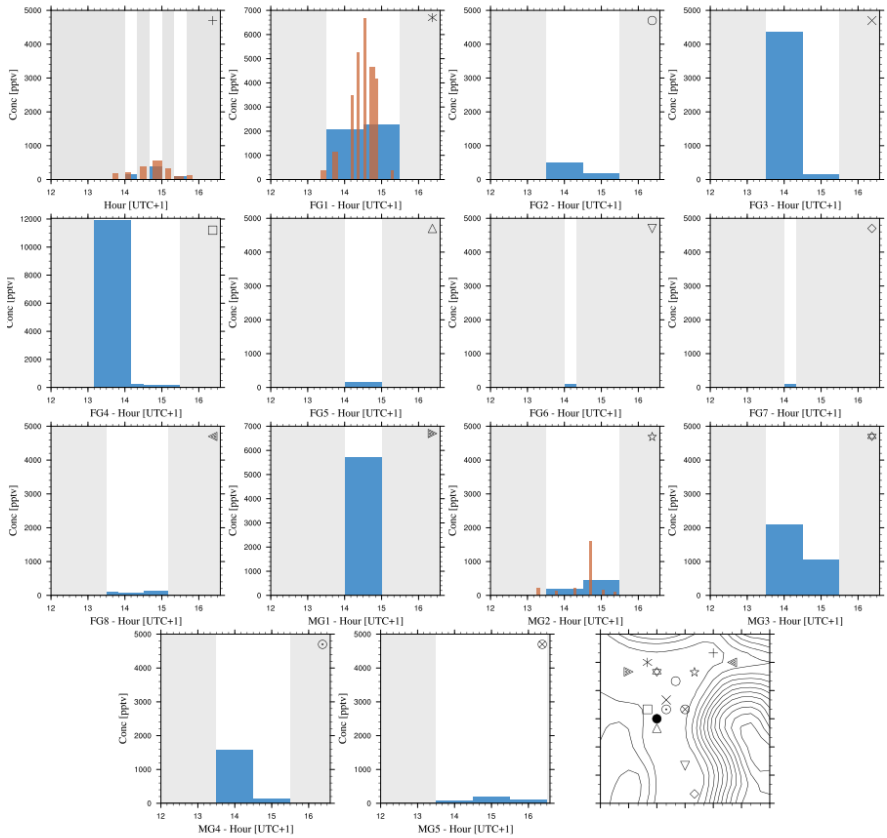

Figure 3.24: The blue histograms show the concentration of tracer gas measured at ground level by the different sampling teams. Grey background means no measurements taken. Measurements taken with the vacuum bottles are shown in blue, while measurements taken with the teflon bags are shown in red. The last panel shows the location of each sampling team with different marker styles.

Figure 3.24 presents the measured concentrations during the 2^{nd} release experiment. The 2^{nd}, 5^{th} and 10^{th} panels have a different scale on the y-axis, as they presented much higher values of concentration. In this case, the earliest observations are registered only 30 min after the release started. This is again consistent with the slightly unstable state of the atmosphere, as recorded by the meteorological instru-

ments. The highest concentration was measured in the sampling point close to the incinerator toward North-west. High concentrations follow in most of the sampling points to the North of the plant with peaks in the north-west locations. The observations therefore suggest that the plume moved towards the North-west, impacting the whole Bolzano basin. Only traces of SF_6 were detected in the sampling points located to the South of the plant. Figure 3.25 shows the measured concentrations on the map, at five different times, and gives an idea of the afternoon dispersion pattern.

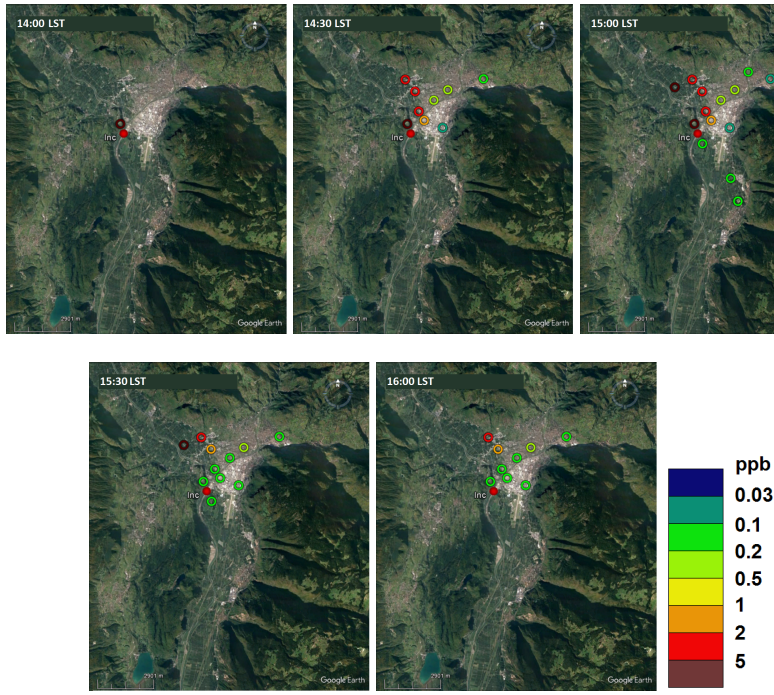

Figure 3.25: Time evolution of the tracer concentrations measured during the 2^{nd} release experiment. Panels from the top left corner to the bottom right corner correspond to 14:00, 14:30, 15:00, 15:30, 16:00 LST (background maps from Google Earth).

Chapter 4

Improving the modeling of wintertime meteorological phenomena over complex terrain

In this Chapter analyses on two different case studies are presented.

The analysis conducted on the Aldeno ALPNAP case study focuses on the influence of LSMs on the results of the WRF model. This study led to the optimization of specific features within the land surface schemes of the WRF model, improving its abilities in capturing peculiar meteorological wintertime phenomena. The presented work has been published on the Monthly Weather Review AMS journal (Tomasi et al., 2017). Refer to the Published Paper Section for the AMS Copyright notice and for the complete paper text.

The second analysis, performed for the Merano case study, allowed to show the differences in the meteorological fields when similar modifications to surface characteristics are applied in the WRF simulations and their effects on the dispersion of pollutants.

4.1 The Aldeno Case Study

High-resolution numerical simulations were performed with the WRF model to assess the performance of the Noah and Noah_MP LSMs over snow-covered ground in an alpine valley. The two LSMs were evaluated by comparing their results against observations from a wintertime field campaign in the Adige valley, in the Italian Alps. The prime aim of the present analysis is the evaluation of the LSMs, and therefore comparisons are made in terms of 2-m temperature, both on the valley floor and on the sidewalls, and of incoming and outgoing SW and LW radiation in a reference station on the valley floor.

The data set from the Aldeno case study, presented in Section 3.1, was used in order to validate the results of four different simulations. The first two simulations (S1 and S2 hereafter) were run in order to test the Noah and the Noah_MP LSMs in their standard versions released with WRF 3.8.1. Then results from S1 and S2 are compared with measurements, and an evaluation of the performance of the standard version of the model, when applied at a high resolution, is made. On the basis of this comparison, some corrections were implemented to the initialization of the model, to the land use classification and to both the LSMs, in order to improve model performance. Other two simulations were then run (S3 and S4 hereafter) with all these changes, using the modified versions of Noah and Noah_MP, respectively.

All the simulations S1, S2, S3 and S4 share the same settings as to the dimensions of the domains, horizontal and vertical grids, meteorological boundary and initial conditions, static input data and all the physics options. The only differences lie in the LSM, which is the Noah LSM in S1 and S3, while the Noah_MP LSM is adopted in S2 and S4, and in the aforementioned modifications to the standard runs. The settings common to all of the four simulations are presented in the following Section 4.1.1, while the modifications implemented in

S3 and S4 are described in Section 4.1.2.

Nest Number [−]	Horizontal grid space [km]	Dimensions [km]	Time step [s]
1	10.8	1080 x 1080	100
2	3.6	327.6 x 327.6	33.3
3	1.2	109.2 x 120	11.1
4	0.4	36.4 x 43.6	3.7

Table 4.1: Characteristics of the nested domains of simulations S1, S2, S3 and S4.

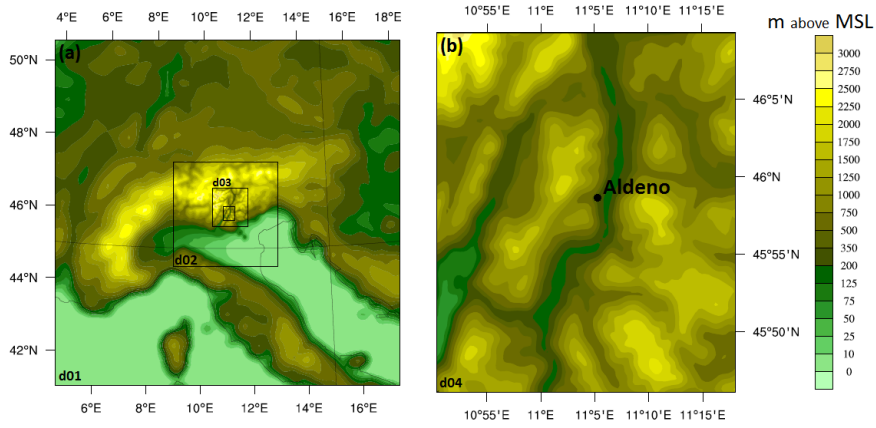

Figure 4.1: Domains of simulations S1, S2, S3 and S4 with their elevation contours: (a) the 4 simulation domains and (b) the innermost domain, centered over the town of Aldeno.

4.1.1 Model set-up

All the simulations are run with four two-way nested domains, with horizontal resolution going from 10.8 km in the external domain to 400 m in the innermost domain, with the recommended 3:1 ratio between successive nests. 40 vertical levels are used as vertical grid spacing in all 4 domains. Table 4.1 reports the details of the set up

domains and Figure 4.1 shows their elevation contours.

The study period (see Section 3.1.2 for details) starts from 1200 UTC (LST=UTC+1 h) 11 February 2006 and ends at 0000 UTC 16 February 2006, covering 108 h. As the model initialization influences the first 12 h of simulation, they are not compared against observations and are used as a spin up period.

6-hourly NCEP Final Operational Global Analysis data on 1-degree grid are used as initial and boundary conditions for the simulations. The default WRF data sets are used to provide topography and land use static data for the three external domains, with a resolution of 1 km. The chosen land cover data set is the MODIS-based (MODerate resolution Imaging Spectroradiometer) data set, with the IGBP Land Cover Type Classification. As to the innermost domain, data sets with much higher resolution were needed in order to properly describe the orographic features and the land use. For this reason, customized static data with a very high resolution were provided. The Digital Terrain Model (DTM) adopted for the 4^{th} domain has an original spatial resolution of 30 m (de Ferranti, 2013), while the land use data set has a resolution of 100 m. To avoid numerical instability, one smoothing pass with the 1-2-1 smoothing filter had to be applied to the topography. As to land use, the Corine Land Cover (CLC) data set (EEA, 2006) was adopted after reclassifing it into the standard IGBP classes, as shown in Giovannini et al. (2014 a), in order to match the WRF land use tables.

The same physics schemes are applied in all the simulations presented, except for the land surface model. The Grell-Freitas cumulus scheme (Grell and Dèvènyi, 2002) is used for domain 1 and 2, while no cumulus physics option is adopted for the two smaller domains. The microphysics scheme employed is the WRF Single-Moment 3-class simple ice scheme (Hong et al., 2004), and the parameterization applied for the planetary boundary layer is the YSU scheme (Hong

et al., 2006). The Dudhia scheme (Dudhia, 1989) and RRTM scheme (Mlawer et al., 1997) are applied for SW and LW radiation, respectively. Radiation schemes are called every 10 min and the effects of shading and slope angle appropriate for complex terrain are taken into account.

Noah_MP LSM is run with the default combination of its internal parameterizations. This include: no dynamic vegetation; a Ball-Berry type stomatal resistance scheme (Ball et al., 1987; Collatz et al., 1991, 1992; Sellers et al., 1996; Bonan, 1996); the simple TOPMODEL by Niu et al. (2007) for runoff and groundwater treatment; the Niu and Yang (2006) approach for supercooled liquid water (or ice fraction) and frozen soil permeability; a two stream radiation transfer model applied to vegetated fraction; the CLASS option for ground snow surface albedo (Verseghy, 1991); the relatively complex functional form of Jordan (1991) for partitioning precipitation into rainfall and snowfall; and the Sakaguchi and Zeng (2009) option for surface evaporation resistance. In addition, lower boundary conditions of long-term bottom (8 m depth) temperatures come from the original Noah reference data, the snow/soil temperature time scheme is semi-implicit, the same soil moisture factor for stomatal resistance as Noah LSM is used, the applied glacier treatment includes phase change of ice and the Monin-Obukhov surface-layer drag coefficients are utilized. The output of WRF is saved every 15 min and the corresponding hourly averages are compared with measurements for consistency.

4.1.2 Applied modifications

Modifications to WRF initialization

The results of S1 and S2, shown in Section 4.1.3, highlight that the initial snow depth in the simulations was highly overestimated, by the standard initialization procedure in the WRF Preprocessing System

(WPS). Unfortunately, snow height measurements are not available for the study period chosen. However, photographs taken during the campaign show the snow condition on the ground and allow estimating the snow depth and density. Comparing these estimates with the model predictions, an overestimation was detected. The causes of this overestimation were found to derive from some assumptions reported in the WPS, and not simply in the input data from the reanalyses.

The first of these assumptions lies in the WRF preprocessor code ungrib. In this code the snow water equivalent (SWE) is doubled if NCEP reanalyses are used. However, if field observations are compared to the values obtained with this procedure, the amount of snow on the ground is overestimated by 20% in the present case study. The second identified problem regards the procedure through which ungrib calculates the snow height from SWE data. To move from one quantity to the other, the ungrib code uses a fixed value of snow density, i.e. 200 $\mathrm{kg\,m^{-3}}$, assuming fresh snow, independently from either the season of the year or the date of the last snowfall. Under this hypothesis, the snow depth is significantly overestimated. The overestimation of both the SWE and snow depth directly affects the snow fraction and the surface albedo calculated by the LSMs. For this reason, the SWE and the snow depth have been here estimated according to field measurements and modifications to the ungrib code were applied in order to calculate initial values that fit the real snow condition at the beginning of the simulation. This operation was done by multiplying the SWE NCEP GFS (Global Forecast System) data by 1.7 times and fixing the snow density to 350 $\mathrm{kg\,m^{-3}}$ (Pomeroy and Brun, 2001; Meloysund et al., 2007) which reproduces the conditions of 15-day-old snow.

Modifications to the land use

On the basis of the adopted MODIS-based data set, the entire Adige Valley floor except for the urban areas is classified as "*cropland*". This category includes all types of cultivation but, in the present case study, the parameters used to describe this land use type appears to be not appropriate. Indeed, these parameters describe the behavior of a typical American crop farming (e.g. corn cultivation) which little resembles the apple orchards present in this contest. This inconsistency is especially relevant when snow covers the ground: in fact, under these circumstances, the vegetated fraction of any domain cell strongly depends on the vegetation type height and it increases considerably if the land use type involves the presence of actual trees. In order to solve this deficiency, a dedicated land use class was needed to describe the apple orchard land use type. This class was introduced and described in the tables of the WRF model (VEGPARM.TBL and MPTABLE.TBL), combining parameters of the IGBP "*deciduous broadleaf forest*" class and of the Corine "*apple orchard*" class.

Parameters	**IGBP Deciduous broadleaf forest**	**New Orchard**
Canopy top height	20	3
Canopy bottom height	11.5	1
Minimum roughness length	0.5	0.3
Maximum roughness length	0.5	0.3
Tree density	0.1	0.25

Table 4.2: Modified parameters in the "deciduous broadleaf forest" class in order to create a new *ad hoc* "orchard" land use class

In particular, the new land use class is described using "*deciduous broadleaf forest*" parameters with modified values for the heights of the canopy top and bottom, for the minimum and maximum roughness

lengths, and for the tree density (Table 4.2). The Snow Cover Fraction (SCF) experienced a significant decrease, in the Noah LSM, thanks to the introduction of this new land use type and, as a consequence, the cell albedo and the 2-m temperature decreased and increased respectively. As to the Noah_MP LSM, another issue was identified in the parameters describing the different land use types. Specifically, within the Noah_MP model, the SCF of each cell is calculated by means of the formulation proposed by Niu and Yang (2007):

$$SCF = tanh\left(\frac{h_{sno}}{2.5 z_{0g} (\rho_{sno}/\rho_{new})^m}\right) \tag{4.1}$$

where h_{sno} is the snow depth, whereas fresh snow density ρ_{new} (100 kg m^{-3}) scales the actual snow density ρ_{sno}, z_{0g} is the ground roughness, and m is a melting factor determining the curves in the melting season. This m factor, following the literature (Niu and Yang, 2007; Su et al., 2008), should be larger for larger scales and should be calibrated case by case against data from measurements of albedo and SCF in the study area. Nevertheless, in Noah_MP, as implemented in WRF v3.8.1, this factor is fixed to 2.5 for each of the existing land use types. In the present case study, this value for the m factor was found to be misleading, as it produced a strong underestimation of the SCF. This evaluation was made on the basis of SCF data from the MODIS/Terra Snow Cover Daily dataset (Hall and Riggs, 2016), with a resolution of 500 m, and of literature suggested values. Given the values of the modified initial snow depth and density and of the measured SCF, equation 4.1 can be inverted and solved to find m. Calibrating m in order to best fit the measured SCF, a value of 1 is obtained. m equal to 1 allows to obtain, in the reference station point, a value of SCF equal to 0.9 (close to the measured value of 1), against a value of 0.2 for SCF obtained with m equal to 2.5.

Modifications to the Noah LSM

The Noah LSM tends to systematically overestimate the values of the albedo in the presence of snow, as shown by results from S1. The procedure followed to obtain the snow cell albedo is the one proposed by Livneh et al. (2010). However, two inconsistencies were identified in the way Livneh's scheme is implemented within the WRF 3.8.1 code. In fact, the albedo of the snow-covered portion of the cell (α_{snow}) is calculated as follows (from Livneh et al. (2010)):

$$\alpha_{snow} = \alpha_{max} A^{t^B} \tag{4.2}$$

where t is the age of the snow (in days), A and B are constant parametric coefficients (different for the accumulation and melting season) and α_{max} is the maximum albedo of fresh snow, which depends on the land use class. Nevertheless, in WRF, t is always initialized to 0 days, which means that the pre-existing snow on the ground is always initialized as fresh. In addition to this, the A and B coefficients, which control the rate at which the albedo of the snow-covered part of the cell decays over time, are forcefully fixed to the values for the accumulation period, no matter the period of the year. Both these assumptions are inadequate for the present case study, because the last snowfall, prior to the starting time of the simulation, occurred 15 days earlier and because the ambient temperatures lead to a rapid melting of the snow throughout the study period. For these reasons, we introduced two modifications in the implementation of Livneh's procedure in WRF v3.8.1: A and B coefficients were set to their melting season values and t was set to 15 days. These arrangements reduced the calculated surface albedo by 50%, as shown in the following sections.

Modifications to the Noah_MP LSM

Besides the interventions on the snow cover initialization and on the land use description, the Noah_MP scheme results still showed problems in the reconstruction of the 2-m temperature. Specifically, the 2-m temperature never increased enough during daytime, compared to observations. One of the causes of this behavior was diagnosed by means of a detailed analysis of the Noah_MP LSM implementation within the WRF code. The analysis revealed that the model intentionally prevents ground temperature from increasing above 0°C when more than 5 cm of snow cover the ground, both under canopy and over bare soil. This choice directly influences the raising of the 2-m temperature and the fixed limit of snow depth appears quite inconsistent, especially if such a thin snow layer lies under sun-exposed canopy. Indeed, on this conditions, it is likely that some patches of snow-free ground emerge under trees, contributing to increase the temperature above 0°C. In order to allow this occurrence, the limitation implemented in Noah_MP LSM was removed for under-canopy snow depths smaller than 10 cm.

4.1.3 Results

This section presents the results of both standard (S1 and S2) and modified (S3 and S4) simulations, comparing them both against each other and against observations of short- and long-wave incoming and outgoing radiation, as to of 2-m temperature. The changing in the results of S3 and S4, with respect to S1 and S2, are to be attributed to all the modifications described above. Further details on the effects of each single modification, are provided in Section 4.1.4.

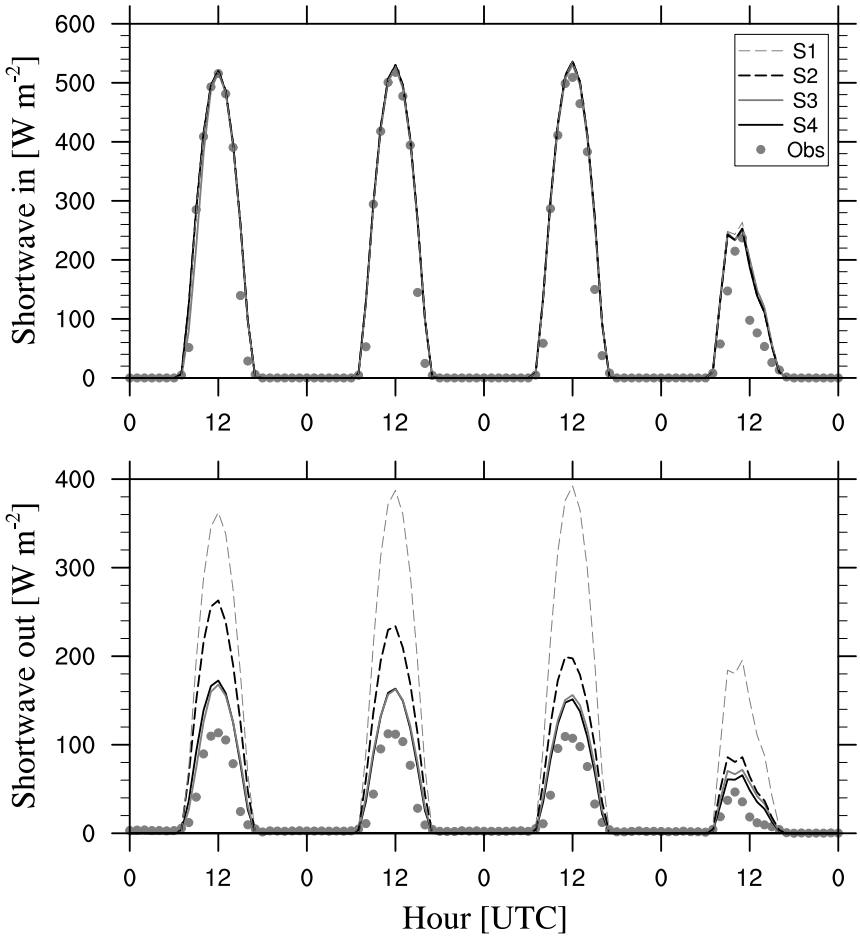

Figure 4.2: Incoming and outgoing shortwave radiation observed and estimated by the four simulations (S1-S4) at the valley floor reference station (AlRef).

Radiation

Incoming and outgoing shortwave radiation are shown in Figure 4.2, as observed and as modeled by the four simulations. All the simulations well reproduced the incoming SW radiation and are able to identify the cloudy sky conditions in the fourth day of the study period. On the contrary, consistently with the overestimation of the

snow cover and of the snow albedo, S1 and S2 greatly overestimate the outgoing SW radiation, with higher errors for S1. Thanks to the applied modifications in S3 and S4 results significantly improve with respect to the observations, with similar results in both the new simulations. At midday peaks the outgoing SW radiation decreases by about 200 $W\,m^{-2}$ in S3 and by about 40-100 $W\,m^{-2}$ in S4, and the bias between calculated and observed values reduces to a maximum value of ~50 $W\,m^{-2}$ around midday.

Longwave radiation, shown in Figure 4.3, is basically underestimated in both its incoming and outgoing components by the default WRF runs, especially by S1. S3 and S4 succeed in increasing the incoming and outgoing LW radiation, getting closer to the measured values. The fact that both changing the LSM (from Noah to Noah_MP) and applying the proposed modifications have an impact on the incoming LW radiation is noteworthy. Indeed, this behavior could be unexpected and questions may arise as to why the SW radiation does not experience the same effects. In order to explain this evidence, it must be taken into account that incoming SW and LW radiation come from two different and independent radiation schemes. Dudhia (1989) radiation scheme is applied to parameterize SW radiation: the downward SW flux is calculated taking into account the solar zenith angle and the effects of clouds and clear air. The flux is also corrected in order to account for slope effects and shading, given the complex topography of the simulation domain. Downward SW flux has no dependence on air temperature. Therefore, the change in LSM or the modifications to snow initialization and land use type have no effects on the results of the incoming SW radiation scheme. Moreover, even if the decrease in outgoing SW flux induced in S3 and S4 increases the temperature on the valley slopes, it has no impact on the downward SW flux on the valley floor because temperature is not taken into account in the Dudhia SW radiation scheme. On the other

hand, the LW radiation scheme is sensitive to model layers air temperature, as emitted LW radiation directly depends on temperature (Mlawer et al., 1997).

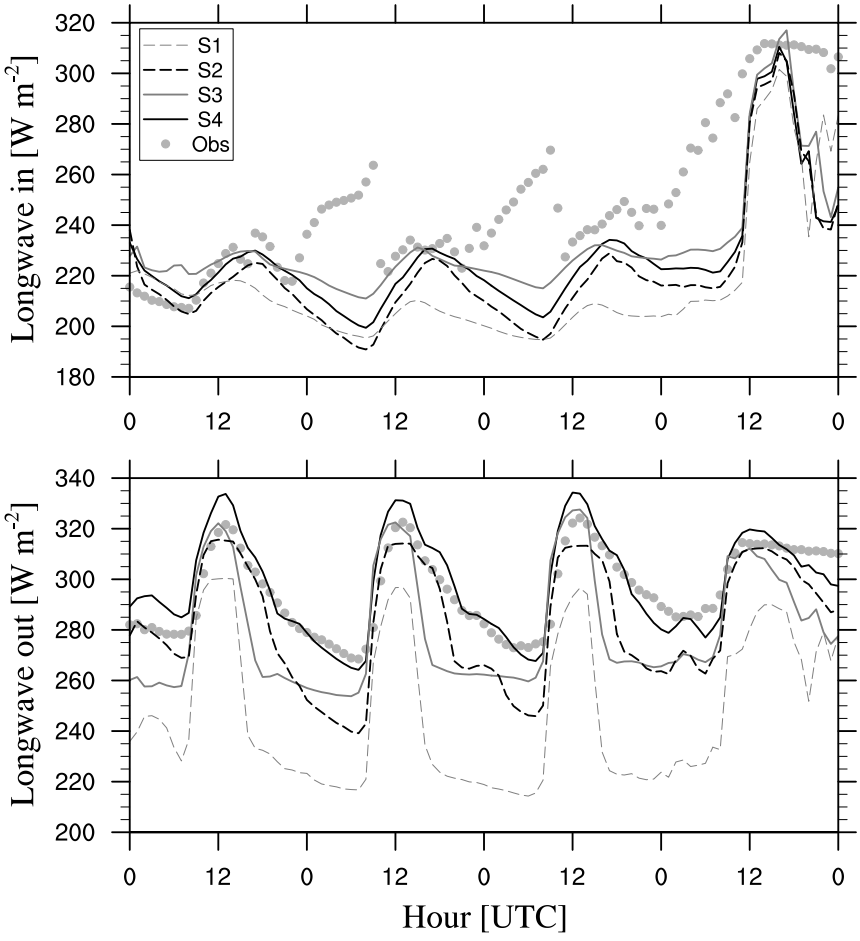

Figure 4.3: Incoming and outgoing longwave radiation observed and estimated by the four simulations (S1-S4) at the valley floor reference station (AlRef).

A change in the WRF LSM leads to a change in the temperature of the first model layers, influencing the calculation of the incoming LW radiation. In the same way, the modifications to snow initialization

and to the land use contribute to modify the vertical temperature profile, which in turn affects the incoming LW flux. Figure 4.4 shows the temperature vertical profiles above the valley floor at 12 LST, 12th February 2006, from the four simulations: different near ground temperatures influence the vertical temperature profile up to 1800 m MSL, due to the complex topography of the area (the Adige valley is rather narrow and the highest crests flanking the valley reach 2000 m MSL). This effect is particularly noticeable in a narrow valley, where an increase in surface temperature on the valley slopes significantly affects radiation budgets in the whole valley atmosphere, increasing the downward LW radiation on the valley floor.

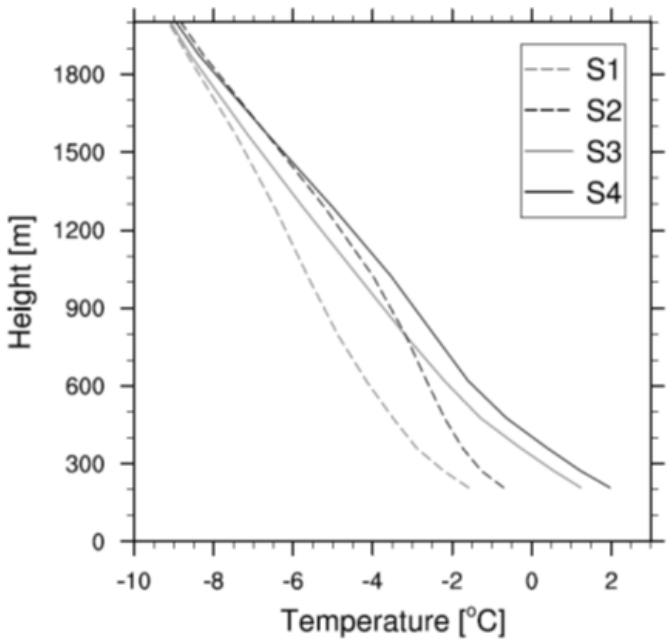

Figure 4.4: Temperature vertical profiles above the valley floor reference station (AlRef) at 12 LST 12th February 2006, from the four simulations.

Results in terms of incoming LW radiation are similar for S3 and S4: midday peaks are quite well captured, but the incoming LW radiation is still considerably underestimated after sunset on the second

and third days, when the observations recorded an increase in this variable. This effect is very likely caused by the formation of low-level clouds developing at night and dissolving after sunrise which are not reproduced by the WRF model. This error in model results, indeed, has no connection with the performance of the land surface scheme, whose assessment is the main focus of the present analysis. On the other hand, the model properly identifies the cloudy sky conditions occurring on February 15^{th}, even if it is not able to fully capture its evolution in time, specifically the gradual increase in incoming LW radiation.

S3 and S4 also capture better the outgoing LW radiation. S3 properly identifies the daytime maxima, still underestimates nighttime minima, but errors are strongly reduced if compared with S1. Despite this, the decrease rate in the outgoing LW radiation after sunset is very different from what observed: the model, in fact, does not produce a gradual decrease in the variable, but presents an almost instantaneous drop and a constant pattern during nighttime. S4, on the contrary, suceeds in better reproducing the decaying phase of outgoing LW radiation, but slightly overestimates the midday maximum values.

2-m Temperature

2-m temperature is strongly underestimated by both S1 and S2, during the night as well as during the day (see Figure 4.5). Higher errors affect simulation 1, especially for temperature minima. This means that, without any modification, in the present case Noah_MP performs better than Noah. Nevertheless, the proposed modifications result in an even better agreement with observations, thanks to an increase in the simulated temperature. In fact, decreasing the outgoing SW radiation allows the surface energy budget to have a significant extra rate of energy, with a consequent increase in the 2-m

temperature.

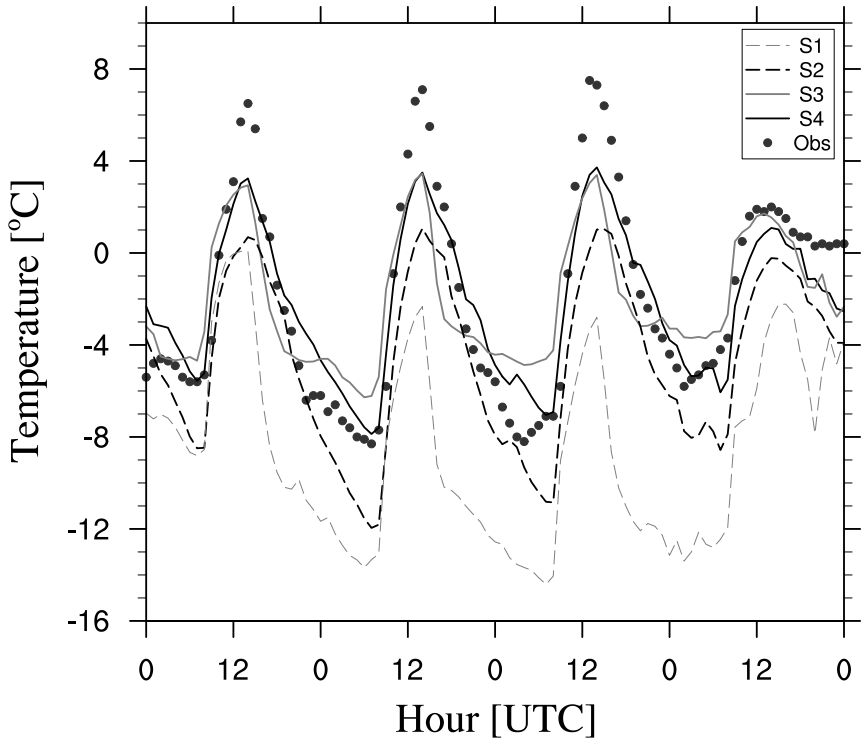

Figure 4.5: 2-m temperature observed and estimated by the four simulations (S1-S4) at the valley floor reference station (AlRef).

The performance of S3 shows an underestimation of daytime maxima by still ~ 3-4°C, and a slight overestimation of nighttime temperatures. Therefore, the overall effect of the implemented modifications in S3 is a significant decrease in the daily temperature range. The best agreement with observations is obtained with S4. This simulation is able to well capture nighttime minima, with a maximum absolute error of ~1°C, and to get closer to observed daytime maxima. The error for daytime maxima is still ~3-4°C, but it only lasts for a short time interval, as temperature rapidly increases and decreases in the central hours of the first three days. Notice that, in the last day of

simulation, the maximum temperature is well captured (especially by S3), while temperature drop after sunset is slightly overestimated. This error is clearly due to the underestimation of the cloud cover, shown by the decrease in the incoming LW radiation in Figure 4.3, and cannot be ascribed to the LSM.

Ground-based thermal inversion

As the ground-based thermal inversion is a particularly relevant phenomenon over complex terrain, it is interesting to evaluate if the model is able to properly reconstruct it. In order to do this, 2-m temperatures observed at the reference station of the valley floor (AlRef) and at the highest available station on the valley sidewalls (Sw1, 200 m above the valley floor) are presented in Figures 4.6 and 4.7.

Observations clearly show a significant difference between the diurnal thermal range on the valley floor and on the sidewalls, which leads to a strong ground-based thermal inversion during nighttime, systematically dropping during daytime. The Noah LSM is unable to reproduce the thermal inversion both before and after the modifications, as shown in Figure 4.6. Indeed, S1 produces a too strong inversion during nighttime, while barely identifies its decay during daytime. S3 is able to reproduce a greater temperature range on the valley floor than along the sidewalls, but completely misses the thermal inversion during nighttime, except for a weak inversion on the second night.

On the other hand, WRF coupled with the Noah_MP scheme better captures the evolution of the thermal inversion, both with S2 and S4 (Figure 4.7): S2 properly identifies the nighttime inversion and slightly captures its morning break-up; the proposed modifications of S4 allow instead a stronger increase in the daytime 2-m temperature and therefore result in a more accurate reconstruction of the evolution in time of the thermal inversion.

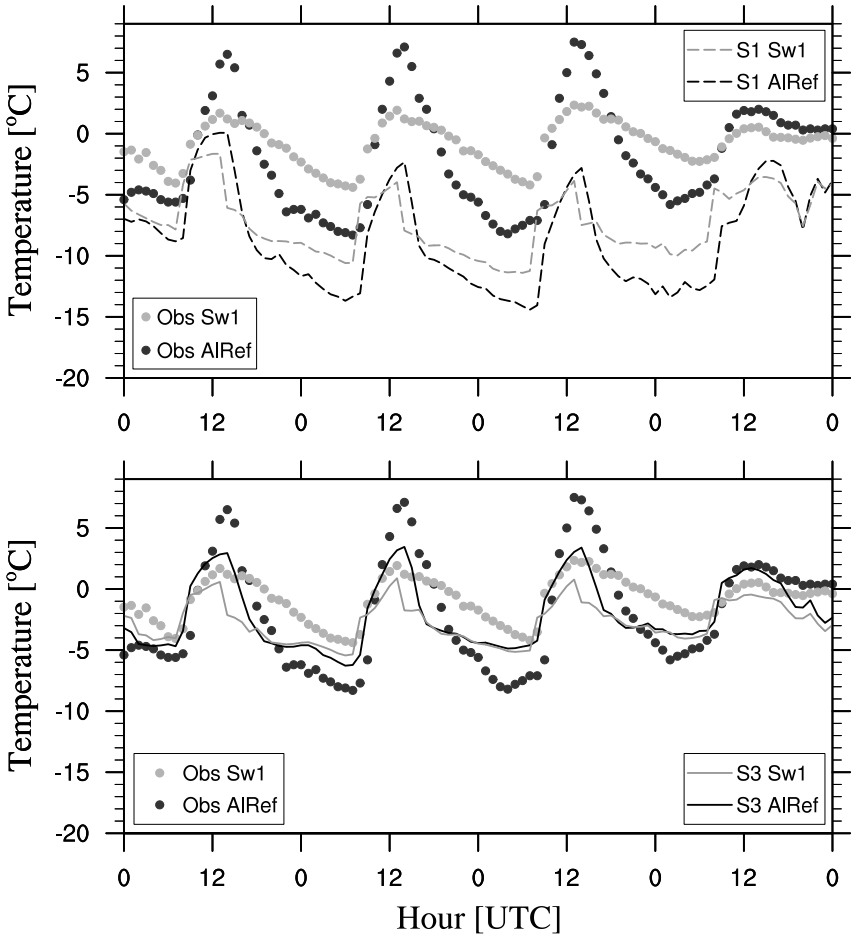

Figure 4.6: Comparison of 2-m temperature at the valley floor and on the sidewall, observed and estimated with S1 (standard Noah LSM), and S3 (modified Noah LSM).

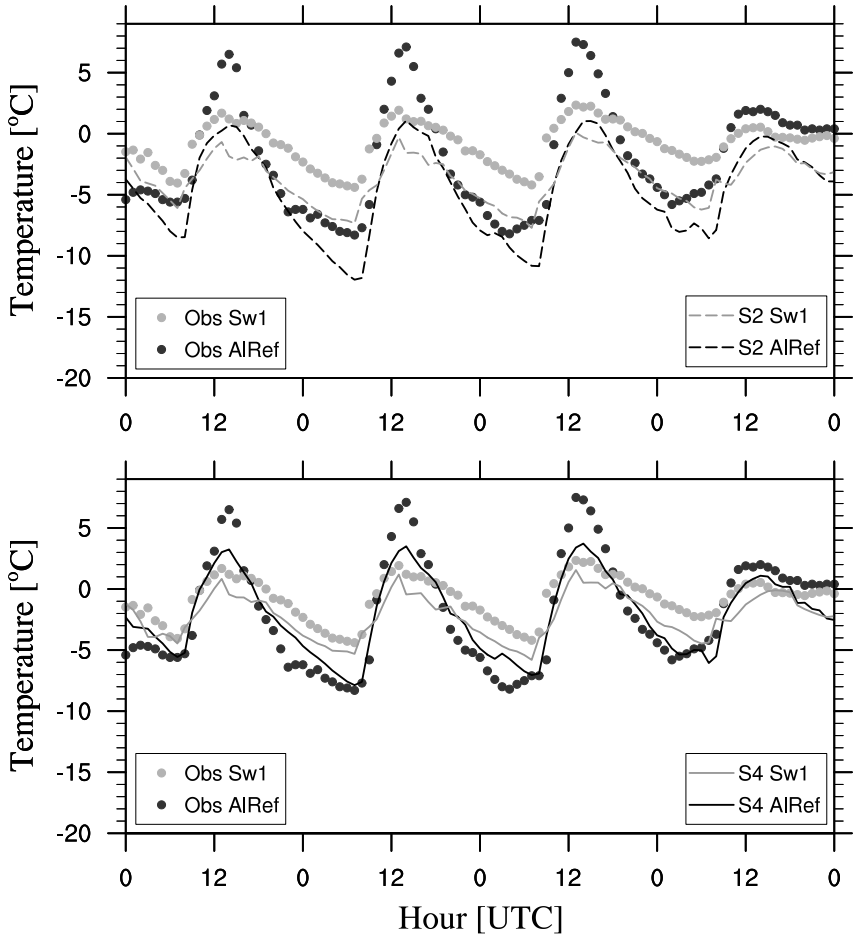

Figure 4.7: Comparison of 2-m temperature at the valley floor and on the sidewall, observed and estimated with simulation 2 (standard Noah_MP LSM), and simulation 4 (modified Noah_MP LSM).

Statistical analysis

In order to summarize the performance of the model in its different configurations, a statistical analysis on the results is presented. The analysis is performed comparing the model results against the observed time series of 2-m temperature, available at 9 different stations within the domain (see Figure 3.1), and of downward and upward

LW radiation and upward SW radiation at the reference station Al-Ref. Incoming SW radiation is not taken into account in this analysis as it is not affected by the modifications of the LSMs.

In the following, the values of different statistical indexes are discussed. First, the average model prediction error are evaluated, analyzing the root mean square error (*RMSE*) and the bias (*BIAS*) values. Second, the mean-centered pattern errors are discussed by means of the Taylor diagrams (Taylor, 2001). The Taylor diagram summarizes the performance of the model against the observations on the basis of the correlation coefficients (R), the normalized centered root mean square differences (E'_n) and the normalized standard deviations (σ_{Mn}), which are second-order statistics calculated subtracting the average value from the time series. Equations from 4.3 to 4.8 report the definition of each statistical index, where M_i and O_i are the modeled and observed values, N is the total number of values in the analyzed time series and $\overline{O}$ and $\overline{M}$ are the observed and modeled averages, respectively.

$$RMSE = \sqrt{\frac{1}{N}\sum_{i=1}^{N}(M_i - O_i)^2} \tag{4.3}$$

$$BIAS = \overline{O} - \overline{M} \tag{4.4}$$

$$\sigma_O^2 = \frac{1}{N}\sum_{i=1}^{N}(O_i - \overline{O})^2 \tag{4.5}$$

$$R = \frac{\sum_{i=1}^{N}\left[(O_i - \overline{O})(M_i - \overline{M})\right]}{N\,\sigma_O\,\sigma_M} \tag{4.6}$$

$$\sigma_{Mn}^2 = \frac{\sigma_M^2}{\sigma_O^2} = \frac{\sum_{i=1}^{N}(M_i - \overline{M})^2}{N\,\sigma_O^2} \tag{4.7}$$

$$E_n'^2 = \frac{E'^2}{\sigma_O^2} = \frac{\sum_{i=1}^{N}\left[(O_i - \overline{O}) - (M_i - \overline{M})\right]^2}{N\,\sigma_O^2} \tag{4.8}$$

Results from the comparison between measured and calculated 2-m temperatures are shown in Table 4.3 in terms of *RMSE* and *BIAS*. Values clearly show that the trend identified for the reference station is similar also for all the other stations: *RMSE* decreases from simulation 1 to simulation 4. In fact, in simulation 1 *RMSE* ranges from ~7°C to ~8.7°C, in simulation 2 it assumes values of ~3.5°C, in simulation 3 it decays to ~2°C while in simulation 4 it reaches values ranging from 1.4°C to 2.1°C. The *BIAS* values are generally positive, identifying an underestimation of the mean 2-m temperature in all the weather stations and they also confirm the improvements obtained with the modified simulations with respect to the standard simulations. The *BIAS* values obtained in simulation 4 are slightly higher than in simulation 3: indeed, overestimation of minima during nighttime and underestimation of daily peaks in simulation 3 tend to compensate each other, decreasing the resulting *BIAS*.

It is interesting to note that station Rov displays the highest *RMSE* and *MR* values in both the standard runs and higher indexes in simulation 4 than in simulation 3. This can be explained by considering the particular location of this weather station, which is situated in a rural area, but very close to Rovereto city center. This location may influence the observations, as the urban heat island (Giovannini et al., 2011) affects the 2-m temperature nocturnal minima, which are higher than at all the other stations. The highest *RMSE* values of simulation 1 and 2 at Rov are then associated with the stronger underestimation of nocturnal temperature produced by the urban heat island. Accordingly, simulation 3, which tends to overestimate nighttime minima, performs better in this specific point. In principle, the effects determined by urban centers could be taken into account in

Station	RMSE [°C]				BIAS [°C]			
	S1	S2	S3	S4	S1	S2	S3	S4
AlRef	7.22	3.12	2.36	1.70	6.63	2.68	0.14	0.18
Al1	8.10	3.90	2.20	1.69	7.59	3.67	0.74	1.18
Al2	7.52	3.25	2.23	1.45	6.91	2.95	0.29	0.47
Al3	7.54	3.58	1.92	1.80	7.09	3.11	0.57	0.77
Ronc	7.53	3.62	2.16	2.08	6.97	2.95	0.72	0.58
TNS	7.83	3.13	2.33	1.55	7.23	2.68	-0.48	-0.03
Rov	8.73	4.60	1.84	2.12	8.33	4.28	1.04	1.78
Sw1	7.63	3.69	2.41	1.81	7.09	3.54	1.65	1.60
Sw2	6.85	2.93	2.27	1.50	6.45	2.82	1.88	1.35
Mean	**7.66**	**3.54**	**2.19**	**1.75**	**7.14**	**3.19**	**0.73**	**0.88**

Table 4.3: Statistical indeces calculated for 2-m temperature time series available at 9 different weather stations: root mean square error (RMSE) and bias (BIAS).

Variable	RMSE [W m^2]			
	S1	S2	S3	S4
Swout	109.88	50.99	23.48	22.67
Lwout	52.18	17.11	21.29	8.37
Lwin	39.87	36.3	26.49	31.64
	BIAS [W m^2]			
Swout	-59.08	-26.19	-11.85	-11.07
Lwout	32.69	27.65	16.69	21.7
Lwin	48.44	13.03	15.65	-2.81

Table 4.4: Statistical indeces calculated for the radiation time series available at the reference station AlRef: outgoing long- and shortwave radiation (LWout and SWout) and incoming longwave radiation (LWin). Root mean square error (RMSE) and bias (BIAS).

the WRF model by selecting an urban parameterization, but none of them is compatible with Noah_MP LSM at the moment and none was therefore applied in the present simulations.

Table 4.4 presents *RMSE* and *BIAS* for the radiation time series modeled and observed. The outgoing SW radiation presents high errors in both simulations 1 and 2, which are strongly reduced with the applied modifications. The *RMSE* is more than halved and the *BIAS* reaches smaller values, always negative, indicating a slight overestimation. A similar trend is found for the outgoing LW radiation, but, in this case, the variable in underestimated. Improvements are smaller for the incoming LW radiation, because, as said before, this variable is only marginally and indirectly affected by the modifications of the LSMs.

In the Taylor diagrams presented in Figure 4.8, R is related to the azimuthal angle, E'_n is proportional to the distance of the dots from the 'OBS' point on the x-axis and σ_{Mn} is proportional to the radial distance from the origin. The top left panel shows that, considering 2-m temperature at all stations, the modifications applied to the Noah model contribute to increase the correlation and to decrease E'_n. The standard deviation of the observations is overestimated by the standard run, while it is underestimated by the modified run. Indeed, as shown in Figure 4.5, simulation 1 presents a wide thermal range (around an underestimated mean temperature), while simulation 3 strongly reduces it. The top right panel shows that 2-m temperature time series calculated with the Noah_MP model are more grouped and lie closer to the curve of unitary normalized standard deviation. The thermal range is therefore better reproduced by the Noah_MP LSM than by the Noah model. The applied modifications contribute to further increase the correlation and to decrease E'_n but their effects are less effective than those obtained for the Noah simulations. Indeed, NoahMP performs better than Noah in its standard configu-

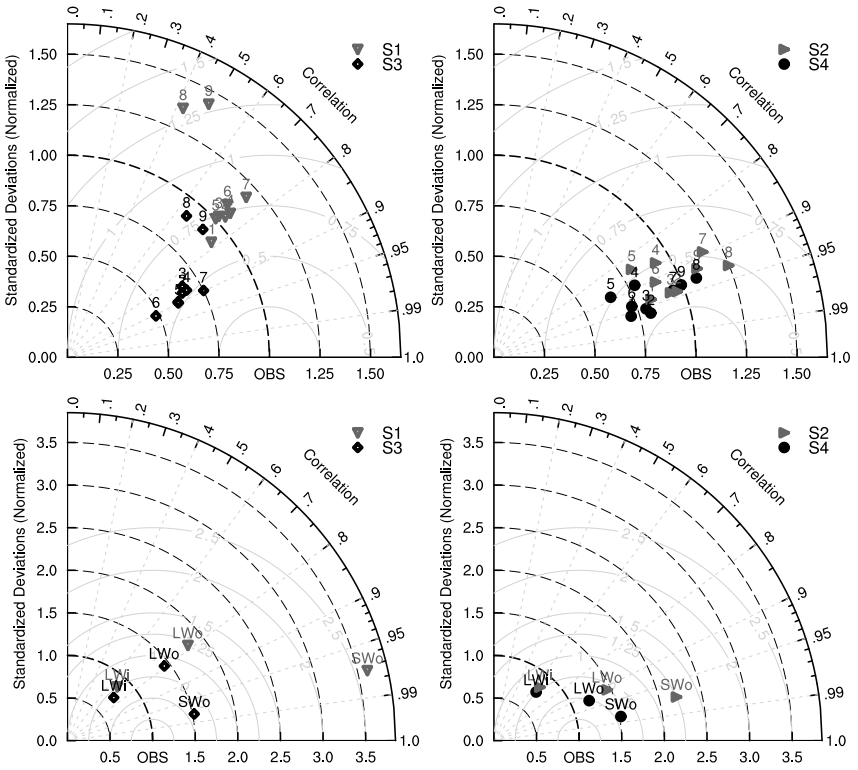

Figure 4.8: Taylor diagrams describing the statistical patterns of the modeled 2-m temperature and radiation time series computed by simulations 1, 2, 3 and 4 with respect to the observations. Top panels present results in terms of 2-m temperature, for each available weather station (from number 1 to 9); bottom panels show results in terms of outgoing LW (LWo) and SW (SWo) radiation and incoming LW (LWi) radiation. Left panels present Noah simulations S1 and S3, while right panels present Noah_MP simulations S2 and S4.

ration and for this reason it is more difficult to further improve model results. A better performance of Noah_MP with respect to Noah was also found by Chen et al. (2014) and Kuribayashi et al. (2013), who assessed the ability of both models in simulating the snowpack evolution in time. The bottom panels of Figure 4.8 present the Taylor

diagrams for radiation time series. The graphics clearly show an improvement in both outgoing LW and SW radiation (especially from simulation 1), while the incoming LW radiation experiences slight changes only. The performance of the modified Noah and Noah_MP LSMs in predicting the radiation fluxes at the ground is in the end very similar, but yet the Noah_MP model better reproduces the 2-m temperature.

4.1.4 Discussion on the effects of each modification

It is interesting to provide an overview of which is the contribution that each single modification gives to the overall improvement of results of S3 and S4. To this purpose, Figures 4.9 and 4.10 show the effects of each single modification on the outgoing SW/LW radiations and on the 2-m temperature. Each figure presents the effects of the modifications on the simulations, providing an overview of the evolution from the standard (S1 in Figure 4.9, and S2 in 4.10) to the improved simulation (S3 in Figure 4.9, and S4 in 4.10). Therefore, the first intermediate step shown in Figure 4.9 and 4.10 results from simulations run with the modification to the land use description only, while the second intermediate step is from simulations run with coupled modifications on land use and snow initialization.

Concerning results from the Noah LSM, only Figure 4.9 can be analyzed. The top panel shows that each intermediate step towards S3 contributes to a relevant decrease in the outgoing SW radiation, stating that all the modifications - to the land use type, to the initial snow cover, and to the implementation of the Livneh formula - have a great impact on this variable. Indeed, in the Noah LSM the cell albedo is a function of both the snow cover fraction and the vegetation land use type. The modification to the implementation of the Livneh formula therefore directly reduces the snow albedo. The modifications of land use type and of snow cover initialization, instead, have a direct imp-

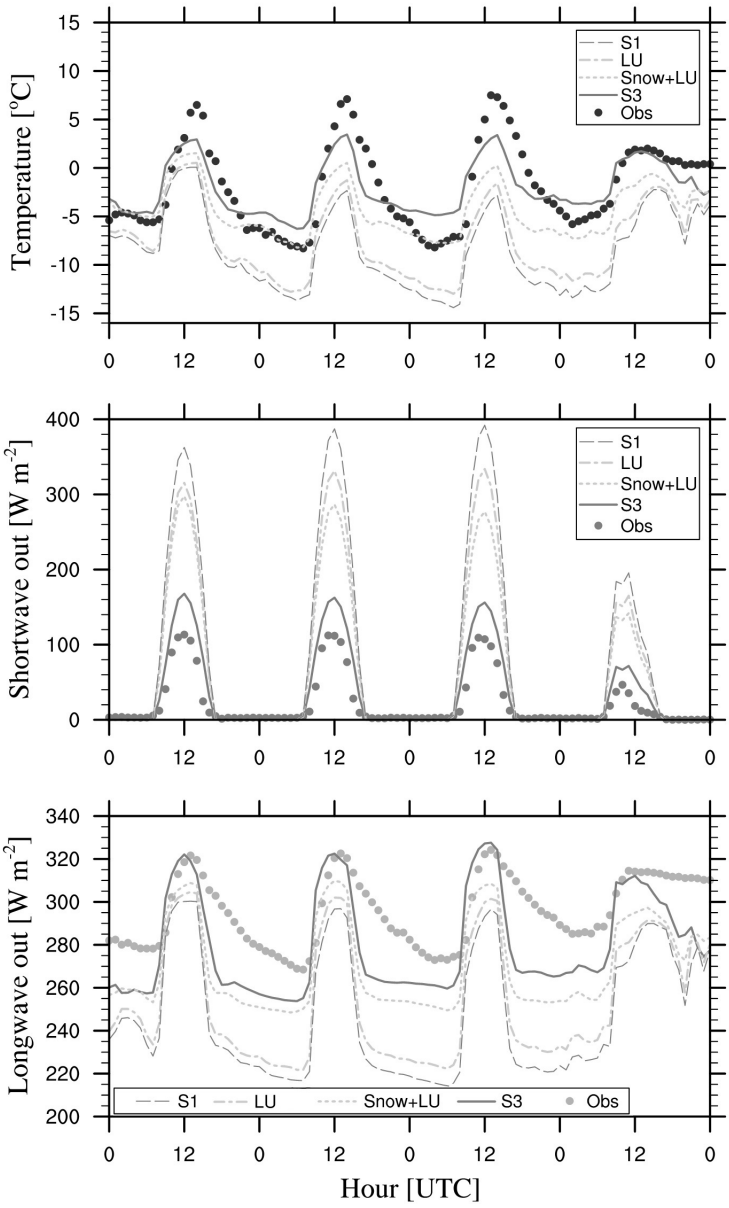

Figure 4.9: 2-m temperature and outgoing short- and longwave radiation observed and estimated adding one by one the proposed modifications, moving from simulation 1 (standard Noah LSM) to simulation 3 (modified Noah LSM): *LU* refers to the modification to the land use classification and *Snow* refers to the modification applied to WRF snow cover initialization.

act on the snow cover fraction and consequently on the cell albedo. Looking at the bottom panel of Figure 4.9, it can be inferred that each applied modification has a significant impact on the 2-m temperature, increasing both nighttime minima and daytime maxima. The strongest impacts are produced by the decrease in the initial snow cover depth and by the changes in the implementation of the Livneh formula.

Interestingly, the reduction of the initial snow depth does have significant positive effects in increasing the 2-m temperature even if the cell albedo does not strongly decrease. This is because the 2-m temperature does not depend on just the surface albedo but it is a function of many other parameters, such as the skin temperature (at the interface between the ground and the snow, if present) and the surface heat flux. The snow depth directly affects the calculation of the skin temperature, which tends to increase over a thinner snow cover. Moreover, a thinner snow cover implies a different calculation of surface fluxes, especially the net upward heat flux. As 2-m temperature is calculated as a function of both these quantities, it is strongly affected by the modification of the initial snow depth, even if the albedo of the cell remains almost constant. Figure 4.9 also shows that the overall effect of the applied modifications is a shift of the temperature curve towards higher values, but the shape of its diurnal cycles is mostly preserved. Specifically, both in the standard and in the modified simulations, Noah produces a too fast decrease in the air temperature after sunset, driven by the fast decrease in the surface temperature which can be identified from the pattern of the outgoing LW radiation.

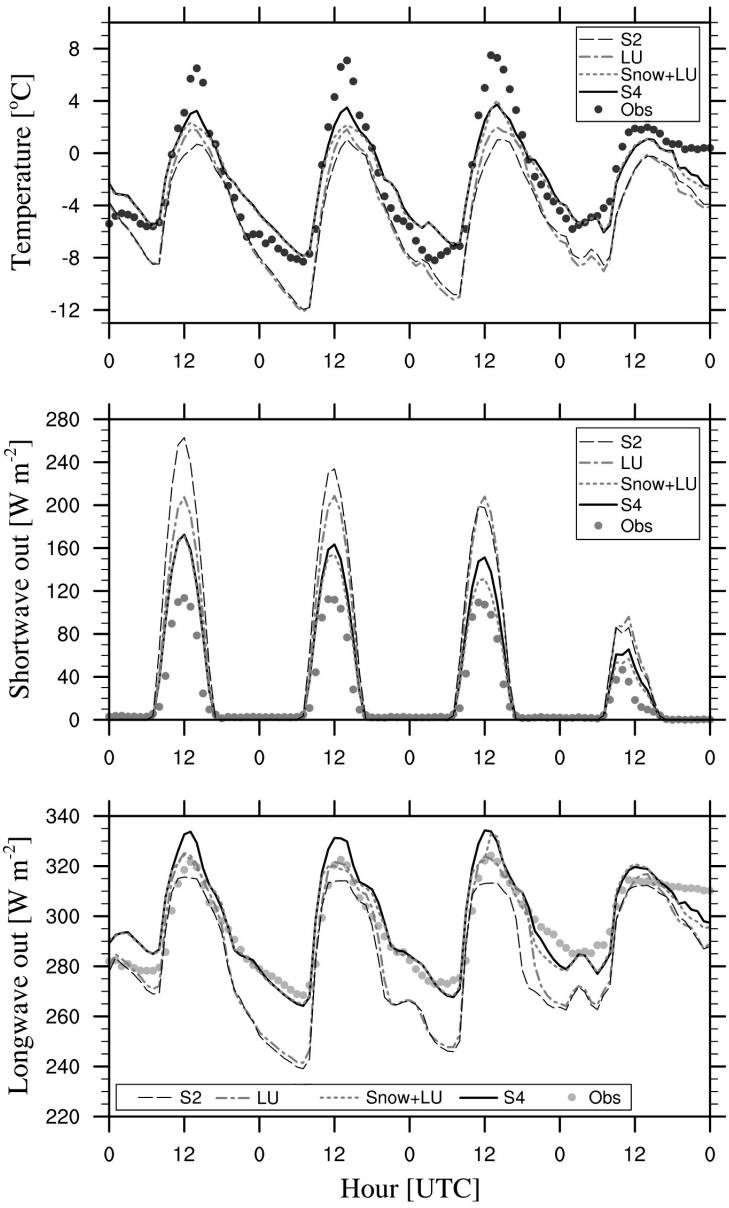

Figure 4.10: 2-m temperature and outgoing short- and longwave radiation observed and estimated adding one by one the proposed modifications, moving from simulation 2 (standard Noah_MP LSM) to simulation 4 (modified Noah_MP LSM): *LU* refers to the modification to the land use classification and *Snow* refers to the modification applied to WRF snow cover initialization.

Noah_MP, instead, differently reacts to the the modifications, as show in Figure 4.10. Specifically, the outgoing SW radiation is reduced, thanks to the modification to the land use classification, which allows the presence of vegetation cropping out of the snow cover. In this way, the vegetation fraction of the cell is increased, the calculation of the cell albedo is directly affected and, as a consequence, the 2-m temperature slightly increases during daytime. The modification relative to the snow cover initialization intervenes in reducing the cell albedo as the SCF decreases together with the snow depth as shown in equation 4.1. Accordingly, the 2-m temperature increases during both daytime and nighttime. Finally, eliminating the snow depth threshold over which ground temperature cannot increase above 0°C causes a slight increase in the daily maxima on the first two days. The fact that the modified simulations slightly overestimate the outgoing LW radiation at midday is noteworthy if compared with the results of 2-m temperature. Indeed, even if the skin temperature is overestimated of about ~2°C, midday 2-m temperature is yet underestimated: this evidence suggests that, in the model, turbulence is over-damped during the day.

The above discussion shows that similar parameters, such as the initial snow depth, the land use type description and the characteristics of the snow pack, affect both the Noah and Noah_MP LSMs. In this case study, the best performing standard scheme was found to be the Noah_MP LSM. The reasons for this better performance are surely the improvements introduced in Noah_MP to reproduce the vegetation canopy layer, to calculate separately the vegetated and the bare ground surface temperatures, and to treat the snow pack. It must be also stressed that many other Noah_MP features were not tested in this case study: indeed, no growing season is analyzed and therefore the new approaches on the growing canopy were not applied. Nevertheless, the standard version of the Noah_MP model greatly takes

advantages in terms of accuracy if specific parameters of the model are calibrated. Indeed, improvements have been obtained when the melting factor m and the land use cover description parameters were adjusted in order to better fit the scale of the simulation and the characteristics of the investigated area.

4.1.5 Conclusions and outlook

Results from simulations using the default version of WRF, coupled with the two LSMs, highlighted a significant underestimation of the 2-m temperature and an overestimation of the outgoing SW radiation, due to an overestimation of the surface albedo. Given these results, both LSMs were analyzed in depth, in order to understand the possible causes of the recorded deficiencies. The first cause turned out to reside, in the present case, in the initialization of the snow cover depth, which was greatly overestimated. Another important role was played by the treatment of certain land-use classes under snow-covered ground. In particular, the IGBP class "cropland" is not representative of fruit tree cultures, which actually respond to a snow cover more like a broadleaf forest than like a cropland, which would be completely covered even under a thin snow layer. In addition to these corrections, other modifications were proposed, directly affecting the calculation of the cell albedo and of the 2-m temperature of both LSMs. In the Noah LSM modifications were introduced in the implementation of the Livneh procedure, in order to change the surface albedo calculation by intervening on the initial snow cover age and on the seasonal parameters describing the ground snow albedo evolution over time. In the Noah_MP scheme, changes were made in the snow cover upper limit, above which ground temperature cannot increase above 0°C.

Thanks to the applied modifications, improved results were obtained for both of the LSMs tested. In particular, in the modified

simulations the outgoing SW radiation decreased, thus increasing the energy available in the surface energy budget, with a consequent increase in the 2-m temperature. Modifications had stronger impact on Noah LSM results but, nevertheless, the best agreement with observations was achieved with the modified Noah_MP LSM, which was able to properly catch nighttime temperature minima, to get closer to daytime maxima and to properly identify the ground-based thermal inversion occurring during the simulated winter nights, and its evolution in time.

Results highlighted that particular attention must be paid to snow cover initialization when running wintertime simulations over complex terrain. This can be crucial for obtaining reliable results in these conditions, as accurate snow cover data are usually not available for high resolution simulations, and the treatment of global reanalysis data may turn out to be misleading over complex terrain. Moreover, an appropriate land use classification and description turned out to be very important for the calculation of the actual snow cover on the ground, with a considerable impact on the near-surface temperature. The calibration of the melting factor m also turned out to be very important in order to obtain an accurate estimate of the surface albedo through the calculation of a realistic value for the SCF. In simulations run at local scale, with a description of land cover types with a very high resolution, the value of m fixed within the Noah_MP model can lead to a severe underestimation of SCF and a consequent possible underestimation of surface albedo.

Modifications applied to the Noah scheme are also relevant, significantly improving the model performance. Moreover, these modifications are easy to introduce within the code, as the only parameters needed are the age of the snow present on the ground at the beginning of the simulation and the season of the year. The modification proposed for the Noah_MP scheme regarding the calculation of sur-

face temperature had actually less effect on the 2-m temperature if applied after the corrections to the snow initialization and to the land use classification, resulting essentially in an increase in the maximum temperature. Nevertheless, this modification is more significant if applied when the cell presents no vegetated fraction.

It must be stressed however that the applied modifications have been tested only for this case study, and further testing over longer periods is needed in order to generalize their potential applicability in different regions and snow melting conditions. Unfortunately, in this study, no measured data of snow depth were available in order to perform a direct comparison of model results against observations: for this reason testing against datasets with detailed snow-height observations would be of essential importance in order to highlight the effectiveness of the presented results. Nonetheless this work shows that the values of a few land surface parameters greatly influence model results and that an optimization of some of them can make the difference in applications over complex terrain. A refinement in the estimation of surface variables and of their effects in the evaluation of surface layer processes is of utmost importance for situations involving strong interactions of the surface with the lower atmosphere. An accurate simulation of quantities such as surface layer turbulence, near-surface stability and surface layer height are key prerequisites for many applications, such as pollutant dispersion modeling in mountain valleys and basins. Indeed the proposed improvements are expected to lead to better performance of WRF in providing a meteorological input for dispersion models, especially with the high resolution available from increasing computational resources, and required by very complex terrain situations (Giovannini et al., 2014 a; Ragazzi et al., 2013).

4.2 The Merano Case Study

High-resolution numerical simulations are performed with the Weather Research and Forecasting (WRF) model and with the CALPUFF dispersion model in order to reproduce meteorological conditions and vertical profiles of particulate concentration close to the city of Merano, in the Adige Valley, in the north-eastern Italian Alps. Simulation results are compared against observations registered both by surface weather stations and by means of balloon soundings, presented in Section 3.2. The soundings registered temperature and particulate concentrations from the surface up to 800 m above ground level in several moments of the day, to evaluate the temporal evolution of the boundary layer. Interesting meteorological phenomena, able to influence the dispersion of particulate matter, were observed during the field campaign, as for instance the break-up of the early morning ground-based thermal inversion after sunrise and the arrival of strong foehn winds. The main aim of this research is that of understanding if the WRF model is able to correctly reproduce these phenomena and, afterwards, to evaluate how these particular meteorological conditions influence pollutants' dispersion simulated by the CALPUFF model. Observations clearly show that these meteorological phenomena are strictly connected with changes in the vertical distribution of particulate matter: concentrations, indeed, are very high near the ground in the early morning, when thermal inversion, biomass burning for domestic heating and the traffic rush hour act simultaneously. Conversely, particulate matter concentrations dilute as the boundary-layer grows and strongly decrease at all heights when the foehn wind starts to blow.

4.2.1 Model set-up and simulations

For the present case study, two WRF simulations are presented, which are run respectively with a standard configuration of the model (SM1), and with modifications concerning the snow cover initialization and treatment presented in Section 4.1 (SM2). The two simulations share the same WRF configuration as to the domain definition, the physics settings and the external forcing. Simulations are run with WRF v3.5.1, with 4 two-way nested domains (shown in Figure 4.11), starting from a resolution of 10.8 km in the external domain down to a resolution of 400 m in the innermost domain, with a ratio of 3:1 between successive nests. The vertical resolution is uniform for all the 4 domains, with 40 stretched eta vertical levels (10 levels within the first 1000 m). Further details on the domain settings can be found in Table 4.5.

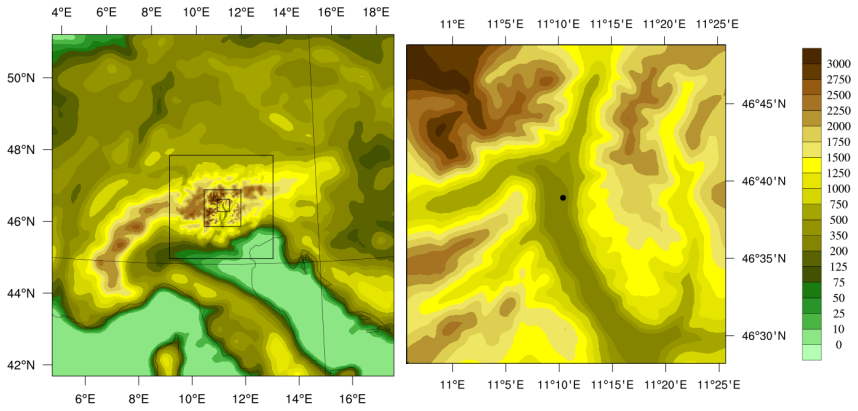

Figure 4.11: Domains of the simulations for the Merano case study with their elevation contours: (left) the 4 simulation domains and (right) the innermost domain, centered over the town of Merano. The black dot indicates the location of the available vertical measurements.

Nest Number [−]	**Horizontal grid space** [km]	**Dimensions** [km]	**Time step** [s]
1	10.8	1080 x 1080	100
2	3.6	327.6 x 327.6	33.3
3	1.2	116.4 x 116.4	11.1
4	0.4	38.8 x 38.8	3.7
AQ	0.1	26.5 x 26.5	3600

Table 4.5: Characteristics of the nested domains of simulations SM1 and SM2 for the Merano case study. Domains 1 to 4 are WRF domains, AQ domain refers to the CALPUFF simulation.

Simulations start at 1200 UTC 02 March 2010 and end at 0000 UTC 05 March 2010, covering a period of 60 h. The first 12 h of simulation are used as a spin up period for the model, to adapt and loose dependency on the initial conditions. The time step in the innermost domain is 3.7 s. The boundary and initial conditions come from 6-hourly, 0.25°grid resolution ECMWF reanalysis data. As for the Aldeno case study, in the innermost domain high-resolution static data for the digital terrain model (DTM) and for the land use classification are provided (30 (de Ferranti, 2013) and 100 m, respectively). Only one smoothing pass with the 1-2-1 smoothing filter was applied to the topography in order to guarantee numerical stability of the simulations. The utilized land use database is the Corine Land Cover (CLC) data set (EEA, 2006), reclassified into the standard 33 IGBP classes, as shown in Giovannini et al. (2014 a), in order to match the classification of the external domains and the WRF land use tables.

Different physics schemes were tested, and the best performance was obtained with the following combination of models: the Lin et al. (1983) microphysics sophisticated scheme; the Grell-Freitas cumulus scheme (Grell and Dèvènyi, 2002) for the two external domains only; the Bougeault and Lacarrere (1989) parameterization for the plane-

tary boundary layer; the Noah land surface scheme from Chen and Dudhia (2001); the Dudhia scheme (Dudhia, 1989) and RRTM scheme (Mlawer et al., 1997) for SW and LW radiation, respectively, called every 10 min, taking into account the effects of shading and slope angle in complex terrain.

Applied modifications

In the present case study, results from the WRF standard simulation showed different problems related to the reconstruction of the early-morning ground-based thermal inversion. In particular, the model underestimates the temperature within the valley, reproducing cold-biased isothermal profiles throughout the whole day (as will be shown in the following Section 4.2.2). The cause of these errors turned out to be the initialization and treatment of the snow at the ground. Indeed, the ECMWF reanalysis, used for the present case study, highly overestimated the snow depth on the ground, both in its absolute values and in its areal extension. Figure 4.12 shows the comparison between the snow cover initialization performed by the ECMWF reanalysis (panel (b)) with 25-km resolution satellite observations from AMSR-E/Aqua data set (Tedesco et al., 2004) (panel (a)). The overestimation of the snow cover is clear in all the domains, and is of particular relevance in the innermost domain, where almost no snow is detected from the satellite, while a snow pack with a depth of more than 1 m is initialized in WRF in the whole innermost domain. Other reanalysis were considered in order to overcome this problem (e.g. NCEP GFS reanalysis), but errors of similar magnitude or higher were encountered.

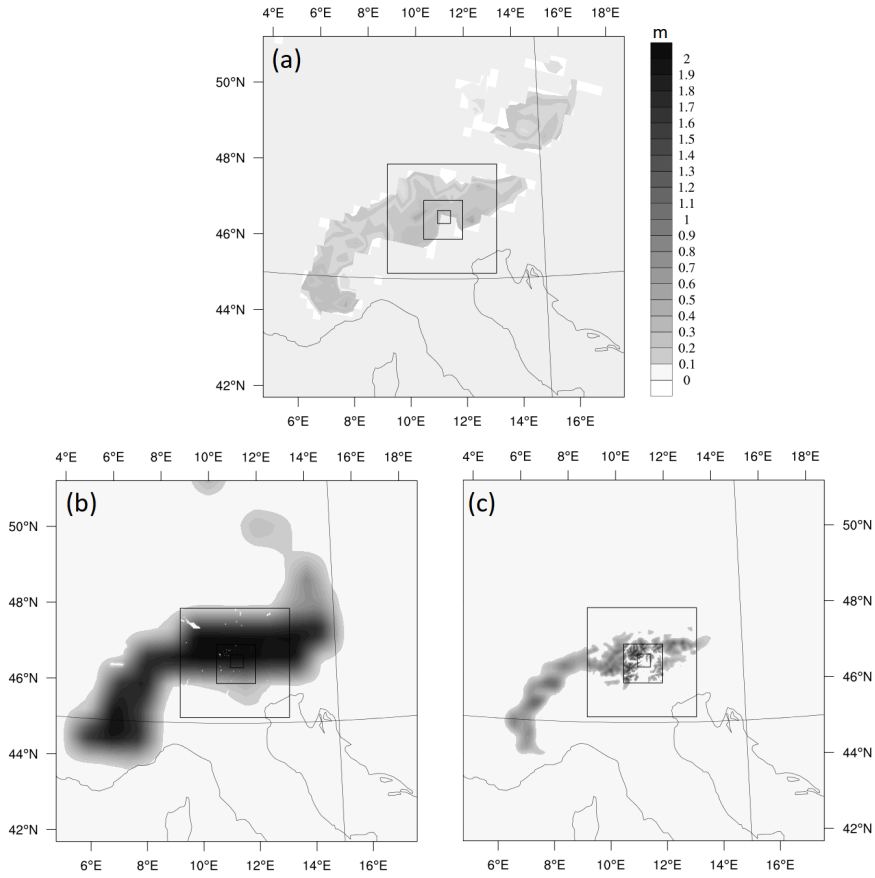

Figure 4.12: Snow depth values on 02 March 2010 over the simulation domains: (a) as captured by the AMSR-E/Aqua satellite (25 km resolution, daily value of snow depth calculated from the observed snow water equivalent); (b) as initialized by default by WRF from the ECMWF reanalysis (SM1); (c) as initialized by WRF after the discussed modifications for an optimized simulation (SM2).

The solution adopted for this case study, and applied to the modified simulation SM2, was to remove part of the exceeding snow cover, limiting the presence of snow only above 1500 m m.s.l. and linearly increasing the snow depth at greater altitudes. The result of this modification is shown in Figure 4.12, panel (c): the snow-covered area is

reduced in all the domains, getting closer to satellite observations, and in the innermost domain the snow-covered areas are limited to the highest mountain peaks, as suggested by the observations. In addition, the modified simulation runs with the modifications presented in Section 4.1.2 to the Noah LSM, in order to allow a proper estimation of the 2-m temperature in the presence of snow at the ground (above 1500 m m.s.l.).

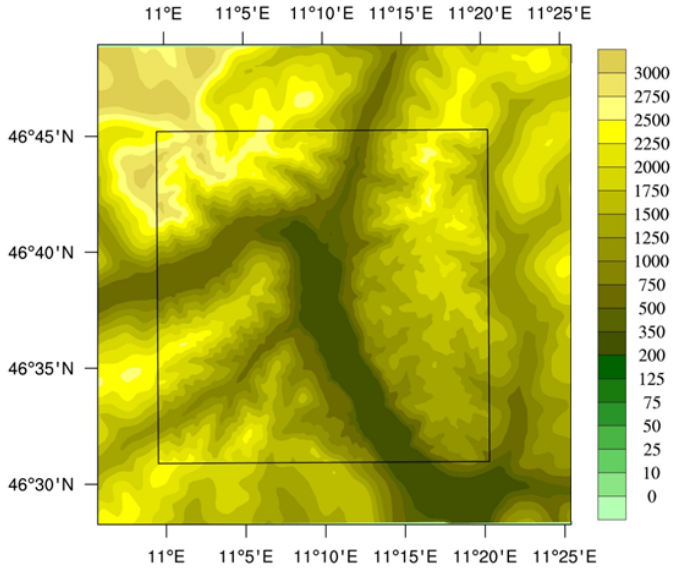

Figure 4.13: Domain of the dispersion simulations for the Merano case study, nested within the WRF innermost domain.

After the meteorological simulations, an air quality simulation was run to evaluate the dispersion of locally released pollutants. The CALPUFF v6.42 model was run on the domain shown in Figure 4.13, nested in the innermost WRF domain, with an horizontal resolution of 100 m, 10 vertical levels, and an hourly time step. More information on the simulation domain are reported in Table 4.5. As for the meteorological simulations, topography and land use input data are provided at a resolution of 30 m and 100 m, respectively, which

are consistent with the high resolution of the simulation. The meteorological WRF output is passed to the CALPUFF model using the CALWRF and CALMET preprocessors, which allow the interpolation of the meteorological field over the finer-scale grid. 8 chemical species are modeled in the simulation (PM10, NO_x, NH_3, SO_2, SO_4, HNO_3 and NO_2) and 4 of them are directly emitted from the sources (PM10, NO_x, NH_3 and SO_2).

In the present work, three major pollutant emission sources are taken into account (Figure 4.14), namely: the town of Merano with its surrounding villages, the main road network and the major local industrial plants. Each of these sources was modeled in detail in order to properly reproduce its contribution to the overall emission on an hourly base. This level of detail in the description of the sources is the achievable given the available input data and the approach of CALPUFF.

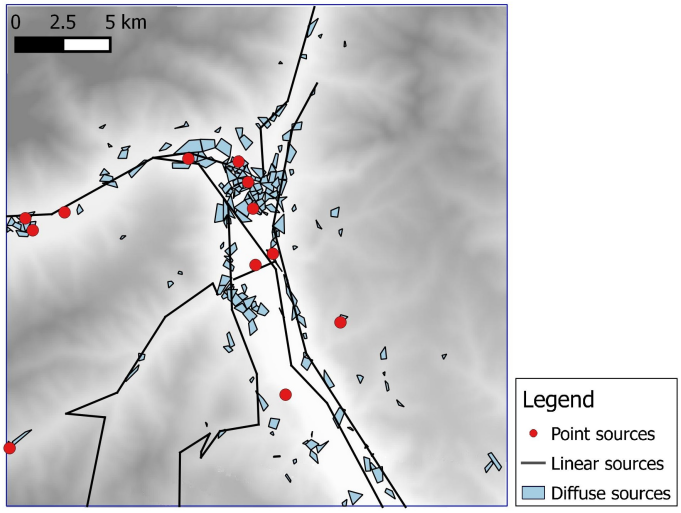

Figure 4.14: Map of the emission sources modeled in the CALPUFF simulations.

Pollutant emissions from the town of Merano and other villages are primarily due to an intensive use of biomass for house heating

Source		PM10	NO_x	SO_2	NH_2
Diffuse	[t yr^{-1} m^{-2}]	1.86E-05	1.61E-05	8.95E-07	2.61E-04
Linear	[t yr^{-1} m^{-1}]	0.17	8.38	-	-
Point	[t yr^{-1}]	0-23.4	2.2-32.6	0-7.1	-

Table 4.6: Average emission rates for each type of source taken into account for the CALPUFF simulation.

and then due to secondary traffic and small manufacturing industry. Emission rates for these sources were evaluated starting from the Regional air pollutant emission inventory (INEMAR 2010 APB (2010)): the inventory allows the calculation of an average emission rate for each municipality, taking into account its specific activities and small scale industries (i.e. those not accounted for explicitly) and weighting them according to the number of people involved, the production volume, etc. These annual average emission rates were characterized with temporal and spatial modulations for each municipality. The spatial modulation was estimated from data coming from the 2011 population census, weighting the overall emission rate considering the population density of each census tract. On the other hand, the temporal modulation was evaluated considering the evolution in time of the main activities taken into account: the house heating and the secondary traffic. House heating is strongly characterized by seasonal and hourly cycles, while secondary traffic mainly varies per hour-of-day and day-of-week. These different patterns were conveniently combined by weighting them on the basis of each activity contribution to the total amount of emission rate, according to the INEMAR emission inventory. The town of Merano and adjacent villages were therefore modeled in CALPUFF as a composition of 194 areas, treated as diffuse areal sources, each emitting an average value hourly modulated in time (for the fixed month and day of the week):

Table 4.6 reports the average emission rate for all the diffuse sources simulated, while Figure 4.15 shows the average temporal modulation of the emission (top panel).

The major traffic routes crossing the domain are the Bolzano-Merano highway, the Stelvio main road (SS38) and other seven main roads basically running along the main valley floors (see Figure 4.14). The emission rate for each axis was calculated by means of the EU standard COPERT model (Gkatzoflias et al., 2012): this procedure requires the number of transiting vehicles, the fleet composition and the mean vehicle speed as input data. For each of the above-mentioned roads, suitable data sets were obtained from data provided by the local institute for statistic (ASTAT) for the speed and transiting vehicles, and by the Italian federation of motorists (ACI) for the fleet composition of all the traffic routes. By combining the input data with the emission factor of each vehicle type, the total amount of emissions for these main roads was obtained (see Table 4.6). The modulation introduced is hourly based for each traffic route, obtained from road-specific measured data for the given month of the year (see Figure 4.15).

The study area considered contains 12 industrial plants (Figure 4.14) requiring specific modeling for the simulations, as they may significantly contribute to pollutants' concentration in the atmosphere. These plants include three district heating plants, some local manufacturing and agri-food industrial plants, and two recreational thermal plants. In order to properly simulate these sources in CALPUFF, their release points of emission must be characterized with the height and diameter of the stack, and with the temperature and velocity of the emissions: these values were known for each plant. The annual mean emission rate of each point source is reported in the INEMAR 2010 inventory for both NO_x and PM10 (Table 4.6 shows the range of point sources emission rates). These values can be modulated with a

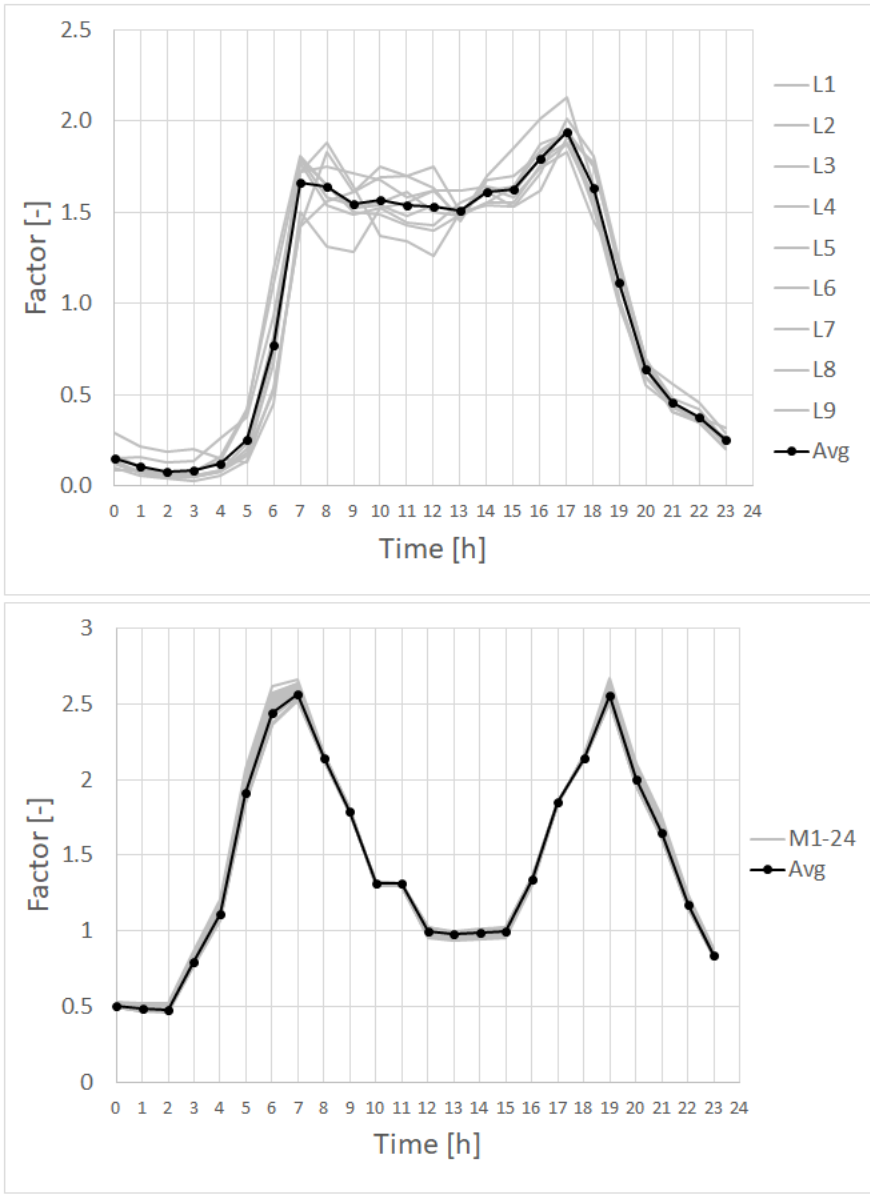

Figure 4.15: Temporal modulation factor for the emissions from linear (top) and diffuse (bottom) sources. Gray lines represent the patterns for each single source (9 different roads for the linear (L*) sources and 24 municipalities (M*) for the area sources) and the black lines represent the average modulation pattern.

suitable pattern in time: on a weekly basis for the small factories, whose production cycle decreases during the weekends, and on a monthly basis for the district heating plants. Factors relative to the given month of the year and day of the week were therefore applied in the simulation.

4.2.2 Meteorological results

The analysis of meteorological results focuses on fields and phenomena which are relevant for the fate of pollutants in the atmosphere, by determining both their transport and dispersion. Specifically, meteorological results are presented in terms of 10-m wind speed and direction, which influence the main trajectories of the pollutant transport, and of temperature vertical profiles, which determine the stability of the atmosphere and therefore the intensity of turbulent mixing. Measurements of these variables are available in the sampling site shown in Section 3.2.3. Figure 4.16 shows the results of the WRF simulations in terms of wind speed and direction, from 03 March 2010 until 04 March 2010. The comparison states that no relevant differences occur between the two simulations and that there is an overall good agree-

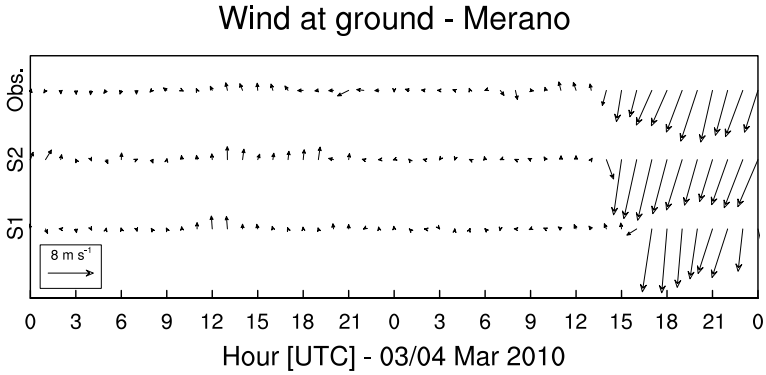

Figure 4.16: 10-m wind speed and direction modeled by the standard (SM1) and modified (SM2) simulations in comparison with observations (Obs).

ment with the observations. Both the simulations succeed in identifying a southerly wind during the first day of simulation, at midday, more prolonged in the modified simulation, and in predicting the strong foehn episode occurring at the end of the second day. The modified simulation better reproduces the timing of this phenomenon, but it overestimates its intensity in the first hours.

Results in terms of temperature vertical profiles, presented in Figures 4.17 and 4.18, show important differences between the two simulations. On the morning of the 03 March 2010 (Figure 4.17), the standard simulation reproduces almost isothermal profiles, at all measurement times, and presents a strong cold bias throughout the whole period of measurements, showing errors always greater than 2 °C, up to 10 °C. This strong underestimation of the temperature was found to be generated by the presence of snow on the ground, erroneously reproduced by the model, as discussed above. Interestingly, the effect of the snow at the ground is not limited to the first layers of the atmosphere, closer to the ground, but affects the whole volume of air, up to and above 800 m m.s.l.. The explanation of this evidence resides in the conformation of the Adige Valley, which is especially deep and steep in the area of interest (the valley floor lies at 280 m m.s.l. while surrounding mountain crests reach 1400 m m.s.l.): the presence of snow in the model simulations both on the valley floor and on the sidewalls contributes in cooling the air close to ground at different heights and, as a consequence of the terrain following levels, the whole volume of air contained in the valley. The modified simulation, running with no snow below 1500 m m.s.l., can to highly improve vertical temperature profile prediction. Specifically, the model properly reproduces the ground temperature with errors less than ~1 °C. In the early morning, the model captures the formation of the ground-based thermal inversion, even if anticipates its breakup by ~1 h: to show this, Figure 4.17 presents

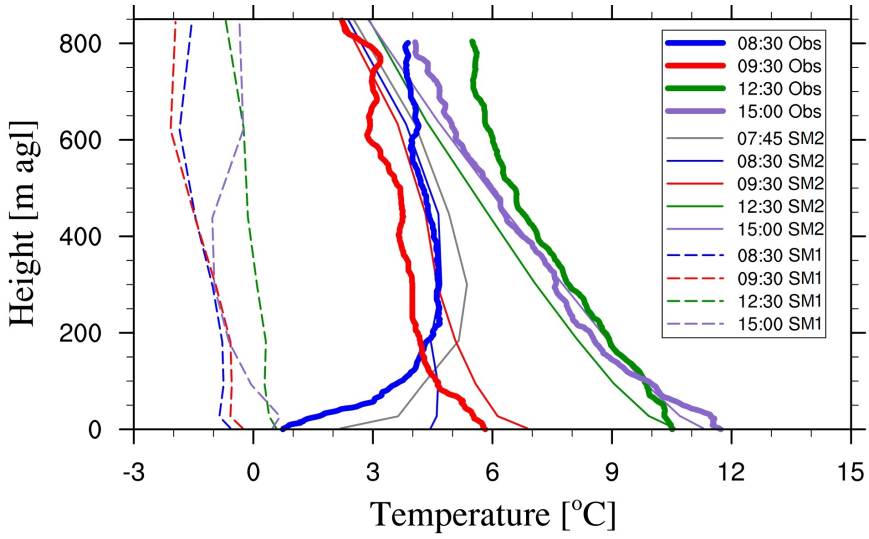

Figure 4.17: Temperature vertical profiles on the 03 March 2010 as modeled by the standard (SM1) and modified (SM2) simulations, and measured by the thetered ballon soundings. Different colors correspond to different times of the day, expressed in LST [UTC+1].

both 7:45 and 8:30 LST [UTC+1] profiles. The modified model well identifies the 9:30 LST profile, with an overestimation of ~1 °C up to 600 m m.s.l. and performs adequately for the 12:30 LST profile also, properly simulating the ground temperature and underestimating 800-m temperature of ~2 °C. The early afternoon profile is properly captured by the model at all heights. On the morning of 04 March 2010, measurements showed only a very weak thermal inversion at 7:45 LST and no inversion afterward. On the contrary, the standard simulation SM1 reproducs a strong thermal inversion throughout the whole morning (Figure 4.18). The modified simulation reproduces the profile with a cold bias of ~2 °C but it is able to correctly capture the trend of the profiles, catching the correct temperature lapse rate, which is the most relevant variable for the dispersion of pollutants.

In order to properly interpret the results of the dispersion model, it is convenient to present an overlook of the evolution in time of

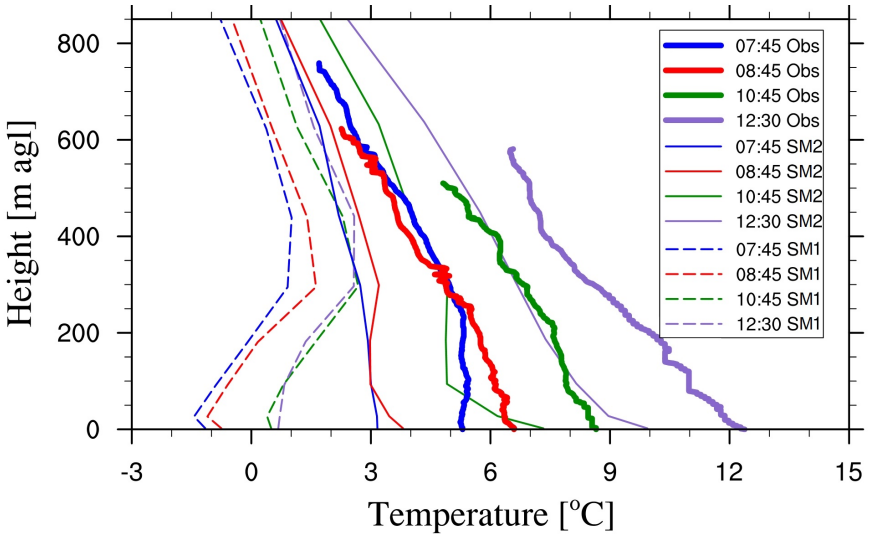

Figure 4.18: Temperature vertical profiles on 04 March 2010 as modeled by the standard (SM1) and modified (SM2) simulations, and measured by the thetered ballon soundings. Different colors correspond to different times of the day, expressed in LST [UTC+1].

the ground-based thermal inversion, as reproduced by the meteorological model (Figure 4.19). The top panel shows the time-height diagram of the temperature lapse rate as reproduced by the standard simulation SM1. On the 03 March 2010, the model reproduces a ground-based thermal inversion only until 3 LST, while in the following hours an inversion is present only at higher altitudes. Later on during the day, the atmosphere remains stable, with an elevated thermal inversion developing from 1300 LST 03 March, and reaching ground level around 0000 LST 04 March. In the early morning of 04 March, the model simulates a strong and thick ground-based thermal inversion, which lasts until the early evening and, weaker, till night. As shown earlier, observations taken during both mornings of the analyzed days show that this reconstruction is incorrect. On the contrary, the modified simulation SM2 (bottom panel, Figure 4.19) reproduces a rather regular alternation of stable atmosphere at night

and in the early morning and of mixed conditions during the central hours of the day. The ground based thermal inversion captured on the 03 March, early morning, is stronger and thicker than that of the second day of simulation. Observations presented above confirm this evolution of the temperature field.

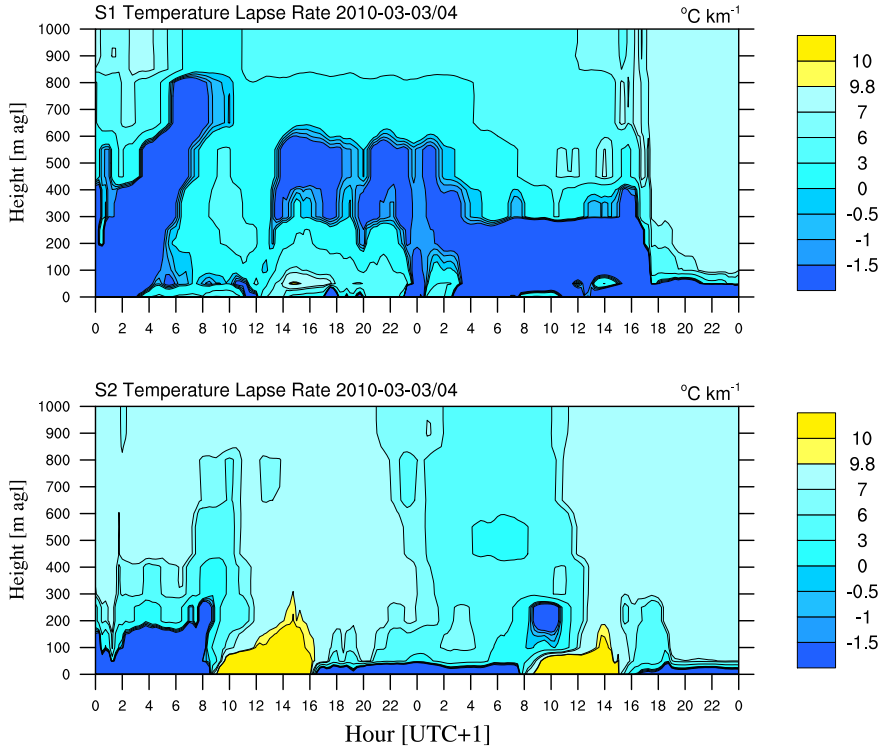

Figure 4.19: Time-height diagrams of temperature lapse rate as modeled by the standard (SM1) and modified (SM2) WRF simulations for 03-04 March 2010. In the plots, blue, cyan and yellow colors identify thermal inversion, stable conditions and unstable conditions, respectively.

The results obtained with the modified WRF simulation, in terms of both wind speed and direction and temperature vertical profiles, prove a satisfactory reconstruction of the meteorological fields and constitute a rather reliable input for the dispersion model. Under

these evidences, the simulation with the CALPUFF model is run with the meteorological input from the modified simulation only (SM2).

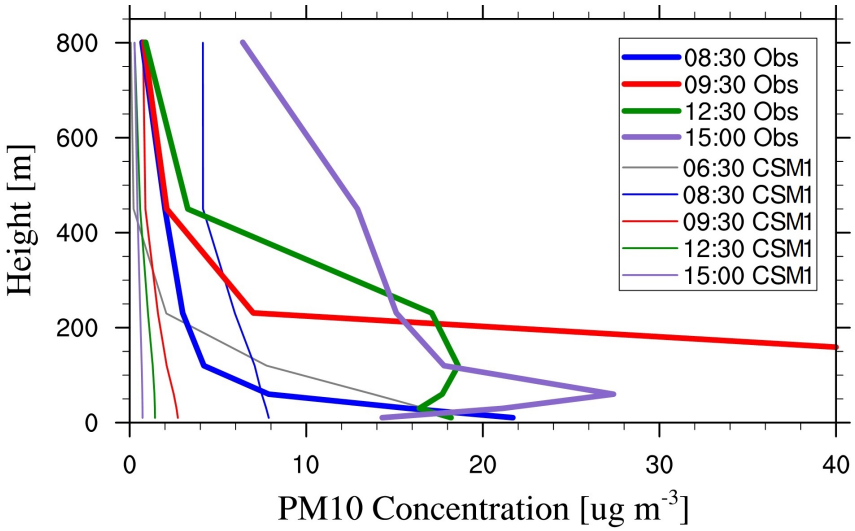

Figure 4.20: PM10 concentration vertical profiles on the 03 March 2010 as modeled by the CALPUFF model with the standard WRF simulation (CSM1) and measured by the thetered ballon soundings. Different colors correspond to different times of the day, expressed in LST [UTC+1]. Concetration measurements are here presented at model heights only.

4.2.3 Air pollution dispersion results

Results of the dispersion simulation are presented first of all by comparing the vertical concentration profiles reproduced by the CALPUFF model (Figure 4.20) with observations. The model is partly able to reproduce the accumulation of the pollutants in the lowest layers of the atmosphere (gray profile in Figure 4.20) but it starts the vertical mixing of pollutants too early, missing the observed accumulation close to the ground with a temporal bias of about 2 h (blue profile in Figure 4.20). Clearly, this anticipation is partly due to the anticipation in the thermal inversion breakup simulated by the meteorological model, but part of the error has to be appointed to the parameter-

ization of the dispersion model which disperses the PM10 too fast. Indeed, according to observations, the accumulation of pollutants continued throughout the morning with a recorded peak at 9:30 LST (right after the thermal inversion breakup) and only after that the concentration increased also in the upper layers of the atmosphere. On the contrary, the CALPUFF model disperses pollutants very fast, right after the breakup of the thermal inversion, capturing almost no concentrations after 9:30 LST in the morning.

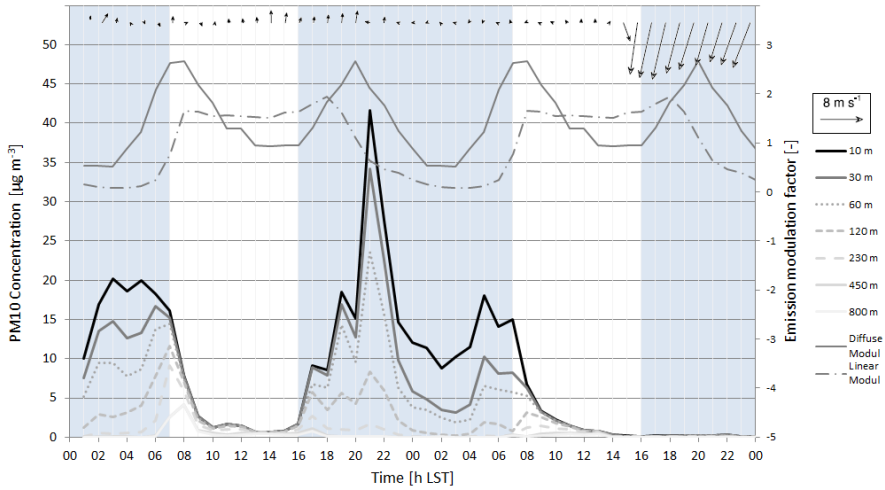

Figure 4.21: PM10 concentration time series as modeled by the CALPUFF model with the standard WRF simulation for the 03 and 04 March 2010, at different model levels. Modulation factors for the areal and linear sources are recalled on the top of the graph together with the modeled wind speed and direction. Shaded areas indicate the presence of ground-based thermal inversion.

Another way to look at the model results is to analyze the evolution in time of the PM10 concentrations at the different model levels (Figure 4.21). The diagram shows that due to the existence of the thermal inversion during the early morning, the model is able to predict an accumulation of pollutants, which anyway starts to decrease an hour earlier than the inversion breakup. Indeed, after 06 LST, the

concentration of pollutants starts to decrease near the ground, even if the sources are emitting at their peak rates and the thermal inversion is still present in the WRF simulation. After 7 LST the emission rates of the sources decrease, and with them the concentrations at all model levels, quickly dropping close to 0 μg m^{-3} and missing the concentration peak recorded by the soundings. This error is probably due to a combination of factors: the erroneous timing of the thermal inversion breakup simulated by the meteorological model and a too fast and intense mixing enhancement performed by the dispersion model right after the thermal inversion breakup. Nevertheless, a partial underestimation of the emitted pollutants must be also considered, as the magnitude of the error in the prediction of the ground peaks is remarkable. No measurements are available during the late afternoon, but the model reproduces a more intense accumulation late at night than in the early morning. This occurrence is probably due to the fact that, in this case, the ground-based thermal inversion persists during the whole cycle of the emissions and, specifically, it persists during peak-time emissions.

Looking at the second day of simulation, an accumulation of pollutants is again reproduced in the early morning, but with lower concentrations: as the emissions are exactly the same of the previous day, and the wind velocity is still low, this difference in accumulation rates is likely due to a weaker thermal inversion (see Figure 4.19). As expected, in the late afternoon and night of 04 March, all the pollutants are carried away by the strong foehn wind, and the model correctly predicts no concentration at any level, independently from the emission peak.

4.2.4 Discussion and conclusions

Meteorological and dispersion simulations with the WRF and CALPUFF models were run over complex terrain in order to evaluate these mod-

els ability to reproduce wintertime phenomena such as the ground based thermal inversion and its effects on pollutant dispersion. The evaluation is carried out by running 2-day-long simulations and comparing the results against observations taken during a field campaign held in Merano (North-Eastern Italian Alps), in March 2010. During the field campaign vertical profiles of temperature and PM10 concentrations were recorded with a tethered balloon.

The WRF model in its standard configuration shows a great underestimation of the temperature field, both at ground level and at higher altitudes. This effect is due to the erroneous initialization of a thick snow cover all over the innermost domain, as a result of the input reanalysis data. Satellite data were therefore used to modify the snow cover initialization of the WRF model and to run a modified meteorological simulation with a more realistic snow cover field. Results of the two different simulations are compared with observations of vertical temperature profiles and near-ground wind field. While the wind field at ground level appears to be adequately captured by both simulations, the comparison demonstrates that the modified simulation only is able to properly reproduce the thermal field both in its absolute values and in its evolution in time. The modified simulation nicely catches the formation and breakup of ground-based thermal inversions, even if it anticipates by ~1 h the transition from thermal inversion to unstable atmosphere on the first morning of simulation.

The dispersion model CALPUFF is therefore run, feeding it with the meteorological output from the best performing WRF simulation. Besides the rather accurate meteorological fields provided, the dispersion model shows different flaws in the reproduction of the measured vertical concentration profiles of PM10. At the beginning of the simulation, the model is able to catch the early morning accumulation of pollutants near the ground, due to the combination of the increasing emissions and the presence of the thermal inversion.

Nevertheless, as soon as the thermal inversion breaks the vertical mixing builds too quickly and disperses the pollutants much earlier than what witnessed by the observations. On the positive side, the model is able to properly respond to the strong foehn wind that arises during the last day of the simulation, removing all the pollutants from the area.

This study illustrates some of the difficulties that may arise when modeling wintertime critical episodes of air pollution over complex terrain. First, the accurate prediction of ground-based thermal inversions is challenging for the mesoscale WRF model, which often needs specific adjustments to guarantee a proper treatment and initialization of the snow cover, in order to properly predict the evolution of the thermal field inside a narrow valley. Second, the parameterizations for the vertical mixing contained in the dispersion model are of major concern as, given the appropriate meteorological conditions, they can still enormously affect the predicted concentration of pollutants both near the ground and at higher altitudes. In addition to this, it has been shown how, over complex terrain, where the meteorological fields and atmospheric conditions vary fast in time, it is essential that the timing of the meteorological phenomena, the emissions patterns and the vertical mixing development are precisely captured, as small temporal shifts can highly influence the overall concentration results.

Chapter 5

Testing different meteorological and air quality modeling approaches over complex terrain for a short-time tracer release

Air quality scenarios provided by coupled meteorological and dispersion models can play a key role in supporting policies for monitoring pollutant dispersion and reducing health risks. However, air quality modeling in complex terrain still poses many challenges, due to the inherent difficulties in accurately reproducing both the atmospheric and the dispersion processes. Here some preliminary evidences from a project carried out in the Bolzano basin, in the Central Italian Alps (Section 3.3), are presented. The construction of a new incinerator plant, in 2013, required policy makers to improve the forecast of dispersion processes in the area (Ragazzi et al., 2013), with the aid of both atmospheric and dispersion models. A dedicated project was

therefore set up to provide a technically-sound support for the design of a permanent air-quality station network, monitoring the effects of pollutants from the incinerator. Accordingly, a trustful modeling chain, able to provide emission-impact scenarios with yearly-based numerical simulations, was needed. In order to understand which modeling chain is the most suitable for this context, many different tests were performed with different modeling approaches. This chapter is intended to give an overview of the tests conducted, with the aim of highlighting deficiencies and advantages of each applied modeling approach.

All the following preliminary tests were conducted on 27 January 2016, chosen as the reference day for this case study as it presented most of the typical wintertime meteorological conditions relevant for the stagnation of locally emitted atmospheric pollutants. Data from measurements showed a strong ground-based thermal inversion, developing up to 700 m above the valley floor, and relatively weak wind speeds at the valley floor (see Section 3.3.3 for details).

5.1 Diagnostic vs prognostic meteorological modeling approaches

The CALPUFF dispersion model is EPA-approved for applicaton over complex terrain and frequently applied in operational contexts to predict dispersion of pollutants. For this reason, the CALMET and CALPUFF modeling chain performance was put to test on the Bolzano basin. Specifically, the performance of the CALMET preprocessing model in its diagnostic mode is here evaluated. CALMET is used for the diagnostic reconstruction of meteorological fields, the input data being provided by a variety of in-situ measurements: surface temperature and wind (speed and direction) from eight different weather stations, wind profiles from a SODAR, and temperature pro-

files from a thermal profiler (see Section 3.3.3). These results are compared with output of prognostic simulations run with WRF, in order to understand if the diagnostic methodology, fed with a rather peculiar and wide observational data set, is able to capture the main features of the meteorological fields.

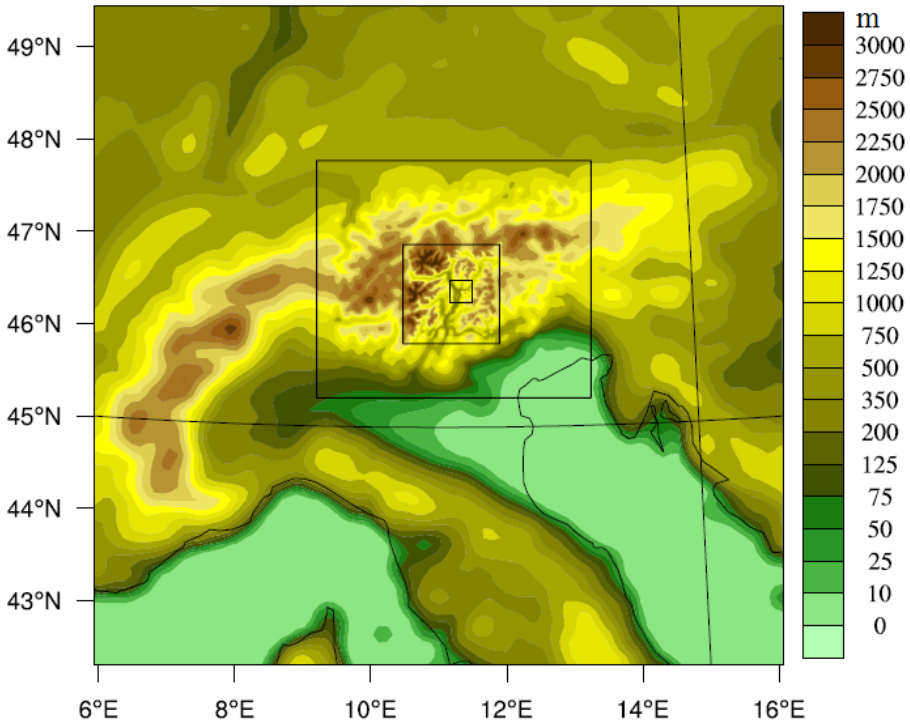

Figure 5.1: WRF nested domains from Northern Italy to Bolzano basin with their elevation contours.

5.1.1 Reference prognostic simulations

In order to have a detailed overview of the meteorological situation occurring on January 27^{th}, high-resolution numerical simulations are run with a prognostic approach, with the WRF model. Simulations with the WRF model are performed with four nested domains, going from 9-km horizontal resolution in the external domain, up to 333-

m resolution over the Bolzano basin (Figure 5.1). 62 vertical levels define the vertical grid and hourly observation nudging is performed in the internal domain. A 30-m resolved Digital Terrain Model and a 100-m land use Modis map are used in order to properly describe the characteristics of the innermost domain. The simulation is driven with 6-h GFS NCEP reanalysis as boundary and initial conditions. The model runs with the YSU PBL scheme (Hong et al., 2006), the WRF Single-Moment 3-class micro physics scheme (Hong et al., 2004), the Noah land surface model Chen and Dudhia (2001), the Grell-Freitas Ensemble cumulus scheme Grell and Dèvènyi (2002) activated in the external domain, and the Dudhia (Dudhia, 1989) and RRTM (Mlawer et al., 1997) radiation schemes. In addition, the effects of shading and slope angle in complex terrain are taken into account.

Hourly observation nudging is performed in the innermost domain using the available meteorological observations (locations of the stations are shown in Figure 5.2): wind speed and direction, temperature and relative humidity from 7 weather stations operated by the local meteorological office; one vertical wind profile from the SODAR instrumentation on the incinerator roof; and 1 vertical temperature profile from the thermal profiler located to the South of the city of Bolzano.

WRF simulations properly reproduce the complex flow field in the Bolzano area (Dosio et al., 2001), capturing the shift of up- and down-valley winds flowing in the valleys which join into the basin (de Franceschi and Zardi, 2009; de Franceschi et al., 2009). In particular, the simulation highlights the occurrence of a low-level nocturnal jet at the exit of the narrow canyon-like Isarco Valley (Figure 5.2 with dots on the assimilated weather stations). This specific local phenomenon is very relevant for the fate of pollutants released from the incinerator, as the jet stream flows exactly over the plant: this fact is also well captured by the wind profile measurements (Figure 3.13),

showing that the wind direction at upper layers is reversed with respect to the lower ones. Properly reproducing this flow feature within the meteorological fields is a necessary condition to guarantee the correct prediction of the pattern of the tracer released from the chimney. It is clear that the simulation of the interaction between these different local circulations, including their correct evolution in space and time, represents a very challenging task for a diagnostic model as CALMET, but their correct reconstruction is of fundamental importance for dispersion issues.

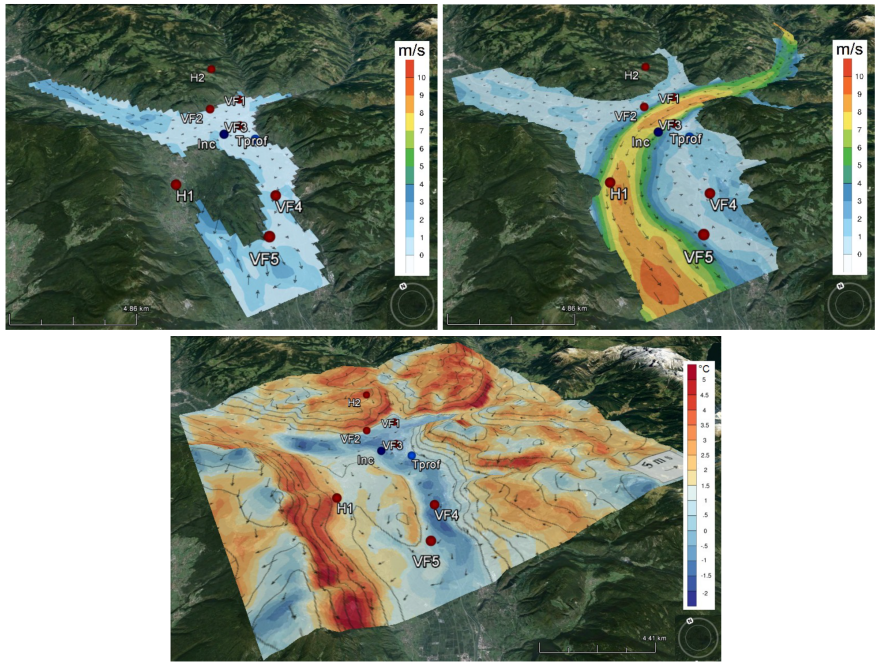

Figure 5.2: Top left panel: near-ground wind speed and direction in the valley floor at 7 LST. Top right panel: wind speed and direction over the valley floor, at 925 hPa, at 7 LST. Bottom panel: near-ground temperature and wind speed and direction at 9 LST.

In addition to this, the WRF simulation shows how meteorological near-ground variables, such as 2-m temperature and incoming radiation, are obviously strictly terrain-related, as shown in Figure

5.3. In particular, the WRF model is able to properly capture the thermal inversion occurring within the Adige Valley, as shown in the bottom panel of Figure 5.3 for 9:00 LST and in the left panel of Figure 5.2 for 7:00 LST.

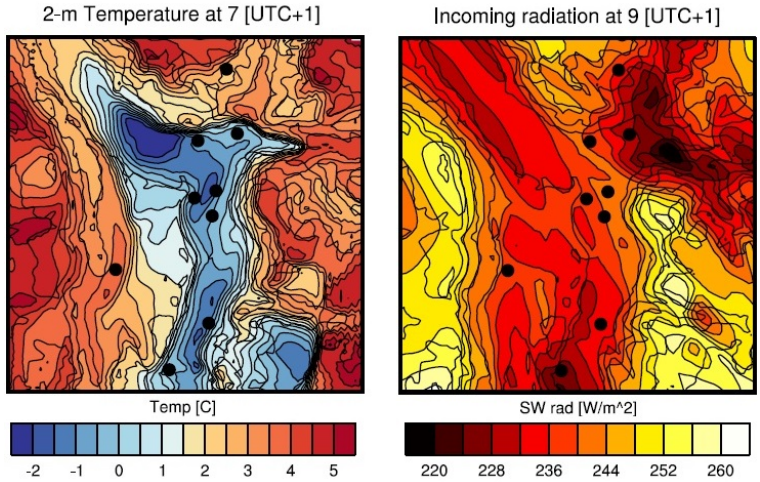

Figure 5.3: WRF output at different times and levels shown on the CALMET/CALPUFF domain.

5.1.2 Diagnostic simulations with CALMET/CALPUFF

Standard simulations with CALMET

Simulations with the CALMET/CALPUFF model are run in diagnostic mode with a horizontal resolution of 200 m over a 20x20 km^2 domain, and with 10 vertical levels from the ground up to 2400 m. The dispersion module is set up to simulate a tracer release from the incinerator chimney starting at 7 LST and lasting 40 min. Nevertheless, the focus of the present work is on the reconstruction of the meteorological fields provided by CALMET. The pre-processor is fed with different observations, both conventional and non-conventional (the same used for observational nudging in WRF). Indeed, the following input data are provided to the model: wind speed and direction, tem-

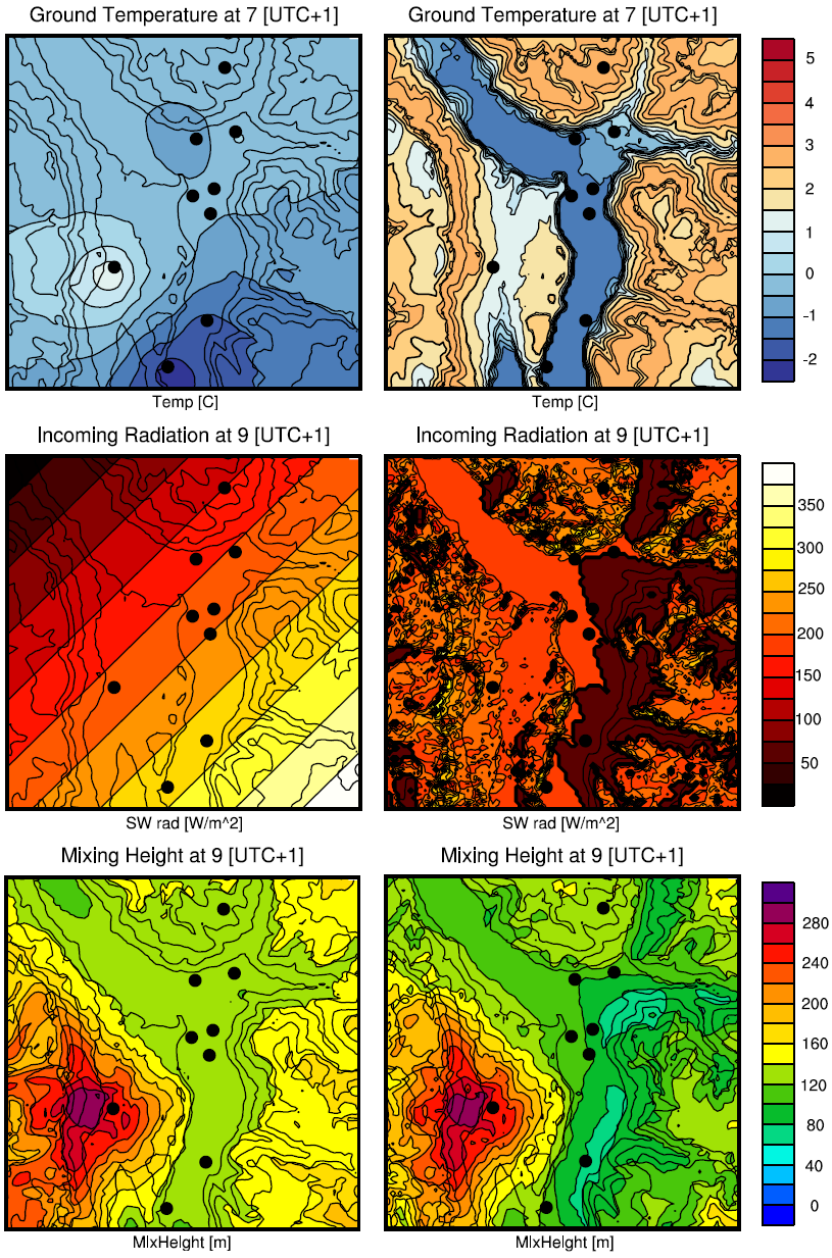

Figure 5.4: Near ground temperature, incoming radiation and mixing height calculated by CALMET in its standard configuration (left) and its modified (external temperature and irradiance fields forced into the model) configuration (right).

perature, relative humidity and atmospheric pressure from eight permanent stations, six distributed on the valley floor and two along the sidewalls (300 m and 700 m above the valley floor, respectively); vertical profiles of wind speed and direction from a SODAR, set up on the roof of the incinerator, reaching heights of 340 m; and a temperature vertical profile up to 1000 m measured in the center of the Adige Valley.

The temperature profile has a 10-min temporal resolution and is vertically 50 m spaced, while the wind profile has a 30-min temporal resolution and is vertically 20 m spaced. The vertical profiles of both temperature and wind, observed within the domain of interest, are uncommon data and should act as a relevant resource to guide the meteorological pre-processor to properly reconstruct meteorological fields, especially when run over complex terrain. Despite the quality and peculiarity of the input data, CALMET performance in reproducing reliable meteorological fields is unsatisfactory. Indeed, the model shows many difficulties in properly spatializing meteorological variables strongly affecting the transport and diffusion of pollutants. Figure 5.4, left panels, shows the inability of the CALMET model to take into account terrain effects on both near-ground temperature and incoming radiation: indeed, no thermal inversion is reproduced nor shadowing effects are accounted for.

Modified simulations with CALMET

In order to overcome these deficiencies, modifications to the CALMET code (Bellasio et al., 2005) are made and temperature and incoming radiation fields are externally forced into the model: a terrain-related near-ground temperature field is obtained on the basis of hourly soundings while an hourly incoming radiation field is calculated by means of GRASS GIS analysis for the given day and DTM. Results of these interventions on the CALMET code are shown in the right

panels of Figure 5.4, which highlight changes in 2-m temperature of 3-4°C and even more relevant changes in incoming radiation. Despite the significant modifications in both these meteorological variables, these changes have little impact on more dispersion-related CALMET fields, such as mixing height and wind speed and direction. In particular, temperature modification has no effect on derived parameters

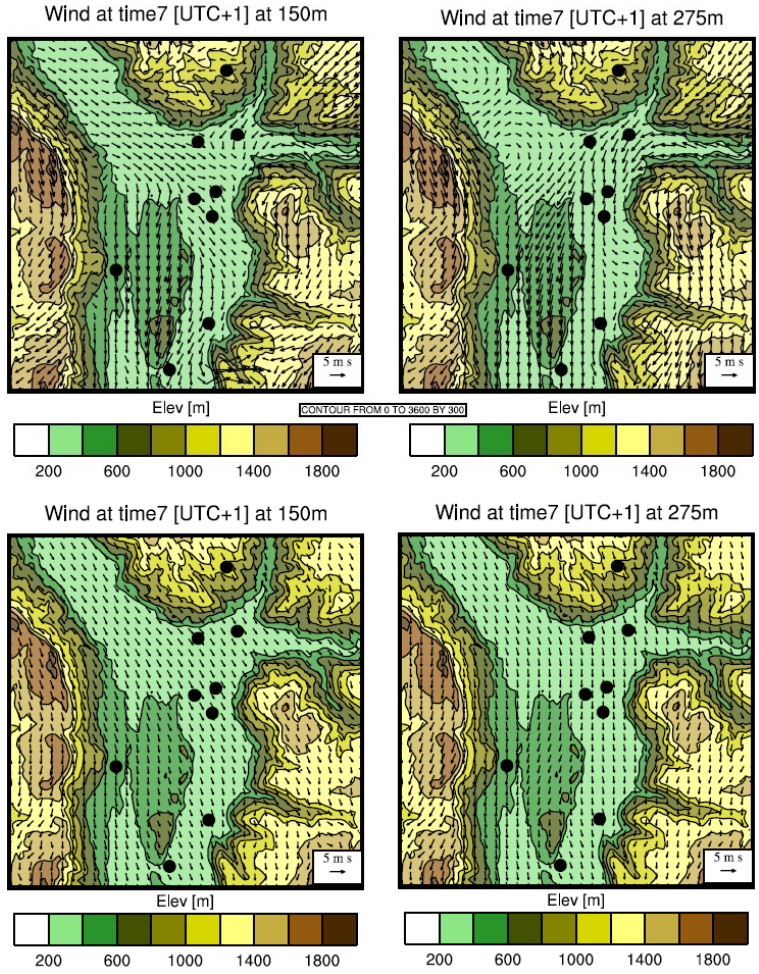

Figure 5.5: Wind speed and direction at release time, at two different vertical levels obtained with WRF simulation (top panels) and with CALMET simulation (bottom panels).

(e.g. the mixing height, the Monin-Obukhov length), confirming that the micrometeorological parameterization included into CALMET is almost non-sensitive to this variable. On the other hand, incoming radiation modification affects wind speed and direction but only near the ground, along shadowed sidewalls: this has an effect on related mixing heights which vary accordingly, as shown in Figure 5.4, bottom panels. Both modifications have no effects on wind speed and direction at higher levels, where standard and modified CALMET results correspond one to each other and where the effective release of the tracer is expected (only one shown in Figure 5.5).

Comparing CALMET wind field, at 150 m a.g.l., with WRF simulation (Figure 5.5, left panels), it is clear that the CALMET model succeeds in reconstructing the main north-easterly wind flow coming from the upper part of the Adige valley and directly flowing over the incinerator plant. On the other hand, in upper layers, e.g. at 275 m a.g.l. (right panels Figure 5.5), CALMET model, as expected, shows its inability to identify the low-level nocturnal jet coming from the Isarco Valley.

5.1.3 Conclusions

Numerical simulations run with the WRF model and a detailed analysis of observed meteorological data show that the strong complexity of the Bolzano area affects the development of ground-based thermal inversions, as well as alternating up- and down-valley winds in the valleys merging into the basin. In such a complex environment, it is unlikely that the CALMET model, run in diagnostic mode, can capture the whole picture of the meteorological fields. Specifically, deficiencies in the reconstruction of near-ground temperature and incoming radiation are identified and interventions are made on the CALMET code in order to solve these difficulties. Despite proper 2-m temperature and incoming radiation fields are forced into the model,

these modifications have little impact on wind field and mixing height results. Indeed, CALMET results are definitely non-sensitive to the near-ground temperature field while only near-ground wind field and mixing heights are slightly affected by changes in the radiation field. In the present case study, for an hypothetical release in the early morning, these small changes have no effects on CALPUFF dispersion patterns, obtained with the standard and modified CALMET input, which basically correspond one to each other (not shown). Nevertheless, this analysis revealed the presence of the low-level jet flowing out of the Isarco Valley and crossing the Bolzano basin. This feature introduces big uncertainties in the prediction of the direction of the tracer dispersion: indeed, small changes in the effective release height may lead, in reality, to very different trajectory scenarios, but no differences would be appreciated with the diagnostic CALMET/CALPUFF simulations. It appears therefore clear that a standard modeling approach, i.e. the CALMET/CALPUFF modeling chain run in diagnostic mode, is not suitable to analyze episodes of tracer release over such a complex terrain, not even if many uncommon observed values are fed into the model.

5.2 Puff-gaussian vs lagrangian dispersion modeling approaches

Preliminary tests of dispersion modeling were also conducted on the 27 January 2016 case study. The models chosen for the test are the EPA-approved CALPUFF model (Scire et al., 2000b) and the research model SPRAYWEB (Tinarelli et al., 2000; Alessandrini and Ferrero, 2009). As no concentration data were collected during the release experiment, no validations of model results could be carried out: nevertheless, some features of the two different models could be pointed out, comparing their results for equal input meteorological

fields. The meteorological input comes from the above mentioned and described (Section 5.1.1) WRF simulation, run at 300 m resolution with observational nudging of all the available observations. Figure 5.6 summarizes the modeling chain for the tests presented. In the following sections the setting of the dispersion simulations are described and a brief and purely qualitative analysis of the results is conducted. The dispersion modules are set up to simulate a tracer release from the incinerator chimney starting at 7 LST and lasting 40 minutes.

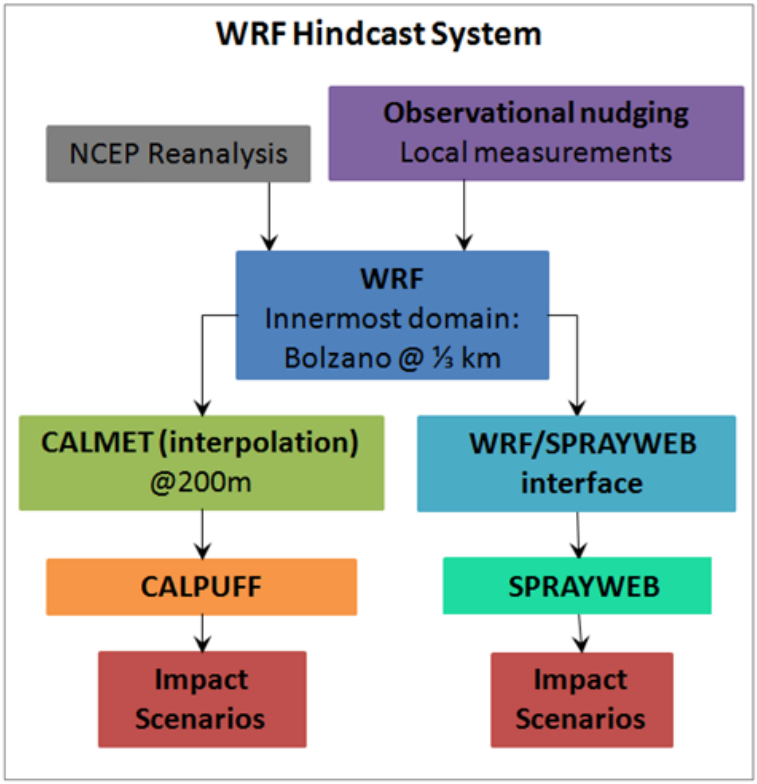

Figure 5.6: Simulation flow chart with the meteorological modeling chain coupled with the two different dispersion modeling approaches tested.

5.2.1 CALPUFF simulation

Simulations with the CALMET/CALPUFF model are run with a horizontal resolution of 200 m over a 20x20 km^2 domain, and with 10 vertical levels from the ground up to 2400 m. As CALMET preprocessor is used in order to increase horizontal resolution from 333 m to 200 m, the wind field results slightly modified with respect to the original WRF output. In addition to this, the CALMET model performs an internal calculation of the SL scales (u_*, w_*, H_{MIX}, L), changing their values from the ones already calculated within the WRF model. These new values are later utilized by the CALPUFF model to calculate the dispersion coefficients σ_i. CALPUFF dispersion pattern is shown in Figure 5.7 (left panels), where near-ground concentrations are shown at 4 different times of the simulation. It is clear that the effective release height calculated by the model is lower than the height of the nocturnal low level jet, as the tracer is transported southeast, according to the wind direction of the layers near the ground.

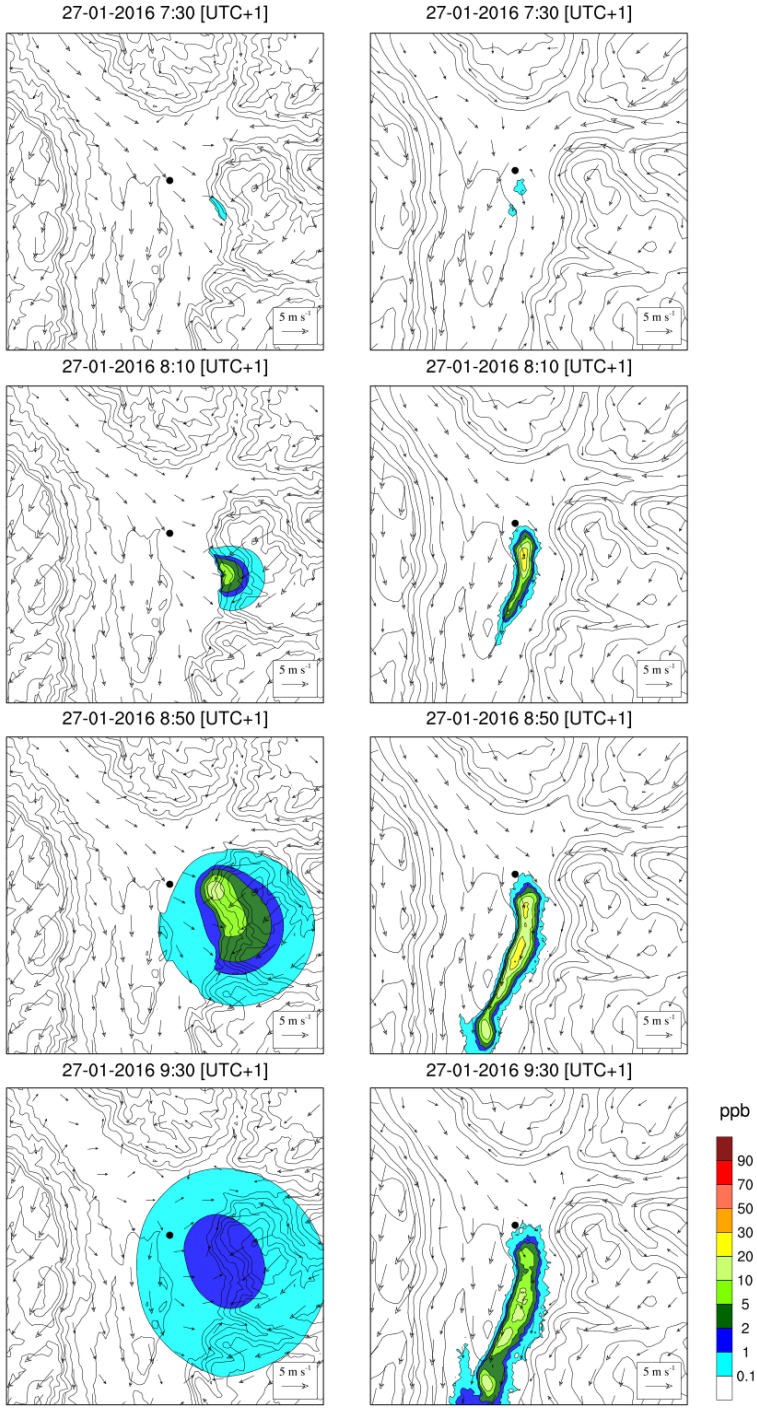

Figure 5.7: Ground concentrations (20-min averages) and wind field at 150 m, in time, calculated by CALMET/CALPUFF (left) and SPRAYWEB (right).

5.2.2 SPRAYWEB simulation

A SPRAYWEB simulation is run to reproduce the exact same test study. The dispersion model is fed with the WRF meteorological input by means of the herein developed WRF/SPRAYWEB Interface, starting from a first implementation from Bisignano et al. (2016). The interface interpolates WRF meteorological and micrometeorological (u*, w*, 1/L) variables over a 26x26 km^2 domain on chosen 30 vertical levels (same as CALPUFF levels from 2 to 7). Within the interface, the calculations of the diffusion coefficients σ_i and of the lagrangian time scales T_{L_i} are performed: specifically, for this test study, the exact same parameterization as the one applied in CALPUFF was implemented in the interface and therefore applied. The SPRAYWEB model takes care of the horizontal interpolation of the wind field in the position of each single tracer particle during the simulation. Results in terms of ground concentration are returned over a 166-m grid. The SPRAYWEB simulation results are shown in Figure 5.7 (right panels).

The model disperses the tracer along the Adige Valley, southward. The tracer cloud persists in the area for longer time and with higher concentrations with respect to the CALPUFF simulation. In this case also, the release height of the tracer is not big enough to reach the wind jet flowing above the incinerator, as the tracer is not carried towards South-West.

5.2.3 Discussion

In a short-time tracer dispersion study, as the one here analyzed, results of ground concentrations depend on the mean wind field fed into the model, the values of the micrometeorological variables (u*, w*, 1/L) used to calculate the dispersion coefficients, the parameterization itself used to calculate the dispersion coefficients (σ_i) and the

model equations used to perform the transport and dispersion of the tracer (in this case, puff-gaussian approach and particle lagrangian approach). When comparing results of two different models it is important to be aware in what they differ, apart from the different model approach itself.

The CALPUFF and SPRAYWEB models are here fed with the exact same meteorological input but their different methodology for the interpolation of the wind field itself produces a different main transport direction of the tracer (see Figure 5.7). Second, the SL scales (L, u_*, H_{mix}, w_*) from which the models calculate the dispersion coefficients, are highly different and the resulting σ_i are consequently very different as well (Figures 5.8 and 5.9 report values for 9:00 LST as an e.g.). These differences, together with the specific approach used by each model, obviously have a big influence on the simulation of the tracer dispersion. For example, CALPUFF σ_i are much higher than the ones calculated by the SPRAYWEB Interface (WSI), explaining the much faster dispersion of the tracer in the CALPUFF simulation.

Without any observations of ground-concentrations, nor turbulence observations at any level in the study area, it is impossible to establish which of the two models is performing better in this case study. Nevertheless, it is a matter of fact that the CALMET/CALPUFF model directly intervenes on the WRF wind field (with slope-effect corrections and divergence minimization) and introduces an additional parameterization for the calculation of the SL scales. On the contrary, the WSI allows to extract all these variables directly from WRF, guaranteeing more congruence between the wind and temperature fields and the micrometeorological variables. The next chapter is dedicated to the quantitative evaluation of the performance of these models, by means of comparison of model results against observations collected during the second test day of the BTEX experiment (Section 3.3.3).

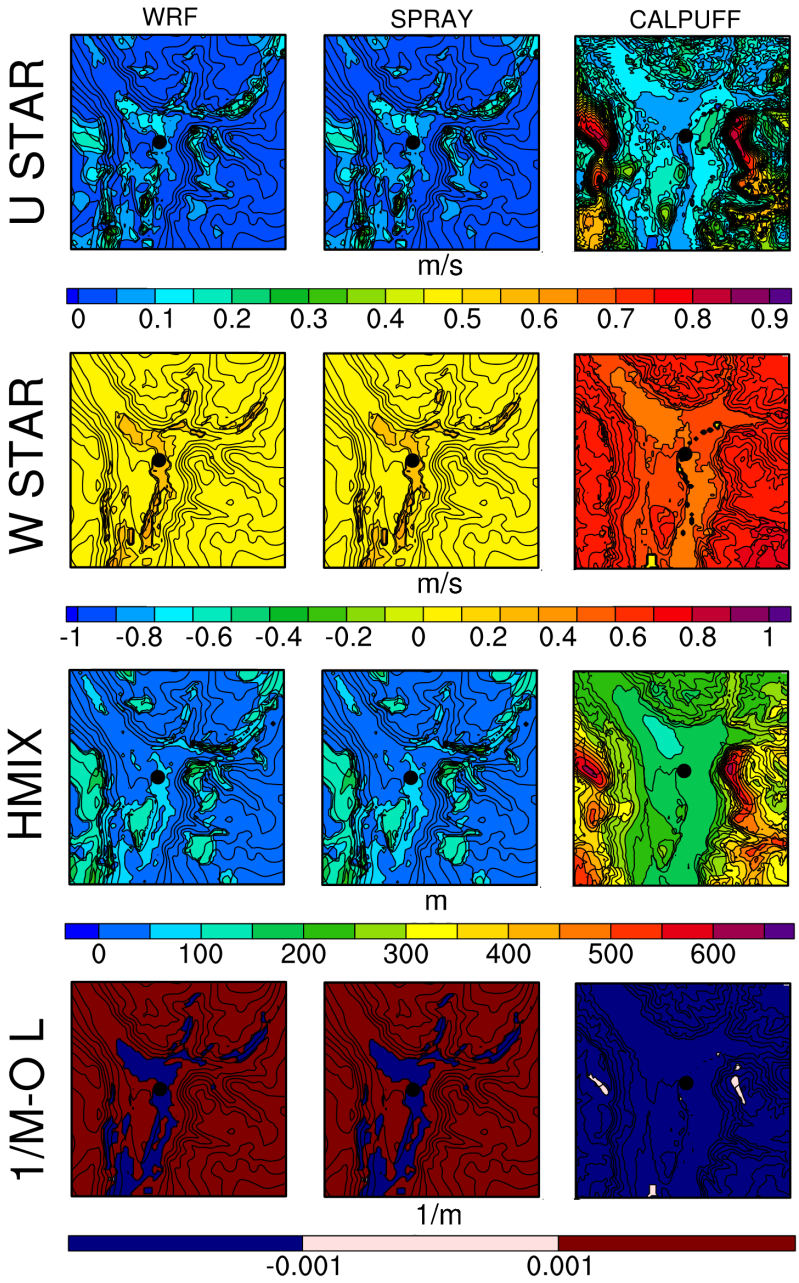

Figure 5.8: Maps of friction velocity (u_*), Deardroff velocity scale (w_*), mixing height (HMIX) and inverse of Monin Obukhov length (1/MOL) calculated by the WRF (left panels), SPRAYWEB (central panels) and CALPUFF (right panels) models, for a fixed hour of the day (9:00 LST).

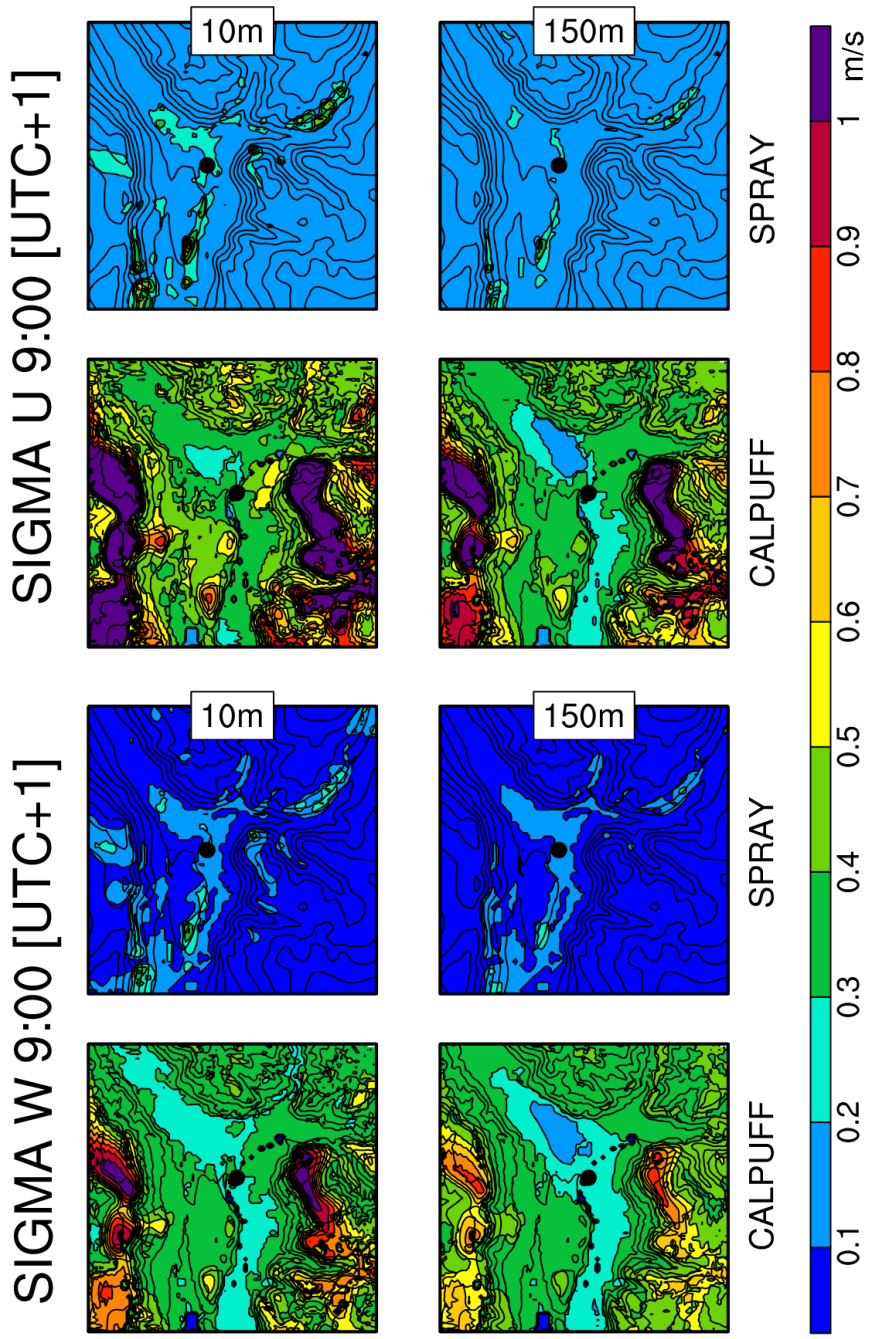

Figure 5.9: σ_U and σ_W coefficients calculated by the SPRAYWEB Interface (top panels) and by the CALMET/CALPUFF model (bottom panels), for a fixed hour of the day (9:00 LST) and for two fixed levels (10 m and 150 m).

Chapter 6

Intercomparison of different dispersion models and turbulence parameterizations over complex terrain.

In the present Chapter, different modeling chains for simulating the dispersion of a point wise tracer release from an incinerator plant are tested, over complex terrain. Ground concentrations from the BTEX (Section 3.3) field campaign are used as reference to evaluate the model performance. During the 2017 campaign, two tracer releases from the chimney of the Bolzano incinerator (Eastern Italian Alps) were performed - one in the early morning and one in the early afternoon - and samples of ground concentrations were collected (~80 samples). Meteorological simulations are run with the WRF model to reconstruct the flow field at sub-kilometer grid (300 m) and with observational nudging of upper-air and surface meteorological obser-

vations. The meteorological simulations are optimized by modifying the snow cover initialization of the WRF model, in order to improve the prediction of valley winds in the afternoon. An additional test is also run by substituting the closure constants of the WRF PBL scheme with a set of constants obtained for complex terrain applications (Section 2.4.2). The optimized meteorological fields provide the input to two different dispersion models: the CALMET/CALPUFF puff-Gaussian model and the WSI/SPRAYWEB Lagrangian particle model (Sections 2.4.1 and 2.4.2). The SPRAYWEB model is run with all the parameterizations available in the WSI for the calculation of the wind velocity standard deviations and the Lagrangian time scales (Section 2.4.2), including two parameterizations using the surface layer (SL) scales and one parameterization using the TKE from the WRF PBL scheme. A statistical analysis of the results from all the models is performed to assess the simulations performance against concentration measurements.

6.1 Methodology and model set-up

For this case study, both meteorological and dispersion simulations are run over the Bolzano basin on 14 February 2017, when the BTEX tracer releases were performed, in order to reproduce the meteorological field and the concentration field of the tracer. WRF simulations run at a sub-kilometer resolution to provide reliable meteorological fields for the dispersion simulations. These meteorological results are afterwards fed into two different dispersion models, the CALPUFF and SPRAYWEB models. The SPRAYWEB model is run with different parameterizations for the calculation of turbulence characteristics, returning three different simulations with different results.

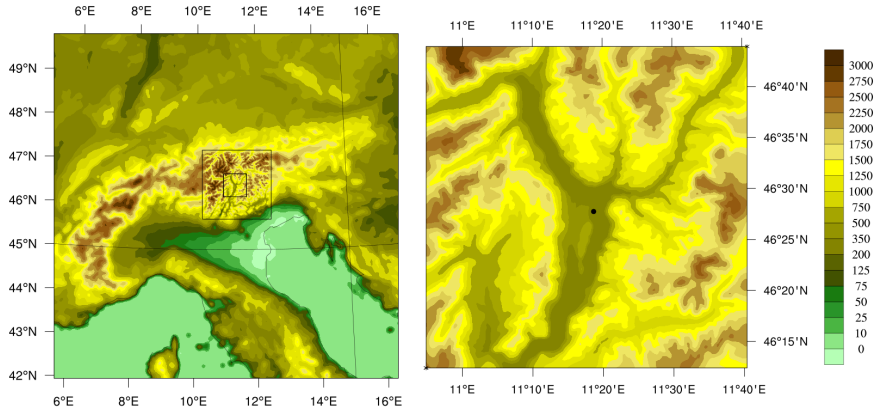

Figure 6.1: WRF nested domains from Northern Italy to the Bolzano basin with their elevation contours. The dot in the right panel indicates the location of the incinerator plant.

6.1.1 Meteorological simulations

The meteorological simulations are run with WRF v.3.8.1 with three two-way nested domains (Figure 6.1) and hourly observational nudging in the innermost domain. The external domain runs on a 4.5-km horizontal grid, and a 300-m resolution is reached in the innermost domain with a 5:1 grid ratio between the two external domains and a 3:1 ratio between the two inner domains (details on the domain characteristics are reported in Table 6.1). Such a fine grid in the external domain is appropriate as the boundary and initial conditions for the simulations come from 6-hourly ECMWF HRES Operational Data, with 9-km resolution. The vertical grid of the simulation is composed of 62 vertical levels distributed so that the resolution is finer closer to the ground: 10 levels lie in the first 300 m from the ground, evenly spaced each 30 m, and other 14 levels lie between 300 m and 1 km. The simulation covers the release day of BTEX, running from 1200 UTC 13 February 2017 to 0000 UTC 15 February 2017, for a total of 36 h of simulation. The first 12 h are used to spin-up the model

and corresponding results are not analyzed. In order to guarantee numerical stability of the simulation, given the complex orography of the area, the time step is 10 s for the external domain, corresponding to a time step 0.67 s for the innermost domain (Table 6.1).

Nest Number [−]	**Horizontal grid space** [km]	**Dimensions** [km]	**Time step** [s]
1	4.5	784 x 784	10
2	0.9	167.4 x 167.4	2
3	0.3	58.8 x 58.8	0.67

Table 6.1: Characteristics of the WRF nested domains for the BTEX case study.

Static data for the two external domains come from default WRF data sets, with a resolution of 30′ for both the topography and the land use. For the innermost domain, 1″ topographic data (de Ferranti, 2013) and 3″ land use cover data (Corine Land Cover data reclassified to the IGBP Land Cover Type Classification, EEA (2006), Giovannini et al. (2014 a)) are provided.

The following physics schemes are adopted: the WRF Single-Moment 3-class scheme for micro physics (Hong et al., 2004); the RRTMG new scheme for long- and shortwave parameterization Iacono et al. (2008); the Noah land surface model Chen and Dudhia (2001) for the surface fluxes parameterization; the Revised MM5 scheme Jimnez et al. (2012) for the surface layer; and the 1.5 order Nakanishi and Niino (2004) scheme for the Planet Boundary Layer parameterization. No cumulus schemes are applied, as the first domain already runs at 4.5-km resolution. The effects of shading and slope angle in complex terrain are taken into account and topographic wind correction is applied for the two external domains.

Hourly observational nudging is performed in the innermost do-

main and all the available meteorological observations (measurement points are shown in Figure 3.8) are assimilated: wind speed and direction, temperature and relative humidity from 15 weather stations operated by the local meteorological office; 2 vertical wind profiles from the SODAR instrumentation on the incinerator roof, and from the LIDAR at the exit of the Isarco Valley; and 1 vertical temperature profile from the thermal profiler located South of the city of Bolzano.

With this configuration, 2 simulations with the WRF model are performed: the 1^{st} simulation (WRF_O) runs with the Original set of turbulence closure constants from Nakanishi and Niino (2004) in the PBL scheme (see Section 2.3.3), while the 2^{nd} simulation (WRF_M) runs with the Modified set of closure constants from Trini Castelli et al. (2001) and Trini Castelli et al. (1999). The selection of the most appropriate meteorological simulation to be used for the dispersion simulations is discussed in the following sections.

6.1.2 Dispersion simulations

In order to reproduce the dispersion pattern of the released tracer, dispersion simulations are run both with the CALPUFF v6.42 and SPRAYWEB models. Dispersion simulations start at 7 LST, when the first release from the chimney was performed, and end at 18 LST, ~5 hours after the second release. In both the dispersion models the incinerator chimney is simulated as a point source, emitting at 60 m a.g.l a constant concentration of tracer throughout the duration of each release. Table 6.2 summarizes the two releases as modeled in the numerical simulations.

Release	Hour [LST]	Duration [h]	Released tracer [kg]	Temperature [°C]	Exit Velocity [m s^{-1}]
1^{st}	7:00	1	150	140	7.9
2^{nd}	12:45	1.5	450	140	7.8

Table 6.2: Summary of the main characteristics of the two tracer gas releases performed during BTEX2017 as modeled in the CALPUFF and SPRAYWEB simulations.

Both CALPUFF and SPRAYWEB are fed with the output of the WRF simulations, by means of the CALMET model and the WSI, respectively. The CALMET preprocessor produces an hourly meteorological input for CALPUFF while the WSI produces an input with 20-min time resolution.

CALPUFF simulation (CP) runs at 300-m horizontal resolution, so that the CALMET pre-processor introduces little changes in the WRF meteorological fields, with 10 vertical levels up to 3000 m (first level is 20 m above the ground) and a 5-min time step. As for the meteorological simulations, topography and land use input data are provided at a resolution of 30 m and 100 m, respectively, which are consistent with the high resolution of the simulation. As to turbulence parameterization, dispersion option 2 is selected in CALPUFF, which calculates standard deviations of the wind velocity as functions of SL scales (L, u_*, H_{mix}, w_*) calculated by the internal micrometeorological model of CALMET (Section 2.4.1).

Being a Lagrangian model, SPRAYWEB does not require to fix neither vertical nor horizontal grid resolutions. Nevertheless, ground concentrations are returned on a grid with 300-m horizontal and 20-m vertical resolutions. The SPRAYWEB simulations run with a varying time step which is internally calculated by the model, on the basis of the Lagrangian time scale values. Minimum time step is set to 2 s and 100 particles are released at every time step. Static data are

directly read from WRF, and have therefore the same resolution as the meteorological simulation. The WSI is run with three different parameterizations for the turbulence characterization (described in Section 2.4.2) and three simulations with SPRAYWEB are therefore performed: simulation SPW_H runs with the Hanna (1982) parameterization for the wind velocity standard deviations, simulation SPW_C runs with the CALPUFF parameterization and simulation SPW_{TKE} runs with the TKE parameterization (Section 2.4.2).

The four dispersion simulations CP, SPW_H, SPW_C and SPW_{TKE} can be tested with the two meteorological simulations run with WRF (WRF_O and WRF_M), obtaining eight different sets of results. Table 6.3 summarizes the simulations that can be performed with the different available configurations of the models. The following Sections present the procedure followed to select which simulations are to be run and analyzed.

WRF simulation	**Dispersion simulation**	**Dispersion model**	**Turbulence parameterization**
WRF_O, WRF_M	CP	CALPUFF	from SL scales CALPUFF param.
	SPW_H	SPRAYWEB	from SL scales Hanna param.
	SPW_C	SPRAYWEB	from SL scales CP CALPUFF param.
	SPW_{TKE}	SPRAYWEB	TKE decomposition

Table 6.3: Summary of the different models' configurations used for the BTEX2017 case study.

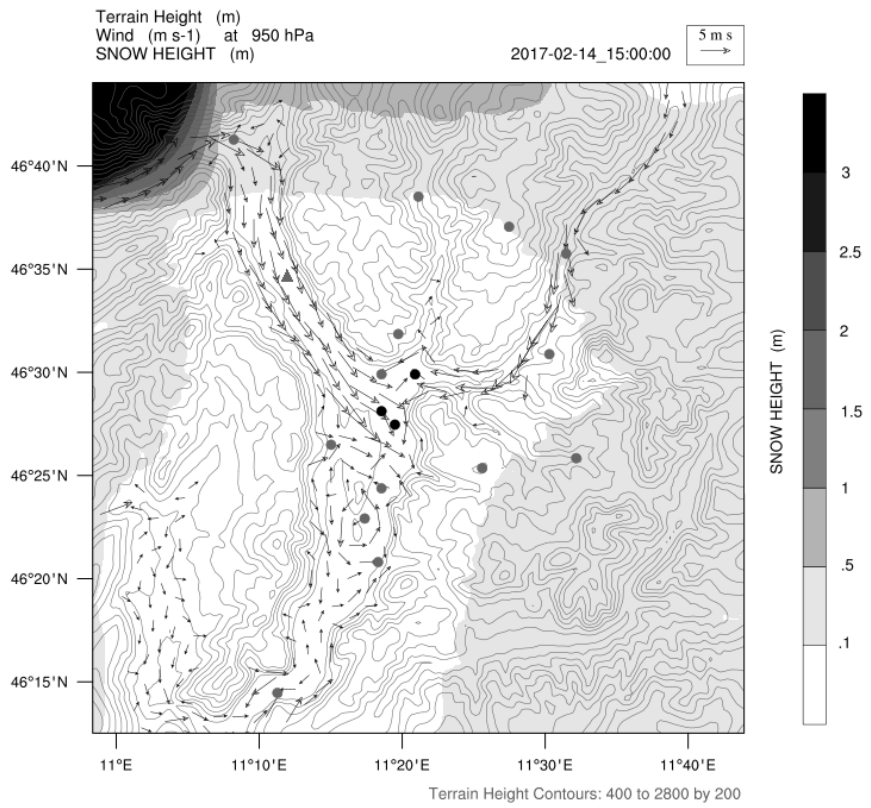

Figure 6.2: Preliminary modeled wind speed and direction at 950 hPa, at 15 UTC over the innermost WRF domain (WRF_O). Gray shades represent snow height as from ECMWF input data. Dots are the weather stations assimilated in the simulation. The triangle is the station recalled in Fig. 6.3.

6.2 Meteorological results

Preliminary results from the WRF simulations showed that the model generated a strong drainage wind in the lowest layers, which flew from the upper Adige Valley toward the Bolzano basin, in the early afternoon: Figure 6.2 shows the modeled wind flow at 1500 UTC at 950 hPa (~300 m agl; the figure reports the output from WRF_O only, as the results are similar in WRF_M simulation). This drainage flow

was not recorded by the weather stations which indeed show very low wind intensities. Figure 6.3 (again reporting the WRF_O results only, as representative of both the simulations) shows how the model forced this strong northerly wind in the central hours of the day, in the upper Adige Valley, even if observations reporting very low wind speed were assimilated. The occurrence of such a strong flow could be very problematic for the dispersion simulations: indeed, given its height, direction and timing, this flow reached the Bolzano basin and hit the incinerator plant, clearly influencing the plume dispersion trajectory. For this reason, a detailed analysis of the causes generating this phenomenon was carried out.

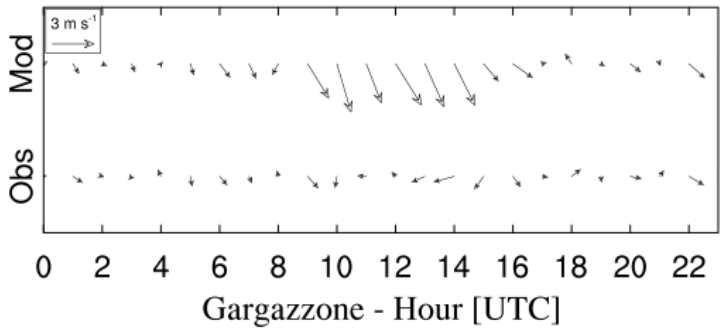

Figure 6.3: Ground wind speed and direction measured and preliminary modeled (WRF_O) at Gargazzone (indicated by a triangle in Figure 6.2).

The cause of the development of this local phenomenon was found to reside in the presence of a thick snow layer in the North-West corner of the domain, also shown in Figure 6.2, with gray shades. The snow pack generated a cold core in the upper left corner of the domain, which created a strong temperature gradient with the center of the domain and, consequently, the drainage flow. In addition, the snow on the valley floor also caused a discontinuity in the surface fluxes, which contributed to the development of the down-valley wind. Once again, as already shown in Chapter 4, the snow cover initialization of the WRF model turns out to be a very delicate issue:

not even initial and boundary conditions with a 9-km resolution are reliable for the description of the snow cover over complex terrain.

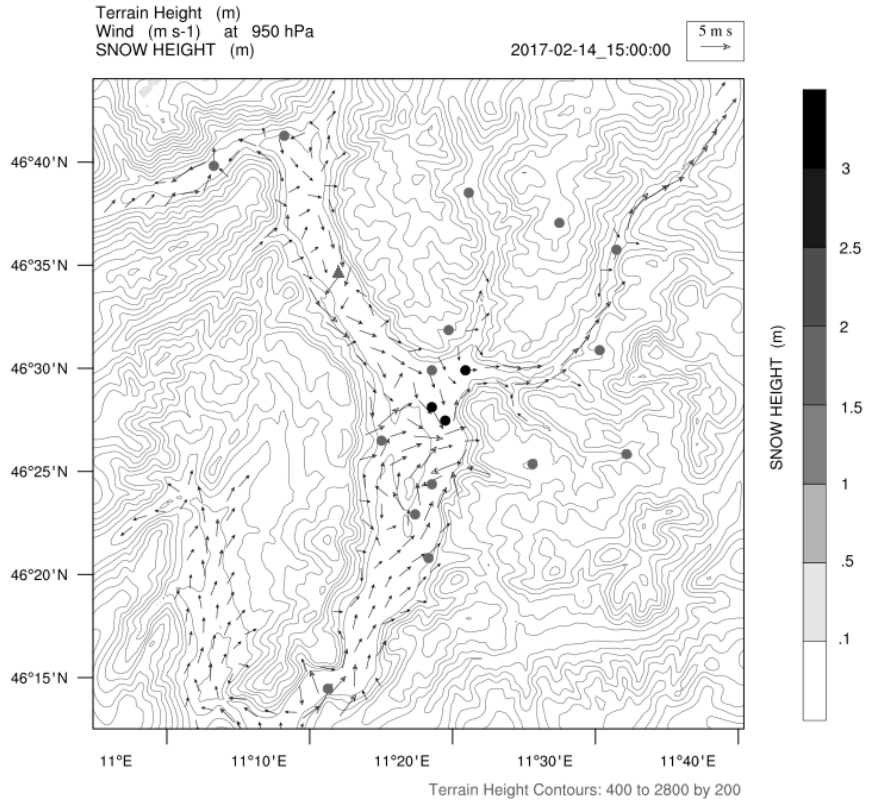

Figure 6.4: Modeled wind speed and direction at 950 hPa, at 15 UTC over the innermost WRF domain after the optimization of the snow cover (WRF_O). Gray shades represent snow height. Dots are the weather stations assimilated in the simulation. The triangle is the station recalled in Fig. 6.5.

As no snow was present over the study area during the day of the release (except for the highest mountains peaks, which are far from the focus of this study), the initialization of the snow cover in the WRF model was manually modified, intervening by completely removing the presence of the snow. Results of this operation are shown in Figure 6.4 (WRF_O results only), which again captures the

wind flow at 950 hPa at 15 UTC. The upper part of the Adige Valley is now characterized by lower wind speeds and the wind flow is hardly organized in prevalent directions. In addition to this, as shown in Figure 6.5, the model is now able to properly assimilate the wind speed and direction observed in the middle of the upper Adige Valley, as there are no more strong forcing driving predominant flows. The effects of the modification on the snow initialization is the same for the WRF_M simulation (not shown).

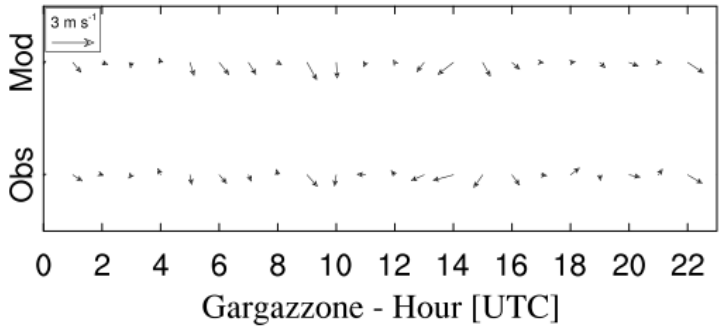

Figure 6.5: Ground wind speed and direction measured and modeled (WRF_O) at Gargazzone (indicated by a triangle in Figure 6.4) after the optimization of snow cover initialization.

In order to give an overview of the results of the optimized simulations, the comparison between the available observations and the model results is reported. It is important to keep in mind that the observations here recalled are assimilated by the model: when discrepancies are encountered between the observations and the model it means that the model is developing forcing which are too strong to be weakened by the assimilation. Since the observations have been assimilated, results from WRF_O only are presented, as differences with WRF_M are minimal in correspondence of measurement locations: considerations made in the following are therefore valid for both the WRF simulations. Results obtained in the LIDAR location (Figure 6.6) show that the model is able to properly follow the timing

of the development and fading of the jet from the Isarco Valley. The vertical extension of the jet is also properly reproduced by the model while the intensity of the phenomenon is slightly underestimated. Temperature profiles produced by the model in the location of the

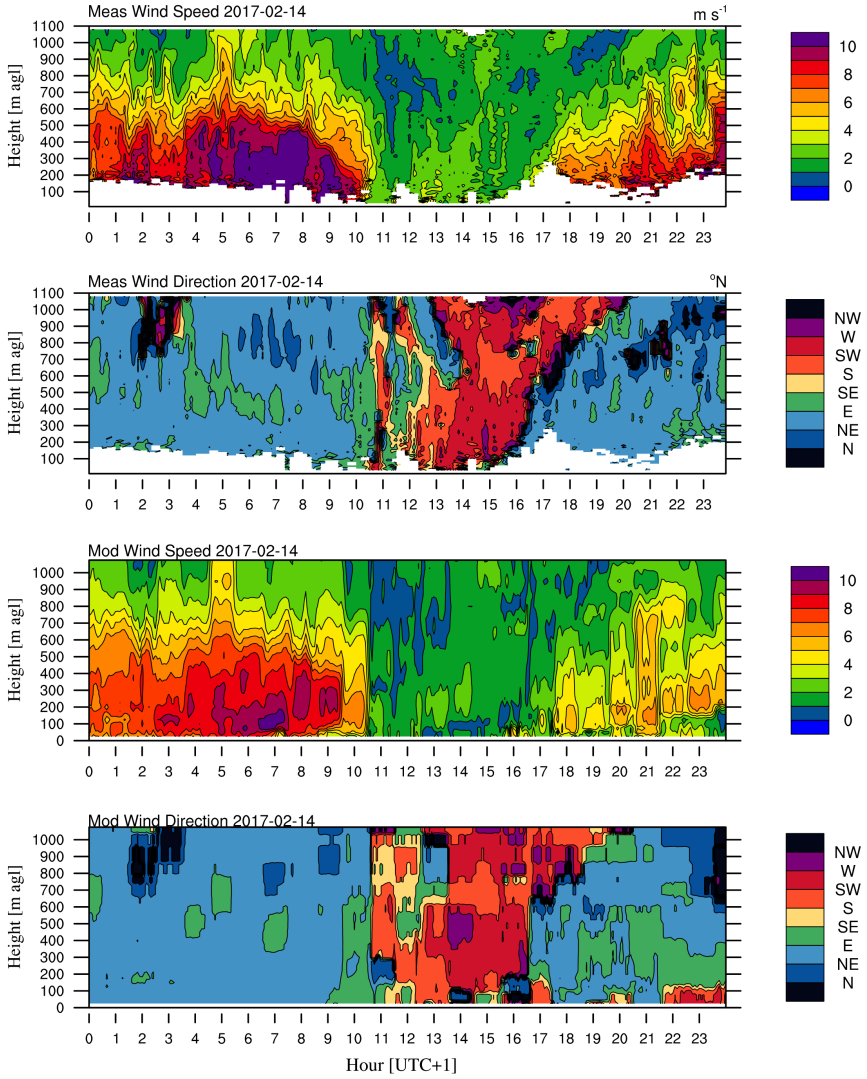

Figure 6.6: Time-height diagrams of wind speed and direction measured by the LIDAR located at the exit of the Isarco Valley (top panels) and modeled by WRF in the same location (WRF_O, bottom panels).

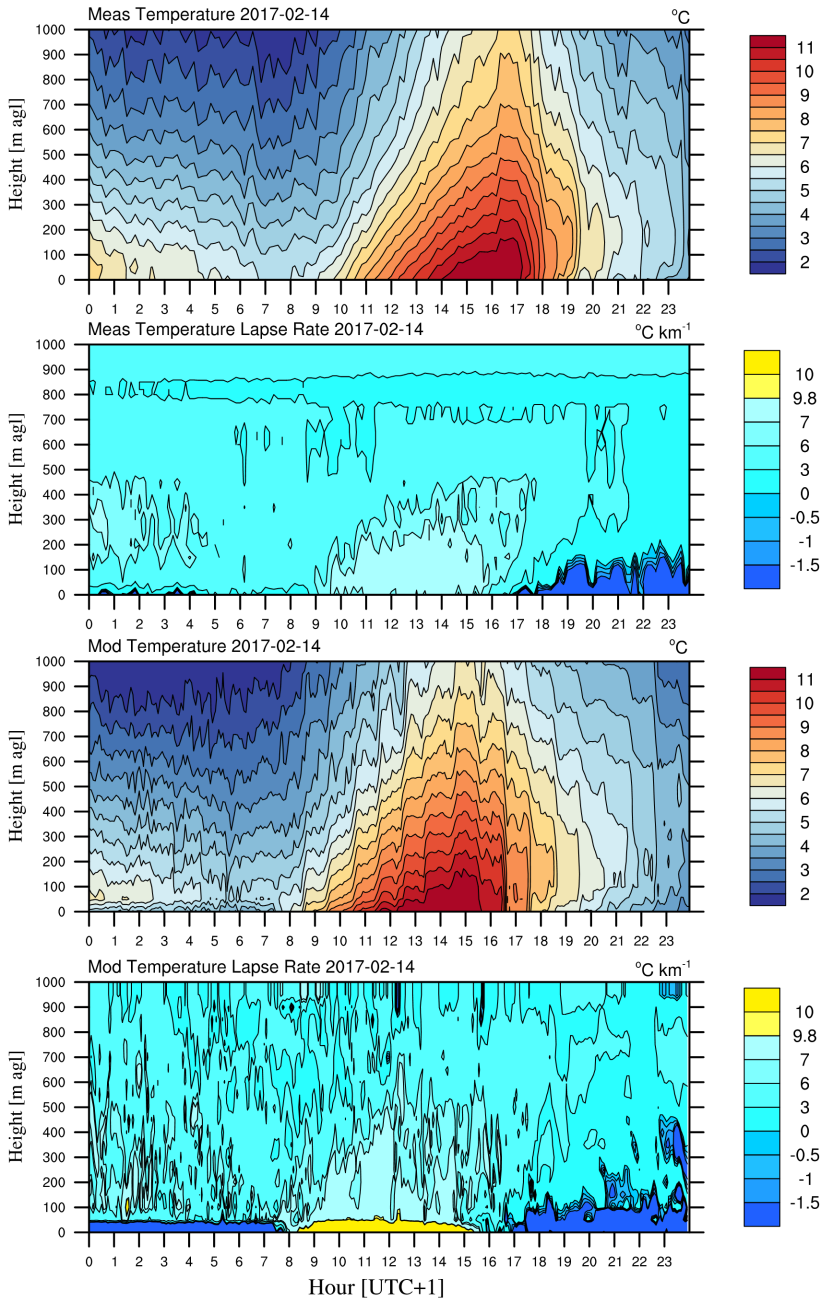

Figure 6.7: Time-height diagrams of temperature and temperature lapse rate observed by the thermal profiler (top panels) and modeled by WRF_O (bottom panels). In the lapse rate plots blue, cyan and yellow identify thermal inversion, stable conditions and unstable conditions, respectively.

thermal profiler properly follow the measurements (Figure 6.7), except for the creation of an unstable thin layer in the central hours of the day.

As shown above, overall results of the meteorological simulations are satisfactory after the intervention on the snow cover initialization and represent a reliable input for the dispersion models. Nevertheless it remains unclear which WRF simulation better represents the meteorological fields for dispersion purposes. In order to answer this question, a statistical comparison of WRF_O and WRF_M results with observed wind speed and direction was carried out, in correspondence of the measurement locations, at 20-min time steps when observations were not assimilated (assimilation was performed hourly). This analysis (as expected) showed no relevant statistical differences between the two simulations. An additional test was conducted by performing both the simulations without data assimilation, nevertheless no best performance was identified comparing results with observations of wind speed and direction. In order to identify a significant difference between the two meteorological simulations, higher order quantities must be analyzed, as shown in the following section.

6.3 The WRF-SPRAYWEB Interface results

In order to select the best meteorological simulation, the output of the different turbulence parameterizations from the WSI are compared with observed wind velocity standard deviations from the SODAR instrumentation, located on the incinerator roof. The same comparison can not be performed for the CALPUFF model as the σ_i are not given as an output from the CALMET/CALPUFF model. A statistical analysis of the results of the three WSI turbulence parameterizations fed with the two different meteorological simulations was conducted

and results of six different simulations are presented. During the day of the releases, measurements of wind speed standard deviations (σ_U and σ_W) reached heights of ~300 m, which allowed a comparison with modeled values at 4 to 6 levels. The statistical indexes used for the evaluation are the mean of the modeled values ($\overline{M}$, compared with the mean of the observations $\overline{O}$), the Correlation (R), the Fractional BIAS (FB) and the Normalized Mean Square Error (NMSE), defined as follows:

$$R = \frac{\sum_{i=1}^{N}(O_i - \overline{O})(M_i - \overline{M})}{\sqrt{\sum_{i=1}^{N}(O_i - \overline{O})^2}\sqrt{\sum_{i=1}^{N}(M_i - \overline{M})^2}} \tag{6.1}$$

$$FB = 2\frac{\overline{O} - \overline{M}}{\overline{O} + \overline{M}} \tag{6.2}$$

$$NMSE = \frac{\overline{(M_i - O_i)^2}}{\overline{M}\,\overline{O}} = N\frac{\sum_{i=1}^{N}(M_i - O_i)^2}{\sum_{i=1}^{N}M_i \sum_{i=1}^{N}O_i} \tag{6.3}$$

where M_i and O_i are the modeled and observed values and N is the total number of values in the analyzed time series. These statistical indexes were calculated for each level and then an average value was calculated for σ_U and σ_W, for each simulation. Results of this analysis are reported in Table 6.4.

The results reported in Table 6.4 show that a significant improvement is achieved in the calculation of both σ_U and σ_W for each parameterization when fed with the modified meteorological input (WRF_M). Indeed, both the σ_U and σ_W modeled averages get closer to the observed values and FB and NMSE indexes experience a decrease if the WRF_M results are used as input to the WSI. The correlation also improves, reaching higher values with the modified turbulence closure constants (the σ_W R for the Hanna parameterization is the only

exception). On the basis of these results, it can be stated that the meteorological fields obtained with the closure constants calibrated over complex terrain allow a better reconstruction of the vertical distribution of the wind speed standard deviations, regardless the turbulence parameterization applied. For this reason, in the following section, results from dispersion simulations run with the WRF_M input only are presented.

		σ_U				
		$\overline{O}$	$\overline{M}$	R	FB	NMSE
WRF_O	SPW_H	1.05	0.63	0.34	-0.36	0.52
	SPW_C	1.05	0.49	0.34	-0.61	0.71
	SPW_{TKE}	1.05	0.54	0.43	-0.52	0.61
WRF_M	SPW_H	1.05	0.7	0.43	-0.27	0.35
	SPW_C	1.05	0.52	0.44	-0.54	0.61
	SPW_{TKE}	1.05	**0.72**	**0.5**	**-0.22**	**0.31**

		σ_W				
		$\overline{O}$	$\overline{M}$	R	FB	NMSE
WRF_O	SPW_H	0.68	0.24	0.18	-1.04	2.08
	SPW_C	0.68	0.38	0.75	-0.65	0.79
	SPW_{TKE}	0.68	0.42	0.60	-0.50	0.59
WRF_M	SPW_H	0.68	0.26	0.11	-0.98	1.85
	SPW_C	0.68	0.41	**0.79**	-0.54	0.55
	SPW_{TKE}	0.68	**0.53**	0.69	**-0.25**	**0.32**

Table 6.4: Statistical indexes calculated for σ_U and σ_W for each turbulence parameterization coupled with both the meteorological simulations. Gray shades indicate the most performing value for each index, for each parameterization. Bold font indicates the absolute best value for each index.

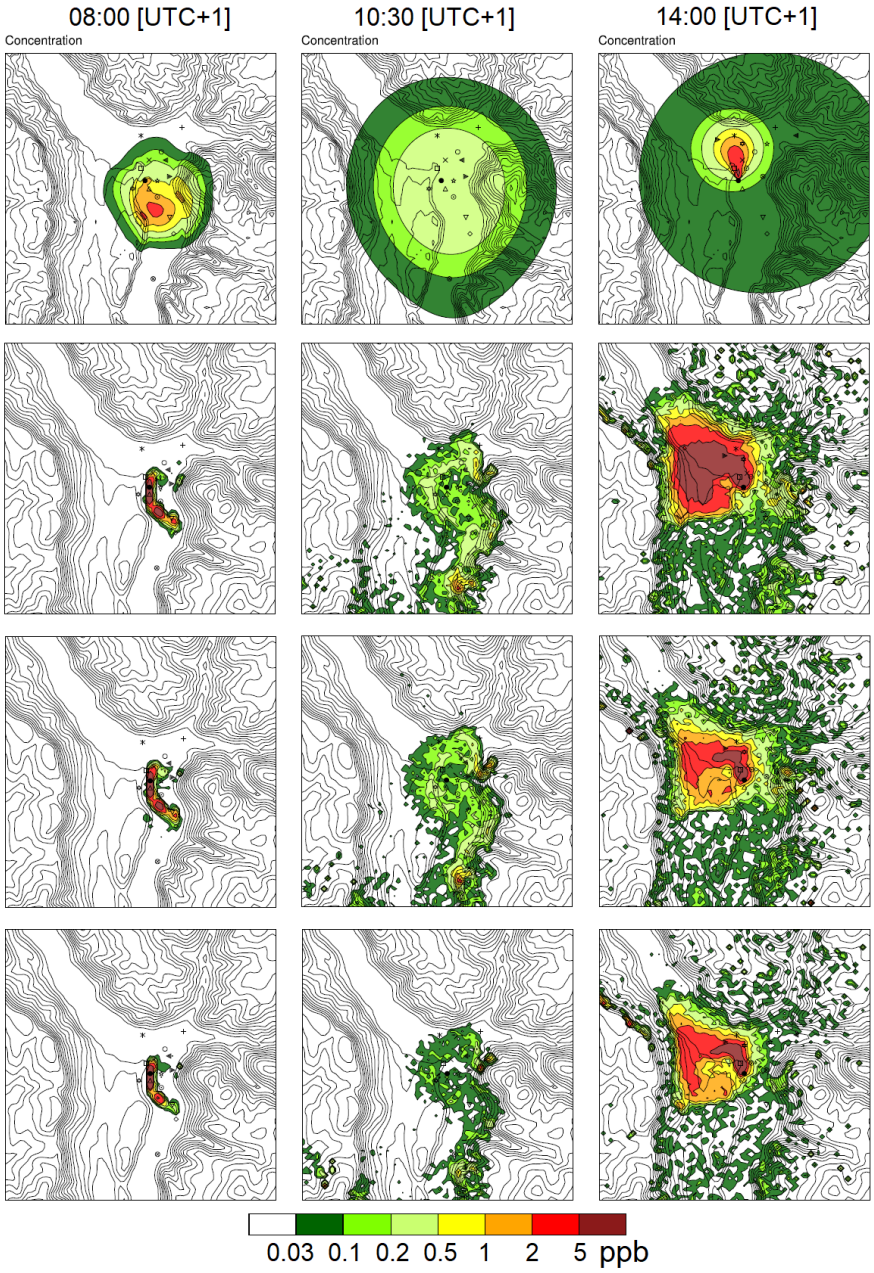

Figure 6.8: Ground level concentrations (5-min averages) in time, calculated by the *CP* simulation (first row), by the SPW_H simulation (second row), by the SPW_C simulation (third row) and SPW_{TKE} simulation (bottom row).

6.4 Dispersion model results

Results obtained with the four different dispersion simulations are qualitatively presented in Figure 6.8. The snapshots presented give an idea of the results of the different approaches tested in this case study. The CALPUFF simulation tends to generate very uniform patterns, which are not highly influenced by the complex topography nor by the complexity of the flow field. On the other hand, the Lagrangian approach shows ground concentrations which look more affected by these to features, which are peculiar of this case study. Figure 6.8 also shows the influence of the turbulence parameterization on the concentration patterns in the SPRAYWEB simulations. In order to evaluate the performance of each model a quantitative, statistical analysis is needed.

The performance of the different models and parameterizations is evaluated on the basis of different statistical indexes. During the day of the releases, 79 samples were collected in different locations, with instruments characterized by different sampling times. Table 6.5 summarizes the characteristics of the available samples.

Time average	**Instrument**	**# of samples**
60 min	Vaq. bottles	34
20 min	Vaq. bottles	21
25 min	Bags	1
15 min	Bags	4
10 min	Bags	8
5 min	Bags	11
TOT		**79**

Table 6.5: Summary of the characteristics and number of the available samples for the BTEX 2017 case study.

The statistical analysis was conducted on three different statistical

samples: one considering all the samples as equals, one considering the sub-sample of 1-h measurements and one considering the sub-sample of 20-min measurements. For the sake of brevity, in this work only results for the overall sample are reported while results on the other sub-samples are just commented in the text.

The following statistical indexes have been calculated for the evaluation of the model performance (Chang and Hanna, 2004), where M_i and O_i are the modeled and observed values, and N is the total number of values in the analyzed time series:

- Mean of the observations
- Mean of the modeled values
- Correlation (Eq. 6.1)
- Fractional BIAS (Eq. 6.2)
- Normalized Mean Square Error (Eq. 6.3)
- Factor 2

  Represents the fraction of modeled values within a factor of two of the observations

$$f2 = \frac{1}{N}\left(\#M_i : 0.5 \leq \frac{M_i}{O_i} \leq 2\right) \tag{6.4}$$

- Factor 5

  Represents the fraction of modeled values within a factor of five of the observations

$$f5 = \frac{1}{N}\left(\#M_i : 0.2 \leq \frac{M_i}{O_i} \leq 5\right) \tag{6.5}$$

On the basis of these indexes, each model has been also tested for the acceptance criteria set by Hanna and Chang (2012). In Hanna

and Chang (2012), the authors set the following as acceptance criteria for applications of air quality models over urban areas: $|FB|$ <~67%, $NMSE$ <~6, $f2$ >~30%. Even if this test was structured for urban applications, it is of interest for this case study for two main reasons: (i) the degree of complexity encountered by the models over such complex terrain could be somehow compared to the one of urban applications; (ii) the test introduces acceptance criteria which are relaxed from those for non-urban cases, which means that if a model is not fulfilling these criteria its performance is unacceptable for any kind of application.

Results obtained for each dispersion simulation and each statistical index are reported in Table 6.6, where the last column reports the fulfillment of the Hanna and Chang (2012) test on acceptance criteria.

	$\overline{O}$ [pptv]	$\overline{M}$ [pptv]	R	FB	NMSE	f5	f2	Test H&C
CP	900	1298	0.05	0.36	6.64	0.71	0.38	no
SPW$_H$	900	1266	0.68	0.34	3.82	**0.77**	**0.48**	yes
SPW$_C$	900	980	0.7	0.09	2.43	0.71	0.43	yes
SPW$_{TKE}$	900	**888**	**0.76**	**-0.01**	**2.23**	0.68	0.36	yes

Table 6.6: Statistical indexes calculated for each air quality dispersion simulation. Bold font and shades indicate the most performing value for each index.

A first comparison can be made between the two types of model applied in this study, the puff-Gaussian CALPUFF model and the Lagrangian SPRAYWEB model. As shown by Table 6.6, the CALPUFF model poorly performs in comparison with any other SPRAYWEB simulation. It largely overestimates the observed mean value and shows the worst values for 4 statistical indexes out of 6 (R, FB, $NMSE$ and $f5$), with respect to the other simulations. To confirm this, the model does not fulfill the acceptance criteria set by Hanna and Chang

(2012). This result can be partly due to the fact that the CALPUFF model is fed with hourly meteorological fields (instead of 20-min fields as in SPRAYWEB), but tests have been run feeding SPRAYWEB with hourly meteorological fields and the comparison with the CALPUFF model led to the same conclusions. It is therefore likely that the poor performance of the model is associated with its own Gaussian formulation, which impedes to capture the inhomogeneity of the flow field over complex terrain. On the positive side, the CALPUFF model overestimates the ground concentrations, which is beneficial in applications for public safety.

The Lagrangian model SPRAYWEB performs better with any turbulence parameterization tested, satisfying the Hanna and Chang (2012) acceptance criteria. The SPRAYWEB simulations share the same wind field and the same dispersion approach, so that differences identified in their performance can be attributed to the turbulence parameterization only. SPW_H shows a significant overestimation of the modeled mean, getting closer to the CALPUFF prediction. On the contrary it presents better values of R, $NMSE$ and $f2$. SPW_C behaves similarly, but is able to improve the prediction of the mean concentration and the FB, showing a good agreement with respect to the observations. Performances of both SPW_H and SPW_C show that parameterizations based on the same SL scales can lead to significantly different results (especially in the mean values). This great variability in the results of similar parameterizations can be ascribed partly to the differences in the two parameterizations themselves, but also (and more likely) to the unreliability of the SL scales they are based on, which are indeed calculated on the basis of SL parameterizations calibrated over flat terrain.

Results from the parameterization decomposing the TKE on the three directions, SPW_{TKE} (see Section 2.4.2), are the best obtained in this case study. The modeled mean, R, FB and $NMSE$ values

calculated for the SPW_{TKE} simulation are the best with respect to all the other simulations ($f2$ and $f5$ values are better in SPW_C). The modeled mean gets very close to the observed value and R, $NMSE$ and FB experience relevant improvement and the acceptance criteria are fulfilled. These results of SPW_{TKE} simulation can be ascribed to many factors. First, it relies on the TKE values which are calculated with a prognostic equation in the PBL scheme (and should therefore carry more reliable physical information with respect to the SL scales). Second, TKE values from the PBL scheme are improved thanks to the substitution of the turbulence closure constants with values calibrated over complex terrain. Third, the procedure of the decomposition on the three directions of the TKE is performed using the complex terrain set of closure constant.

To give a further overview of the improvements obtained, not only in terms of mean values but also in terms of pattern, the Taylor diagram for the SPRAYWEB simulations is presented in Figure 6.9 (refer to Section 4.1.3 for a description of the diagram). The diagram shows that the SPW_{TKE} and SPW_C simulations greatly improve the identification of the pattern of the ground concentration, with respect to the SPW_H simulation, bringing the standard deviation and the normalized centered root mean square differences of the predictions very close to the one of the observations. Improvements in terms of R are less evident but still present and are greater for SPW_{TKE}.

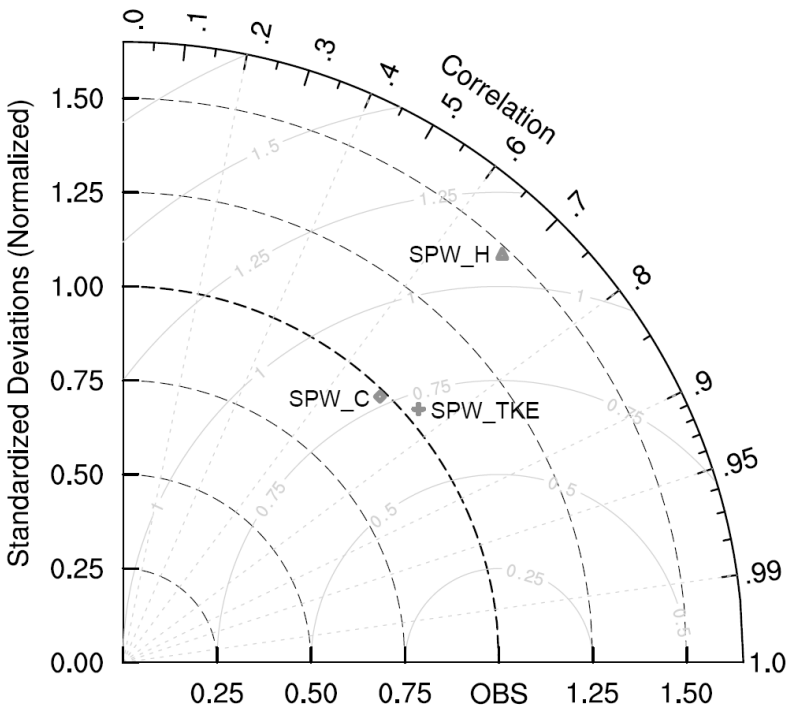

Figure 6.9: Taylor diagram describing the statistical patterns of the modeled ground concentrations computed by simulations SPW_H, SPW_C, SPW_{TKE} and SPW_{TKE_M} with respect to the observations.

Additional information on the performance of the SPRAYWEB simulations can be read from Figures 6.10 and 6.11, which report the percentile curves and the qqplots for each simulation, respectively.

Percentile curves show that the SPW_H simulation tends to overestimate the concentrations from the lowest to the highest percentiles, with significant errors at concentration peaks. This is confirmed by the qqplot, which shows good agreement between the model and the observations for low concentrations and a relevant overestimation of concentrations greater than 4000 pptv.

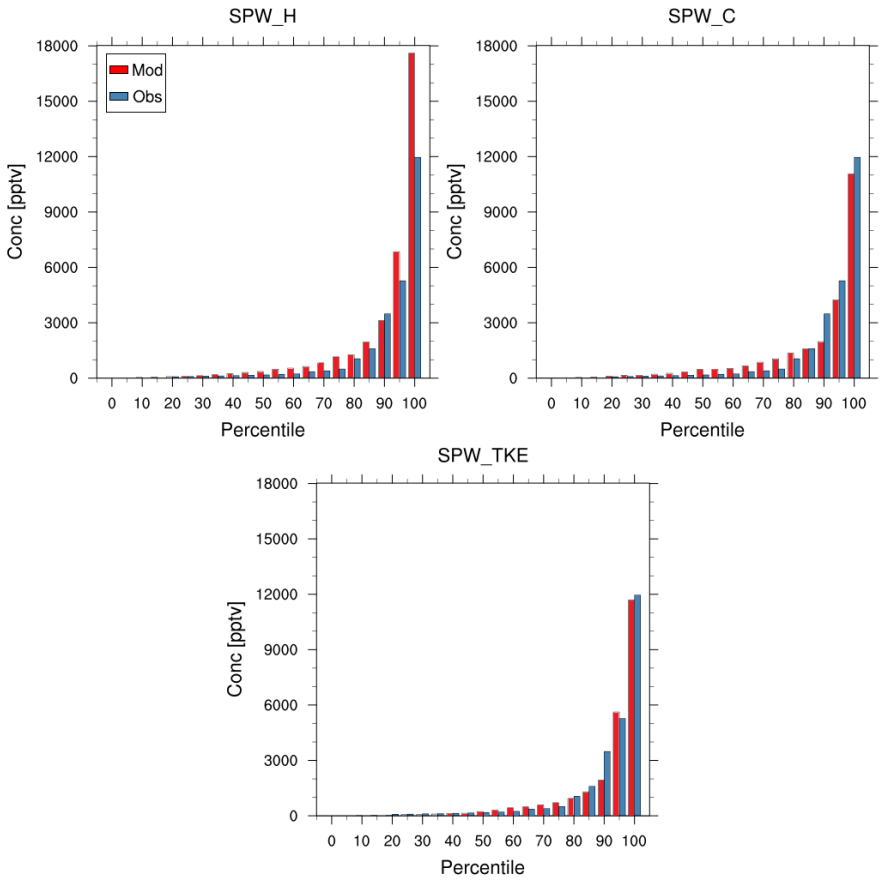

Figure 6.10: Percentile curves of the observed (Obs) ground concentrations and corresponding values modeled (Mod) by SPW_H, SPW_C and SPW_{TKE}.

SPW_C has a similar behavior up to the 85^{th} percentile, but for higher percentiles shows an underestimation of the concentrations. Its good performance in terms of predicted mean is therefore the result of the compensation of the overestimation on the low concentrations with the underestimation of the concentration peaks. This pattern is even more evident in the qqplot of Figure 6.11.

On the contrary, SPW_{TKE_M} performs better in the prediction of both low and high percentiles. Low concentrations are captured very well as well as peak values. The 90^{th} percentile only is quite under-

estimated. For this reason, the result obtained in terms of overall mean concentration is even more relevant, as it is not the result of a compensation of under- and overestimation.

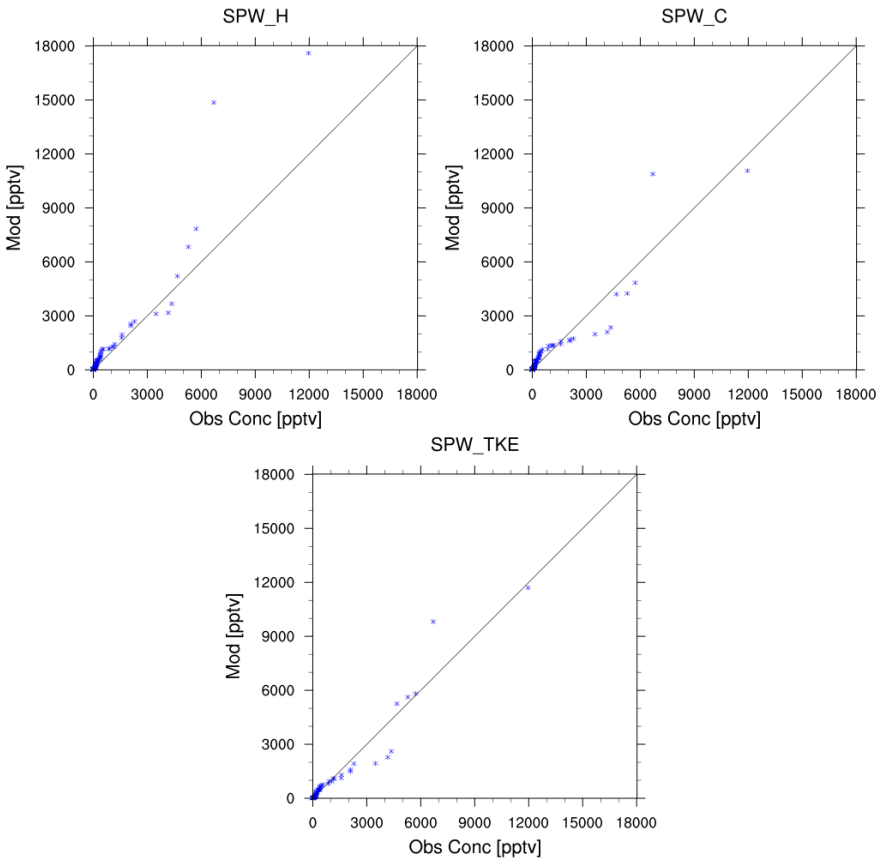

Figure 6.11: Qqplots of the observed (Obs) ground concentrations and corresponding values modeled (Mod) by SPW_H, SPW_C, SPW_{TKE} and SPW_{TKE_M}.

6.5 Conclusions

In this analysis, both meteorological and dispersion simulations are run in order to reconstruct the fate of the tracer released from the incinerator of Bolzano during the 2017 Bolzano Tracer Experiment.

The meteorological fields are reproduced by means of WRF simulations of the day of the tracer releases, running at a sub-kilometer resolution. The standard simulations with WRF showed deficiencies in initializing the snow cover on the innermost domain. Indeed, the snow cover was overestimated on most of the domain and its significant presence in the North-West corner of the domain generated a strong down-valley wind in the Adige Valley, passing above the incinerator plant. The presence of this drainage flow, not recorded by the weather stations, would have greatly affected the dispersion simulations. By intervening on the WRF initialization, the snow cover was therefore removed and optimized and satisfactory meteorological simulations were obtained. With this configuration, 2 simulations were performed, which differ by the set of turbulence closure constants only, used within the PBL scheme of the WRF model. The first simulation runs with the standard Nakanishi and Niino (2004) set of closure constants, while the second runs with an optimized set of constants. This new set of closure constants comes from a calibration of the Mellor and Yamada (1982) closure against wind tunnel measurements over an idealized valley (Trini Castelli et al., 2001). This specific set of closure constants should therefore be more suitable for applications over complex terrain, with respect to the standard one implemented in Nakanishi and Niino (2004) PBL scheme.

The two WRF simulations present differences in the flow fields but a comparison of the two simulations against the observations shows that no significant statistical differences can be identified in terms of mean wind speed and direction: a better simulation cannot therefore be chosen, in terms of mean quantities. For this reason, the analysis of the results in terms of higher order variables was needed and conducted. As observed values of the wind speed standard deviations are available from the SODAR instrumentation for the day of the release, at the incinerator chimney location, a comparison between

these measurements and the results from different turbulence parameterizations was performed. Three different parameterizations were tested, coupled with both the WRF simulations. Results show that a better agreement with observations is obtained with the modified meteorological simulation (with the complex terrain set of constants), regardless the turbulent parameterization used. This result suggests that the closure constants calibrated over complex terrain allow the reconstruction of more reliable both SL scales and turbulence characteristics (TKE and K_M).

The modified meteorological fields are fed into two different types of dispersion models, the CALPUFF and SPRAYWEB models, and a statistical analysis is carried out to evaluate the model performance for this case study. Results show that, as expected, over such a complex terrain, the puff-Gaussian model performs much worse if compared with the Lagrangian model. The mean value of the observations is greatly overestimated, as the emitted puffs essentially uniformly hit the ground. Responsible for this behavior is certainly the Gaussian approach itself, but part of the error can also be attributed to the fact that the turbulence parameterization of the CALPUFF model uses SL scales coming from an internal micrometeorological model. This calculation introduces additional approximations in the process of calculating the dispersion coefficients (as shown in section 5.2.3), which could be avoided by directly using SL scales already calculated in WRF.

On the contrary, the SPRAYWEB model shows better performance with all the turbulence parameterizations tested. The Hanna (1982) parameterization shows the worst performance, highly overestimating ground concentrations. The parameterization based on CALPUFF parameterization improves the identification of the concentration mean value but this result is given by the compensation of the overestimation of the low concentrations and the underestima-

tion of the maxima. Results obtained with the parameterization based on the TKE decomposition show great improvements: the observed mean is properly caught by the model and the pattern of the measurements is also much better reproduced, as shown by the increase in the correlation index and in the approach to 1 of the normalized standard deviation.

These results suggest that, combining a meteorological simulation run with PBL turbulence closure constants appropriate for complex terrain and a dispersion simulation run with a turbulence parameterization based on the TKE, can lead to an optimized reconstruction of the dispersion parameters and, therefore, of the ground concentrations. The introduction of closure constants calibrated for complex terrain in any involved parameterization, for applications in mountainous areas, is of fundamental importance for the improvement of the results.

Chapter 7

Conclusions

In this thesis, different aspects connected to numerical modeling of atmospheric pollutants' dispersion have been addressed, for identifying and developing the best practices to approach this problem over complex terrain.

First, the reliability of the WRF model was tested over complex terrain for the reconstruction of meteorological phenomena which are relevant for the atmospheric dispersion of pollutants. Two case studies are presented, the Aldeno ALPNAP and the Merano case studies. Both were characterized by a strong ground-based thermal inversion and late winter atmospheric conditions. In both cases, the WRF model fails to properly initialize and treat of the snow cover. Therefore, to get reliable results, modifications of the initialization process and of the LSM within WRF were tested and optimized results were obtained in terms of surface fluxes, 2-m temperature and related ground-based thermal inversion. Different LSMs were tested and the importance of specific snow-related coefficients in each parameterization was shown: indeed, these coefficients have a great impact on WRF results and their fixed values within the LSM can be misleading for high resolution simulations over complex terrain. The Merano case study showed that the initialization of the snow

cover can change the reconstruction of the thermal profiles in the WRF model, which have a key impact on the dispersion modeling. In addition, the evolution in time of these phenomena is also relevant for dispersion purposes on short-term time scales: indeed, the timing of the meteorological and emission patterns must be reconstructed accurately in order to capture local peaks of air pollution.

The Bolzano Tracer Experiment, conducted in wintertime, 2016 and 2017, allowed a detailed study on the approaches to dispersion modeling for an elevated point release over complex terrain. The experiment was particularly useful as the uncertainties on the emission source are almost suppressed, as the releases of tracer gas were controlled and monitored, and a constant, homogeneous release was guaranteed. The first BTEX tests, conducted in 2016, were meant to evaluate the abilities and performance of a standard and recommended model, the puff-Gaussian CALPUFF model, in such a complex case study. Tests were conducted using CALPUFF coupled with CALMET in both diagnostic and prognostic mode. In the first case, when CALMET is fed with observations only, the model shows its inability to reproduce the complexities of the meteorological fields, confirming that simulations with a NWP model, run at high resolution, are needed. The second test consisted in the comparison of results from the puff-Gaussian CALPUFF model and the Lagrangian SPRAYWEB model, both fed with the same WRF numerical simulation. No observations of ground concentrations were available for the 2016 campaign. Nevertheless, some interesting considerations could be made discussing the evidence of different results between the two models. This preliminary analysis, indeed, showed that differences arise between the two approaches not only because of their intrinsic diverse conceptual forms but also, first, because of the different process of interpolation performed by the two models and, second, because of the source of information used for the calculation

of turbulence parameters. Specifically, the application of an internal micro meteorological model within CALMET for the calculation of SL scales is found to introduce additional uncertainties and parameterizations in the process, with the loss of more accurate information calculated within the WRF model.

The successful 2017 BTEX campaign provided a unique data set of ground concentrations, which has been used to further investigate the evidences from 2016 analyses. Numerical simulations run with WRF again demonstrated that an accurate snow cover initialization is fundamental for an accurate reconstruction of the temperature and flow fields. With optimized meteorological results, different tests were performed with different dispersion models (CALPUFF and SPRAYWEB) and with different turbulence parameterizations within the WRF/SPRAYWEB Interface. Finally, a statistical analysis of the results has been carried out. Results showed first of all that the puff-Gaussian model performs worse than the Lagrangian model, due to the Gaussian approach itself and to the additional approximation introduced for the turbulence parameterization performed by means of an internal micrometeorological model. Results with the Lagrangian SPRAYWEB model show better agreement with the observations. Simulations run with turbulence parametrizations based on the SL scales from the WRF model show very different results, suggesting the unreliability of the source information. The simulation run calculating the turbulence parameters from the physically-based information on TKE and K_M from the PBL scheme performs much better, properly capturing both mean values and patterns of the observations. The success of this parameterization directly depends on the reliability of the information coming from the WRF PBL scheme. Indeed, the modification of the closure parameters within the WRF PBL scheme, substituting original values with values obtained for complex terrain applications, greatly improves the performance of the SPRAYWEB

model, due to a better representation of the wind speed standard deviations (with any turbulence parameterization). The importance of these closure constants, within both the NWP model and the turbulence parameterization of the dispersion model, has therefore been highlighted and proved.

The present thesis work overall contributed to test and improve different parts of the modeling chain applied for the simulation of local pollutants' releases over complex terrain, from the meteorological model, to the turbulence parameterizations in the dispersion models. The analyses showed that difficulties still arise in the simulation of the meteorological fields over complex terrain, especially in wintertime conditions, but, with accurate evaluation and appropriate treatment of the heat flux exchange (more specifically, of the snow cover conditions), great improvements can be achieved. Optimization can also be obtained for the performance of the tested dispersion models, using the best available information on the turbulence field from a NWP model and working on the calibration of the many involved parameterizations over complex terrain.

Bibliography

Alessandrini, S. and E. Ferrero, 2009: A hybrid lagrangian-eulerian particle model for reacting pollutant dispersion in non-homogeneous non-isotropic turbulence. *Physica A: Statistical Mechanics and its Applications*, **388 (8)**, 1375 – 1387, doi:http://dx.doi.org/10.1016/j.physa.2008.12.015, URL `http://www.sciencedirect.com/science/article/pii/S0378437108010248`.

Alessandrini, S., E. Ferrero, C. Pertot, and E. Orlandi, 2005: Comparison of different dispersion models with tracer experiment. *Nuovo Cimento C Geophysics Space Physics C*, **28**, 141, doi:10.1393/ncc/i2005-10187-0.

Allwine, K. and C. Whiteman, 1985: MELSAR: A mesoscale air quality model for complex terrain: Volume 1 - Overview technical description and user's guide. Tech. rep., Pacific Northwest Laboratory, Richland, Washington.

Allwine, K. J. and J. E. Flaherty, 2006: Joint Urban 2003: Study Overview and Instrument Locations. Tech. rep., Pacific Northwest National Laboratory, operated by Battelle for the U.S. Department of Energy.

Ambrosetti, P., et al., 1994: The TRANSALP-90 Campaign. The second tracer release experiment in a sub-alpine valley. Tech. Rep. EUR 15952 EN, Commission of the European Communities, 70 pp.

APB, 2010: Inventario delle emissioni in atmosfera della Provincia Autonoma di Bolzano - aggiornamento 2010. Tech. rep., Autonomous Province of Bolzano.

Arya, S., 1984: Parametric relations for the atmospheric boundary layer. *Bound. Layer Meteor.*, **30**, 57–73.

Ball, J. T., I. E. Woodrow, and J. A. Berry, 1987: A Model Predicting Stomatal Conductance and its Contribution to the Control of Photosynthesis under Different Environmental Conditions. *Progress in Photosynthesis Research: Volume 4 Proceedings of the VIIth International Congress on Photosynthesis Providence, Rhode Island, USA, August 10-15, 1986*, J. Biggins, Ed., Springer Netherlands, 221–224.

Bellasio, R., G. Maffeis, J. S. Scire, M. G. Longoni, R. Bianconi, and N. Quaranta, 2005: Algorithms to account for topographic shading effects and surface temperature dependence on terrain elevation in diagnostic me-teorological models. *Boundary-Layer Meteorology*, **114 (3)**, 595614.

Bisignano, A., L. Mortarini, E. Ferrero, and S. Alessandrini, 2016: Model chain for buoyant plume dispersion. *Int. J. of Environment and Pollution*.

Blackadar, A. and H. Tennekes, 1968: Asymptotic similarity in neutral barotropic planetary boundary layers. *J. Atmos. Sci.*, **25**, 1025–1020.

Bonan, G. B., 1996: A land surface model (LSM version 1.0) for ecological, hydrological, and atmospheric studies: technical description and user's guide. NCAR Tech. Note NCAR/TN-417+STR, National Center for Atmospheric Research, 150 pp., Boulder, CO.

Bougeault, P. and P. Lacarrere, 1989: Parameterization of orography-induced turbulence in a mesobeta–scale

model. *Monthly Weather Review*, **117 (8)**, 1872–1890, doi: 10.1175/1520-0493(1989)117⟨1872:POOITI⟩2.0.CO;2, URL https://doi.org/10.1175/1520-0493(1989)117<1872:POOITI>2.0.CO;2, https://doi.org/10.1175/1520-0493(1989)117<1872:POOITI>2.0.CO;2.

Britter, R. E., S. Di Sabatino, F. Caton, K. M. Cooke, P. G. Simmonds, and G. Nickless, 2002: Results from Three Field Tracer Experiments on the Neighbourhood Scale in the City of Birmingham UK. *Water, Air and Soil Pollution: Focus*, **2 (5)**, 79–90, doi: 10.1023/A:1021306612036, URL http://dx.doi.org/10.1023/A:1021306612036.

Britter, R. E. and S. R. Hanna, 2003: Flow and dispersion in urban areas. *Annual Review of Fluid Mechanics*, **35 (1)**, 469–496, doi: 10.1146/annurev.fluid.35.101101.161147, URL https://doi.org/10.1146/annurev.fluid.35.101101.161147, https://doi.org/10.1146/annurev.fluid.35.101101.161147.

Businger, J. A., 1982: *Equations and Concepts*, 1–36. Springer Netherlands, Dordrecht, doi:10.1007/978-94-010-9112-1_1, URL https://doi.org/10.1007/978-94-010-9112-1_1.

Canuto, V., 1992: Turbulent convection with overshooting - Reynolds stress approach. *Atmospheric Physics Journal*, **392**, 218–232, doi:10.1086/171420.

Caughey, S. J., J. C. Wyngaard, and J. C. Kaimal, 1979: Turbulence in the evolving stable boundary layer. *Journal of the Atmospheric Sciences*, **36 (6)**, 1041–1052, doi:10.1175/1520-0469(1979)036⟨1041:TITESB⟩2.0.CO;2.

Chang, J. C. and S. R. Hanna, 2004: Air quality model performance evaluation. *Meteorology and Atmospheric Physics*, **87 (1)**, 167–196,

doi:10.1007/s00703-003-0070-7, URL https://doi.org/10.1007/s00703-003-0070-7.

Chen, F. and J. Dudhia, 2001: Coupling an advanced land surface-hydrology model with the Penn State-NCAR MM5 modeling system. Part I: Model implementation and sensitivity. *Mon. Wea. Rev.*, **129**, 569–585.

Chen, F., et al., 2014: Modeling seasonal snowpack evolution in the complex terrain and forested colorado headwaters region: A model intercomparison study. *Journal of Geophysical Research: Atmospheres*, **119 (24)**, 13,795–13,819, doi:10.1002/2014JD022167, URL http://dx.doi.org/10.1002/2014JD022167, 2014JD022167.

Collatz, G. J., J. T. Ball, C. Grivet, and J. A. Berry, 1991: Physiological and environmental regulation of stomatal conductance, photosynthesis and transpiration: a model that includes a laminar boundary layer. *Agric. For. Meteor.*, **54 (2-4)**, 107 – 136, doi:10.1016/0168-1923(91)90002-8.

Collatz, G. J., M. Ribas-Carbo, and J. A. Berry, 1992: Coupled photosynthesis-stomatal conductance model for leaves of C_4 plants. *Aust. J. Plant Physiology*, **19**, 519 – 538, doi:10.1071/PP9920519.

de Ferranti, J., 2013: 30-m topography dataset. [Available online at http://viewfinderpanoramas.org/].

de Franceschi, M. and D. Zardi, 2009: Study of wintertime high pollution episodes during the Brenner-South ALPNAP measurement campaign. *Meteorol. Atmos. Phys.*, **103**, 237–250, dOI 10.1007/s00703-008-0327-2.

de Franceschi, M., D. Zardi, M. Tagliazucca, and F. Tampieri, 2009: Analysis of second-order moments in surface layer turbulence in

an alpine valley. *Quarterly Journal of the Royal Meteorological Society*, **135 (644)**, 1750–1765, doi:10.1002/qj.506, URL http://dx.doi.org/10.1002/qj.506.

Dosio, A., S. Emeis, G. Graziani, W. Junkermann, and A. Levy, 2001: Assessing the meteorological conditions of a deep italian alpine valley system by means of a measuring campaign and simulations with two models during a summer smog episode. *Atmospheric Environment*, **35 (32)**, 5441 – 5454, doi:https://doi.org/10.1016/S1352-2310(01)00285-0, URL http://www.sciencedirect.com/science/article/pii/S1352231001002850.

Dudhia, J., 1989: Numerical study of convection observed during the winter monsoon experiment using a mesoscale two-dimensional model. *J. Atmos. Sci.*, **46**, 3077–3107, doi:10.1175/1520-0469(1989)046⟨3077:NSOCOD⟩2.0.CO;2.

Dudhia, J., 2011a: WRF Modeling System Overview. URL http://www.mmm.ucar.edu/wrf/users/tutorial/201107/WRF_Overview_Dudhia.ppt.pdf.

Dudhia, J., 2011b: WRF Physics Options. URL http://www.mmm.ucar.edu/wrf/users/tutorial/201107/WRF_Physics_Dudhia.ppt.pdf.

Dyer, A. J. and B. B. Hicks, 1970: Flux-gradient relationships in the constant flux layer. *Quart. J. Roy. Meteor. Soc.*, **96**, 715721.

EAA, 2009: EMEP/EEA air pollutant emission inventory guidebook 2009. Technical guidance to prepare national emission inventories. Tech. rep., European Environmental Agency - EEA.

EEA, 2006: 100-m landuse cover data. European Environment Agency, [Available online at http://land.copernicus.eu/pan-european/corine-land-cover/clc-2006/view].

EPA, 2005: Revision to the Guideline on Air Quality Models: Adoption of a Preferred General Purpose (Flat and Complex Terrain) Dispersion Model and Other Revisions - Appendix W. Tech. rep., U.S. Environmental Protection Agency, 45 pp.

Ferrero, E. and N. Colonna, 2006: Nonlocal treatment of the buoyancy-shear-driven boundary layer. *Journal of the Atmospheric Sciences*, **63 (10)**, 2653–2662, doi:10.1175/JAS3789.1, URL https://doi.org/10.1175/JAS3789.1, https://doi.org/10.1175/JAS3789.1.

Ferrero, E., S. Trini Castelli, and D. Anfossi, 2003: Turbulence fields for atmospheric dispersion models in horizontally non-homogeneous conditions. *Atmospheric Environment*, **37 (17)**, 2305 – 2315, doi:http://dx.doi.org/10.1016/S1352-2310(03)00179-1, URL http://www.sciencedirect.com/science/article/pii/S1352231003001791.

Ferrero, L., et al., 2014: Impact of black carbon aerosol over italian basin valleys: high-resolution measurements along vertical profiles, radiative forcing and heating rate. *Atmospheric Chemistry and Physics*, **14 (18)**, 9641–9664, doi:10.5194/acp-14-9641-2014, URL http://www.atmos-chem-phys.net/14/9641/2014/.

Giovannini, L., D. Zardi, and M. de Franceschi, 2011: Analysis of the urban thermal fingerprint of the city of Trento in the Alps. *J. Appl. Meteor. Climatol.*, **50**, 1145–1162, doi:10.1007/s00703-008-0327-2.

Giovannini, L., D. Zardi, M. de Franceschi, and F. Chen, 2014 a: Numerical simulations of boundary-layer processes and urban-induced alterations in an Alpine valley. *Int. J. Climatol.*, **34**, 1111–1131, doi:10.1002/joc.3750.

Gkatzoflias, D., C. Kouridis, L. Ntziachristos, and Z. Samaras, 2012: COPERT IV Computer programme to calculate emissions from

road transport. Tech. rep., European Environmental Agency - EEA, 71 pp.

Grell, G. A. and D. Dèvènyi, 2002: A generalized approach to parameterizing convection combining ensemble and data assimilation techniques. *Geoph. Research Letters*, **29**, 38–1–38–4, doi: 10.1029/2002GL015311.

Hall, D. K. and G. A. Riggs, 2016: MODIS/Terra Snow Cover Daily L3 Global 500m Grid, Version 6.[February 2006, Europe]. Boulder, Colorado USA. NASA National Snow and Ice Data Center Distributed Active Archive Center, doi: http://dx.doi.org/10.5067/MODIS/MOD10A1.006. [03/2017].

Hanna, S. R., 1968: A method of estimating vertical eddy transport in the planetary boundary layer using characteristics of the vertical velocity spectrum. *Journal of the Atmospheric Sciences*, **25 (6)**, 1026–1033, doi:10.1175/1520-0469(1968)025⟨1026:AMOEVE⟩2.0.CO;2, URL https://doi.org/10.1175/1520-0469(1968)025<1026:AMOEVE>2.0.CO;2, https://doi.org/10.1175/1520-0469(1968)025<1026:AMOEVE>2.0.CO;2.

Hanna, S. R., 1981: Lagrangian and eulerian time-scale relations in the daytime boundary layer. *Journal of Applied Meteorology*, **20 (3)**, 242–249, doi:10.1175/1520-0450(1981)020⟨0242:LAETSR⟩2.0.CO;2, URL https://doi.org/10.1175/1520-0450(1981)020<0242:LAETSR>2.0.CO;2, https://doi.org/10.1175/1520-0450(1981)020<0242:LAETSR>2.0.CO;2.

Hanna, S. R., 1982: *Applications in Air Pollution Modeling*, 275–310. Springer Netherlands, Dordrecht, doi:10.1007/978-94-010-9112-1_7, URL https://doi.org/10.1007/978-94-010-9112-1_7.

Hanna, S. R. and J. Chang, 2012: *Setting Acceptance Criteria for Air Quality Models*, 479–484. Springer Netherlands, Dordrecht, doi:

10.1007/978-94-007-1359-8_80, URL https://doi.org/10.1007/978-94-007-1359-8_80.

Hanna, S. R. and R. J. Paine, 1989: Hybrid plume dispersion model (hpdm) development and evaluation. *Journal of Applied Meteorology*, **28 (3)**, 206–224, doi:10.1175/1520-0450(1989)028⟨0206:HPDMDA⟩2.0.CO;2, URL https://doi.org/10.1175/1520-0450(1989)028<0206:HPDMDA>2.0.CO;2, https://doi.org/10.1175/1520-0450(1989)028<0206:HPDMDA>2.0.CO;2.

Hanna, S. R., J. Weil, and R. Paine, 1986: Plume model development and evaluation. Tech. Rep. Report Number D034-500, Electric Power Research Institute, Palo Alto, CA.

Heimann, D., M. de Franceschi, S. Emeis, P. Lercher, and P. S. (Eds.), 2007: Air Pollution, Traffic Noise and Related Health Effects in the Alpine Space - A Guide for Authorities and Consulters. ALPNAP comprehensive report. Tech. rep., Università degli Studi di Trento, Dipartimento di Ingegneria Civile e Ambientale, Trento, Italy.

Hicks, B. B., 1985: Behavior of turbulence statistics in the convective boundary layer. *J. Clim. and Appl. Meteor.*, **24**, 607–614.

Hong, S.-Y., J. Dudhia, and S.-H. Chen, 2004: A revised approach to ice microphysical processes for the bulk parameterization of clouds and precipitation. *Mon. Wea. Rev.*, **132**, 103–120, doi:10.1175/1520-0493(2004)132⟨0103:ARATIM⟩2.0.CO;2.

Hong, S.-Y., Y. Noh, and J. Dudhia, 2006: A new vertical diffusion package with an explicit treatment of entrainment processes. *Mon. Wea. Rev.*, **134 (9)**, 2318–2341, doi:10.1175/MWR3199.1, URL https://doi.org/10.1175/MWR3199.1, https://doi.org/10.1175/MWR3199.1.

Iacono, M. J., J. S. Delamere, E. J. Mlawer, M. W. Shephard, S. A. Clough, and W. D. Collins, 2008: Radiative forcing by long-lived greenhouse gases: Calculations with the aer radiative transfer models. *Journal of Geophysical Research: Atmospheres*, **113 (D13)**, n/a–n/a, doi:10.1029/2008JD009944, URL `http://dx.doi.org/10.1029/2008JD009944`, d13103.

Irwin, J. S., 1979: A theoretical variation of the wind profile power-law exponent as a function of surface roughness and stability. *Atmospheric Environment (1967)*, **13 (1)**, 191–194, doi:http://dx.doi.org/10.1016/0004-6981(79)90260-9, URL `http://www.sciencedirect.com/science/article/pii/0004698179902609`.

J. Boussinesq, 1877: Essai sur la theorie des eaux courants. Tech. rep., Mem. Pres. Par div. Savants a lAcademie Sci., Paris, 23, 1680 pp.

Janjic, Z. I., 1996: The surface layer in the NCEP Eta Model. *Progress in Photosynthesis Research: Volume 4 Proceedings of the Eleventh Conference on Numerical Weather Prediction, Norfolk, VA, 1923 August; Amer. Meteor. Soc., Boston, MA*, J. Biggins, Ed., Springer Netherlands, 354355.

Jimnez, P. A., J. Dudhia, J. F. Gonzlez-Rouco, J. Navarro, J. P. Montvez, and E. Garca-Bustamante, 2012: A revised scheme for the wrf surface layer formulation. *Monthly Weather Review*, **140 (3)**, 898–918, doi:10.1175/MWR-D-11-00056.1, URL `https://doi.org/10.1175/MWR-D-11-00056.1`, `https://doi.org/10.1175/MWR-D-11-00056.1`.

Jordan, R., 1991: A one-dimensional temperature model for a snow cover. Spec. rep., Cold Reg. Res. and Eng. Lab., U.S. Army Corps of Eng., 61 pp., Hanover, N. H.

Kaimal, J. C., J. C. Wyngaard, D. A. Haugen, O. R. Cot, Y. Izumi, S. J. Caughey, and C. J. Readings, 1976: Turbulence structure in the con-

vective boundary layer. *Journal of the Atmospheric Sciences*, **33 (11)**, 2152–2169, doi:10.1175/1520-0469(1976)033⟨2152:TSITCB⟩2.0.CO;2, URL https://doi.org/10.1175/1520-0469(1976)033<2152:TSITCB>2.0.CO;2, https://doi.org/10.1175/1520-0469(1976)033<2152:TSITCB>2.0.CO;2.

Khurshudyan, L. H., W. H. Snyder, I. V. Nekrasov, R. E. Lawson, R. S. Thompson, and F. A. Schiermeier, 1990: Flow and Dispersion of Pollutants within Two-Dimensional Valleys, Summary Report on Joint Soviet-American Study. Tech. rep., U. S. Environmental Protection Agency, No.-600/3-90/025 pp.

Kuribayashi, M., N. J. Noh, T. M. Saitoh, I. Tamagawa, Y. Wakazuki, and H. Muraoka, 2013: Comparison of snow water equivalent estimated in central Japan by high-resolution simulations using different land-surface models. *Scientific Online Letters on the Atmosphere*, **9**, 148–152, doi:10.2151/sola.2013-033.

Lin, Y.-L., R. D. Farley, and H. D. Orville, 1983: Bulk parameterization of the snow field in a cloud model. *Journal of Climate and Applied Meteorology*, **22 (6)**, 1065–1092, doi:10.1175/1520-0450(1983)022⟨1065:BPOTSF⟩2.0.CO;2, URL https://doi.org/10.1175/1520-0450(1983)022<1065:BPOTSF>2.0.CO;2, https://doi.org/10.1175/1520-0450(1983)022<1065:BPOTSF>2.0.CO;2.

Liu, M. and M. A. Yocke, 1980: Siting of wind turbine generators in complex terrain. *J. Energy*, **4**, 10–16.

Livneh, B., Y. Xia, K. E. Mitchell, M. B. Ek, and D. P. Lettenmaier, 2010: Noah LSM snow model diagnostics and enhancements. *J. Hydrometeor.*, **11**, 721–738.

Mahrt, L., 1982: Momentum balance of gravity flows. *Journal of the Atmospheric Sciences*, **39 (12)**, 2701–2711, doi:10.1175/1520-0469(1982)

039⟨2701:MBOGF⟩2.0.CO;2, URL https://doi.org/10.1175/1520-0469(1982)039<2701:MBOGF>2.0.CO;2, https://doi.org/10.1175/1520-0469(1982)039<2701:MBOGF>2.0.CO;2.

Martin, D., K. F. Petersson, and D. E. Shallcross, 2011: The use of cyclic perfluoroalkanes and sf6 in atmospheric dispersion experiments. *Quarterly Journal of the Royal Meteorological Society*, **137 (661)**, 2047–2063, doi:10.1002/qj.881, URL http://dx.doi.org/10.1002/qj.881.

Mellor, G. L. and T. Yamada, 1982: Development of a turbulence closure model for geophysical fluid problems. *Reviews of Geophysics*, **20 (4)**, 851–875, doi:10.1029/RG020i004p00851, URL http://dx.doi.org/10.1029/RG020i004p00851.

Meloysund, V., B. Leira, K. V. Hoiseth, and K. R. Liso, 2007: Predicting snow density using meteorological data. *Meteor. Appl.*, **14 (4)**, 413–423, doi:10.1002/met.40.

Mlawer, E. J., S. J. Taubman, P. D. Brown, M. J. Iacono, and S. A. Clough, 1997: Radiative transfer for inhomogeneous atmospheres: RRTM, a validated correlated-k model for the longwave. *J. Geophys. Research*, **102 (D14)**, 16 663–16 682, doi:10.1029/97JD00237.

Monin, A. and A. Obukhov, 1954: Basic laws of turbulent mixing in the surface layer of the atmosphere. *Contrib. Geophys. Inst. Acad. Sci., USSR*, **151**, 163187.

Nakanishi, M., 2001: Improvement of the mellor–yamada turbulence closure model based on large-eddy simulation data. *Boundary-Layer Meteorology*, **99 (3)**, 349–378, doi:10.1023/A:1018915827400, URL https://doi.org/10.1023/A:1018915827400.

Nakanishi, M. and H. Niino, 2004: An improved mellor–yamada level-3 model with condensation physics: Its design and veri-

fication. *Boundary-Layer Meteorology*, **112 (1)**, 1–31, doi:10.1023/B:BOUN.0000020164.04146.98, URL https://doi.org/10.1023/B:BOUN.0000020164.04146.98.

Nieuwstadt, F., 1984: Some aspects of the turbulent stable boundary layer. *Bound. Layer Meteor.*, **30**, 31–55.

Niu, G.-Y. and Z.-L. Yang, 2006: Effects of frozen soil on snowmelt runoff and soil water storage at a continental scale. *J. Hydrometeor.*, **7**, 937–952, doi:10.1175/JHM538.1.

Niu, G.-Y. and Z.-L. Yang, 2007: An observation-based formulation of snow cover fraction and its evaluation over large North American river basins. *J. Geophys. Res.*, **112 (D21)**, doi:10.1029/2007JD008674, d21101.

Niu, G.-Y., Z.-L. Yang, R. E. Dickinson, L. E. Gulden, and H. Su, 2007: Development of a simple groundwater model for use in climate models and evaluation with gravity recovery and climate experiment data. *J. Geophys. Res.*, **112 (D7)**, doi:10.1029/2006JD007522, d07103.

Niu, G. Y., Z.-L. Yang, K. E. Mitchell, F. Chen, M. B. Ek, and M. B. et al., 2011: The community Noah land surface model with multiparameterization options (Noah_MP): 1. Model description and evaluation with local scale measurements. *J. Geophys. Res.*, **116 (D12)**.

O'Brien, J., 1970: A note on the vertical structure of the eddy exchange coefficient in the planetary boundary layer. *J. Atmos. Sci.*, **27**, 1213–1215.

Panofsky, H., H. Tennekes, D. Lenschow, and J. Wyngaard, 1977: The characteristics of turbulent velocity components in the surface layer under convective conditions. *Bound. Layer Meteor.*, **11**, 355–361.

Pasquill, F. and F. B. Smith, 1983: *Atmospheric Diffusion (3rd Edition)*. John Wiley & Sons Chichester, 437 pp.

Paulson, C. A., 1970: The mathematical representation of wind speed and temperature profiles in the unstable atmospheric surface layer. *Journal of Applied Meteorology*, **9 (6)**, 857–861, doi:10.1175/1520-0450(1970)009⟨0857:TMROWS⟩2.0.CO;2, URL https://doi.org/10.1175/1520-0450(1970)009<0857:TMROWS>2.0.CO;2, https://doi.org/10.1175/1520-0450(1970)009<0857:TMROWS>2.0.CO;2.

Pomeroy, J. W. and E. Brun, 2001: Physical properties of snow. *Snow Ecology: an Interdisciplinary Examination of Snow-covered Ecosystems*, H. G. Jones, J. W. Pomeroy, D. A. Walker, and R. Hoham, Eds., Cambridge University Press, 45–118.

Ragazzi, M., W. Tirler, G. Angelucci, D. Zardi, and E. C. Rada, 2013: Management of atmospheric pollutants from waste incineration processes: the case of Bozen. *Waste Management & Research*, **31 (3)**, 235–240, doi:10.1177/0734242X12472707, URL http://dx.doi.org/10.1177/0734242X12472707, pMID: 23363737, http://dx.doi.org/10.1177/0734242X12472707.

Sakaguchi, K. and X. Zeng, 2009: Effects of soil wetness, plant litter, and under-canopy atmospheric stability on ground evaporation in the Community Land Model (CLM3.5). *J. Geophys. Res.*, **114 (D1)**, doi:10.1029/2008JD010834, d01107.

Scire, J., F. Robe, M. Fernau, and R. Yamartino, 2000a: A Users Guide for the CALMET Meteorological Model. Tech. rep., Earth Tech, Inc, Concord, MA.

Scire, J., D. Strimaitis, and R. Yamartino, 2000b: A Users Guide for the CALPUFF Dispersion Model. Tech. rep., Earth Tech, Inc, Concord, MA.

Sellers, P. J., et al., 1996: A Revised Land Surface Parameterization (SiB2) for Atmospheric GCMS. Part I: Model Formulation. *JCLI*, **9**, 676–705, doi:10.1175/1520-0442(1996)009⟨0676:ARLSPF⟩2.0.CO;2.

Skamarock, W. C., J. B. Klemp, J. Dudhia, D. O. Gill, D. M. Barker, M. G. Duda, X.-Y. Huang, and W. W. et al., 2008: A description of the advanced research WRF version 3. Tech. rep., NCAR Technical Note TN-475+STR, 125.

Steyn, D., S. F. J. D. Wekker, M. Kossmann, and A. Martilli, 2013: *Boundary Layers and Air Quality in Mountainous Terrain*, 261–289. Springer Netherlands, Dordrecht, doi:10.1007/978-94-007-4098-3_5, URL https://doi.org/10.1007/978-94-007-4098-3_5.

Stull, R. B., 1984: Transilient turbulence theory. part i: The concept of eddy-mixing across finite distances. *Journal of the Atmospheric Sciences*, **41 (23)**, 3351–3367, doi:10.1175/1520-0469(1984)041⟨3351:TTTPIT⟩2.0.CO;2, URL https://doi.org/10.1175/1520-0469(1984)041<3351:TTTPIT>2.0.CO;2, https://doi.org/10.1175/1520-0469(1984)041<3351:TTTPIT>2.0.CO;2.

Stull, R. B., 1988: *Turbulence Closure Techniques*, 197–250. Springer Netherlands, Dordrecht, doi:10.1007/978-94-009-3027-8_6, URL https://doi.org/10.1007/978-94-009-3027-8_6.

Su, H., Z.-L. Yang, G.-Y. Niu, and R. Dickinson, 2008: Enhancing the estimation of continental-scale snow water equivalent by assimilating MODIS snow cover with the ensemble Kalman filter. *J. Geophys. Res.*, **113 (D8)**, doi:10.1029/2007JD009232, d08120.

Szintai, B., P. Kaufmann, and M. W. Rotach, 2010: Simulation of pollutant transport in complex terrain with a numerical weather prediction–particle dispersion model combination. *Boundary-Layer*

Meteorology, **137 (3)**, 373–396, doi:10.1007/s10546-010-9541-9, URL https://doi.org/10.1007/s10546-010-9541-9.

Taylor, K. E., 2001: Summarizing multiple aspects of model performance in a single diagram. *Journal of Geophysical Research: Atmospheres*, **106 (D7)**, 7183–7192, doi:10.1029/2000JD900719, URL http://dx.doi.org/10.1029/2000JD900719.

Tedesco, M., R. Kelly, J. L. Foster, and A. T. Chang, 2004: AMSR-E/Aqua Daily L3 Global Snow Water Equivalent EASE-Grids, Version 2. [2010.03.02]. Tech. rep., Boulder, Colorado USA. NASA National Snow and Ice Data Center Distributed Active Archive Center.[2017.07.31]. doi:10.5067/AMSR-E/AE_DYSNO.002.

Thomson, D. J., 1987: Criteria for the selection of stochastic models of particle trajectories in turbulent flows. *Journal of Fluid Mechanics*, **180**, 529556, doi:10.1017/S0022112087001940.

Tinarelli, G., D. Anfossi, S. Trini Castelli, M. Bider, and E. Ferrero, 2000: *A New High Performance Version of the Lagrangian Particle Dispersion Model Spray, Some Case Studies*, 499–507. Springer US, Boston, MA, doi:10.1007/978-1-4615-4153-0_51, URL https://doi.org/10.1007/978-1-4615-4153-0_51.

Tomasi, E., L. Giovannini, D. Zardi, and M. de Franceschi, 2017: Optimization of noah and noah_mp wrf land surface schemes in snow-melting conditions over complex terrain. *Monthly Weather Review*, **145 (12)**, 4727–4745, doi:10.1175/MWR-D-16-0408.1, URL https://doi.org/10.1175/MWR-D-16-0408.1, https://doi.org/10.1175/MWR-D-16-0408.1.

Trini Castelli, S., E. Ferrero, and D. Anfossi, 2001: Turbulence closures in neutral boundary layer over complex terrain. *Boundary-Layer Meteorology*, **100 (3)**, 405–419, doi:10.1023/A:1019208518127, URL https://doi.org/10.1023/A:1019208518127.

Trini Castelli, S., E. Ferrero, D. Anfossi, and R. Ying, 1999: Comparison of turbulence closure models over a schematic valley in a neutral boundary layer. *Proceeding of the 13th symposium on boundary layers and turbulence79th AMS Annual Meeting*, 601–604.

Vandop, H., et al., 1998: Etex: A european tracer experiment; observations, dispersion modelling and emergency response. *Atmospheric Environment*, **32 (24)**, 4089 – 4094, doi:https://doi.org/10.1016/S1352-2310(98)00248-9, URL `http://www.sciencedirect.com/science/article/pii/S1352231098002489`.

Verseghy, D. L., 1991: ClassA Canadian land surface scheme for GCMS. I. Soil model. *Int. J. Climatol.*, **11 (2)**, 111–133, doi:10.1002/joc.3370110202.

Wang, W., C. Bruyére, M. Duda, J. Dudhia, D. Gill, and M. K. et al., 2013: ARW Version 3 modeling system user's guide. Tech. rep., National Center for Atmospheric Research's Mesoscale and Microscale Meteorology Division.

Webb, E. K., 1970: Profile relationships: The log-linear range, and extension to strong stability. *Quart. J. Roy. Meteor. Soc.*, **96**, 6790.

Whiteman, C. D., 2000: *Mountain meteorology: fundamentals and applications*. Oxford University.

Wyngaard, J. C., 2010: *Turbulence in the Atmosphere*. Cambridge University Press, Cambridge, UK.

Wyngaard, J. C. and O. R. Coté, 1974: The evolution of a convective planetary boundary layer — a higher-order-closure model study. *Boundary-Layer Meteorology*, **7 (3)**, 289–308, doi:10.1007/BF00240833, URL `https://doi.org/10.1007/BF00240833`.

Z. I. Janjic, 2002: Nonsingular Implementation of the MellorYamada

Level 2.5 Scheme in the NCEP Meso model. Tech. rep., NCEP Office Note, No. 437, 61 pp.

Zannetti, P., 2005: *Air Quality Modeling*. Air and Waste Management Association (A&WMA), USA.

Published Paper

Part of the present Doctoral Thesis has been published in the Monthly Weather Review of the American Meteorological Society. Following the AMS Copyright Policy in the following, the author reports (i) the AMS copyright notice and (ii) the final published PDF of the article.

AMS copyright notice

Optimization of Noah and Noah_MP WRF Land Surface Schemes in Snow-Melting Conditions over Complex Terrain

ELENA TOMASI, LORENZO GIOVANNINI, DINO ZARDI, AND MASSIMILIANO DE FRANCESCHI

Atmospheric Physics Group, Department of Civil, Environmental and Mechanical Engineering, University of Trento, Trento, Italy

(Manuscript received 25 October 2016, in final form 14 September 2017)

ABSTRACT

The paper presents the results of high-resolution simulations performed with the WRF Model, coupled with two different land surface schemes, Noah and Noah_MP, with the aim of accurately reproducing winter season meteorological conditions in a typical Alpine valley. Accordingly, model results are compared against data collected during an intensive field campaign performed in the Adige Valley, in the eastern Italian Alps. In particular, the ability of the model in reproducing the time evolution of 2-m temperature and of incoming and outgoing shortwave and longwave radiation is examined. The validation of model results highlights that, in this context, WRF reproduces rather poorly near-surface temperature over snow-covered terrain, with an evident underestimation, during both daytime and nighttime. Furthermore it fails to capture specific atmospheric processes, such as the temporal evolution of the ground-based thermal inversion. The main cause of these errors lies in the miscalculation of the mean gridcell albedo, resulting in an inaccurate estimate of the reflected solar radiation calculated by both Noah and Noah_MP. Therefore, modifications to the initialization, to the land-use classification, and to both land surface models are performed to improve model results, by intervening in the calculation of the albedo, of the snow cover, and of the surface temperature. Qualitative and quantitative analyses show that, after these changes, a significant improvement in the comparability between model results and observations is achieved. In particular, outgoing shortwave radiation is lowered, 2-m temperature maxima increased accordingly, and ground-based thermal inversions are better captured.

1. Introduction

Accurate predictions of meteorological variables over complex terrain are a particularly challenging task for numerical weather models. On one hand, the resolution of the numerical simulation has to be sufficiently fine to adequately describe relevant topographic features. Yet original topography datasets often have to be smoothed, to prevent numerical instability problems when using terrain-following coordinates (Zängl 2012). On the other hand, complex terrain strongly influences meteorological fields, especially in the lowest layers, where energy and mass fluxes between the ground and the atmosphere regulate temperature and wind regimes within the boundary layer. This requires numerical weather prediction models to include appropriate parameterizations, accurately reproducing small-scale processes and land surface interactions with the atmosphere. In particular, calculations of the energy and mass transfer at the ground interface are performed by land surface models (LSMs), which provide bottom boundary conditions to the atmospheric model. Many different LSMs have been developed, refined, and tested over the past decades (Oleson et al. 2013; Xue et al. 1991; Noilhan and Planton 1989), but great uncertainty still affects their results (Dirmeyer et al. 2006; Zhang et al. 2013). Particularly challenging for LSMs is the calculation of surface fluxes over snow-covered surfaces. Indeed, snowpack strongly alters energy and mass balances, influencing surface heat fluxes, ground temperature, runoff, and soil moisture. Several studies (e.g., Barlage et al. 2010; Jin et al. 2010) highlighted that LSMs often poorly simulate snow water equivalent and its evolution in time, and that this can directly influence atmospheric feedbacks (e.g., Qu and Hall 2006; Jin and Miller 2007). For this reason, it is essential to keep evaluating and improving LSMs performance with particular care for the snow cover treatment.

The present work focuses on two of the LSMs available within the Weather Research and Forecasting (WRF) Model (Skamarock et al. 2008): the Noah (Chen and Dudhia 2001; Chen et al. 1996; Ek et al. 2003) and the Noah_MP (Niu et al. 2011; Yang et al. 2011) schemes.

Corresponding author: Elena Tomasi, elena.tomasi@unitn.it

DOI: 10.1175/MWR-D-16-0408.1

The Noah model represents probably the most widely used land surface scheme among the WRF community, being applied in the research field and in different weather and regional climate models [e.g., the operational North American Mesoscale Forecast System (NAM) run by the National Centers for Environmental Prediction (NCEP)]. It can be considered the combination of different physical approaches (Chen and Dudhia 2001), each describing one of the processes influencing energy and mass fluxes at the ground. The Mahrt and Ek (1984) approach is used for potential evapotranspiration, and the Simple Water Balance method by Schaake et al. (1996) is applied for the runoff calculation. In addition, the multilayer soil model by Mahrt and Pan (1984), the simple canopy model by Pan and Mahrt (1987), extended by Chen et al. (1996), and a single layer snowpack scheme (Koren et al. 1999; Livneh et al. 2010) are implemented in the Noah LSM.

The Noah_MP model represents an evolutional version of Noah LSM, including structural changes and multiparameterization (MP) options in order to improve model performance, allowing physically based ensembles and selection of optimal scheme combinations (Niu et al. 2011). This approach introduces a great variety of options in the application of the model, as the user is given nearly 5000 possible combinations (Yang et al. 2011) of different schemes, but even in its standard version (i.e., with a fixed set of parameterizations) Noah_MP represents an augmented version of Noah LSM. In particular, vegetated and bare portions of cells are treated separately, snow cover is described with a three-layer model, the vegetation canopy is dynamically treated, and a simple groundwater model is introduced.

The aim of this paper is to test and improve these LSMs' performance over complex terrain, in snow-melting conditions. To achieve this objective, we compare results of simulations run with WRF coupled with both LSMs, testing their abilities in reproducing 2-m temperature as well as incoming and outgoing surface short- and longwave radiation, over complex terrain and at a local scale. Simulations are conducted in early February 2006, when melting snow was covering both the valley floor and the sidewalls at the target site, in the Adige Valley. This situation represents a challenging task for the LSMs, which are tested in a transitional phase between different ground thermal regimes, when the proper description of snowpack depletion is essential. Indeed, the ability of Noah and Noah_MP to reproduce snow-related variables has already been compared in Niu et al. (2011), but the assessment was performed on short-grass-covered sites only. Nevertheless, land-use type is a relevant parameter, as LSMs are usually very sensitive to this. In this paper, comparisons are made over apple orchard and broadleaf forest land cover, where Noah and Noah_MP differences are expected to be maximized, because of the differences in the two LSMs in separating vegetated and bare ground and in treating the vegetation canopy. Moreover, after assessing the abilities and deficiencies of the standard model, some modifications to both WRF initialization and LSMs are applied, and their effects on the results are evaluated. Snow cover, land use, and snow-covered surface albedo are found to be relevant variables in the calculation of 2-m temperature, affecting the model's ability to reproduce peculiar phenomena over complex terrain, such as nighttime ground-based thermal inversions (i.e., cold air pooling).

The paper is organized as follows. Section 2 briefly introduces the area of interest, the experimental dataset used for the validation process, and the period of study. Section 3 describes the methodology and the modeling setup of the presented simulations, focusing on the modifications applied. In section 4 numerical results are presented and compared with observations for the standard and modified model setup: a qualitative evaluation is conducted, together with a statistical analysis of the model performance. A discussion on the effects of the modifications implemented is presented in section 5. Finally, section 6 contains a summary of the results and some conclusions.

2. Study area and experimental dataset

a. *Study area*

The target area for the present work is the lower part of the Adige Valley, in the eastern Italian Alps (Fig. 1a). The portion of the valley analyzed in this paper is about 45 km long, 2 km wide, and mainly north–south oriented. The valley floor elevation ranges between 150 m above mean sea level (MSL) in the southern part, up to 200 m MSL in the northern part, and the surrounding mountain peaks range between 1500 and 2000 m MSL. The sidewalls are mostly very steep, especially in the northwestern side of the valley. The study area includes the cities of Trento and Rovereto and other minor urbanized centers, including the town of Aldeno, where the intensive field campaign, whose measurements are used in this work, was performed (Fig. 1b). Except for these urban areas, the valley floor is mainly devoted to agriculture (apple orchards), while most of the sidewalls are covered with deciduous broadleaf and evergreen needleleaf forests.

b. *Experimental dataset*

In the present work two different datasets are used. The first dataset comes from an intensive measurement campaign carried out in 2006, near the town of Aldeno, Italy, within the Monitoring and Minimisation

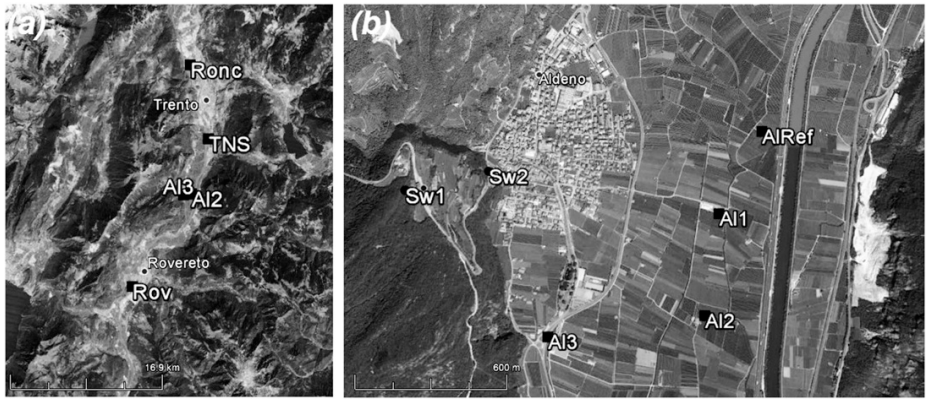

FIG. 1. Topography of the lower part of the Adige Valley: (a) study domain with the cities of Trento and Rovereto, the town of Aldeno, and the permanent weather stations used in this paper; (b) zoom-in on the town of Aldeno with the measurement stations of the ALPNAP project (squares for valley floor stations and dots for sidewall stations; background map from Google Earth).

of Traffic-Induced Noise and Air Pollution Along Major Alpine Transport Routes project (ALPNAP; Heimann et al. 2007): a complete description of the ALPNAP field instrumentation can be found in de Franceschi and Zardi (2009) (M. de Franceschi and D. Zardi 2006, unpublished manuscript). The present work utilizes observations from 1) a meteorological station and a four-channel net radiometer located on the valley floor (AlRef), which is used as the reference observation site to evaluate model results; 2) a conventional weather station on the valley floor (Al1); and 3) two portable thermohygrometers located on the western sidewall at different elevations (Sw1 and Sw2), respectively at 390 and 240 m MSL (Fig. 1b). The 2-m temperature measurements were recorded at all the observation sites, while incoming and outgoing shortwave (SW) and longwave (LW) radiation measurements are available only for the reference station (AlRef). This dataset provides a fairly complete view of the evolution of the principal meteorological variables on the valley floor close to Aldeno, including incoming and outgoing SW and LW radiation, which are of fundamental importance for the evaluation of land surface model results. Moreover, the thermohygrometers on the western valley sidewall allow the evaluation of the development of ground-based thermal inversions.

The second dataset comprises measurements from five permanent weather stations on the valley floor (Al2, Al3, Ronc, TNS, and Rov), operated by Meteotrentino (i.e., the local meteorological office), and by the Edmund Mach Foundation (2013, unpublished manuscript). Measurements of 2-m temperature from these weather stations are also used to validate model results farther away from the town of Aldeno, along the Adige Valley floor. All data used in the present work are hourly averages.

c. *Study period*

For the purpose of the present work, 4 days were selected out of the ALPNAP measurement campaign in Aldeno (viz., 12–15 February 2006) for their interesting meteorological conditions. First of all a transition from clear sky to cloudy conditions, occurred between the third and the last day of simulation; second, a ground-based thermal inversion developed during nighttime, breaking up in the central hours of the day, with strong temperature differences between the valley floor and the sidewalls; third, 15-day-old snow was covering the ground, after a snowfall at the end of January 2006.

3. Methodology and model setup

In the present paper, the results of four different simulations are presented. Simulations 1 and 2 aim at testing the standard versions of the Noah and of the Noah_MP LSMs, respectively, released with WRF 3.8.1. Results of these simulations are used to evaluate the performance of the standard version of the model when applied at a high resolution, as it might be done by a common user. After evaluating the results of the standard simulations, in order to improve model performance, some corrections were implemented to the initialization of the model, to the land-use classification and to both the LSMs. Simulations 3 and 4 were performed with all these changes, using the modified versions of Noah and Noah_MP, respectively.

Except for the use of the two different LSMs, all the simulations share the same settings as to domain

TABLE 1. List of nested domain characteristics.

Nest No.	Horizontal grid space (km)	Dimensions (km × km)	Time resolution (s)
1	10.8	1080 × 1080	5
2	3.6	327.6 × 327.6	1.6
3	1.2	109.2 × 120	0.55
4	0.4	36.4 × 43.6	0.19

dimensions, horizontal and vertical grid spacing, meteorological boundary/initial conditions, static input data, and all the physics options. In the following sections the basic settings regarding all the simulations are presented and the modifications implemented in simulations 3 and 4 are described.

a. Model setup

The horizontal domain used for the simulations consists of four two-way nested domains, with grid spacing ranging from 10.8 km in the external domain to 400 m in the innermost, with a 3:1 ratio between successive nests, while 40 vertical levels are used for the vertical discretization (see Table 1 and Fig. 2 for details). Simulations cover a period of 108 h, starting at 1200 UTC (LST = UTC + 1 h) 11 February 2006 and ending at 0000 UTC 16 February 2006. The first 12 h, being influenced by the model initialization, are not considered for the comparison with observations.

The initial and boundary conditions are supplied by the 6-hourly NCEP Final Operational Global Analysis (FNL) data on 1° grids. Topography and land-use data in the three external domains come from the default WRF datasets, with a resolution of 1 km. The Moderate Resolution Imaging Spectroradiometer (MODIS)-based dataset is used for land cover, with the IGBP Land Cover Type Classification. Nevertheless, these data are not sufficient in order to properly describe the orographic features and the land use in the inner domain; therefore, customized static data with a very high resolution were provided. The adopted topography dataset has an original spatial resolution of 30 m (de Ferranti 2013). One smoothing pass with the 1–2–1 smoothing filter was used to prevent numerical instability. The topography of the simulation domains is shown in Fig. 2. Similarly, the land use also needs to be described with a high resolution in order to obtain a realistic characterization of meteorological phenomena at local scale in the innermost domain. For this reason, the Corine Land Cover (CLC) dataset (European Environment Agency 2006) was adopted for the present simulations. This 100-m resolution dataset was reclassified into the standard IGBP classes, as shown in Giovannini et al. (2014a), in order to match the WRF land-use tables.

All the presented simulations share the same physics schemes, except for the land surface model. The microphysics scheme used is the WRF single-moment 3-class simple ice scheme (Hong et al. 2004), while the parameterization applied for the PBL is the Yonsei University (YSU) scheme (Hong et al. 2006). The Grell–Freitas cumulus scheme (Grell and Dévényi 2002) is employed for the two external domains, while no cumulus physics option is adopted for domains 3 and 4. The Dudhia scheme (Dudhia 1989) and RRTM scheme (Mlawer et al. 1997) are used for SW and LW radiation, respectively. Radiation schemes are called every 10 min and are applied taking into account both the effects of shading and slope angle in complex terrain.

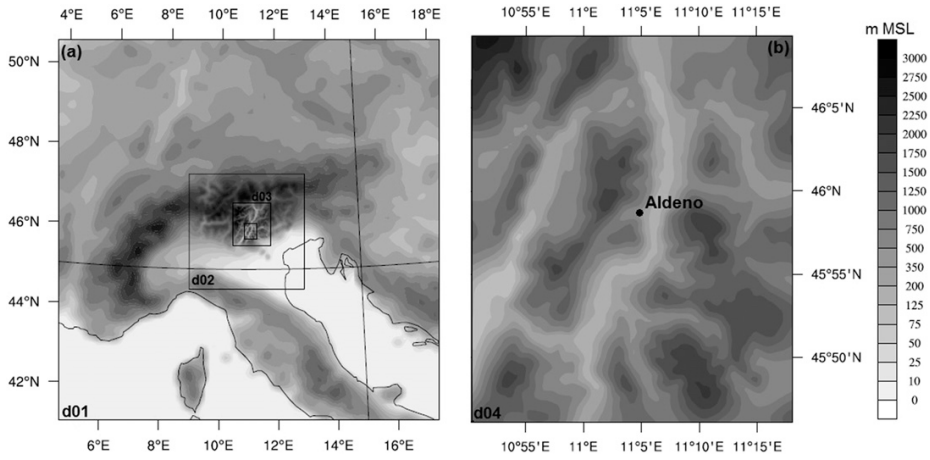

FIG. 2. Elevation contours of the simulation domains: (a) the four simulation domains and (b) the inner domain, centered on the town of Aldeno

Noah_MP LSM is always run with its default combination of internal parameterizations, which include the following: no dynamic vegetation, a Ball–Berry-type stomatal resistance scheme (Ball et al. 1987; Collatz et al. 1991, 1992; Sellers et al. 1996; Bonan 1996), the simple TOPMODEL by Niu et al. (2007) for runoff and groundwater treatment, the Niu and Yang (2006) approach for supercooled liquid water (or ice fraction) and frozen soil permeability, a two stream radiation transfer model applied to vegetated fraction, the CLASS option for ground snow surface albedo (Verseghy 1991), the relatively complex functional form of Jordan (1991) for partitioning precipitation into rainfall and snowfall, and the Sakaguchi and Zeng (2009) option for surface evaporation resistance. In addition, lower boundary conditions of long-term bottom (8-m depth) temperatures come from original Noah reference data, the snow/soil temperature time scheme is semi-implicit, the same soil moisture factor for stomatal resistance as Noah LSM is used, the applied glacier treatment includes phase change of ice and the Monin–Obukhov surface-layer drag coefficients are utilized.

Model output is written every 15 min for all four simulations; the corresponding hourly averages are compared with observations.

b. *Applied modifications*

1) MODIFICATIONS TO WRF INITIALIZATION

As will be shown in section 4, the results of simulations 1 and 2 highlighted that the standard procedure for the initialization of ground-covering snow in the WRF Preprocessing System (WPS) resulted in a consistent overestimation of the snow depth. Unfortunately during the ALPNAP field campaign no snow height measurements were collected, and none of the permanent weather stations along the valley floor performed snow height measurements. However, on the basis of photographs taken during the field campaign, showing the snow condition on the ground, an estimate of the snow depth and of the snow density was made and the overestimation of the model was pointed out. This overestimation was mainly due to assumptions in the WPS, and not simply to the reanalysis.

First, the WRF preprocessor code ungrib doubles the snow water equivalent (SWE) value when using NCEP reanalysis. However, compared to field observations, this operation produced an overestimation of the amount of snow on the ground of almost 20% in the present case study. Second, the snow density, through which ungrib calculates snow height from SWE data, is always assumed by the ungrib code to be that of fresh snow (i.e., 200 kg m^{-3}), no matter the season of the year or the date of the last snowfall. This assumption results in a significant overestimation of snow height. The combination of SWE and snow depth overestimations directly affects the snow fraction and the surface albedo calculated by the LSMs. After estimating both the SWE and the snow height on the ground according to field observations, the ungrib code was modified so that the calculated initial values reproduced a realistic snow condition at the simulation starting time. This was obtained by multiplying the SWE NCEP Global Forecast System (GFS) value by 1.7 times and fixing the 15-day-old snow density to 350 kg m^{-3} (Pomeroy and Brun 2001; Meloysund et al. 2007).

2) MODIFICATIONS TO THE LAND USE

According to the used MODIS-based dataset, the valley floor of the Adige valley is classified, apart from the urban areas, entirely as ''cropland,'' which includes all types of cultivation. However the land-use parameters of the cropland class seemed not appropriate for the present case. In fact, cropland land use refers to typical American crop farming (e.g., corn cultivation), which has little in common with apple orchards. In particular, when snow lies on the ground, the vegetated fraction of a domain cell changes enormously depending on the height of the crop, and is much higher if actual trees (such as apple trees) cover the terrain. For this reason, a new land-use class was introduced and described (in VEGPARM.TBL and MPTABLE.TBL at http://www2.mmm.ucar.edu/wrf/users/download/get_source.html) as a composition of parameters of the class labeled by IGBP as ''deciduous broadleaf forest'' and of the class labeled by the CLC as ''apple orchard'': specifically, deciduous broadleaf forest parameters are utilized with locally estimated values for the canopy top and bottom heights, for the minimum and maximum roughness lengths, and for the tree density (Table 2). In the Noah LSM, this modification in the land-use classification produced a significant decrease in the snow cover fraction (SCF) in the interested cells, with significant effects on the cell albedo and, as a consequence, on the 2-m temperature calculation. Moreover, an additional issue in describing the characteristics of land-use classes was identified in the Noah_MP parameters table. Specifically, the Noah_MP model calculates the SCF of a cell following the formulation of Niu and Yang (2007):

$$\mathrm{SCF} = \tanh\left[\frac{h_{\mathrm{sno}}}{2.5 z_{0_g} (\rho_{\mathrm{sno}}/\rho_{\mathrm{new}})^m}\right], \tag{1}$$

where h_{sno} is the snow depth, fresh snow density ρ_{new} (100 kg m^{-3}) scales the actual snow density ρ_{sno}, z_{0_g} is the ground roughness, and m is a melting factor determining

TABLE 2. Modified parameters in the "deciduous broadleaf forest" class in order to create a new ad hoc "orchard" land-use class.

Parameters	IGBP deciduous broadleaf forest	New orchard
Canopy top height	20	3
Canopy bottom height	11.5	1
Min roughness length	0.5	0.3
Max roughness length	0.5	0.3
Tree density	0.1	0.25

the curves in the melting season. According to Niu and Yang (2007) and Su et al. (2008), this factor is generally larger for larger scale and should be calibrated against observed snow cover fraction or surface albedo. In the Noah_MP scheme, as implemented in WRF 3.8.1, m is fixed to 2.5 for every land-use type. In this study, the factor m was adjusted to the value of 1, on the basis of snow cover fraction data coming from the MODIS/*Terra* Snow Cover Daily dataset (Hall and Riggs 2016), with a resolution of 500 m, and of previously suggested values (Niu and Yang 2007; Su et al. 2008). Equation (1) was indeed applied with the modified initial snow depth and density, and the value of m was calibrated so as to obtain the satellite-observed snow cover fraction. Specifically, with m equal to 2.5 the calculated SCF resulted in a value of about 0.2 in the reference station, while satellite observations suggest a value for SCF at around 0.9, which is reached with m equal to 1.

3) MODIFICATIONS TO THE NOAH LSM

The results of simulation 1 highlighted that the snow-covered cell albedo was systematically overestimated by the Noah LSM, which implements the procedure proposed by Livneh et al. (2010) for calculating snow albedo. However, a closer look at how Livneh's scheme is implemented within the WRF 3.8.1 code highlighted two inconsistencies. Following Livneh et al. (2010), the albedo of the snow-covered portion of the cell (α_{snow}) is calculated as

$$\alpha_{\text{snow}} = \alpha_{\text{max}} A^{t^B}, \tag{2}$$

where t is the age of the snow (in days), A and B are constant parametric coefficients (different for either the accumulation or melting season), and α_{max} is the maximum albedo of fresh snow, dependent on the land-use class. However, in WRF, the A and B coefficients are fixed to the values for the accumulation period only. In other words, the albedo of the part of the cell covered by snow decays over time at a fixed rate, independently of the season of the year. Moreover, t is always initialized to 0 days (i.e., with a fresh snow cover). Neither of these assumptions are appropriate for the present case, as the snow was progressively melting during the field campaign, and the last snowfall occurred 15 days before the beginning of the study period. Accordingly two changes in to the implementation of the Livneh formulation were introduced: the A and B parametric coefficients were fixed to the melting season values, and the time since the last snowfall, t, was set to 15 days. After these changes the surface albedo in the valley floor resulted in a value almost half of its previous one.

4) MODIFICATIONS TO THE NOAH_MP LSM

After the application of the modifications to the snow cover initialization and to the land-use classification, the Noah_MP model still showed some deficiencies in increasing the 2-m temperature during daytime. A detailed analysis of the Noah_MP LSM implementation within the WRF code revealed that the model intrinsically prevents the ground temperature from exceeding 0°C in the case of a snow depth greater than 5 cm, both under canopy and over bare soil. This assumption determines in turn a strong limitation to the increase of the 2-m temperature. However this restriction appears quite questionable, especially if applied over a thin snow layer, under sun-exposed canopy. It is in fact reasonable to assume that some patches of snow-free ground may emerge under trees when the snow depth is small. For this reason, the implemented limitation in Noah_MP LSM was removed for under-canopy snow depths smaller than 10 cm.

4. Results

In this section results from the standard simulations (1 and 2) and from the modified simulations (3 and 4) are compared and discussed in terms of incoming and outgoing short- and longwave radiation and 2-m temperature. Differences in the results between simulations 3 and 4 and the standard simulations are the effects of all the aforementioned modifications combined together. Section 5 discusses the effects of each modification on the results.

a. Radiation

Figure 3 shows incoming and outgoing shortwave radiation as observed during the 4-day study period and as reproduced by model simulations. Incoming SW radiation is well reproduced by all the simulations, which are also able to identify the cloudy-sky conditions during the fourth day. On the other hand, as expected due to the overestimation of the snow cover and of the snow albedo, the outgoing SW radiation is greatly overestimated by simulations 1 and 2, with higher errors for simulation 1. The proposed modifications significantly

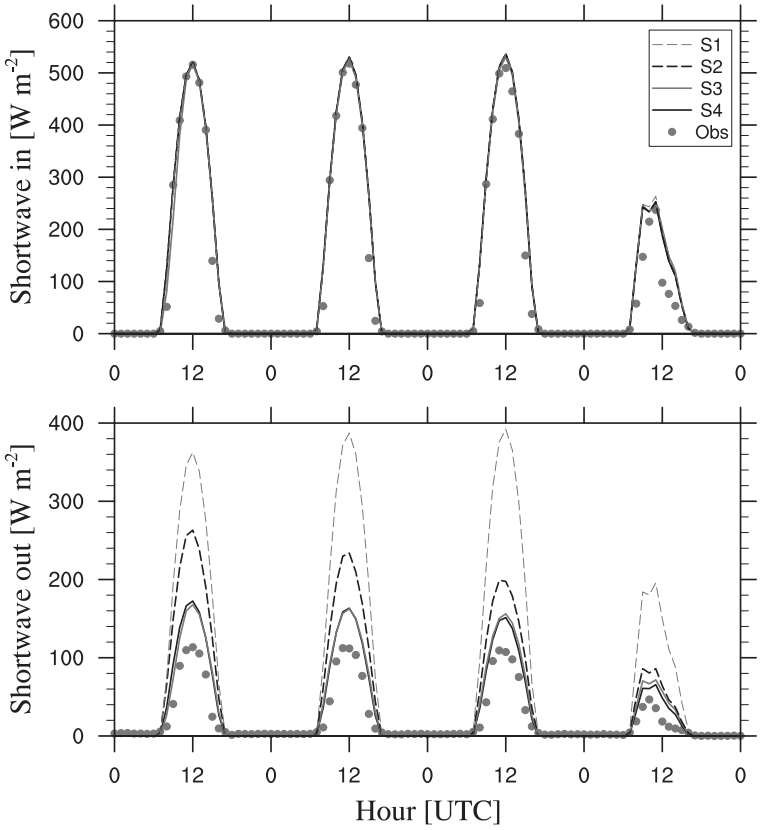

FIG. 3. Incoming and outgoing shortwave radiation observed and estimated by the four simulations (S1–S4) at the valley floor reference station (AlRef).

improve the agreement with observations, with similar results in both simulations 3 and 4. The outgoing SW radiation decreases, at midday peaks, by about $\sim$200 W m^{-2} in simulation 1 and by about $\sim$40–100 W m^{-2} in simulation 2, and the bias between calculated and observed values reduces to a maximum value of $\sim$50 W m^{-2} around midday.

Concerning longwave radiation, Fig. 4 shows that incoming and outgoing LW radiation are basically underestimated by the default WRF runs, especially by simulation 1. The modified simulations allow the incoming and outgoing LW radiation to be increased, reducing the differences with the observed values. It is interesting to notice that both the change of LSM (from Noah to Noah_MP) and the modifications introduced have an influence on the incoming LW radiation. Indeed, modifications of surface temperature in the model affect the temperature of the lower layers of the atmosphere. The incoming LW radiation thus changes, as it directly depends on the temperature of the emitting source. This effect is particularly noticeable in a narrow valley, where an increase in surface temperature on the valley slopes significantly affects radiation budgets in the whole valley atmosphere, increasing the downward LW radiation on the valley floor. Results in terms of incoming LW radiation are similar for simulations 3 and 4: midday peaks are quite well reproduced, whereas the incoming LW radiation is still considerably underestimated after sunset on the second and third days, when the model does not capture the observed increase in this variable. This effect is very likely caused by the formation of low-level clouds developing at night and dissipating after sunrise. This error, however, is not directly connected with the performance of the land surface scheme, whose assessment is the main focus of the present analysis. On the other hand, the model correctly reproduces the cloudy-sky conditions occurring on the fourth day, although without fully capturing its evolution in time, and in particular the gradual increase in incoming LW radiation.

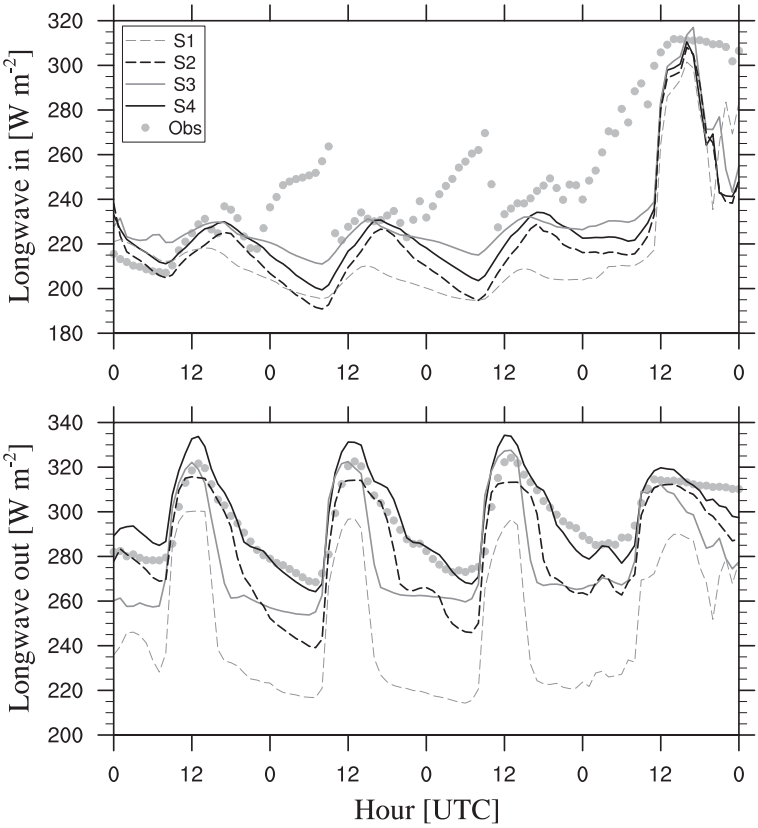

FIG. 4. Incoming and outgoing longwave radiation observed and estimated by the four simulations (S1–S4) at the valley floor reference station (AlRef).

The outgoing LW radiation is also better reproduced by the modified simulations. Simulation 3 properly identifies the daytime maxima. It still underestimates nighttime minima, but errors are strongly reduced with respect to simulation 1. Nevertheless, the rate of decrease in the outgoing LW radiation after sunset looks very different from observations: the model, in fact, instead of a gradual decrease in the variable, produces an almost instantaneous drop and a constant pattern during nighttime. Simulation 4, instead, better reproduces the decaying phase of outgoing LW radiation, whereas midday maximum values are slightly overestimated.

b. Temperature

Simulations 1 and 2 display evident underestimates of 2-m temperature, both during daytime and nighttime (Fig. 5). Higher errors affect simulation 1, especially for temperature minima. This means that, without any modification, in the present case Noah_MP performs better than Noah. Nevertheless, the proposed modifications result in an even better agreement with observations, due to an increase in the simulated temperature. In fact, decreasing the outgoing SW radiation allows the surface energy budget to have a significant extra rate of energy, with a consequent increase in the 2-m temperature. In simulation 3, maxima are still underestimated by ~3°–4°C, while nighttime temperatures are slightly overestimated. The net effect of the implemented modifications in simulation 3 is therefore a significant decrease in the daily thermal range. Simulation 4 exhibits the best agreement with observations. Nighttime minima are well captured by the model, with a maximum absolute error of ~1°C, while daytime maxima get closer to observations, but still underestimate real values by ~3°–4°C. Notice that on the last day the maximum temperature is well identified (especially by simulation 3), while the temperature drop after sunset is slightly overestimated. However this error follows the underestimation of the cloud cover and does not depend on the LSM, as can be

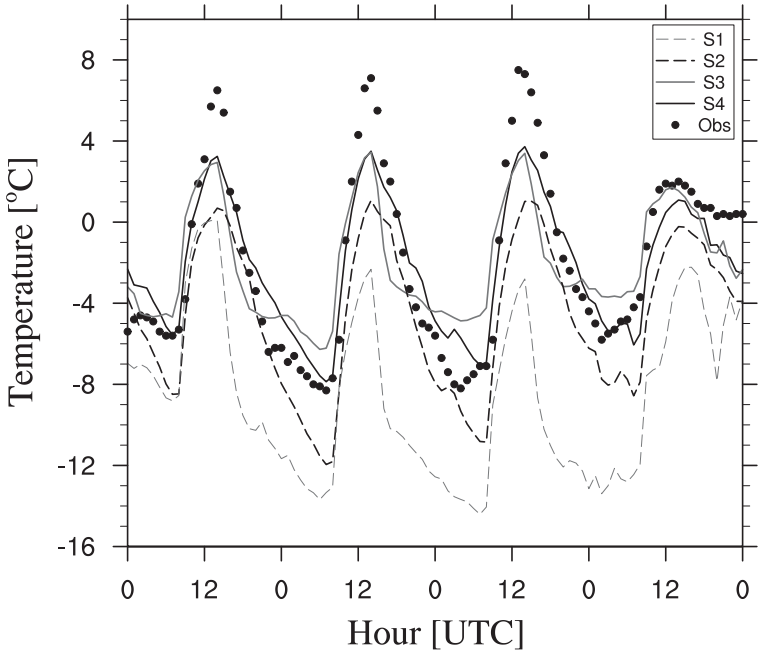

FIG. 5. The 2-m temperature observed and estimated by the four simulations (S1–S4) at the valley floor reference station (AlRef).

inferred also by the decrease in the incoming LW radiation in Fig. 4.

c. *Ground-based thermal inversion*

Some interesting considerations can be made regarding the model ability in reproducing the ground-based thermal inversion observed during the field campaign. Figures 6 and 7 show the 2-m temperature observed at the reference station of the valley floor (AlRef) and at the highest available station on the valley sidewalls (Sw1, 200 m above the valley floor). Data show a strong ground-based thermal inversion during nighttime, which systematically drops during daytime, due to the significant difference between the diurnal thermal range on the valley floor and on the sidewalls. Figure 6 shows that the inversion phenomenon is poorly reproduced when using Noah LSM, both before and after the modifications. While simulation 1 results in a too strong inversion during nighttime and barely identifies its decay during daytime, simulation 3 is able to increase daytime temperature more on the valley floor than along the sidewalls, but completely misses the thermal inversion during nighttime, except for a weak inversion on the second night. Conversely, WRF coupled with the Noah_MP scheme better reproduces the evolution of the thermal inversion, both in the standard and in the modified version (Fig. 7): simulation 2 can properly identify the nighttime inversion and slightly captures its morning breakup; the proposed modifications allow a stronger increase in the daytime 2-m temperature and therefore result in a more accurate reconstruction of the evolution in time of the thermal inversion.

d. *Statistical analysis*

To summarize the performance of the model in its different configurations, a statistical analysis on the results is presented. The analysis is performed comparing the model results against the observed time series of 2-m temperature, available at 9 different stations within the domain (see Fig. 1), and of downward and upward LW radiation and upward SW radiation at the reference station AlRef. Incoming SW radiation is not taken into account in this analysis as it is not affected by the modifications of the LSMs.

In the following, the values of different statistical indexes are discussed. First, the average model prediction errors are evaluated, analyzing the root-mean-square error (RMSE) and the bias (BIAS) values. Second, the mean-centered pattern errors are discussed by means of

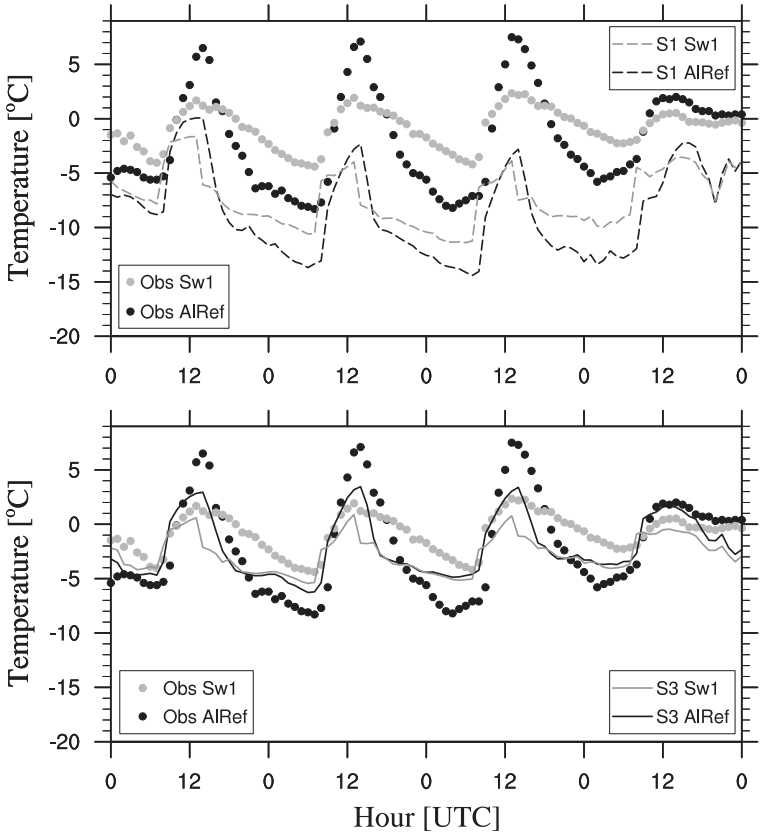

FIG. 6. Comparison of 2-m temperature at the valley floor and on the sidewall, observed and estimated with simulation 1 (standard Noah LSM) and simulation 3 (modified Noah LSM).

the Taylor diagrams (Taylor 2001). The Taylor diagram summarizes the performance of the model against the observations on the basis of the correlation coefficients R, the normalized centered root-mean-square differences E'_n, and the normalized standard deviations σ_{Mn}, which are second-order statistics calculated subtracting the average value from the time series. Equations (3)–(8) report the definition of each statistical index, where M_i and O_i are the modeled and observed values, N is the total number of values in the analyzed time series, and $\overline{O}$ and $\overline{M}$ are the observed and modeled averages, respectively:

$$\mathrm{RMSE} = \sqrt{\frac{1}{N}\sum_{i=1}^{N}(M_i - O_i)^2}, \tag{3}$$

$$\mathrm{BIAS} = \overline{O} - \overline{M}, \tag{4}$$

$$\sigma_O^2 = \frac{1}{N}\sum_{i=1}^{N}(O_i - \overline{O})^2, \tag{5}$$

$$R = \frac{\sum_{i=1}^{N}[(O_i - \overline{O})(M_i - \overline{M})]}{N\sigma_O\sigma_M}, \tag{6}$$

$$\sigma_{Mn}^2 = \frac{\sigma_M^2}{\sigma_O^2} = \frac{\sum_{i=1}^{N}(M_i - \overline{M})^2}{N\sigma_O^2}, \tag{7}$$

$$E_n'^2 = \frac{E'^2}{\sigma_O^2} = \frac{\sum_{i=1}^{N}[(O_i - \overline{O}) - (M_i - \overline{M})]^2}{N\sigma_O^2}. \tag{8}$$

Results from the comparison between measured and calculated 2-m temperatures are shown in Table 3 in terms of RMSE and BIAS. Values clearly show that the trend identified for the reference station is similar also for all the other stations: RMSE decreases from simulation 1 to simulation 4. In fact, in simulation 1 RMSE ranges from ~7° to ~8.7°C, in simulation 2 it assumes values of ~3.5°C, in simulation 3 it decays to ~2°C while in simulation 4 it reaches values ranging from 1.4° to

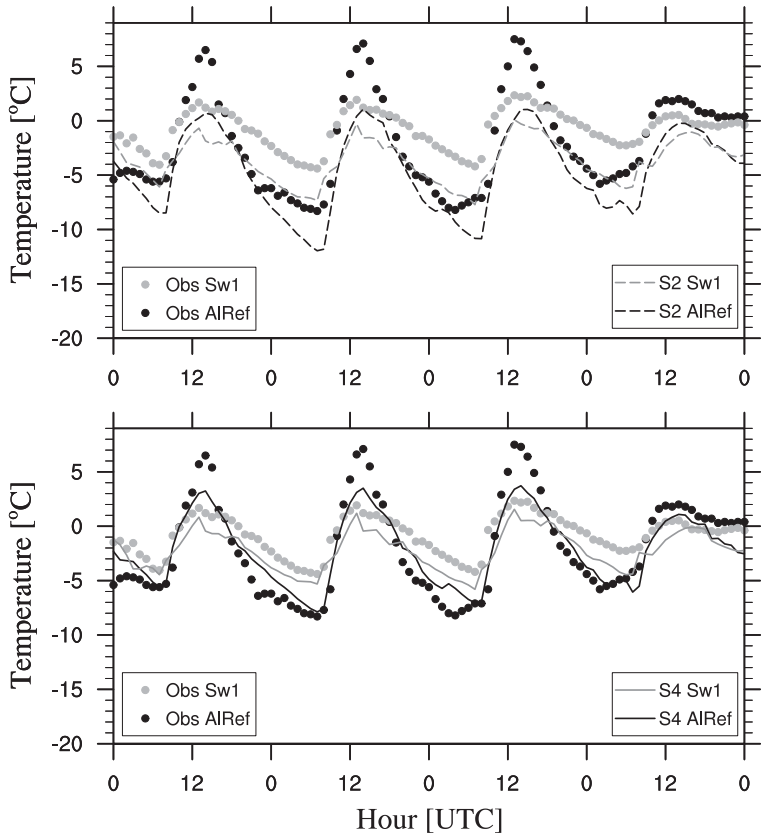

FIG. 7. Comparison of 2-m temperature at the valley floor and on the sidewall, observed and estimated with simulation 2 (standard Noah_MP LSM) and simulation 4 (modified Noah_MP LSM).

2.1°C. The BIAS values are generally positive, identifying an underestimation of the mean 2-m temperature in all the weather stations and they also confirm the improvements obtained with the modified simulations with respect to the standard simulations. The BIAS values obtained in simulation 4 are slightly higher than in simulation 3: indeed, overestimation of minima during nighttime and underestimation of daily peaks in simulation 3 tend to compensate each other, decreasing the resulting BIAS.

It is interesting to note that station Rov displays the highest RMSE and BIAS values in both the standard runs and higher indexes in simulation 4 than in simulation 3. This can be explained by considering the particular location of this weather station, which is situated in a rural area, but very close to the Rovereto city center. This location may influence the observations, as the urban heat island (Giovannini et al. 2011) affects the 2-m temperature nocturnal minima, which are higher than at all the other stations. The highest RMSE values of simulation 1 and 2 at Rov are then associated with the stronger underestimation of nocturnal temperature produced by the urban heat island. Accordingly, simulation 3, which tends to overestimate nighttime minima, performs better in this specific point. In principle, the effects determined by urban centers could be taken into account in the WRF Model by selecting an urban parameterization, but none of them is compatible with Noah_MP LSM and none was therefore applied in the present simulations.

Table 4 presents RMSE and BIAS for the radiation time series modeled and observed. The outgoing SW radiation presents high errors in both simulations 1 and 2, which are strongly reduced with the applied modifications. The RMSE is more than halved and the BIAS reaches smaller values, always negative, indicating a slight overestimation. A similar trend is found for the outgoing LW radiation, but, in this case, the variable is

TABLE 3. Statistical indexes calculated for 2-m temperature time series available at 9 different weather stations: root-mean-square error (RMSE) and bias (BIAS).

		RMSE (°C)				BIAS (°C)			
No.	Station	S1	S2	S3	S4	S1	S2	S3	S4
1	AlRef	7.22	3.12	2.36	1.70	6.63	2.68	0.14	0.18
2	Al1	8.10	3.90	2.20	1.69	7.59	3.67	0.74	1.18
3	Al2	7.52	3.25	2.23	1.45	6.91	2.95	0.29	0.47
4	Al3	7.54	3.58	1.92	1.80	7.09	3.11	0.57	0.77
5	Ronc	7.53	3.62	2.16	2.08	6.97	2.95	0.72	0.58
6	TNS	7.83	3.13	2.33	1.55	7.23	2.68	−0.48	−0.03
7	Rov	8.73	4.60	1.84	2.12	8.33	4.28	1.04	1.78
8	Sw1	7.63	3.69	2.41	1.81	7.09	3.54	1.65	1.60
9	Sw2	6.85	2.93	2.27	1.50	6.45	2.82	1.88	1.35
	Mean	7.66	3.54	2.19	1.75	7.14	3.19	0.73	0.88

underestimated. Improvements are smaller for the incoming LW radiation, because, as said before, this variable is only marginally and indirectly affected by the modifications of the LSMs.

In the Taylor diagrams presented in Fig. 8, R is related to the azimuthal angle, E'_n is proportional to the distance of the dots from the "OBS" point on the x axis, and σ_{Mn} is proportional to the radial distance from the origin. The top-left panel shows that, considering 2-m temperature at all stations, the modifications applied to the Noah model contribute to increase the correlation and to decrease E'_n. The standard deviation of the observations is overestimated by the standard run, while it is underestimated by the modified run. Indeed, as shown in Fig. 5, simulation 1 presents a wide thermal range (around an underestimated mean temperature), while simulation 3 strongly reduces it. The top-right panel shows that 2-m temperature time series calculated with the Noah_MP model are more grouped and lie closer to the curve of unitary normalized standard deviation. The thermal range is therefore better reproduced by the Noah_MP LSM than by the Noah model. The applied modifications contribute to further increase the correlation and to decrease E'_n but their effects are less effective than those obtained for the Noah simulations. Indeed, NoahMP performs better than Noah in its standard configuration and for this reason it is more difficult to further improve model results. A better performance of Noah_MP with respect to Noah was also found by Chen et al. (2014) and Kuribayashi et al. (2013), who assessed the ability of both models in simulating the snowpack evolution in time. The bottom panels of Fig. 8 present the Taylor diagrams for radiation time series. The graphics clearly show an improvement in both outgoing LW and SW radiation (especially from simulation 1), while the incoming LW radiation experiences slight changes only. The performance of the modified Noah and Noah_MP LSMs in predicting the radiation fluxes at the ground is in the end very similar, but yet the Noah_MP model better reproduces the 2-m temperature.

5. Discussion on the effects of each modification

To better highlight the influence on the model results of the different modifications implemented, Figs. 9 and 10 show the effects of each single modification on the outgoing SW and LW radiations and on the 2-m temperature. Figure 9 presents the effects of the modifications on the Noah simulations, providing an overview of the evolution from the standard simulation 1 to simulation 3. On the other hand, Fig. 10 shows the effects of the modifications on the Noah_MP simulations, highlighting the evolution from the standard simulation 2 to simulation 4. Therefore, the first intermediate step shown in Figs. 9 and 10 results from simulations run with only the modification to the land-use description, while the second intermediate step is from simulations run with coupled land-use and snow initialization modifications.

Focusing on simulations using Noah, Fig. 9 shows that an important decrease in the outgoing SW radiation is due to the modifications of land-use type, of initial snow cover, as well as to the implementation of the Livneh formula. In fact, cell albedo is a function of both snow cover fraction and vegetation land-use type: the modification of land-use type and of snow cover initialization has an impact on the cell snow cover fraction, decreasing with the change in land-use parameters and snow depth, while the modification to the implementation of the Livneh formula directly reduces the snow albedo. Furthermore each proposed modification has a significant impact on the 2-m temperature, increasing both nighttime minima and daytime maxima. In terms of 2-m temperature, the most significant effects arise from the decrease in the initial snow cover

TABLE 4. Statistical indexes calculated for the radiation time series available at the reference station AlRef: outgoing long- and shortwave radiation (LWout and SWout) and incoming longwave radiation (LWin). Root-mean-square error (RMSE) and bias (BIAS).

	RMSE ($W m^{-2}$)				BIAS ($W m^{-2}$)			
Variable	S1	S2	S3	S4	S1	S2	S3	S4
Swout	109.88	50.99	23.48	22.67	−59.08	−26.19	−11.85	−11.07
Lwout	52.18	17.11	21.29	8.37	32.69	27.65	16.69	21.7
Lwin	39.87	36.3	26.49	31.64	48.44	13.03	15.65	−2.81

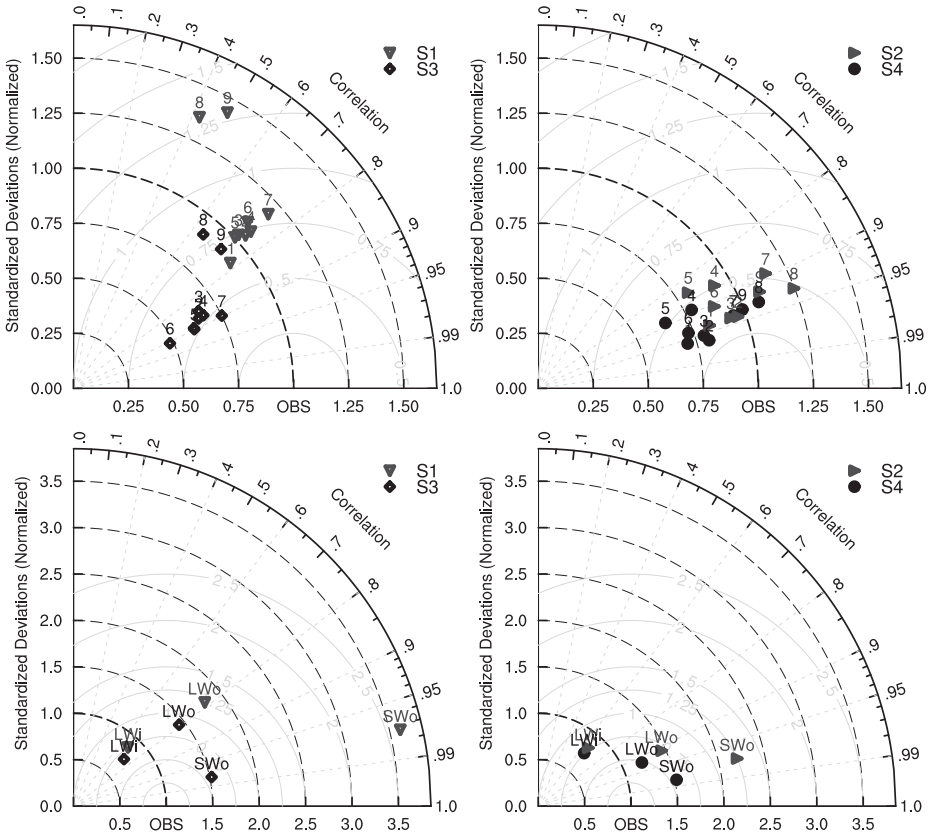

FIG. 8. Taylor diagrams describing the statistical patterns of the modeled 2-m temperature and radiation time series computed by simulations 1, 2, 3, and 4 with respect to the observations. (top) Results in terms of 2-m temperature, for each available weather station (from 1 to 9); (bottom) results in terms of outgoing LW (LWo) and SW (SWo) radiation and incoming LW (LWi) radiation. (left) Noah simulations S1 and S3 and (right) Noah_MP simulations S2 and S4.

height and from the changes in the implementation of the Livneh formula. It is interesting to note that the reduction of snow height in the simulation does have relevant positive effects in increasing the 2-m temperature even if the cell albedo does not strongly decrease: indeed, snow height reduction directly affects the calculation of the skin temperature (at the interface between the ground and the snow, if present), which tends to increase over a thinner snow cover; in addition to this, a thinner snow cover implies a different calculation of surface fluxes, especially the net upward heat flux. As 2-m temperature is calculated as a function of both the skin temperature and the surface heat flux, it is strongly affected by the modification of the initial snow depth. Figure 9 also shows that the major effect of the implemented modifications is a positive temperature shift, while the shape of the diurnal cycles is mostly preserved. In particular, in all cases Noah simulates a too fast decrease in the air temperature after sunset, probably due to a too fast decrease in the surface temperature, as also suggested by the rapid decrease in the outgoing LW radiation.

Noah_MP responds in a different way to the modifications (Fig. 10). Modifications to the land-use classification help in decreasing the outgoing SW radiation thanks to the presence of vegetation arising from the snow cover, which does not influence the SCF but directly influences the calculation of the cell albedo. This affects the 2-m temperature also, which slightly increases during daytime. The modification regarding the snow cover initialization intervenes again in reducing the cell albedo as the SCF decreases together with the snow depth as shown in Eq. (1). Accordingly, the 2-m temperature experiences an increase during both daytime and nighttime. Finally, eliminating the

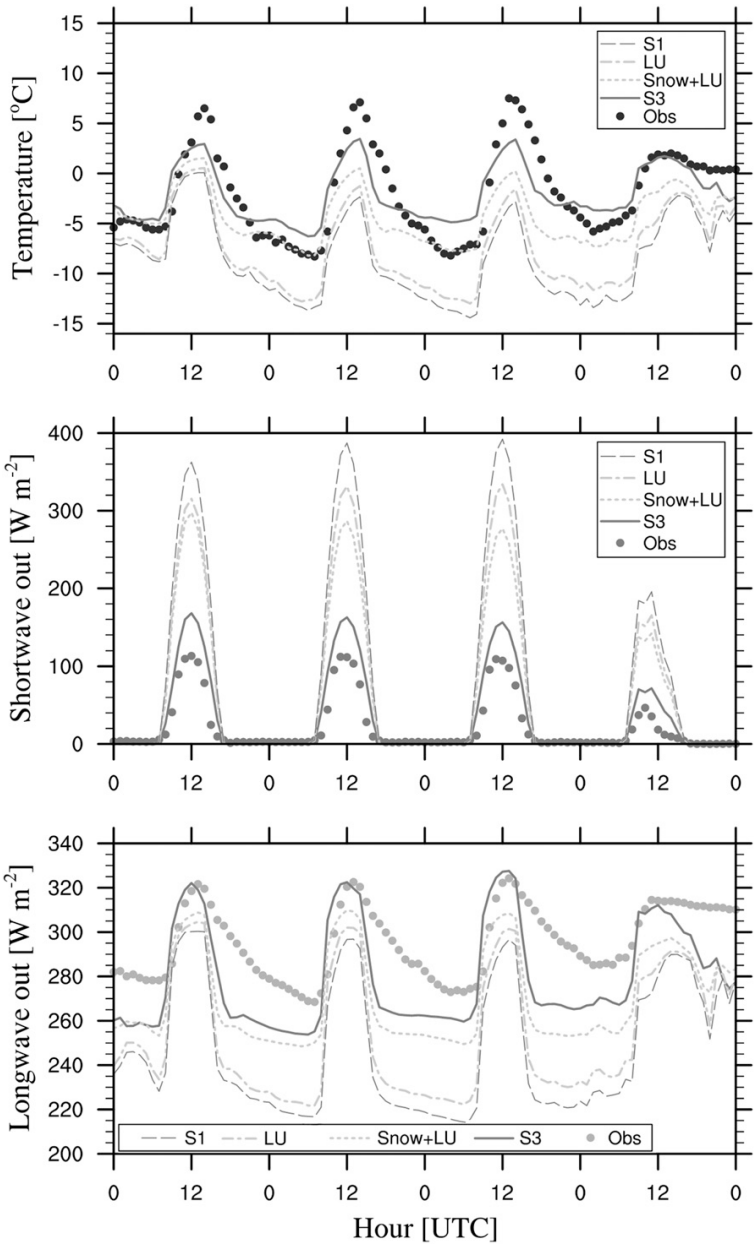

FIG. 9. The 2-m temperature and outgoing short- and longwave radiation observed and estimated adding one by one the proposed modifications, moving from simulation 1 (standard Noah LSM) to simulation 3 (modified Noah LSM): "Snow" refers to the modification applied to WRF snow cover initialization and "LU" refers to the modification to the land-use classification.

snow height threshold over which ground temperature cannot increase above 0°C causes a slight increase in the daily maxima on the first two days. It is interesting to notice that the modified simulations slightly overestimate the outgoing LW radiation at midday ($\sim$10 W m^{-2}). This overestimation implies, using the Stefan–Boltzmann's law, an overestimation of skin temperature of $\sim$2°C. Nonetheless, midday 2-m temperature

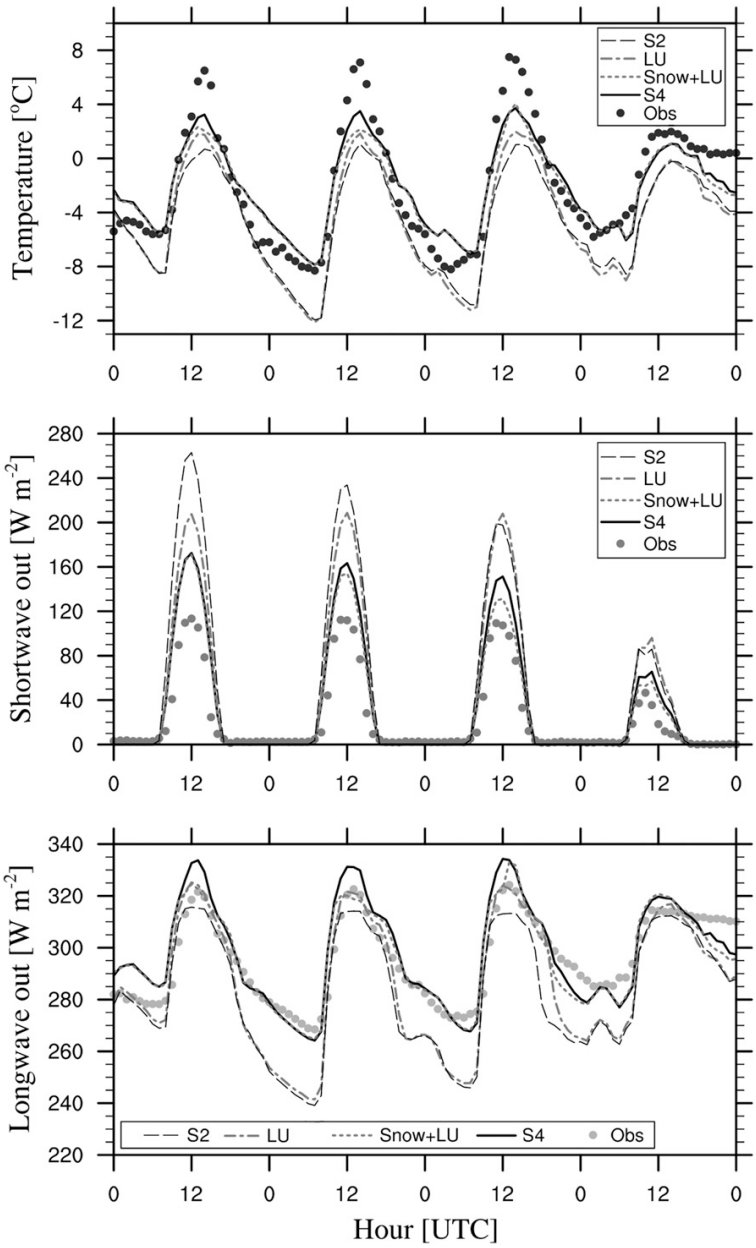

FIG. 10. The 2-m temperature and outgoing short- and longwave radiation observed and estimated adding one by one the proposed modifications, moving from simulation 2 (standard Noah_MP LSM) to simulation 4 (modified Noah_MP LSM): "Snow" refers to the modification applied to WRF snow cover initialization and "LU" refers to the modification to the land-use classification.

is yet underestimated: this fact implies that in the model the turbulence is overdamped during the day.

The above discussion highlights that both the Noah and Noah_MP LSMs are sensitive to very similar parameters, such as the initial snow depth, the land-use-type description, and the characteristics of the snowpack. In this case study, the Noah_MP LSM turns out to be the best performing scheme. The reasons for this better performance are primarily the improvements introduced in Noah_MP to reproduce the vegetation canopy layer, to calculate separately the vegetated and the bare ground surface temperatures, and to treat the snowpack. Indeed, other Noah_MP features were not tested here (e.g., no growing season is analyzed and therefore no new approaches on growing canopy are applied). Nevertheless, further accuracy is achieved by calibrating specific parameters of the model, such as the melting factor m and the land-use cover description parameters, in order to better fit the scale of the simulation and the characteristics of the investigated area. In conclusion, even though this case study takes advantage of few of the new features of Noah_MP, better results in both 2-m temperatures and outgoing SW radiation are achieved, if compared with the Noah LSM.

6. Conclusions and outlook

High-resolution numerical simulations with the WRF Model were performed to assess the performance of the Noah and Noah_MP LSMs over snow-covered ground in an Alpine valley. The two LSMs were evaluated by comparing their results against observations from a wintertime field campaign in the Adige valley, in the Italian Alps. As the aim of the present work was primarily the evaluation of the LSMs, comparisons were made in terms of 2-m temperature, both on the valley floor and on the sidewalls, and of incoming and outgoing SW and LW radiation in a reference station on the valley floor. Results from simulations using the default version of WRF, coupled with the two LSMs, highlighted a significant underestimation of the 2-m temperature and an overestimation of the outgoing SW radiation, due to an overestimation of the surface albedo. Given these results, both LSMs were analyzed in detail, in order to understand the possible causes of the recorded deficiencies. The first cause turned out to reside, in the present case, in the initialization of the snow cover depth, which was greatly overestimated. Another important role was played by the treatment of certain land-use classes under snow-covered ground. In particular, the IGBP class ''cropland'' is not representative of fruit tree cultures, which actually respond to a snow cover more like a broadleaf forest than like a cropland, which would be completely covered even under a thin snow layer. In addition to these corrections, other modifications were proposed, directly affecting the calculation of the cell albedo and of the 2-m temperature of both LSMs. In the Noah LSM modifications were introduced in the implementation of the Livneh procedure, in order to change the surface albedo calculation by intervening on the initial snow cover age and on the seasonal parameters describing the ground snow albedo evolution over time. In the Noah_MP scheme, changes were made in the snow cover upper limit, above which ground temperature cannot increase above 0°C.

Thanks to the applied modifications, improved results were obtained for both of the LSMs tested. In particular, in the modified simulations the outgoing SW radiation decreased, thus increasing the energy available in the surface energy budget, with a consequent increase in the 2-m temperature. Modifications had stronger impact on Noah LSM results. Nevertheless, the best agreement with observations was achieved with the modified Noah_MP LSM. Indeed, Noah_MP was able to properly catch nighttime temperature minima. Also, it can get closer to daytime maxima and to properly identify the nighttime ground-based thermal inversion and its evolution in time. All these improvements were quantitatively evaluated with a statistical analysis, which showed lowest RMSE and BIAS, and best agreement of the centered patterns with the observations for the modified simulations.

Results highlighted that particular attention must be paid to snow cover initialization when running wintertime simulations over complex terrain. This can be crucial for obtaining reliable results in these conditions, as accurate snow cover data are usually not available for high-resolution simulations, and the treatment of global reanalysis data may turn out to be misleading over complex terrain. Moreover, an appropriate land-use classification and description turned out to be very important for the calculation of the actual snow cover on the ground, with a considerable impact on the near-surface temperature. The calibration of the melting factor m also resulted to be significant in order to obtain an accurate estimate of the surface albedo through the calculation of a realistic value for the SCF. In simulations run at local scale, with a description of land cover types with a very high resolution, the value of m fixed within the Noah_MP model can lead to a severe underestimation of SCF and a consequent possible underestimation of surface albedo.

Modifications applied to the Noah scheme are also relevant, significantly improving the model performance. Moreover, these modifications are easy to introduce within the code, as the only parameters needed

are the age of the snow present on the ground at the beginning of the simulation and the season of the year. The modification proposed for the Noah_MP scheme regarding the calculation of surface temperature had actually less effect on the 2-m temperature if applied after the corrections to the snow initialization and to the land-use classification, resulting essentially in an increase in the maximum temperature. Nevertheless, this modification is more significant if applied when the cell presents no vegetated fraction.

It must be stressed, however, that the applied modifications have been tested only for this case study, and further testing over longer periods is needed in order to generalize their potential applicability in different regions and snowmelting conditions. Unfortunately, in this study, no measured data of snow depth were available in order to perform a direct comparison of model results against observations: for this reason testing against datasets with detailed snow-height observations would be of essential importance in order to highlight the effectiveness of the presented results. Nonetheless this work shows that the values of a few land surface parameters greatly influence model results and that an optimization of some of them can make the difference in applications over complex terrain. A refinement in the estimation of surface variables and of their effects in the evaluation of surface layer processes is of utmost importance for situations involving strong interactions of the surface with the lower atmosphere. An accurate simulation of quantities such as surface layer turbulence, near-surface stability, and surface layer height are key prerequisites for many applications, such as pollutant dispersion modeling in mountain valleys and basins. Indeed, the proposed improvements are expected to lead to better performance of WRF in providing a meteorological input for pollutant dispersion models, especially with the high resolution available from increasingly powerful computational resources, and required by very complex terrain situations (Giovannini et al. 2014b, 2017; Ragazzi et al. 2013).

Acknowledgments. Special thanks to Prof. Enrico Ferrero for his valuable suggestions and help in developing the statistical analysis for this paper. Meteotrentino, the Meteorological Office of the Autonomous Province of Trento, and the Edmund Mach Foundation are also kindly acknowledged for providing data from their permanent weather stations.

REFERENCES

Ball, J. T., I. E. Woodrow, and J. A. Berry, 1987: A model predicting stomatal conductance and its contribution to the control of photosynthesis under different environmental conditions. *Progress in Photosynthesis Research*, J. Biggins, Ed., Vol. 4, Springer, 221–224, doi:10.1007/978-94-017-0519-6_48.

Barlage, M., and Coauthors, 2010: Noah land surface model modifications to improve snowpack prediction in the Colorado Rocky Mountains. *J. Geophys. Res.*, **115**, D22101, doi:10.1029/2009JD013470.

Bonan, G. B., 1996: A land surface model (LSM version 1.0) for ecological, hydrological, and atmospheric studies: Technical description and user's guide. NCAR Tech. Note NCAR/TN-417+STR, National Center for Atmospheric Research, Boulder, CO, 150 pp.

Chen, F., and J. Dudhia, 2001: Coupling an advanced land surface-hydrology model with the Penn State–NCAR MM5 modeling system. Part I: Model implementation and sensitivity. *Mon. Wea. Rev.*, **129**, 569–585, doi:10.1175/1520-0493(2001)129<0569:CAALSH>2.0.CO;2.

——, and Coauthors, 1996: Modeling of land surface evaporation by four schemes and comparison with FIFE observations. *J. Geophys. Res.*, **101**, 7251–7268, doi:10.1029/95JD02165.

——, and Coauthors, 2014: Modeling seasonal snowpack evolution in the complex terrain and forested Colorado Headwaters region: A model intercomparison study. *J. Geophys. Res. Atmos.*, **119**, 13 795–13 819, doi:10.1002/2014JD022167.

Collatz, G. J., J. T. Ball, C. Grivet, and J. A. Berry, 1991: Physiological and environmental regulation of stomatal conductance, photosynthesis and transpiration: A model that includes a laminar boundary layer. *Agric. For. Meteor.*, **54**, 107–136, doi:10.1016/0168-1923(91)90002-8.

——, M. Ribas-Carbo, and J. A. Berry, 1992: Coupled photosynthesis-stomatal conductance model for leaves of C_4 plants. *Aust. J. Plant Physiol.*, **19**, 519–538, doi:10.1071/PP9920519.

de Ferranti, J., 2013: 30-m topography dataset. Accessed March 2015, http://viewfinderpanoramas.org/.

de Franceschi, M., and D. Zardi, 2009: Study of wintertime high pollution episodes during the Brenner-South ALPNAP measurement campaign. *Meteor. Atmos. Phys.*, **103**, 237–250, doi:10.1007/s00703-008-0327-2.

Dirmeyer, P. A., X. Gao, M. Zhao, Z. Guo, T. Oki, and N. Hanasaki, 2006: SGSWP-2: Multimodel analysis and implications for our perception of the land surface. *Bull. Amer. Meteor. Soc.*, **87**, 1381–1397, doi:10.1175/BAMS-87-10-1381.

Dudhia, J., 1989: Numerical study of convection observed during the Winter Monsoon Experiment using a mesoscale two-dimensional model. *J. Atmos. Sci.*, **46**, 3077–3107, doi:10.1175/1520-0469(1989)046<3077:NSOCOD>2.0.CO;2.

Ek, M. B., K. E. Mitchell, Y. Lin, E. Rogers, P. Grunmann, V. Koren, G. Gayno, and J. D. Tarpley, 2003: Implementation of Noah land surface model advances in the National Centers for Environmental Prediction operational mesoscale Eta model. *J. Geophys. Res.*, **108**, 8851, doi:10.1029/2002JD003296.

European Environment Agency, 2006: 100-m landuse cover data. European Environment Agency, http://land.copernicus.eu/pan-european/corine-land-cover/clc-2006/view.

Giovannini, L., D. Zardi, and M. de Franceschi, 2011: Analysis of the urban thermal fingerprint of the city of Trento in the Alps. *J. Appl. Meteor. Climatol.*, **50**, 1145–1162, doi:10.1175/2010JAMC2613.1.

——, ——, ——, and F. Chen, 2014a: Numerical simulations of boundary-layer processes and urban-induced alterations in an Alpine valley. *Int. J. Climatol.*, **34**, 1111–1131, doi:10.1002/joc.3750.

——, G. Antonacci, D. Zardi, L. Laiti, and L. Panziera, 2014b: Sensitivity of simulated wind speed to spatial resolution over complex terrain. *Energy Procedia*, **59**, 323–329, doi:10.1016/j.egypro.2014.10.384.

——, L. Laiti, S. Serafin, and D. Zardi, 2017: The thermally driven diurnal wind system of the Adige Valley in the Italian Alps. *Quart. J. Roy. Meteor. Soc.*, **143**, 2389–2402, doi:10.1002/qj.3092.

Grell, G. A., and D. Dévényi, 2002: A generalized approach to parameterizing convection combining ensemble and data assimilation techniques. *Geophys. Res. Lett.*, **29**, doi:10.1029/2002GL015311.

Hall, D. K., and G. A. Riggs, 2016: MODIS/*Terra* snow cover daily L3 global 500m grid, version 6 [February 2006, Europe]. NASA National Snow and Ice Data Center Distributed Active Archive Center, Boulder, Colorado, accessed March 2017, doi:10.5067/MODIS/MOD10A1.006.

Heimann, D., and Coauthors, 2007: Air pollution, traffic noise and related health effects in the alpine space—A guide for authorities and consulters. ALPNAP Comprehensive Report. Tech. Rep., Department of Civil, Environmental and Mechanical Engineering, University of Trento, Trento, Italy, 335 pp., http://www.imk-ifu.kit.edu/downloads/institute/ALPNAP_electronic_version.pdf.

Hong, S.-Y., J. Dudhia, and S.-H. Chen, 2004: A revised approach to ice microphysical processes for the bulk parameterization of clouds and precipitation. *Mon. Wea. Rev.*, **132**, 103–120, doi:10.1175/1520-0493(2004)132<0103:ARATIM>2.0.CO;2.

——, Y. Noh, and J. Dudhia, 2006: A new vertical diffusion package with an explicit treatment of entrainment processes. *Mon. Wea. Rev.*, **134**, 2318–2341, doi:10.1175/MWR3199.1.

Jin, J., and N. L. Miller, 2007: Analysis of the impact of snow on daily weather variability in mountainous regions using MM5. *J. Hydrometeor.*, **8**, 245–258, doi:10.1175/JHM565.1.

——, ——, and N. Schlegel, 2010: Sensitivity study of four land surface schemes in the WRF Model. *Adv. Meteor.*, **2010**, 167436, doi:10.1155/2010/167436.

Jordan, R., 1991: A one-dimensional temperature model for a snow cover. Special Rep. SR 91-16, Cold Region Research and Engineering Lab., U.S. Army Corps. of Engineers, Hanover, NH, 61 pp.

Koren, V., J. Schaake, K. Mitchell, Q. Duan, F. Chen, and J. Baker, 1999: A parameterization of snowpack and frozen ground intended for NCEP weather and climate models. *J. Geophys. Res.*, **104**, 19 569–19 585, doi:10.1029/1999JD900232.

Kuribayashi, M., N. J. Noh, T. M. Saitoh, I. Tamagawa, Y. Wakazuki, and H. Muraoka, 2013: Comparison of snow water equivalent estimated in central Japan by high-resolution simulations using different land-surface models. *SOLA*, **9**, 148–152, doi:10.2151/sola.2013-033.

Livneh, B., Y. Xia, K. E. Mitchell, M. B. Ek, and D. P. Lettenmaier, 2010: Noah LSM snow model diagnostics and enhancements. *J. Hydrometeor.*, **11**, 721–738, doi:10.1175/2009JHM1174.1.

Mahrt, L., and M. Ek, 1984: The influence of atmospheric stability on potential evaporation. *J. Climate Appl. Meteor.*, **23**, 222–234, doi:10.1175/1520-0450(1984)023<0222:TIOASO>2.0.CO;2.

——, and H. L. Pan, 1984: A two-layer model of soil hydrology. *Bound.-Layer Meteor.*, **29**, 1–20, doi:10.1007/BF00119116.

Meloysund, V., B. Leira, K. V. Hoiseth, and K. R. Liso, 2007: Predicting snow density using meteorological data. *Meteor. Appl.*, **14**, 413–423, doi:10.1002/met.40.

Mlawer, E. J., S. J. Taubman, P. D. Brown, M. J. Iacono, and S. A. Clough, 1997: Radiative transfer for inhomogeneous atmospheres: RRTM, a validated correlated-k model for the longwave. *J. Geophys. Res.*, **102**, 16 663–16 682, doi:10.1029/97JD00237.

Niu, G.-Y., and Z.-L. Yang, 2006: Effects of frozen soil on snowmelt runoff and soil water storage at a continental scale. *J. Hydrometeor.*, **7**, 937–952, doi:10.1175/JHM538.1.

——, and ——, 2007: An observation-based formulation of snow cover fraction and its evaluation over large North American river basins. *J. Geophys. Res.*, **112**, D21101, doi:10.1029/2007JD008674.

——, ——, R. E. Dickinson, L. E. Gulden, and H. Su, 2007: Development of a simple groundwater model for use in climate models and evaluation with gravity recovery and climate experiment data. *J. Geophys. Res.*, **112**, D07103, doi:10.1029/2006JD007522.

——, and Coauthors, 2011: The community Noah land surface model with multiparameterization options (Noah_MP): 1. Model description and evaluation with local-scale measurements. *J. Geophys. Res.*, **116**, D12109, doi:10.1029/2010JD015139.

Noilhan, J., and S. Planton, 1989: A simple parameterization of land surface processes for meteorological models. *Mon. Wea. Rev.*, **117**, 536–549, doi:10.1175/1520-0493(1989)117<0536:ASPOLS>2.0.CO;2.

Oleson, K. W., and Coauthors, 2013: Technical description of version 4.5 of the Community Land Model (CLM). NCAR Tech. Note NCAR/TN-503+STR, National Center for Atmospheric Research, Boulder, CO, 422 pp., accessed February 2016, doi:10.5065/D6RR1W7M.

Pan, H.-L., and L. Mahrt, 1987: Interaction between soil hydrology and boundary-layer development. *Bound.-Layer Meteor.*, **38**, 185–202, doi:10.1007/BF00121563.

Pomeroy, J. W., and E. Brun, 2001: Physical properties of snow. *Snow Ecology: An Interdisciplinary Examination of Snow-Covered Ecosystems*, H. G. Jones et al., Eds., Cambridge University Press, 45–118.

Qu, X., and A. Hall, 2006: Assessing snow albedo feedback in simulated climate change. *J. Climate*, **19**, 2617–2630, doi:10.1175/JCLI3750.1.

Ragazzi, M., W. Tirler, G. Angelucci, D. Zardi, and E. Rada, 2013: Management of atmospheric pollutants from waste incineration processes: The case of Bozen. *Waste Manage. Res.*, **31**, 235–240, doi:10.1177/0734242X12472707.

Sakaguchi, K., and X. Zeng, 2009: Effects of soil wetness, plant litter, and under-canopy atmospheric stability on ground evaporation in the Community Land Model (CLM3.5). *J. Geophys. Res.*, **114**, D01107, doi:10.1029/2008JD010834.

Schaake, J. C., V. I. Koren, Q. Y. Duan, K. Mitchell, and F. Chen, 1996: A simple water balance model (SWB) for estimating runoff at different spatial and temporal scales. *J. Geophys. Res.*, **101**, 7461–7475, doi:10.1029/95JD02892.

Sellers, P. J., and Coauthors, 1996: A Revised Land Surface Parameterization (SiB2) for atmospheric GCMS. Part I: Model formulation. *J. Climate*, **9**, 676–705, doi:10.1175/1520-0442(1996)009<0676:ARLSPF>2.0.CO;2.

Skamarock, W. C., and Coauthors, 2008: A description of the Advanced Research WRF version 3. NCAR Tech. Note NCAR/TN-475+STR, 113 pp., http://dx.doi.org/10.5065/D68S4MVH.

Su, H., Z.-L. Yang, G.-Y. Niu, and R. Dickinson, 2008: Enhancing the estimation of continental-scale snow water equivalent by assimilating MODIS snow cover with the ensemble Kalman filter. *J. Geophys. Res.*, **113**, D08120, doi:10.1029/2007JD009232.

Taylor, K. E., 2001: Summarizing multiple aspects of model performance in a single diagram. *J. Geophys. Res.*, **106**, 7183–7192, doi:10.1029/2000JD900719.

Verseghy, D. L., 1991: Class—A Canadian land surface scheme for GCMS. I. Soil model. *Int. J. Climatol.*, **11**, 111–133, doi:10.1002/joc.3370110202.

Xue, Y., P. J. Sellers, J. L. Kinter, and J. Shukla, 1991: A simplified biosphere model for global climate studies. *J. Climate*, **4**, 345–364, doi:10.1175/1520-0442(1991)004<0345:ASBMFG>2.0.CO;2.

Yang, Z.-L., and Coauthors, 2011: The community Noah land surface model with multiparameterization options (Noah-MP): 2. Evaluation over global river basins. *J. Geophys. Res.*, **116**, D12110, doi:10.1029/2010JD015140.

Zängl, G., 2012: Extending the numerical stability limit of terrain-following coordinate models over steep slopes. *Mon. Wea. Rev.*, **140**, 3722–3733, doi:10.1175/MWR-D-12-00049.1.

Zhang, H., Z. Pu, and X. Zhang, 2013: Examination of errors in near-surface temperature and wind from WRF numerical simulations in regions of complex terrain. *Wea. Forecasting*, **28**, 893–914, doi:10.1175/WAF-D-12-00109.1.